UNIVERSITY OF CALIFORNIA

Los Angeles

Demand Fragility Surfaces for Bridges in Liquefied Laterally Spreading Ground

A dissertation submitted in partial satisfaction of the
requirements for the degree Doctor of Philosophy
in Civil Engineering

by

Pirooz Kashighandi

2009

The dissertation of Pirooz Kashighandi is approved:

Scott A. Ashford

Jonathan P. Stewart

Mladen Vucetic

Jian Zhang

Scott J. Brandenberg, Committee Chair

University of California, Los Angeles

2009

To my parents and my sister

TABLE OF CONTENTS

LIST OF FIGURES

LIST OF TABLES

ACKNOWLEDGEMENTS

Funding for this work is provided by the Pacific Earthquake Engineering Research Center under project no. 2572005, and by the Pacific Earthquake Engineering Research Center Lifelines program under project task no. 9C. The contents of this dissertation do not necessarily represent a policy of either agency or endorsement by the state or federal government.

My PhD experience at UCLA has been a great journey, and many people played a role in making this journey so great. First, I would like to thank my PhD advisor, Professor Scott Brandenberg, who has taught me all the fundamentals and the tools required for my academic work. I enjoyed our interesting discussions on the topic that guided me in the direction of finding the right solutions. I am thankful to him for being patient during challenging times, and grateful to him for providing funding for me throughout the years.

I would also like to thank Professor Zhang for providing guidance on the structural aspects of my research topic, and for being a great company on our trips to Sacramento for the coordination meetings. I was extremely lucky to have none other than the experts on the topic on my committee. My other committee members Professors Jonathan Stewart, Mladen Vucetic and Scott Ashford, all provided great guidance and feedback on my research, and I appreciate their help and guidance on my work.

I would also like to thank the coordinator of the project Mr. Tom Shantz, for providing resources for my research and coordinating meetings with other Caltrans engineers which also helped in guiding the research in the right direction. Mr. Yili Huo helped me significantly in structural modeling of the bridges as well as providing the appropriate structural input parameters. His help is greatly appreciated. Numerical modeling analyses were performed by utilizing the Hoffman2 cluster of the academic technology services (ATS) at UCLA. Mr. Prakashan Korambath at ATS helped compile the OpenSees source code for UNIX and taught me how to utilize the cluster. His help is also greatly valued.

In the four years of my PhD experience, I made some great friends who created joyous memories for me and kept me going during occasional tough times. I met Salih Tileylioglu in my first quarter in UCLA and soon we connected and became best friends. His presence definitely made my time at UCLA a lot more pleasant. I thank him very much for his friendship. Anne Lemnitzer has also been a great friend throughout my graduate study in UCLA. She always cheered me up and brought a smile to my face. I would like to thank her for her friendship as well. Lisa Star, Christine Goulet, Joseph Coe and Timothy Ancheta were my wonderful officemates. I would like to thank them all for being such great friends and officemates. Roshanak Omrani, Payman Khalili Tehrani, Ahmadreza Mortezaie and Derek Skolnik were only a few of my other great friends at UCLA. I would like to thank them all for their friendship.

My undergraduate academic advisor Prof. Donald Leitch was the best academic advisor and a great man. He always accommodated all my academic needs during my undergraduate years at UMASS Lowell and provided great support during those years. He made my time at UMASS very pleasant and I am very grateful to him for his support.

Finally, I would like to thank my wonderful parents, Ali Akbar and Afsa and my sweet and loving sister Taravat, for their love and support throughout my life. Their constant unconditional love and support is what kept me going through the years. I am truly lucky and grateful for having such a wonderful family and I love them very much.

VITA

August 12, 1981	Born, Rasht, Iran
2004	B.S. Civil and Environmental Engineering University of Massachusetts, Lowell
2005	M.S. Civil and Environmental Engineering Focus on Geotechnical Engineering University of California, Berkeley
2005-2009	Graduate Research Assistant and Teaching Assistnant Department of Civil Engineering University of California, Los Angeles

PUBLICATIONS

Zhang, J., Huo, Y., Brandenberg, S.J., and Kashighandi, P. (2008). "Effects of Structural Characterizations on Fragility Functions of Bridges Subject to Seismic Shaking and Lateral Spreading." Earthquake Engineering and Engineering Vibrations. 7(4):369-382.

Kashighandi, P., Brandenberg, S.J., Zhang, J., Huo, Y. and Zhao, M., "Fragility of old-vintage continuous California bridges to liquefaction and lateral spreading", Proc. 14th World Conference on Earthquake Engineering, Beijing, China, October 2008.

Zhang, J., Huo, Y., Brandenberg, S.J. and Kashighandi, P., "Fragility Functions of Different Bridge Types Subject to Seismic Shaking and Lateral Spreading", Proc. 14th World Conference on Earthquake Engineering, Beijing, China, October 2008.

Zhang, J., Huo, Y., Kashighandi, P., and Brandenberg, S.J. (2008). "Effects of structural characterization on fragility functions of bridges subjected to seismic shaking and lateral spreading." Proc. Sixth National Seismic Conference on Bridges and Highways, Charleston, SC, July.

Brandenberg, S.J., Kashighandi, P., Zhang, J., Huo, Y., and Zhao, M. (2008). "Sensitivity study of an older-vintage bridge subjected to lateral spreading." Proc. 4th Conf. Geotechnical Earthquake Engineering and Soil Dynamics, Geotechnical Special Publication No. 181.

Kashighandi, P., and Brandenberg, S.J. (2007) "Fragility curves for lateral spreading-induced damage to the Landing Road Bridge", Proc. 4th International Conference on Urban Earthquake Engineering. Center for Urban Earthquake Engineering, Tokyo Institute of Technology, Tokyo, Japan.

ABSTRACT OF THE DISSERTATION

Demand Fragility Surfaces for Bridges in Liquefied Laterally Spreading Ground

by

Pirooz Kashighandi
Doctor of Philosophy in Civil Engineering
University of California, Los Angeles, 2009
Professor Scott J. Brandenberg, Chair

The purpose of this research has been to evaluate the fragility of bridges in liquefied laterally spreading ground and generate demand fragility surfaces for different engineering demand parameters (EDP) at a range of values for each of the EDPs. The analyses have been performed numerically using the finite element program OpenSees. The method used in performing the analyses is the "global equivalent static analysis method", in which the entire structural components of the bridge are modeled and the lateral spreading displacement demands of the soil are modeled using nonlinear soil-structure (p-y, t-z, and q-z) springs with considerations for liquefaction.

To capture the variability in the bridge and site properties, distributions were assigned to all of the input parameters of the models. The distributions were selected based on the available information and the bridge models represented realistic scenarios. The ground displacement patterns applied on the bridge were also varied to represent the natural variability of the ground displacement patterns.

Bridge models for different classes of bridges were created. Roughly 1000 analyses were performed for bridges of every class. During the analyses the maximum free-field ground displacements were recorded at different values of several EDPs. Demand fragility function which is the probability of exceeding a certain EDP value for a given EDP at a given value of ground displacement, was generated for different values of different EDPs. Fragility functions for different EDP values were fitted by a single "Demand Fragility Surface" per EDP. Each surface was characterized by only 6 fitting parameters.

The results of the demand fragility surfaces showed that the pre-1971 bridges were more fragile that the newer bridges, due to lack of proper transverse reinforcement in the piers and poor quality piles. Also it was found that simply-supported bridges mobilize less demand on the piers (due to rotational flexibility at the top), while they often have more demand at foundation and abutment level (i.e. pile cap and abutment displacement and rotation). The damages in different components of the continuous bridges were better correlated, since this type of bridges is more effective in transferring demands.

1 Introduction

1.1 Liquefaction and Lateral Spreading

Liquefaction is the process of substantial strength loss of loose saturated cohesionless soils during undrained loading. The tendency for densification in saturated loose soils during drained loading is expressed as generation of excess pore pressures and consequently reduction of effective stresses and loss of strength during undrained loading. Earthquakes are a common cause of liquefaction and numerous problems can rise in the event that soils are liquefied. Issues like stability failures, lateral spreading, and post-earthquake settlements are some of the examples of damages that are caused as a result of liquefaction. This dissertation focuses on lateral spreading as a result of liquefaction and its damages to bridges.

Lateral spreading is the permanent lateral deformation of soils during liquefaction, typically on the order of centimeters up to a few meters. Lateral spreading occurs when ground shaking causes the driving shear stresses demand to temporarily exceed the undrained shear strength, thereby causing an accumulation of displacement in the direction of static shear stress. Static shear stresses are present in slopes or in level ground located near a free-face (usually adjacent to rivers, lakes, etc).

Lateral movement of the soil can result in a wide range of structural damage, ranging from none, when ground displacements are small and/or the structure is resistant to lateral spreading forces, to collapse when lateral spreading demands exceed structural capacity, significantly.

1.2 Case Histories of Damage to Pile Foundations in Lateral Spreads

Many cases of damage to structures related to liquefaction and lateral spreading are observed during and after earthquakes over the years. A large number of these case histories of damage were observed on pile-supported bridges and other structures. A classic example of liquefaction and liquefaction-related damage is the 1964 earthquake in Niigata, Japan. The reported and documented examples of damage to structures during this earthquake are numerous. Figure 1.1 shows the damage to Showa bridge during the 1964 Niigata earthquake. Excessive lateral deformation of the liquefiable soils that supported the bridge caused damage to the pile foundations and the resulting large deformations of the piers cause the decks of bridge to unseat and fall into the river.

Another case of lateral spreading is the damage to the wharf of the port of Oakland during the 1989 Loma Prieta earthquake (Figs 1.2 to 1.4). Spreading of the rock fill material on top of liquefied loose hydraulic fill imposed significant loads on the piles that supported the wharf. The battered piles supporting the wharf near its connection with the soil had a small unsupported length and carried some fraction of the lateral load demands in axial loads due to the frame interaction of the battered piles. The stiff piles attracted large loads that exceeded their capacity and were damaged at the connection beneath the wharf (Figure 1.4). The formation of a gap at the wharf-to-soil connection caused the crane rails to separate, rendering them useless for moving cargo onto and off of freighter ships. Damage to ports causes significant economic loss due to the importance of imports and exports for local, national, and global economies

It should be noted that the case histories of damage are not limited to older structures where seismic performance and the consequences of liquefaction were not considered.

Nishinomiya Bridge in Kobe is an example of a modern bridge where out-of-phase movement of the bridge abutments, due at least in part to the liquefaction and lateral spreading apparent in Figure 1.5, caused one of the span decks to fall off its seat during the 1995 Kobe earthquake. The bents of this bridge are on caissons rather than driven pile foundations, but the fundamental mechanisms of load transfer bear some similarities to load transfer against pile foundations.

Fortunately, not all case histories of damage to bridges and other structures that undergo lateral spreading are as dramatic as the abovementioned examples. In many cases the bridge or structure was subjected to large lateral spreading ground displacements and yet survived with minor to intermediate levels of repairable damage. Even though cases with little or no damage are often not well-documented or investigated, they are equally important from the engineering standpoint, because they can provide valuable information about the factors that were responsible for the good performance of the bridge under such severe demand. Therefore, analyzing such case histories is very insightful in understanding the fundamental mechanisms of damage to structures under lateral spreading.

One of the case histories where the bridge suffered intermediate levels of damage is the case of Landing Road Bridge in Whakatane, New Zealand (Figure 1.6). During the 1987 Edgecumbe earthquake, the ground liquefied and spread laterally up to 2 m, over 5 spans in the left bank of the bridge. The bridge damage was moderate with cracks in some of the piers and near the head of some of the piles, about 1 % rotation at some of the piers, and 0.3 to 0.5 meter of ground settlements at one of the abutments and also some buckled footpaths which was a sign of compressive force in the superstructure (Berrill et al. 2001). The bridge was repaired by epoxy injections into the concrete cracks, and it remained in service following the earthquake (after the approach fill had been repaired, providing access onto the bridge at the left abutment).

1.3 Implications for Caltrans Bridges

The California Department of Transportation (Caltrans) owns about 13,000 bridges constructed since 1900. Figure 1.7 shows the distribution of California bridges based on the year of construction, extracted from National Bridge Inventory (NBI) database. It is evident from the figure that majority of the bridges in California were built before 1971, the year in which San Fernando earthquake caused great damage to many structures. Damage caused by the San Fernando earthquake resulted in major improvements to the building codes, including addition of many seismic provisions to the codes. Since most of the California bridges were constructed prior to 1971, with limited considerations for seismic loading a significant number of these bridges may be susceptible to damage under earthquake shaking. Many of the older-vintage bridges have been retrofitted to improve their performance during earthquake-induced ground shaking, but it is unclear to what extent these retrofits will improve performance in laterally spreading ground.

Even after seismic codes were introduced for design of newer bridges, the knowledge of liquefaction and liquefaction-induced damages (e.g. lateral spreading) was very limited and therefore, the bridges were not considered for the types of loadings that could be imposed on them in an event of an earthquake and subsequently liquefaction and lateral spreading of the underlying soils. Methods for analyzing bridges in liquefied ground have only recently emerged following the 1995 Kobe earthquake and a concerted research effort using centrifuge models, 1-g shake table tests, blast-induced field liquefaction tests, and case history analysis.

Therefore, many of the older bridges as well as some of the newer bridges may be susceptible to damage or complete loss in an event of an earthquake, if the underlying soils liquefy. However, the extent of anticipated damage from earthquake-induced liquefaction and lateral spreading is not currently known, and particular bridge configurations and locations that are susceptible to such damage have not been identified. Analyzing the entire suite of 13,000 bridges is not feasible. A screening procedure is therefore required to identify the bridges that (1) are in regions where liquefaction and lateral spreading might be expected to accompany earthquake shaking (the focus of a companion research study) and (2) are structurally most susceptible to the loads imposed by liquefaction and lateral spreading (the focus of this research).

Caltrans has undertaken an extensive seismic retrofit program in which bridge structures were screened based on structural response to ground shaking, while vulnerability to liquefaction and lateral spreading was not considered. The potential damage to the bridge during lateral spreading depends on physical properties of the bridge (structural and geometric configuration), the mechanical characteristics and deformation potential of the soils underlying the bridge, and ground motion. The primary mechanism of damage to bridges founded on liquefiable soils is large displacements of the bridge components in response to large ground displacements. Mechanisms of damage to bridges as a result of lateral spreading include three components as are described below:

- Large Relative Displacements between the superstructure and the substructure: This mode of damage applies to bridges with simply-supported superstructure where the superstructure rests on bearings atop the piers and abutments. During lateral spreading, different foundation components can move different amounts in different directions, thereby causing relative displacement between the superstructure and substructure components. Large relative displacements could result in “un-seating” of the decks of the bridge, and consequently loss of the bridge. This is the mechanism that occurred in Showa bridge and Nishinomiya bridge.

- Excessive Curvature Ductility in Bridge Piers: Relative displacements between the pile caps and the superstructure can cause damage to bridge piers. Large drift in the piers could cause damage to the piers due to a combination of flexural and shear demands. Modern ductile bridges usually tolerate larger amounts of drift than older more brittle bridges. Effects of mobilizing high levels of curvature ductility usually results in spalling of the concrete and loss of axial load capacity of the bridge in flexural mode and rupture of the reinforcing steel in shear mode. For example, some cracks were observed in the shear walls at Landing Road Bridge due to mobilization of some curvature ductility.
- Excessive Curvature Ductility in Piles: During the lateral spreading, large demands can be induced in piles due to the kinematic demands imposed by the soil. Damage to the piles would be expected to result in damage to the piers and bridge superstructure caused by settlement and excessive lateral deformation of the pile caps. The extent of damage to the above-ground bridge components would depend on the bridge configuration, and in some cases pile damage may not cause damage to the above ground bridge components. Damage to the piles in the form of cracks near the pile cap was observed at some piers and at the left abutment of Landing Road Bridge. Piles beneath the Niigata family courthouse building were severely damaged in the 1964 Niigata earthquake, but the damage was only discovered about 20

years later when the foundation was excavated. These examples illustrate the difficulty in relating structural damage to foundation damage.

On the basis of the vulnerability of the Caltrans bridges to the types of loading and mechanisms of damage described above, the need for a screening tool that can evaluate the susceptibility of the bridges to damage is evident. The screening tool consists of two criteria:

1. Is the bridge located in liquefiable soils?
2. How susceptible is the bridge, if located in liquefiable soils?

The first criteria is dealt with in a separate project by Keith Knudsen and his colleagues at the California Geological Survey, which focuses on whether or not the bridge is founded on materials that are susceptible to liquefaction and if they are, what is the extent of lateral ground displacement at the site of the bridge. The deliverable from this project will be a prediction of ground deformation potential at all 13,000+ Caltrans bridge sites.

This dissertation deals with the latter criteria by evaluating the bridges for susceptibility to lateral spreading by investigating various bridges with different structural properties and different soil properties under different load combinations. Several demand fragility surfaces will be developed which can enable Caltrans to assess the fragility of their bridges based on simple geotechnical or structural properties, such as vintage of the bridge, structural configurations, thickness of the crust, diameter of the piles, etc. Therefore, the bridges are classified into several different classes, and a large number of bridges within every class are analyzed, so that the relative susceptibility of the bridges of different classes could be investigated. The results of this study, when combined with Knudsen's ground displacement potential map, will provide a rational means for screening Caltrans bridges for damage potential due to liquefaction and lateral spreading.

1.4 Available Fragility Functions

A fragility function has traditionally been defined as a probabilistic relation between a damage measure (DM) and an engineering demand parameter (EDP), represented as a probability of exceeding some DM given some EDP. However, fragility functions have also been used to represent the probability of exceeding an EDP given and intensity measure (IM), or as probability of exceeding a DM given an IM. Figure 1.8 shows a schematic of a fragility curves for bridges with different vintages that relates DM to IM.

In HAZUS (1999), which is a software program for loss estimation developed by FEMA, damage states for bridges are divided into five states and are defined as follows:

1) **None (ds_1):** is defined by no damage to the bridge
2) **Slight/Minor Damage (ds_2):** is defined by minor cracking and spalling to the abutment, cracks in shear keys at abutments, minor spalling and cracks at hinges, minor spalling at the column (damage required no more than cosmetic repair) or minor cracking to the deck.

3) **Moderate Damage (ds_3):** is defined by any column experiencing moderate (shear cracks) cracking and spalling (column structurally still sound), moderate movement of the abutment (<2”), extensive cracking and spalling of shear keys, any connection having cracked shear keys or bent bolts, keeper bar failure without unseating, rocker bearing failure or moderate settlement of the approach.

4) **Extensive Damage (ds_4):** is defined by column degrading without collapse – shear failure – (column structurally unsafe), significant residual movement at connections, or major settlement approach, vertical offset of the abutment, differential settlement at connections, shear key failure at abutments.

5) **Complete Damage (ds_5):** is defined by any column collapsing and connection losing all bearing support, which may lead to imminent deck collapse, tilting of the substructure due to foundation failure.

Even though the descriptions of the damage states in HAZUS are rather elaborate, the existing fragility functions for damage to bridges as a result of liquefaction-induced lateral spreading based on free-field ground displacements are very crude and rather simplistic. The existing fragility functions in HAZUS are adopted from Basoz and Mander (1999) reports. Based on HAZUS, regardless of type of bridge and its foundation components and characteristic of the soils underlying the bridge, 10 cm (3.9 inches) of ground displacement is sufficient to put the bridge in damage state 4 (extensive damage), and 35 cm (13.8 inches) of displacement is enough to cause complete damage (ds_5 or collapse) in the bridge. The graphical representation of the available fragility functions is shown in Figure 1.9.

These fragility functions were intended to characterize structural damage in single-span bridges due to abutment displacements, and were not originally intended to be used in liquefied ground. Extension to laterally spreading ground was based on the assumption that foundation displacements are equal to free-field ground displacements. This is a false assumption because free-field ground displacements would typically cause much lower foundation displacements in the structure due to the pinning effects and compression or extension of the soils under lateral loading, or the flowing mechanism of soils around foundation components. Furthermore, different bridge characteristics would result in different bridge responses and different types of bridges should have different fragility functions, as they do for ground shaking in HAZUS.

The unreasonableness of the HAZUS fragility functions is clearly evident in the relatively good performance of Landing Road Bridge (ds_3 based on HAZUS damage state definitions) in spite of as much as 2 meters of lateral ground displacement near the bridge. The HAZUS fragility functions were also found to be inaccurate in a transportation network analysis by Kiremidjian et al. (2006), which predicted widespread bridge collapse caused by the 1989 Loma Prieta earthquake (Figure 1.10) due to liquefaction and lateral spreading. Such levels of collapse did not occur, and the collapses that did occur during the earthquake (i.e. the Cypress Structure and one span of the Bay Bridge) were not caused by liquefaction.

Additionally, the recent Niigata Chuetsu-Oki earthquake of July 16th, 2007 in Japan caused lateral ground displacements near bridges on the order of tens of centimeters, which would be sufficient to place bridges in ds4 or ds5 based on HAZUS criteria. However, the bridges were nearly all in service, experiencing only moderate damage consisting primarily of permanent offsets in the elastomeric bearings at the abutments and cracks in the abutments (Figure 1.11). Development of more reliable and meaningful fragility curves for different classes of bridges of different vintages or other simple properties comprises a big portion of this project as will be discussed in greater detail in the following chapters.

1.5 Analysis Method

A numerical method was adopted to evaluate bridges under liquefaction and lateral spreading demands. Several analysis methods are available for analyzing bridges, as are discussed here.

The ideal numerical model would include a three-dimensional representation of the soil using constitutive models that capture liquefaction, a global structural model of the entire bridge, and would impose ground shaking on the base of the soil. Only one such study has been conducted to date (Elgamal et al. 2008) due to the computational cost. There have been a few studies that have used two-dimensional dynamic models of the bridge with continuum soil elements attached to the structural elements using soil-structure zero length elements, to predict the performance of a bridge during liquefaction and lateral spreading (Kramer et al. 2008, Zhang et al. 2008). These methods are also computationally expensive, and often require several months of time for modeling and performing a limited number of dynamic analyses.

Since evaluating the fragility of different classes of bridges requires performing many analyses of bridges with different structural configurations, structural properties, geometry with different soil profiles, performing the former types of analyses was not feasible during the time span of the project, therefore a simpler analysis method had to be devised that would allow a reliable and accurate prediction of the bridge performance in the liquefied ground.

A considerable body of recent research has clarified many of the fundamental loading mechanisms between pile foundations in liquefied and laterally spreading ground (e.g., ASCE special issue ref), and many of the initially contradictory findings have been explained in terms of fundamental behaviors. Effort is now needed to synthesize the body of research into analysis methods that can produce reliably accurate predictions of bridge performance in liquefied ground. The Caltrans seismic design criteria (SDC 2006) specifies several global methods for analyzing bridges exposed to ground shaking, including "Equivalent Static Analysis" (ESA), “Elastic Dynamic Analysis” (EDA) otherwise known as “Response Spectrum Anlysis” (RSA), "Nonlinear Static Pushover Analysis", and "Nonlinear Global Dynamic Analysis” also known as “Time History Analysis”. However none of these analysis methods explained in the Seismic Design Criteria is suitable for evaluating the bridge performance undergoing liquefaction and lateral spreading. The method proposed and used in this document synthesizes the body of research of the loading mechanisms present during liquefaction and lateral spreading in order to evaluate the nonlinear performance of bridges under both displacements and inertial demands applied to the bridge during liquefaction and lateral spreading. This method is referred to as the "Nonlinear Equivalent Static Analyses" in this document, and the details about modeling and the boundary conditions used in this method is discussed in great depth in chapter 2 of this dissertation.

1.6 Organization of the Dissertation

This dissertation evaluates the fragility of different classes of bridges by creating realistic finite element models of bridges using OpenSees finite element platform, and generating demand fragility surfaces of different components of the bridge using the nonlinear equivalent static analyses method. This dissertation consists of five chapters. The organizing of the following chapters is outlined here, as follows:

- ***Chapter 2: Global Equivalent Static Analysis Method***

  Chapter 2 presented the methodology of the global equivalent static analysis method, as was utilized in performing the numerical analyses of the bridge models in OpenSees. The details of the modeling approach and the fundamental behaviors in liquefaction and lateral spreading found in recent research are described, and several examples of the global equivalent static analyses are presented.

- ***Chapter 3: Input Parameters Selection***

Chapter 3 outlines the basis for selection of the parameters that were inputted in the numerical models as well as specifying the classes of that were analyzed. The distributions of the bridge parameters, geotechnical parameters, and inertia are presented in chapter 3. Numbers were sample using Monte Carlo method from the distributions specified in chapter 3, to be used in the numerical models.

- ***Chapter 4: Fragility of Bridges to Lateral Spreading***

In chapter 4 discussed the way that the analyses were performed and the way that the engineering demand parameters were controlled during the analyses. Then, it discusses how the fragility surfaces were fit to the raw recorded data. Next, the fragility surfaces for several classes of bridges are presented, while the observed trends are discussed. This chapter also depicts the correlations between the engineering demand parameters, as well as presenting the disaggregation of the input parameters.

- ***Chapter 5: Conclusions and Future Works***

The important conclusions of the conducted research are summarized in chapter 5 of the dissertation. Limitations of the studies performed in the thesis are discussed in this chapter, and the needs for related potential future works are also presented in chapter 5 of this dissertation.

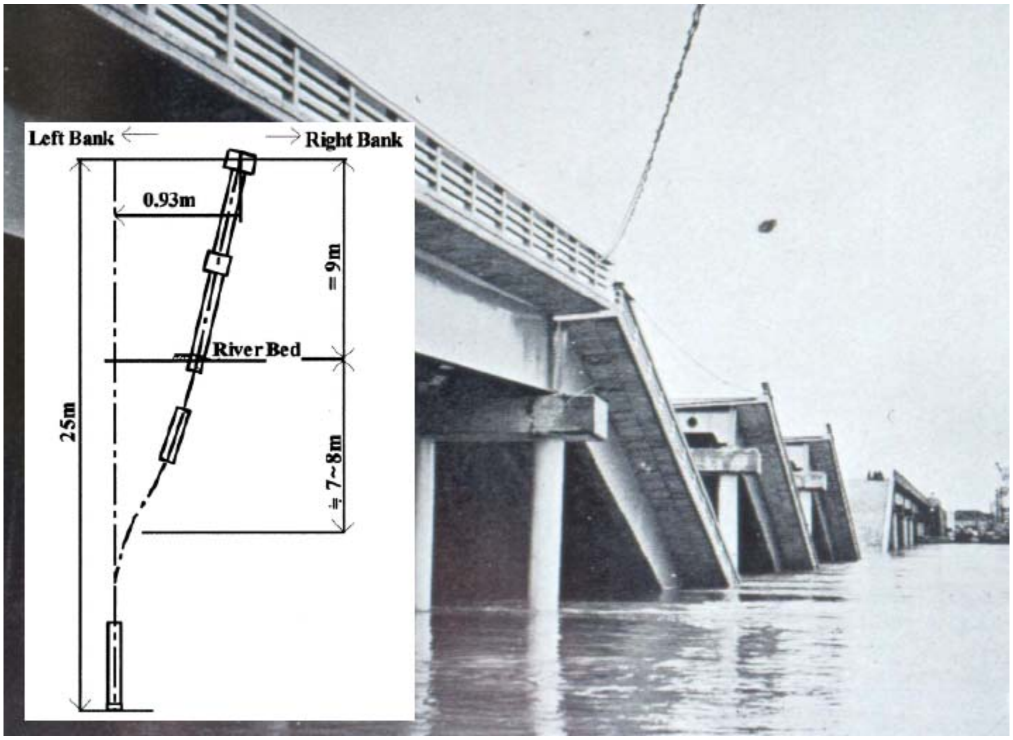

Figure 1.1: Damage to steel piles of Showa Bridge (From Yasuda and Berill, 2000)

Figure 1.2: Top of the wharf of port of Oakland following the1989 Loma Prieta Earthquake. The cranes were separated and could not operate as a result of the extension of the wharf (Courtesy of John Egan, Geomatrix)

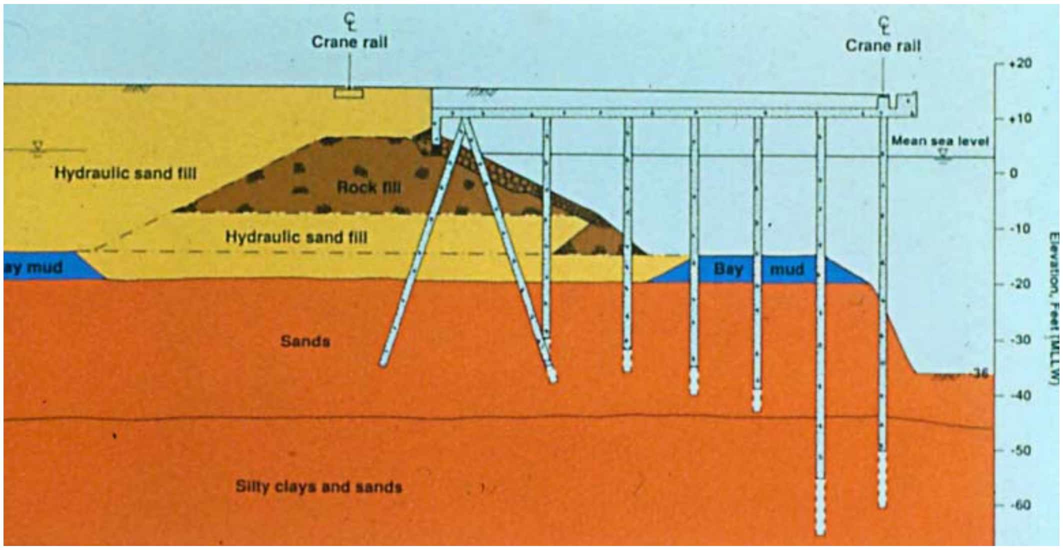

Figure 1.3: Soil profile and pile configuration of the wharf at the port of Oakland (Courtesy of John Egan, Geomatrix)

Figure 1.4: Damage to the battered piles supporting the wharf at the Port of Oakland, during the Loma Prieta 1989 earthquake (Courtesy of John Egan)

Figure 1.5: Un-seating of the Nishinomiya Bridge as a result of lateral spreading during Kobe, Japan, 1995 earthquake

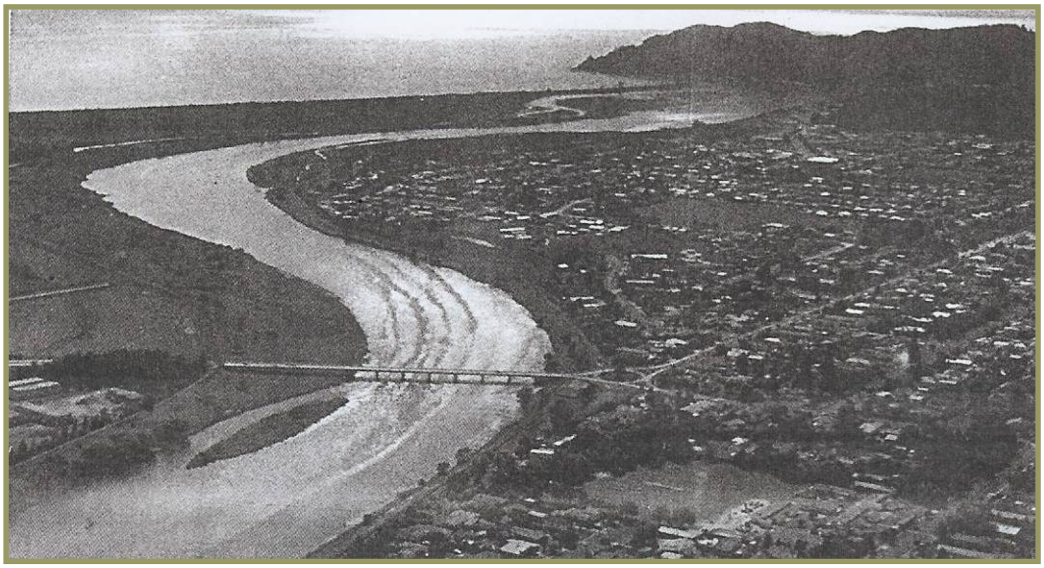

Figure 1.6: Side view of the Landing Road Bridge, in Whakatane, New Zealand which underwent 2 m of lateral spreading during the 1987 Edgecumbe earthquake

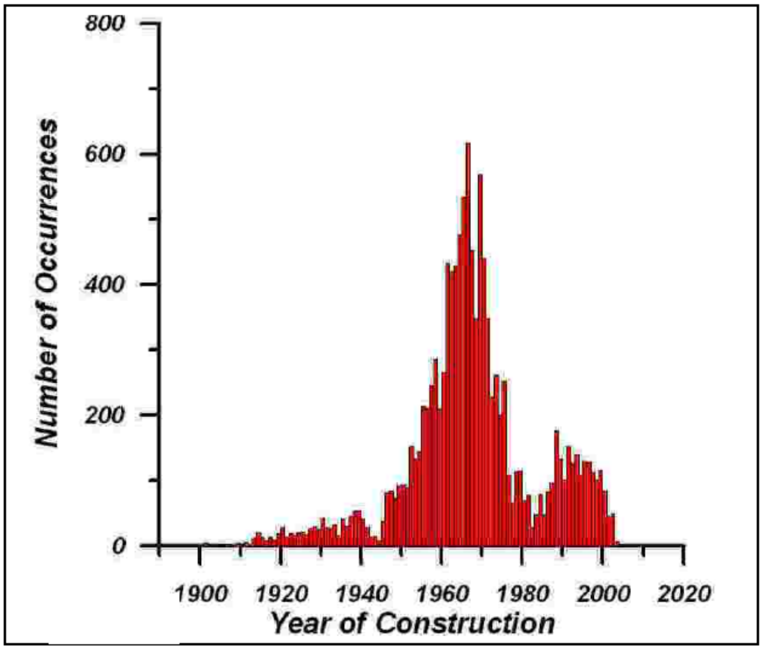

Figure 1.7: Distribution of California Bridges by Year of Construction extracted from NBI database

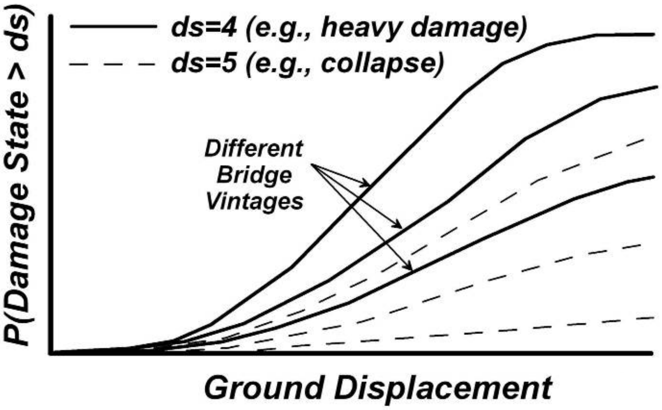

Figure 1.8: Schematic of a set of fragility curves for bridges with different vintages

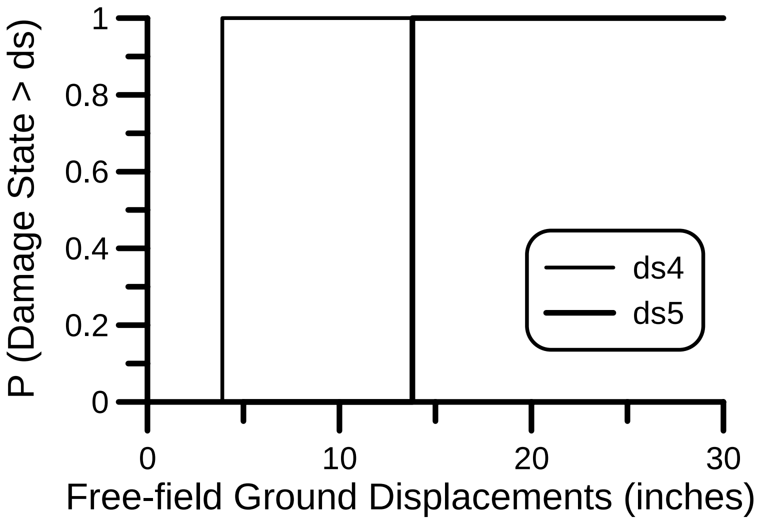

Figure 1.9: HAZUS fragility curves for damage to bridges as a result of lateral spreading

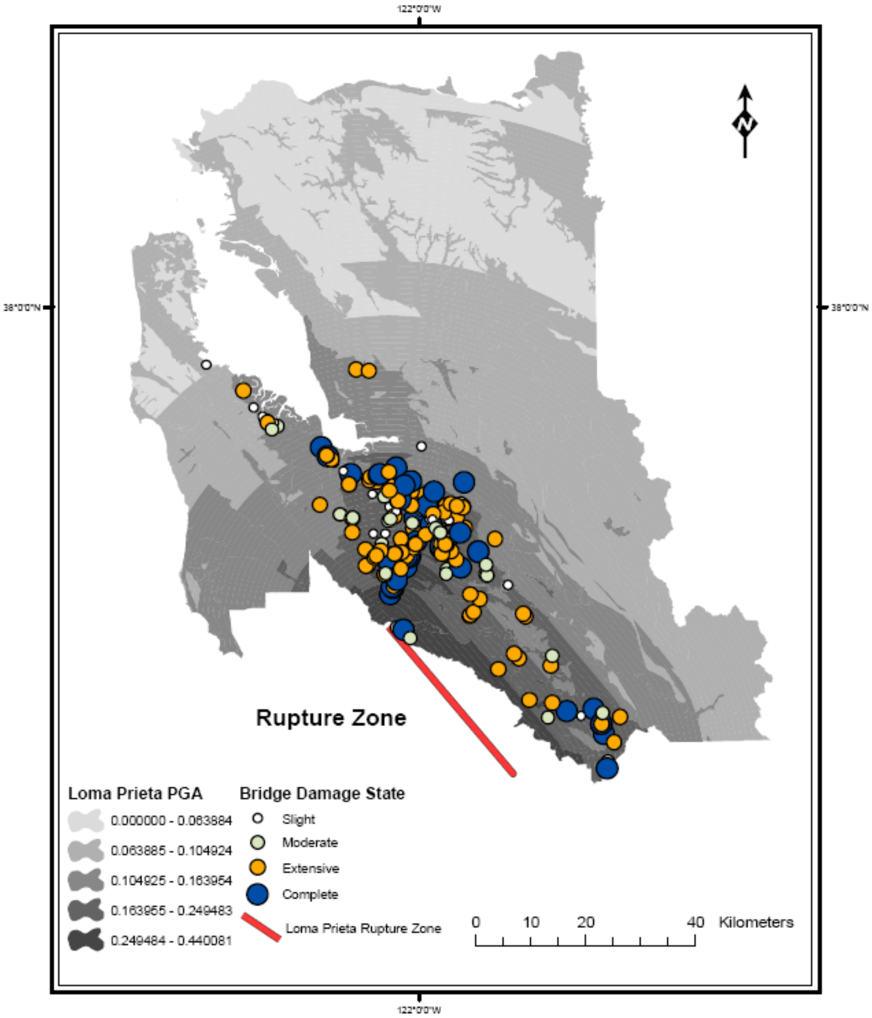

Figure 1.10: Estimated damage to bridges during the Loma Prieta 1989 Earthquake in the Transportation Network Analysis (Kiremidjian et al. 2006)

Figure 1.11: Permanent offset in elastomeric bearing at Nagomi Bridge caused by ground deformation during the Niigata Chuetsu-Oki earthquake (Kayen et al. 2007).

2 Global Equivalent Static Analysis Method

Commonly used methods in evaluation of the global performance of a bridge due to ground shaking are summarized in the Caltrans Seismic Design Criteria (Caltrans SDC 2006), and include "Elastic Equivalent Static Analysis" (ESA), "Elastic Dynamic Analysis" (EDA), "Nonlinear Static Pushover Analysis" and "Nonlinear Global Dynamic Analysis".

ESA applies equivalent static forces or spectral displacements at individual frames, with the seismic demand determined from spectral design response spectrum. ESA can reasonably estimate displacement demands for bridges whose response can be characterized by a predominantly translational mode of vibration, and therefore may be inappropriate for curved or skew bridges, bridges with many spans and/or expansion joints. EDA, which is also known as the Response Spectrum Analysis (RSA), is a linear elastic multi-modal spectral analysis and should include sufficient number of modes to capture at least 90 % mass participation in the longitudinal and transverse directions of the bridge. Since this method is a linear elastic method it can only indirectly account for sources of nonlinearity in the system including the effects of surrounding soil, yielding of the structural components, opening and closing of expansion joints and abutment behavior. According to SDC 2006, both ESA and EDA are appropriate only for Ordinary Standard bridges. This implies that these methods are not suitable for bridges in sites with potential of liquefaction and lateral spreading, since this is one of the criteria for the bridge to be considered an Ordinary Standard bridge.

Nonlinear static pushover analysis imposes an increasing displacement pattern to identify potential failure mechanisms and establish tolerable displacement limits of the bridge. In this method, displacements are applied incrementally to push the frame of the bridge in the nonlinear range until the potential collapse mechanism is reached. This is a recommended method for analyzing the inelastic (nonlinear) response of bridges because it accounts for interaction of the bridge components and redistribution of the loads within different components, once the components behave nonlinearly. However, the applicability of this method for bridges under liquefaction and lateral spreading demands is not evaluated, and it is not immediately clear how the displacements demands to the superstructure frames should be concurrently applied with the displacement demands due to lateral spreading at the foundation level or at the abutments.

Nonlinear Global Dynamic Analysis also known as Time History Analysis is the most accurate and robust method of evaluating the bridge performance. In this method of analysis, the response of the bridge is evaluated directly by applying a suite of ground motions at the boundaries of the model. In cases with only ground shaking, the structural engineers typically model the foundation using simple soil-structure-interaction elements at the boundaries of the bridge frame. However, this method of applying the boundary conditions cannot capture the complex response of the bridge during liquefaction and lateral spreading which may involve significant displacements and rotation of the foundations. Therefore, the proper modeling of the bridge under liquefaction and lateral spreading using nonlinear global dynamic analysis requires explicitly modeling the structure (including the foundation) and soil elements with advanced soil constitutive models that can capture complex behavior of soils during liquefaction and lateral spreading, including generation and dissipation of pore pressures and reduction of shear strength of the soil during liquefaction. The most robust method for performing nonlinear global analysis of bridge in liquefied ground is to use a three-dimensional soil continuum with constitutive models that can capture liquefaction behavior (e.g., Elgamal et al. 2008). Such models could explicitly capture soil-structure-interaction in liquefied ground by directly modeling the soil continuum and nonlinear pile elements, and do not require SSI elements. However, this approach is extremely computationally expensive and not a viable option except for the most important bridges.

A less computationally expensive dynamic approach involves modeling the bridge in two dimensions, with two-dimensional soil continuum elements (e.g., Zhang et al. 2008, Kramer et al. 2008). However, since soil-structure interaction is inherently a three-dimensional problem, SSI elements (i.e. p-y, t-z and q-z) are required at the interface of the soil elements and the structural elements to capture the 3-D loading mechanisms. The two-dimensional soil mesh provides a free-field displacement that is imposed on the free-ends of the soil-structure-interaction elements, and the SSI elements can be adjusted to account for the effects of liquefaction [e.g., the PyLiq1 material in OpenSees (Boulanger et al. 2003)]. While the cost of performing this type of two-dimensional analyses is significantly lower than the three-dimensional analyses, they are still computationally very demanding and not currently amenable to routine evaluation of ordinary bridges.

Caltrans Seismic Design Criteria (SDC 2006) also mentions stand-alone local analyses of a single component (e.g. a single pier) of the bridge in longitudinal and transverse directions. Local analysis is the most common approach for analyzing piles in liquefied ground because software platforms such as LPile are amenable to this type of analysis (e.g., Brandenberg et al. 2007, Ashford and Juirnarongrit 2006, Dobry et al. 2003). Local analysis may be appropriate in cases where boundary conditions imposed on the foundation from the superstructure are clearly understood. However, these boundary conditions are often not known a priori because loads may be transmitted between adjacent piers through axial forces in the superstructure. For example, the displacement and rotation demands at the top of a single pier depend on how the lateral spreading demands on the foundation of that pier are transmitted to other piers or abutments through axial loads in the superstructure. Furthermore, lateral spreading at one pier may place demands on other piers and abutments in nonliquefied ground, and these demands are very difficult to assess using local analysis methods. Global analyses of a bridge can capture these important features, while local analyses cannot. A few examples of global analyses of a bridge are presented later in this chapter, and the response of the bridge is compared with a few cases of the response of an individual component of the bridge using local equivalent static analysis, to further clarify this point and provide guidance on cases where local analysis is sufficient and where global analysis is needed.

2.1 Modeling Approach

The method proposed here is the Nonlinear Equivalent Static Global Analysis, wherein a global structural model of the bridge (including foundation elements) is constructed from nonlinear beam-column elements, SSI elements are attached to embedded components, and free-field ground displacements are imposed on the free-ends of the SSI elements simultaneously with inertia demands consistent with the effects of liquefaction. A soil continuum is not modeled, which greatly reduces the computational complexity of the model. This approach incorporates the recent body of research and advances in understanding the load transfer mechanisms during liquefaction and lateral spreading, in a simpler, computationally less demanding approach. The details of the modeling and boundary conditions are discussed in the following sections of this chapter.

Global analysis of bridges in liquefied ground requires more collaboration between the geotechnical and structural engineers compared with local analyses and requires a more sophisticated level of modeling where all the structural and foundation elements of the bridge are modeled and soil-structure elements are appropriately specified to account for complex soil behaviors observed during liquefaction and lateral spreading. A number of numerical modeling programs, such as OpenSees and SAP2000, are capable of performing this level of modeling. In this document, all the numerical analyses are performed using the OpenSees finite element platform (McKenna and Fenves. 2006) developed by Pacific Earthquake Engineering Research Center.

2.1.1 Structural Modeling

The numerical modeling of the bridges is performed in two dimensions and the lateral spreading displacements and inertial demands are applied in the longitudinal direction of the bridge. Hence, these models do not account for bridges with a curved geometry or significant skew. Also bridges with significant lateral spreading demands in the transverse direction are not accounted for in the analyses.

Two-dimensional beam column elements with three-degrees of freedom per node are required to model the longitudinal response of the bridge. The models used in this study utilized three-dimensional beam column elements with six-degrees of freedom per node with the out-of-plane DOF's constrained to restrict response to the two-dimensional plane of interest. This approach was adopted so that the bridge models could be adapted to three-dimensional loading conditions for future research studies. Multi-column bents and pile groups with multiple members in the out-of-plane direction are represented using single elements in the plane with structural properties adjusted to represent the number of out-of-plane members.

2.1.1.1 Pier Columns and Piles:

The pier columns and piles were modeled using nonlinear beam-column elements. A bilinear moment curvature relationship was aggregated with linear elastic shear deformation response and elastic axial response. Each nonlinear beam-column elements consisted three integration points with two of the points at the nodes where maximum bending moments are anticipated (i.e. Lobatto integration).

Moment-curvature relationships of pier columns were evaluated using fiber-section analyses of columns with proper size and longitudinal and transverse reinforcement ratios as well as proper axial load ratios. Subsequently the moment-curvature relationship was approximated using a bilinear curve using the Hardening material model in OpenSees by specifying the initial stiffness of moment-curvature curve (EI_{eff}), the yield moment of the column (M_y) and the post-yield stiffness of the curve, which is conveniently chosen to be 5 % of the initial stiffness of the column.

The axial and shear force-deformation relationships were modeled elastically with stiffness equal to EA, and GA, respectively. My fellow graduate student in the structural engineering program, Mr. Yili Huo, performed the fiber-section analyses and provided help in modeling of structural properties of the superstructure and pier columns.

The moment-curvature response of the piles was obtained using the fiber section analysis program Xtract by Imbsen (ref). The moment-curvature relationship was then approximated using a bilinear relationship similar to the pier column elements.

Figure 2.1 shows an example of a moment curvature analysis performed in Xtract for a 24" CIDH pile.

2.1.1.2 Abutments, Superstructure, and Pile Caps:

The abutments, superstructure, and pile caps were assumed to remain linear elastic under the applied boundary conditions. Hence, linear elastic beam-column elements were used for modeling. For these elements only the elastic properties of the materials, i.e. modulus of elasticity (E) and moment of inertia (I), as well as the cross-sectional area (A) of the elements were needed. Pile caps and abutments are blocky elements that violate the plane-sections assumption in beam theory and the EI and EA for these elements was selected to simply be so large that they behaved essentially as rigid bodies. The EI and EA for the superstructure elements were based on the cross-sectional properties of the reinforced concrete box girder section. For the bridges with simply-supported superstructure or seat-type abutments, the interface between the superstructure deck and the bent caps or the abutments were modeled with zero-length springs with appropriate types and capacities, so that the proper response of the bridge could be captured.

2.1.1.3 <u>Bearings at Abutments</u>:

Figure 2.2 shows the schematic of a typical seat-type abutment as well as the different types of springs needed to capture the response at the abutments. As can be observed in Figure 2.2 three types of springs are needed for the seat-type abutments.

Spring 1 connects the superstructure deck node to the node at the top of the stem wall models the horizontal load transfer mechanism at the abutment bearing. The bearing load deformation usually can be captured by an elastoplastic material spring in which the capacity of the bearing (i.e. plastic ordinate) is Q and the horizontal stiffness of the bearing is K_H. For elastomeric bearings, the capacity, Q is calculated using coulomb friction as follows:

$$Q = \mu.N \tag{2.1}$$

Where, N = the normal tributary force acting on the bearing

μ = the coefficient of friction of the elastomeric bearing

The coefficient of the friction for the elastomeric bearing is between 0.35 and 0.4 according to SDC 2006.

The horizontal stiffness of the bearing K_H is calculated using the following formula:

$$K_H = \frac{G.A}{t_r} \tag{2.2}$$

Where, A = surface area of the bearing pads

t_r = total thickness of the bearing pads

G = effective shear modulus of rubber $\approx$ 1 MN/m^2 (150 psi)

Consequently the yield displacement of the bearing can be calculated as:

$$U_y = \frac{Q}{K_H} \tag{2.3}$$

In modern bridges, typically the total surface area of the elastomeric bearings is selected so that the vertical stress on the bearings, σ_v, does not exceed 100 *psi* (~ 690 *kPa*).

Rocking and rollout displacements of the bearings are important design considerations for dynamic shaking of the bridges. Multi-layer bearings with steel sheets in between the rubber pads are typically used to increase the vertical stiffness of the bearing by modifying its shape factor, in order to reduce the damages due to rocking or rollout of the bearings. However, bearings with the same total rubber pad thickness essentially have the same horizontal stiffness. Since the loading demands in the nonlinear equivalent static analyses are applied statically and incrementally, dynamic response of the bearings (i.e. rocking and rollout) are not captured. Thus, the vertical degrees of the freedom of the two nodes connecting to *spring 1* are equal, which causes the spring to be rigid in vertical direction since the two nodes move together.

Spring 2 is a horizontally oriented spring connecting the top node of the stem wall to the bottom node of the back wall of the abutment. This spring follows a rigid plastic load deformation relationship with a capacity, V_{BW}, equal to the shear capacity of the connection between the back wall and the stem wall. Note that modern abutment backwalls are designed to break away from the stem wall to mobilize the passive soil resistance of the approach embankment. This spring causes the two nodes to move together until the shear capacity of the back wall is exceeded, at which point the back wall is no longer connected to the stem wall and can translate into or away from the abutment backfill depending on the direction of the loading.

Springs 3 and *4* model the expansion joint gap between the superstructure deck end nodes and the nodes at the top and bottom of the back wall. These springs do not carry any load in tension or compression, unless they are compressed the distance of the expansion gap - typically 1 inch – at which point they behave rigidly allowing the loads to be carried by soil p-y springs as well as the bridge structural elements. The end element of the deck is extended vertically using a rigid elastic beam-column element, so that the top node of the deck could be connected to the top node of the back wall. This way of modeling the deck enforces compliance between back wall rotation and superstructure rotation at the abutment when the gap is closed both at the top and bottom of the back wall (*springs 3 and 4*).

Diaphragm abutments are also sometimes used in Caltrans bridges, and these moment-resisting connections were modeled by having the stiff abutment beam column element share a node with the superstructure element. Hence, a 90° angle was maintained between the superstructure and abutment, though the connection could rotate.

2.1.1.4 **Bearings at Simply-Supported Spans**:

Figure 2.3 shows the schematic of a typical connection of simply-supported spans and the required spring to model this connection properly. Two types of springs exist at this connection.

Springs 1, 2 are horizontally oriented elastoplastic springs connecting the top node of the pier column to the end nodes of the two spans sitting above it. These springs are symmetrical and model the stiffness and shear capacity of the interface between the deck spans and pier columns in a similar manner as the bearing spring in the abutment (i.e. *Spring 1* in Figure 2.2). Generally speaking, the capacity of these springs is equal to the shear capacity of the interface, while the stiffness of the springs is governed by the amount of relative displacements between the deck and the pier column at the connection, before the shear capacity of the connection is reached. Consequently, in case the interface is an elastomeric bearing the stiffness and capacity of the springs follows the relationships mentioned earlier for the abutment bearings. In the case that the interface is grouted and the superstructure is connected to the pier column using dowels, the capacity of *springs 1* and *2* would equal the shear capacity of the dowels and the grout, while the stiffness of the springs would essentially be rigid. Adjusting the capacities and the stiffnesses of these springs allows for appropriate modeling of other kind of interfaces typically used in construction of these connections.

Spring 3, is a horizontally oriented no-tension rigid spring connecting the end nodes of the two spans of the deck. This spring allows the spans of the deck to move away from each other without interacting with the other span. However, once the spans are compressed to each other the spring becomes rigid resulting in the two spans moving together without penetration of one span into the other.

2.1.2 Soil-Structure Interaction Modeling

A beam on nonlinear Winkler foundation approach is used for modeling the soil-structure-interaction effects at both the bridge abutment components (i.e. abutment walls and piles) and the foundation components supporting the pier columns (i.e. piles and pile cap). The soil-structure elements include p-y springs for lateral interaction, t-z springs for axial interaction and q-z springs for pile tip bearing. The soil-structure interaction effects on piles are fundamentally different from the non-pile components of the bridge. Thus, the discussion on the soil-structure-interaction modeling is divided to soil-structure interaction springs on pile caps and abutment walls and soil-structure interaction springs on piles, as follows:

2.1.2.1 Soil-Structure Interaction Springs on Pile Caps and Abutment Walls:

In order to capture the proper soil-structure interaction effects of lateral spreading occurring at the pile caps and abutment walls level, both the capacity and stiffness of the p-y springs acting on these components should be determined first, as will be discussed here.

***Determination of the stiffness of the p-y springs at pile caps and abutment walls*:**

The soil profile in liquefying ground often consists of a nonliquefiable layer above the liquefied sand layer, often called a nonliquefied crust. Many researchers (e.g., Dobry et al. 2003, Brandenberg et al. 2007) have shown that passive pressures exerted by a nonliquefied crust spreading against a pile or embedded bridge component can be the dominant loads during lateral spreading since the crust remains strong as it spreads and imposes displacement demands on a structure. These loads can be particularly large on pile caps or abutment walls, which have a large out-of-plane thickness. Considerable effort has been devoted to characterizing load transfer between piles and liquefied sand, and also to load transfer between pile caps and abutment walls in nonliquefied soil profiles. However, less attention has been devoted to load transfer between laterally spreading crusts and embedded bridge components.

In a classical retaining wall problem at a site where the soils do not liquefy, the passive earth pressures develop in the backfill soils if the retaining wall is pushed into the soil. This might be the case when the diaphragm wall (abutment wall) of a bridge is pushed into the abutment by earthquake shaking. Static load tests in non-liquefied ground have shown that the ultimate passive pressures are mobilized at a wall displacement of 1% to 7% of the wall height. For example, Rollins and Sparks (2002) performed static load tests on pile groups in granular soil and observed that the peak load was mobilized at displacements of about 2.5% to 6% of the wall height, while Duncan and Mokwa (2001) and Mokwa and Duncan (2001) reported peak load occurring at displacements of about 1% to 4% of the pile cap height. Abutment wall tests performed by Lemnitzer et al. (2009) also showed that the peak passive load was attained at about 3% of the wall height.

However, the stiffness of the load transfer is fundamentally different for the cases where the nonliquefiable crust is spreading against a pile cap or abutment wall or another embedded component of the bridge. Brandenberg et al. (2007) showed that underlying soft soil (including liquefied sand) softens the load transfer between a crust and embedded bridge component. The primary cause of this soft response is the reduction of friction along the base of the spreading crust due to liquefaction of the underlying soils. Additional contributions may also come from gaps and cracks in the crust, and cyclic degradation in clayey crusts. The liquefaction of the ground under the crust influences distribution of stresses in the crust by creating an almost frictionless boundary which permits horizontal stresses to spread to large distances upslope from the embedded component, thereby increasing the zone of influence. Relative displacement is the integral of horizontal displacement in the zone of influence, hence a large zone of influence equates to a soft load transfer behavior. Centrifuge tests performed by Brandenberg et al. (2007) shows that the load transfer response in the nonliquefied crust is about an order of magnitude softer that the traditional p-y response in nonliquefiable soil profiles, meaning that an order of magnitude larger relative displacement is required to mobilize passive pressures (Figure 2.4). Therefore, in order to capture the load transfer observed in nonliquefied crust, the stiffness of the traditional p-y curves should be modified to account for this soft response. This can be done by adjusting the y_{50} value (deflection at one-half the ultimate soil resistance) in clays and by adjusting the modulus of subgrade reaction, k, for sands so that the shape of the p-y curve resembles the soft load transfer response of the nonliquefied crust.

Brandenberg et al. (2007) proposes a mathematical model for determining the proper load transfer behavior for lateral spreading of the nonliquefied against a stationary pile cap. This procedure was used in determining the appropriate stiffness of the p-y springs at the piles caps and also abutment walls.

***Determination of the Capacity of the p-y springs at pile caps and abutment walls*:**

The spreading of soils against a wall or pile cap, mobilizes passive pressures behind the wall similar to the case where the wall is pushed into the soil. Log-spiral passive pressure is generally believed to yield a more accurate estimate of the passive pressures behind the walls and usually agrees well with the observed failure surface behind the walls. However, regardless of what theory is used to calculate the passive pressures behind a wall, the magnitude of the force depends highly on the magnitude and direction of the wall friction along a rough wall. The direction of the wall friction force is typically assumed to act downward on the soil since the soil typically bulges up as the wall is pushed horizontally into the soil. However, the direction of the mobilized friction force is highly uncertain when a nonliquefied crust spreads laterally against an embedded pile cap or abutment backwall because of the boundary condition along the bottom of the crust posed by the liquefied layer. The crust may settle relative to the wall due to sand boil formation and extensional strains in the crust or it may bulge up relative to the wall as the crust is compressed against the embedded structure (Figure 2.5). Since the direction and the magnitude of the friction force at the wall interface is very important in the magnitude of the passive pressures behind a wall, it is very important to account for its variability and quantify the uncertainty in the passive pressures.

The total crust load from the nonliquefied crust spreading against the embedded part of a structure (i.e. pile group or abutment wall), is the smaller of the load calculated by the two mechanisms explained below.

The first mechanism is the mechanism where the soil spreads around the piles or around the sides of a pile cap or an abutment wall. In the second mechanism however, the soil is trapped between the piles and the whole group acts as an equivalent block. Figure 2.6 represents the two mechanisms of spreading. In reality the mechanism with the lower overall crust load controls.

The components of the crust load for the flowing mechanism includes the passive pressures on the upslope face of the pile cap or the abutment wall, lateral loads as would normally be applied on the piles (i.e. soil reaction forces in p-y springs) and friction on the sides and base of the pile cap or the abutment wall. On the other hand, the components of the crust load for the equivalent block mechanism are as follows: the passive pressures on the entire upslope face of the equivalent block, side friction and base friction of the equivalent block.

2.1.2.2 Soil-Structure Interaction Elements on Piles:

Three different types of soil-structure-interaction springs are necessary for modeling the interaction of the piles and the surrounding soils. SSI elements on the piles were based on existing relationships for piles in nonliquefied ground, and subsequently modified for the effects of liquefaction.

***Lateral Interaction Modeling using p-y springs*:**

p-y springs are used for lateral interaction modeling on piles. p-y elements in clay followed relations developed by Matlock (1970), and p-y elements in sand followed API (1993).

Matlock's equations are in the following form:

$$\frac{p}{p_{ult}} = 0.5\left(\frac{y}{y_{50}}\right)^{\frac{1}{3}} \tag{2.4}$$

Where, p = soil resistance

y = deflection

p_{ult} = ultimate soil resistance

y_{50} = deflection at one-half the ultimate soil resistance

The capacity of the p-y spring, p_{ult}, only depends on pile diameter, undrained shear strength of clay, at deeper depths, while at shallow depth, it also depends on the depth and unit weight of the clay. y_{50} is the measure of stiffness of the spring.

API (1993) p-y curves for sands follow the form:

$$p = Ap_{ult} \tanh\left(\frac{kx}{Ap_{ult}} y \right) \tag{2.5}$$

Where, k = modulus of subgrade reaction of sand

x = depth of interest

A = factor to account for cyclic or static loading

The capacity of the spring, p_{ult}, in sands depends on the friction angle of the sand and its unit weight.

The p-y elements were modeled using the PySimple1 material available in OpenSees assigned to zero-length elements oriented normal to the length of the piles and attached at pile nodes. The PySimple1 material fits a hyperbolic load-displacement function to the forms suggested by Matlock (1970) (PySimple1 Type 1) API (1993) (PySimple1 Type 2). The PySimple1Gen command was used to automate the generate the PySimple1 materials and zeroLength elements, which would be an otherwise tedious task to perform by hand since different materials are required at different depths along the piles.

These relationships are good approximations and are appropriate for characterizing lateral interaction of the piles in clayey and sandy soils in sites where no liquefaction is present, but the p-y behavior in sites where liquefaction occurs is much more complex.

The dynamic load deflection behavior in liquefied sands was first observed by Wilson et al. (1998, 2000) by back-calculation of the results of dynamic centrifuge model tests of pile-supported structures (Figures 2.7 and 2.8).

As can be seen in Figure 2.7, for loose sand (D_r = 35 %) the p-y response is very soft and weak relative to the traditional API (1993) curves. However the medium dense sand (D_r = 55 %) exhibits an inverted s-shaped displacement-hardening behavior, similar to the stress-strain behavior in undrained loading of dilatant saturated sands. Several studies, such as studies done by Tokimatsu et al. (2001), Ashford and Rollins (2002) and Rollins et al. (2005) have since observed similar responses as the response observed by Wilson et al. (1998, 2000).

The inverted s-shape of the load transfer is attributed to dilatancy of the medium dense sand during undrained loading. Sands that are dense of the critical state have the tendency to dilate, and since there is no plastic volumetric strain in undrained loading, the dilatant tendency manifests as a drop in pore pressure and associated increase in effective stress. The increase in effective stresses causes the soil to strain-stiffen, thereby causing the inverted s-shaped stress-strain behavior (Figure 2.9).

These features of dynamic p-y behavior in liquefied soil cannot be reasonably captured in static analysis. The most common approach for softening p-y elements to account for liquefaction is to apply reduction factors in the form of p-multipliers to the traditional API (1993) sand p-y curves. Brandenberg (2005) proposes p-multipliers for liquefied sands based on penetration resistance of the sand, using $(N_1)_{60\text{-}CS}$, which is a directly related to the relative density of the sand, as can be summarized in Table 2.1.

Table 2.1: p-multipliers, m_p, to account for liquefaction (Brandenberg 2005)

$(N_1)_{60\text{-}CS}$	m_p
<8	0.0 to 0.1
8-16	0.05 to 0.2
16-24	0.1 to 0.3
>24	0.2 to 0.5

The p-multipliers in Table 2.1 are appropriate for conditions where excess pore pressure ratios reach unity. However, excess pore pressure ratios often reach an intermediate value between 0 and 1. Dobry et al (1995) suggests that the p-multiplier can be linearly interpolated, as shown in Figure 2.10.

For piles in group configurations located in nonliquefied soil, often there is a group effect, causing a reduction in loads on the nonleading rows of piles. These group effects are usually accounted for by applying group effect multipliers. The group effects were accounted for the portions of the piles that were embedded in dense nonliquefiable soils, however these group effects should not be applied in the portions of the piles that were embedded in liquefiable sands since the liquefied sand is weak (Rollins et al. 2005). Thus group multipliers were not included for liquefied sands.

For p-y springs on portions of the piles embedded in the nonliquefiable crust, the stiffness of the p-y springs (y_{50}) should be modified in a similar manner as the p-y springs behind an abutment wall or a pile cap, as described in the previous section.

***Axial interaction and tip bearing modeling using t-z and q-z springs*:**

Axial interaction of the piles with the surrounding soil is modeled using t-z springs. T-z springs in the analyses are modeled by assigning TzSimple1 material to the zero-length elements that are oriented along the length of the piles. The free node of the zero-length t-z elements are fixed in all directions. TzSimple1 material is symmetrical similar to the PySimple1 material. Little is known about the effects of liquefaction on the behavior of t-z elements. In the absence of data, p-multipliers may be assumed to characterize the effects of liquefaction on t-z and behavior as well. Therefore, similar p-multipliers as the p-multipliers for liquefaction effects on the p-y springs were also applied to the t-z springs.

Tip bearing capacity of the piles is modeled by attaching q-z springs at the tip of the piles along the length of the pile. The free node of the q-z springs should also be fixed in all directions. In OpenSees analyses, QzSimple1 material is used for the q-z zero-length elements. Unlike PySimple1 and TzSimple1 material in Opensees QzSimple1 material is not symmetrical, since the capacity of the springs is much less in tension than it is in compression. As a result care should be taken in orienting the zero-length element in the correct direction.

2.1.2.3 Determination of Appropriate Passive Pressure Behind the Wall:

The magnitude of the passive pressures is dependent on the magnitude and direction of the wall friction force, as well as the magnitude and direction of the horizontal seismic coefficients acting on the spreading block, in addition to the properties of the soils in the backfill. In order to capture the effects of variations of wall friction and the horizontal seismic coefficients of the backfill, two separate Monte Carlo studies one based on the log-spiral theory of passive pressures, and the other based of a coulomb-type passive pressure with a planar failure surface were performed to investigate the baseline and variations of passive pressures behind a wall representative of the passive pressures formed behind abutment walls or pile caps of bridges undergoing liquefaction and lateral spreading.

To demonstrate the effect of interface friction angle uncertainty on passive pressure, consider a case with the properties summarized in Table 2.2.

Table 2.2: Properties of the wall and backfill soil.

Parameter	**Mean Value**	**Standard Deviation**
Height, H	2 m	
Tangent of Friction Angle	tan(38°)	0.15 · tan(38°)
Cohesion, c	20 kPa	10 kPa
Unit Weight, γ	20 kN/m^3	1 kN/m^3

These properties were selected to reasonably characterize the soil properties within a compacted backfill in an approach embankment. The abutment back wall height is 2 m, the friction angle is 38°, and the tangent of the friction angle is assumed to be distributed normally with a coefficient of variation equal to 0.15 (i.e. $\sigma = 0.15 \cdot \mu$). Compacted backfills typically exhibit a cohesion intercept since the material is unsaturated, hence a mean value of cohesion of 20 *kPa* and standard deviation of 10 *kPa* were selected and a normal distribution was assumed. The mean unit weight of the material is 20 *kN/m*^{3} and the standard deviation is 1 *kN/m*^{3}, also assumed normally distributed.

***Monte Carlo Analysis of the Effect of Wall Friction on the Range of Passive Pressures based on log-spiral theory of passive pressures*:**

As mentioned earlier the magnitude of passive pressures behind a wall depends greatly on the magnitude and the direction of the friction force acting on a rough wall. During lateral spreading happening as a result of ground shaking the lateral movement of the soil about the wall is highly unpredictable, which results on the unpredictability of the magnitude and direction of the friction force. Conventionally, for a rough soil wall interface, the interface friction angle (δ) is assumed to be about $\frac{1}{2}$ to $\frac{2}{3}$ of the friction angle (ϕ). However, for the case of lateral spreading, it is conceivable that the soil could settle relative to a pile cap or abutment wall due to underlying liquefaction, thereby mobilizing a negative δ. Thus, for the purpose of this study the range of values for δ was assumed to vary uniformly between $-\phi$ and ϕ.

Zhu and Qian (2000) used the method of slices to model passive pressures in cohesionless soil for various values of friction angle, backfill inclination angle, and wall interface friction angle, δ, in the range $-0.5\phi \leq \delta \leq 1.0\phi$ (Figure 2.11). Their result for a horizontal backfill fits well with an expression of the form in Equation 2.6, with constants depending on friction angle as summarized in Table 2.3.

$$\frac{K_p}{K_p(\delta = 0)} = A_1 \cdot \exp(A_2 \cdot \delta / \phi) + (1 - A_1) \tag{2.6}$$

Table 2.3: Curve fit parameters for Zhu and Qian (2000) results.

ϕ (deg)	**A_1**	**A_2**
20	0.76	1.50
25	0.68	1.78
30	0.60	2.20
35	0.55	2.87
40	0.48	3.96
45	0.42	6.07

Assuming that the value of interface friction angle, δ, is uniformly distributed between –ϕ and +ϕ, an expression can be obtained for the mean and standard deviation of $K_p/K_p(\delta=0)$ using the closed-form expressions in Equations. 2.7 and 2.8.

$$\mu = \frac{1}{2}\int_{-1}^{1} A_1 \cdot \exp(A_2 \cdot \delta / \phi) + (1 - A_1) \tag{2.7}$$

$$\sigma = \frac{1}{2}\int_{-1}^{1} \left[A_1 \cdot \exp(A_2 \cdot \delta / \phi) + (1 - A_1) - \mu\right]^2 \tag{2.8}$$

The mean and standard deviation in natural log units are plotted as a function of friction angle in Figure 2.12. Note that $\sigma_{\ln}^2 = \ln(1+\sigma^2/\mu^2)$. This figure characterizes the mean earth pressure and standard deviation for $K_p/K_p(\delta=0)$ assuming that the interface friction angle is a random uniformly distributed variable between –ϕ and +ϕ.

The mean and standard deviation both increase with friction angle. The expressions for μ and $\sigma_{\ln}$ closely fit Equations 2.9 and 2.10 (superposed on the data in Figure 2.12), where ϕ is in degrees.

$$\mu(\phi) = 0.00395 \cdot e^{0.114 \cdot \phi} + 0.963 \tag{2.9}$$

$$\sigma_{\ln}(\phi) = 1.567 \cdot e^{0.009645 \cdot \phi} - 1.624 \tag{2.10}$$

A Monte Carlo simulation was conducted wherein 10,000 realizations of ϕ, c and γ were selected from their respective distributions. For each realization, $K_p(\delta=0)$ was computed using Rankine theory, and a random value of $K_p/K_p(\delta=0)$ was selected from a log-normal distribution with the mean and standard deviation in Equations 2.9 and 2.10. The passive earth pressure was computed using Equations 2.11:

$$K_p = K_p(\delta = 0) \cdot \frac{K_p}{K_p(\delta = 0)} \tag{2.11}$$

$$P_p = \frac{\gamma \cdot H^2}{2} \cdot K_p + 2 \cdot c \cdot H \cdot \sqrt{K_p}$$

Equation 2.11 assumes that K_p is a function of ϕ and δ alone, and does not depend on cohesion. However, the combined effects of friction and cohesion are known to affect the passive and active earth pressure failure mechanisms (e.g., Mazindrani and Ganjali 1997), but this influence is often neglected as it has been here.

The distribution of passive pressure is shown in Figure 2.13(a). The mean value of P_p is 402 *kN/m*, the median value of P_p is 334 and the standard deviation of the natural logs is 0.66. For comparison, Figure 2.13(b) shows the distribution of P_p obtained using Rankine earth pressure theory (i.e. without the influence of the uncertainty introduced by wall friction). Note that the mean value of δ is 0 since it is uniformly distributed between $-\phi$ and $+\phi$, hence Rankine earth pressure is a good comparison for showing the influence of wall friction. The mean of P_p is 334 *kN/m* and the standard deviation of the natural logs is 0.31. The mean value with wall friction is 20% larger than the mean value of Rankine earth pressure theory, while its median which is associated with δ of 0 is equal to the mean (or median) value of P_p based on Rankine theory of passive pressures which is normally distributed. It can be seen here, that the Rankine earth pressure without wall friction is a good approximation for the median value of pressure distribution behind the wall, and the high standard deviation in log units for the Monte Carlo analysis implies that the variations in δ makes the passive pressures highly uncertain.

***Monte Carlo Analysis of the Effects of Wall Friction and Horizontal Seismic Coefficient on the Range of Passive Pressures based on Coulomb Theory*:**

A Monte Carlo Analysis based on a Coulomb-type passive earth pressure theory was performed to investigate the effects of both the wall friction and horizontal seismic coefficient on the magnitude of the passive loading behind a wall. In this study, the inertia of the failure wedge was also included in the calculation of the passive force, using the method first proposed by Okabe (1926) and Mononobe (1929), and subsequently called the "Mononobe-Okabe" method. The Mononobe-Okabe method uses Coulomb earth pressure theory in conjunction with additional force vectors to represent pseudo-static inertia forces. Coulomb earth pressure theory is known to significantly over-predict passive earth pressures for high δ. Hence, the calculations presented in this section are not as accurate as those in the previous section, where log-spiral failure surfaces were utilized. However, the log-spiral study did not include seismic coefficients, and assessing the influence of a seismic coefficient is important. Hence, the purpose of this study is to observe the change in the mean and standard deviation of the earth pressure introduced by the seismic coefficient. In this study, unlike the previous study the friction angle of the sandy embankment was kept constant. As a result the only variation existed in the range of interface friction angle at the interface of the soil and the wall and the range of horizontal seismic coefficient used in the estimation of the passive pressure. Table 2.4 summarizes the variations and the distribution of the parameters.

Table 2.4: Range and Distribution of the Parameters varied in the Coulomb-type Analyses

Parameter Varied	Range	Distribution
δ	$-\phi$ to ϕ	Uniform
K_h	0 to 0.5g	Uniform

In this study, the Monte Carlo analyses were performed by sampling 100,000 values belonging to a uniform distribution for δ and K_h and using the baseline sand friction angle of 38^o. The distribution of passive forces associated with this Monte Carlo study is depicted in Figure 2.14. Again, similar to the study based on the log-spiral theory, the distribution of the passive force seems to be log-normally distributed. The mean value of P_p with variation of seismic horizontal coefficient is 340 kN/*m*, the median value of P_p is 187 and the standard deviation of the natural logs is 1.051 (Figure 2.14a). For comparison, Figure 2.14b shows the distribution of P_p obtained using Coulomb earth pressure theory but without consideration for seismic coefficient. Considering the seismic horizontal coefficient increases, the values of mean, median and standard deviation of natural logs by, 18 %, 11% and 10 %, respectively.

The anticipated distribution of passive pressure for this embankment can be estimated by combining the previous two analyses. The former analysis with the log-spiral failure surfaces is deemed more accurate; hence while the median from those analyses are kept the same the standard deviations from those analyses were increased by 10% and based on the results of the second analysis to account for the variability on the seismic horizontal coefficient. Thus, based on the abovementioned studies, it was deduced that the passive pressures are log-normally distributed with a median on the range of Rankine passive pressures and a standard deviations of natural logs equal to 0.73.

2.1.3 Selection of Inertia Loads

Inertia forces can occur simultaneously with lateral spreading displacement demands, and the two loads should be accounted for simultaneously in global equivalent static analysis procedures. However, the inertia demands must be altered to account for the effects of liquefaction. Changes in inertia demands compared with those for the non-liquefied case are caused by (1) the influence of liquefaction on site response, and (2) inertia forces acting out-of-phase with ground displacements. Brandenberg et al. (2005) showed that inertia demands can occur during lateral spreading, and can be an important contributor to the lateral loads on the foundation. A number of case histories and model studies have shown that lateral spreading may also occur after ground shaking has ceased due to void redistribution. For example, the Landing Road Bridge and Showa Bridge were both affected by lateral spreading that occurred after shaking had stopped. For design, assuming the inertia demands and lateral spreading demands occur simultaneously is prudent. The probability of having zero inertia force can also be included in a probabilistic framework in performance-based earthquake engineering.

Boulanger et al. (2007) presented two modification factors for adjusting the inertia demands to account for the effects of liquefaction. Table 2.5 shows the suggested modification factors to use in the equation:

$$Sa_{liq} = C_{cc}.C_{liq}.Sa_{\max\_nonliq} \tag{2.12}$$

Where, Sa_{liq} = spectral acceleration when liquefaction is present

$Sa_{\max\_nonliq}$ = spectral acceleration for the nonliquefaction case

C_{liq} quantifies the influence of liquefaction on surface motion, and is equal to the ratio of the peak horizontal surface acceleration with liquefaction to the peak horizontal surface acceleration without liquefaction. C_{cc} quantifies the phasing between the inertia demand and the total peak demand, expressed as the inertia value at the time that the critical loading cycle occurred (i.e. when the peak bending moment was measured in the piles) divided by the peak inertia value for the entire record. The values of C_{liq} and C_{cc} were based on dynamic finite element models calibrated with centrifuge test data. C_{liq} and C_{cc} varied with the frequency content of the ground motion that was imposed on the base of the finite element models, with low-frequency motions exciting the liquefied soil more than high frequency motions. The frequency content of the motion was quantified as $Sa_{T=1s}$ / $Sa_{T=0s}$. The input motions appropriate for the analyses performed by Boulanger et al. (2007) would be rock motions, assuming that the site response analysis is performed on the soil layers lying above rock. Based on the spectral shapes for the Caltrans SDC, the middle row in Table 2.5 corresponding to $Sa_{T=1s}$ / $Sa_{T=0s}$ = 0.5 to 1.6 contains the controlling factors. These factors should be applied to the ground surface motion expected without liquefaction.

Table. 2.5: Factors C_{liq} and C_{cc} for modification of the nonliquefied inertia loads

Response spectra for nonliquefied condition, $Sa_{T=1s}$ / $Sa_{T=0s}$	Pile cap		Superstructure	
	C_{liq}	C_{cc}	C_{liq}	C_{cc}
1.7 – 2.4	1.4	0.85	0.75	0.65
0.5 – 1.6	0.75	0.85	0.55	0.65
$\leq$ 0.4	0.35	0.85	0.45	0.65

Inertia demands are typically applied as displacements in spectral design of bridges. However, applying spectral displacements is complicated by the simultaneous application of lateral spreading displacements because only global boundary conditions can be controlled in a numerical model, whereas the displacement demand is a relative displacement measure. Applying the inertia demands as forces rather than displacements is more convenient, and is permitted in the Caltrans SDC. However, this approach may not be numerically stable if a collapse mechanism forms.

2.2 Example Analyses

In this section, a few examples of the nonlinear global equivalent static analyses are presented and explained in detail. The examples are intended to demonstrate the global ESA method that was used to derive the fragility functions in Chapter 4, and to show features of interaction among bridge components captured using global analysis that cannot be modeled using a local analysis. First I will consider a perfectly symmetrical three-span simply-supported bridge with equal-length spans and single-column bents of the same height and dimensions, with seat-type abutments under several lateral spreading displacement patterns (load cases). Then I will compare the global response with local analyses of a single component of the bridge (i.e. a single pile group and pier column) under similar loading conditions and the differences between the local and global analyses will be investigated. Next, the response of this bridge under a certain loading condition will be compared with the response of a similar bridge with continuous super-structure and monolithic abutments, under similar loading conditions.

2.2.1 Configuration of the Example Simply-supported Bridge with Seat-type Abutments

This example bridge is a simply-supported 3-span straight bridge with equal spans with circular identical single-column bents (Figure. 2.15 and Table 2.6).

Table 2.6: 3-Span Simply-supported Bridge with Seat-type Abutment Properties

Parameter	Value
Spans Length	25 m
Pier Height	6.5 m
Pier Diameter	1.46 m
Pier Yield Moment	7011 kN.m
Pier Initial Stiffness, EI	2.107×10^{6} kN.m^2
Pier Shear Capacity	3049 kN
Pile Diameter	0.61 m
Pile Yield Moment	400 kN.m
Pile Initial Stiffness	5.797×10^{4} kN.m^2
Bearing Height	0.051 m
Bearing Capacity	490 kN
Bearing Yield Displacement	0.035 m

Each bent is supported on a $3\,X\,4$ group of 24-inch CIDH (Cast-in-drilled-hole) reinforced concrete piles connected by a 1-meter thick 4m X 5m pile cap, with the longer dimension in the transverse direction of the bridge. The superstructure is a 12.2 m (40 ft) wide concrete box-girder structure supported on pile-supported seat-type abutments with a total height of 3.3 m for the back wall and stem wall. The abutments are supported on a 0.7 m pile cap which itself rests on two rows of six 24-inch CIDH piles. The superstructure rests on elastomeric bearings with total pad thickness of 2 inches (0.051 m) at the abutments, while they are connected at the top of pier columns using dowels (i.e. pinned connection).

The soil profile used in this example is a typical liquefiable site soil profile. In this example, the natural crust overlying the liquefied sand layer is a clayey crust. The ground water level is assumed to be at surface of the crust. The properties of the soils in this soil profile are summarized in Table 2.7.

Table 2.7: Thickness and properties of the soil layers in the layers used in the example problems

Soil Layer	Thickness of The layer (m)	Unit Weight, γ (kN/m3)	Friction Angle φ (degrees)	cohesion, c (kPa)	Subgrade Reaction, k (kN/m^3)	m_p
Embankment	6	20	38	20	80-1357 *	1
Natural Crust	3	19	0	70	-	1
Liquefied Sand	2	19	32	-	25,541	0.05
Dense Sand	-	20	38	-	55,450	0.65 **

* The subgrade reaction stiffness at the embankment crust is adjusted to match the y_{50} value calculated using Brandenberg et al. 2007 relations for the stiffness of the nonliquefiable crust.

** The multiplier in the dense sand layer is selected based on Dobry et al.1995 assuming an excess pore pressure of about 40 %.

The p-multiplier in the liquefied sand is selected to be 0.05 based on recommendations by Brandenberg (2005) and Dobry et al. (1995). The p-multiplier for the dense sand underlying the liquefied sand was selected using the relation recommended by Dobry et al. (1995) ($m_p = 1 - 0.95 r_u$) assuming an excess pore water pressure of about 40%.

The stiffness of the p-y springs in the nonliquefied crust was estimated using the relations presented by Brandenberg et al. (2007) for both the crust at the abutment (embankment fill and nonliquefied crust) and the clayey crust at the intermediate piers and the y_{50} values for the crust at the abutment and pile caps were estimated to be 0.2m and 0.05m, respectively. The subgrade reaction in the embankment fill sands was adjusted so that the load transfer at the embankment is consistent with the soft response typical of nonliquefied crusts spreading over liquefied sand layers.

The displacement profile in liquefied ground often exhibits a discontinuity at the interface of the liquefied sand and the nonliquefied crust. The discontinuity is caused by the relative sliding of nonliquefied crust over liquefiable sands due to void redistribution (Malvick et al. 2008). In these examples, the displacement at the interface of the crust and the liquefied sand is half of the displacement in the liquefied crust. The displacements in the denser sand layer are zero. The displacements in the liquefied sand layer increase linearly (i.e. constant strain), while the displacements in the crust are constant throughout the thickness of the layer (i.e. zero strain).

The inertia loads on the bridge are calculated by estimating the spectral acceleration of the bridge in a nonliquefied site (i.e. $Sa_{\max\_nonliq}$) and modifying the demand using the modifications for the demand in liquefiable sites as discussed earlier in this chapter. The spectral acceleration of the bridge in a nonliquefied site was obtained from Caltrans ARS (Acceleration Response Spectra) at the desired level of shaking and using the appropriate soil class site, based on the first-mode natural period of the bridge. The period of the bridge in the longitudinal direction was approximated according to the formula:

$$T = 2\pi\sqrt{\frac{m_{trib.}}{k_{cl}}} \tag{2.13}$$

Where, $m_{trib.}$ = the tributary mass acting on each of the columns.

k_{cl} = the stiffness of the column

The lateral stiffness of the column for a Simply-supported bridge can be calculated to be:

$$k_{cl} = \frac{3EI_{eff}}{h^3} \qquad (2.14)$$

Where, EI_{eff} = the effective bending stiffness of the column

h = the height of the column

The lateral stiffness of this continuous bridge is:

$$k_{cl} = \frac{3 \times (2.107 \times 10^6 kN.m^2)}{(6.5m)^3} = 23{,}107 kN/m$$

and the tributary of mass acting on each pier is

$$m_{trib.} = 308.8Mg$$

Subsequently the fundamental period of the bridge in the longitudinal direction can be approximated to be:

$$T = 2\pi\sqrt{\frac{308.8Mg}{23{,}107kN/m}} = 0.73s$$

This approach neglects the period lengthening caused by soil-structure interaction, but estimating natural period in liquefied ground is difficult and suitable relations are unavailable. The method also neglects the influence of the abutments on the natural period of the bridge.

The shear wave velocity of this site associated with the first 30 meters ($V_{s_{30}}$) of this profile was estimated to be about 270 m/s which, puts this site in Site Class D (i.e. 180 <$V_{s_{30}}$< 360) according to Caltrans SDC (2006). The nonliquefiable spectral acceleration for a bridge located in site class D, undergoing rock shaking of $a_{\max} = 0.4g$ during an earthquake of magnitude 7.25 ± 0.25 using the ARS curves available in Caltrans Seismic Design Criteria is 0.85g at the period of this bridge (Figure 2.16) . The liquefied spectral acceleration for this bridge is then, 0.3g ($C_{cc} = 0.65, C_{liq.} = 0.55$).

Lateral spreading displacements can occur in many different combinations at different bridge components. For example, spreading might occur only on one side of a channel, or on both sides. Spreading may be larger at a pier near a channel than at the abutment further upslope. Furthermore, the maximum demand on the bridge components may occur when the direction of the application of the inertia is in the direction of lateral spreading, or when the direction of the inertial force is against the direction of spreading. Therefore, it is important to consider different possible scenarios (i.e. load cases) when performing nonlinear global equivalent static analyses. The examples that follow explore several possible load cases and bridge configurations.

2.2.2 Effect of Different Displacement Patterns on the Response of the Bridge

Table 2.8 summarizes the response of the piers of the example bridge described above under different global and local loading conditions.

Table: 2.8: Summary of Pier Responses under Different Global and Local Loading Conditions

Analysis ID	$M_{\max}$ (kN.m)		Δ_{cap} (m)		μ_{ϕ}		$\Delta_{Top\ Pier}$ (m)		θ_{Cap} (%)	
	Left Pier	Right Pier	Left Pier	Right Pier	Left Pier	Right Pier	Left Pier	Right Pier	Left Pier	Right Pier
Global 1	5771	-9980	0.34	0.018	<1	9.5	0.3	0.3	-0.04	-0.76
Global 2	-6436	-6238	0.015	0.014	<1	<1	0.078	0.074	-0.31	0.28
Global 3	6759	-9007	0.26	0.01	<1	6.7	0.19	0.19	0	0.47
Local 1	-5710	N/A	1.965	N/A	<1	N/A	3.94	N/A	-29.8	N/A
Local 2	9228	N/A	0.168	N/A	7.3	N/A	0	N/A	-0.1	N/A
Local 3	5710	N/A	0.319	N/A	<1	N/A	0.282	N/A	-0.03	N/A

Load Case 1 (Figure 2.17) considers the bridge under lateral spreading displacements happening in the left spreading feature (i.e. left abutment and left pier) of the bridge with 0.5 m of free-field ground displacement at the left abutment with 2 m of lateral spreading at the left pier. It is also assumed that in this loading condition the inertia is still present while the lateral spreading is occurring. In this load case, the inertia load is considered to be happening in the direction of spreading. As a result inertia loads are applied as a force equal to the product of the mass times spectral acceleration of the bridge while the displacement demands on the bridge are linearly increasing. The loading condition and the deformed mesh of the response of the bridge are shown in Figure 2.17a, while the moment distribution is shown on Figure 2.17b.

Under this loading condition the entire bridge is moving from left-to–right under the combined effects of lateral spreading and inertia demands. Large demands are mobilized in the piles supporting the left abutment and the left pier, which are the locations where lateral spreading displacements were imposed. The pile cap displacement at the left pier is 0.34 m, while the superstructure displacement is 0.30

m, which places only 0.04 m of displacement demand on the pier. In contrast, the pile cap displacement at the right pier is less than 0.02 m while the displacement of the top of the pier is 0.3 m, placing a much more significant displacement demand that yields the pier and mobilizes a curvature ductility of 9.5 (M_{max} = -9980 *kN·m*). This global analysis demonstrates how lateral spreading demands on some bridge components can transfer demands to other components founded in firm ground. This type of interaction can only be properly modeled using a global analysis.

Load case 2 considers the bridge under symmetrical displacement demand from both abutments of the bridge, such that the lateral spreading displacements are equal in magnitude (maximum ground displacement is 0.5 m) but opposite in direction toward the center of the bridge. The inertia demand is also present and is applied from left to right. Figure 2.18 shows this loading condition with the corresponding deformed mesh and the bending moment distributions on the piles and the piers of the bridge. Since the spreading is perfectly symmetrical the only demand on the piers comes from the inertia load that is being concurrently applied with lateral spreading displacements which moves the superstructure about 0.08 m to the right. However, the inertia demand is not large enough to cause the pier columns to yield. The piles that support the abutments suffer extensive deformations that would be anticipated to fail the piles and thereby reduce their axial load carrying capacity. While the analysis clearly predicts extensive damage to these piles, the amount of damage predicted may be unreasonable due to several assumptions in the analysis approach. The large demands are in part an artifact of the Winkler assumption that the p-y element behaviors are independent of the adjacent elements, and the fact that free-field ground displacements are being imposed on the piles. In essence these assumptions result in an unrealistic soil deformation pattern wherein the actual soil deformation would be small behind the abutment backwall and large deeper down at the piles. A two- or three-dimensional pinning analysis could more reasonably capture the manner in which the forces imposed on the embankment by the abutment backwall would reduce deformations in the underlying soils. However, such an analysis is beyond the scope of this work. Nevertheless, the predicted abutment displacement is consistent with the bridge deformation mechanism observed at several bridges in past earthquakes (e.g., in Kashiwazaki during the 2007 Niigata Chuetsu-Oki earthquake; Kayen et al. 2007).

2.2.3 Effect of the Direction of the Inertia Demands on the Bridge Response

Inertia demand on bridges and other structures is transient and alternating in all directions. As a result, during earthquakes when liquefaction and lateral spreading is occurring at the site of the bridge, at an instant in time the inertia load acting on the bridge can range from being perfectly in-phase with the lateral spreading displacement demands to being perfectly out-of-phase. Thus, it is important to consider inertia loads in-phase and out-of-phase with lateral spreading, since the overall demand may be more severe in one case or the other. Load case 3 (Figure 2.19), has the same lateral spreading demand as load case 1 (Figure 2.17), however the inertia demand in load case 3, is out-of-phase with lateral spreading demands. In this case, the displacement demand due to inertia in the opposite direction of spreading displacement demand increases the bending moment in the left pier from 5771 $kN.m$ to 6759 $kN.m$. While this demand is still lower than the yield moment of the pier (7011 $kN.m$) in this case, it is obvious that load cases with out-of-phase inertia, may apply higher demands on the piers and cause them to yield or reach higher curvature ductilities. On the other hand, the inertia acting in the opposite direction of spreading results in lowering the superstructure displacement from 0.3m to 0.19m. This results in reduction of displacement demands on the right pier causing a reduction in curvature ductility from 9.5 to 6.7 (M_{max} = -9980 $kN.m$ to M_{max} = -9007 $kN.m$). Pile cap displacement at the left pier is also reduced from 0.34m to 0.26m. Generally speaking the demand on the bridge can be significantly affected by the direction of inertia, and the above example points to the importance of considering both load cases when evaluating the performance of the bridge under liquefaction-induced demands.

2.2.4 Effect of Bridge Type on the Response of Bridges

In order to investigate the effect of bridge type on the response of the bridge under lateral spreading demands, consider the bridge similar to the bridges in load cases 1 to 3 with a bridge with exactly the same geometry but with a continuous superstructure and with monolithic abutments. The superstructure is connected to a 3-meter tall diaphragm wall supported on a single row of six 24-inch CIDH piles (Figure 2.20) (consistent with common foundations for diaphragm abutments).

Since the boundary conditions of this bridge are different (i.e. fixed-fixed) the period of the bridge should be calculated based on a lateral stiffness of a column fixed at top and bottom, as follows:

$$k_{cl} = \frac{12EI_{eff}}{h^3} \tag{2.15}$$

Therefore,

$$k_{cl} = \frac{12 \times (2.107 \times 10^6 kN.m^2)}{(6.5m)^3} = 92,428kN/m$$

And subsequently the period of the bridge is:

$$T = 2\pi \sqrt{\frac{308.8Mg}{92,428kN/m}} = 0.37s$$

The nonliquefiable spectral acceleration for a bridge located in site class D, undergoing rock shaking of $a_{\max} = 0.4g$ during an earthquake of magnitude 7.25 ± 0.25 using the ARS curves (Figure 2.16) is 1.10g at the period of this bridge. The liquefied spectral acceleration for this bridge is then, 0.4g ($C_{cc} = 0.65, C_{liq.} = 0.55$).

Load case 4 (Figure 2.21) considers this continuous bridge under the same lateral spreading displacement pattern as in load case 1 (i.e. 2*m* of spreading at the left pier and 0.5*m* of spreading at the left abutment), and with inertia acting in-phase with the lateral spreading demands but with inertia demands associated with a spectral acceleration equal to 0.4g based on the period of this bridge.

Table 2.9 shows the comparison of the results of the two bridges considered in load cases 1 and 4.

Table: 2.9: Comparison of the Response between a Simply-Supported Bridge with Seat-Type Abutments and a Continuous Bridge with Monolithic Abutments under the same Loading Condition

	M_{max} (kN.m)		Δ_{cap} (m)		μ_{ϕ}		$\Delta_{Top\ Pier}$ (m)		θ_{Cap} (%)	
Analysis ID	Left Pier	Right Pier	Left Pier	Right Pier	Left Pier	Right Pier	Left Pier	Right Pier	Left Pier	Right Pier
Global 1	5771	-9980	0.34	0.018	<1	9.5	0.3	0.3	-0.04	-0.76
Global 4	-5734	9557	0.146	0.035	<1	8.3	0.136	0.132	0	-1.3

As can be seen in Figure 2.21b the moment distribution mobilized at the end of load case 4 shows a double curvature as would be expected in bridges with columns with double fixity. Compared with the bridge with seat type abutments, the diaphragm abutments increase the stiffness of the bridge and reduce the superstructure displacement from $0.3m$ to $0.13m$. Also the pile cap displacements at the left pier reduced from $0.34m$ to about $0.15m$. Furthermore, the stiffer right pier in this case, imposes more displacement and rotation demand at the right pile cap because of the displacement of the superstructure.

2.2.5 Comparison of Global Analyses and Local Analyses

Global equivalent static analyses can capture the interaction between different bridge components, but the computational demand required to model the entire bridge is often not justified, and local analysis of a single sub-system is performed instead. However, since local analysis does not directly capture the interaction of multiple sub-systems, the boundary conditions imposed in the local analysis should envelope the possible global boundary conditions. In this section, local analyses of a single pier are performed and compared with the global analyses. The left pier and pile group are modeled in the local analysis, and several different boundary conditions are imposed at the top of the pier. The rotational restraint at the top of the pier is free for a simply supported bridge and fixed for a monolithic bridge. The displacement degrees of freedom are modeled in three separate manners intended to capture possible global loading mechanisms. First, the inertia force is imposed in-phase with lateral spreading displacements to represent a condition where the superstructure displacement is driven largely by inertia loading (Figure 2.22). Second, the top of the pier is held fixed at zero displacement to model the possible case where the superstructure is held in place by other sub-systems in non-liquefiable stable ground (Figure 2.23), and in turn fixes the top of the pier against displacement. Finally, the inertia force is imposed in the opposite direction from lateral spreading displacements since this condition may cause large displacement demands on the pier (Figure 2.24). The free-field ground deformation profile applied to the left pier in global load cases 1 and 3 is applied to the pile group in the local analysis.

Global load case 1 (Figure 2.17) and local load case 1 (Figure 2.22) have identical displacement and inertia demands, however as can be seen in Table 2.8 the response of the local analyses does not capture the response observed in the global load case 1.

The local analysis predicts significant displacement at the pile cap (1.97*m*) due to yielding of the piles and a pile cap rotation of about 30%. The superstructure displacement is 3.94*m*. The difference between the local and global analysis in this case is that the local analysis does not permit the pier to help resist lateral loads from the spreading soil by transferring forces to the abutments and the other pier.

Local load case 2 attempts to better capture the distribution of forces through the pier to other components by fixing the top of the pier against horizontal translation (Figure 2.23). Compared with global analysis 1, local load case 2 predicts smaller pile cap displacement (0.17*m* compared with 0.34*m*) and larger flexural demand on the pier (M_{max} = 9228 *kN·m* compared with 5771 *kN·m*), causing the pier to reach a curvature ductility of 7.3.

Global load case 3 (Figure 2.19) and local load case 3 (Figure 2.24) have the same free-field ground deformation profile and inertia demand, with inertia load acting out-of-phase relative to the lateral spreading displacements. However, differences arise in the predicted response. Local load case 3 predicts large pier top displacement (0.28*m* compared with 0.19*m*), larger pile cap displacement (0.319m compared with 0.26m) and smaller bending moment demand (5710 kN·m compared with 6759 kN·m). These trends are consistent with the distribution of demands from the pier to other components through the superstructure in the global analysis

The local analysis approach has been shown to differ significantly from the global analysis method, but in general the three different loading conditions imposed in the local analyses enveloped the responses from the global analyses. For this case, significant pile cap displacements and demands on the piers would be predicted using either global or local analysis methods, and the conclusion that the foundation performance is inadequate would result from either. Hence, local analysis may be a feasible design tool. However, global analysis is believed to more accurately model behavior of the entire bridge, and the purpose of this dissertation is not to formulate a design method but rather to evaluate the behavior of bridges (many of them old and fragile) to liquefaction and lateral spreading. The global method is better suited to this goal.

2.2.6 Effect of Pile Strength on the Response of the Bridges

Since the foundation in the previous section would be considered inadequate from a design perspective, the analysis was repeated with larger diameter piles. Global load case 1 (i.e. inertia load in-phase with lateral spreading displacements) was repeated with the 24"CIDH piles are substituted with 24" cast in steel shell (CISS) piles with properties summarized in Table 2.10. This analysis is called global load case 5.

Table 2.10: Properties of the 24" CISS Piles

Parameter	Value
Pile Diameter	0.61 m
Pile Yield Moment	1977 kN.m
Pile Initial Stiffness	2.865×10^5 kN.m^2

Local load cases 1, 2, and 3were also repeated with the 24" CISS piles, and called loca load case 4, 5 and 6, so that a comparison between the local load cases can be made with the global analysis. Table 2.11 summarizes the results of the analyses performed using 24" CISS piles.

Table: 2.11: Comparison of the Response of the Bridge with Strong CISS piles under Global and Local Analyses

	M_{max} (kN.m)		Δ_{cap} (m)		μ_{ϕ}		$\Delta_{Top\ Pier}$ (m)		θ_{Cap} (%)	
Analysis ID	Left Pier	Right Pier	Left Pier	Right Pier	Left Pier	Right Pier	Left Pier	Right Pier	Left Pier	Right Pier
Global 5	2518	-5404	0.04	0.003	< 1	< 1	0.048	0.048	0	0
Local 4	-5710	N/A	0.147	N/A	< 1	N/A	0.36	N/A	-2.6	N/A
Local 5	4967	N/A	0.027	N/A	< 1	N/A	0	N/A	-0.11	N/A
Local 6	5710	N/A	0.025	N/A	< 1	N/A	-0.007	N/A	-0.11	N/A

Figure 2.25 shows the deformed mesh and moment distribution for the global load case 5, with CISS piles. It is evident from Table 2.11 and also Figure 2.25 that these strong CISS piles are much more effective than the CIDH piles in resisting lateral spreading demands on the bridge. The pile cap supporting the left pier displaced only 0.04m (compared with 0.34m for the CIDH piles) despite 2m of lateral spreading displacements being applied at this pier. Also the superstructure displaced less that 0.05m. Neither pier column yielded with the CISS piles because the pile cap did not displace significantly.

The local load cases better envelope the global response for the CISS piles, indicating that local analyses are more appropriate when the foundation performance is good. This is consistent with the observation that (1) the primary difference between the local and global analysis is the ability of the latter to distribute demands to other components through the superstructure, and (2) less demand is distributed through the pier to the superstructure when the foundations are stiff and strong. This confirms the previous observation that local analysis can be a useful design tool, but global analysis is better for predicting the distribution of demands throughout the bridge.

2.2.7 Pile Pinning Effect of Reducing Displacement Demands on Abutments

Abutment walls and piles at the abutments reduce the displacement demands imposed on the bridge by restraining the finite-width slope. This reduction in demand has been called "pile pinning", though bridge components other than the piles also contribute to pinning and the procedure is referred to as a "pinning" analysis herein. Free-field lateral spreading ground deformation is not the appropriate demand to place on bridge components in a finite-sized lateral spread (e.g., when the out-of-plane thickness is small for an embankment, or when the upslope extent of the spread is small). Rather, a displacement demand that is compatible with the pinning forces should be used. The procedure for finding a pinning-compatible displacement is a two-step procedure that was proposed by the Transportation Research Board (TRB, 2002) and subsequently updated by Boulanger et al. (2007). These methods were developed for local analysis, and are extended to global analysis in this section.

The first step of the procedure involves performing an equivalent static analysis where the embankment soils are displaced against the bridge to develop a relation between the mobilized forces and free-field ground surface displacement. The distribution of horizontal force mobilized against the embedded structural components is recorded to model the restraining forces imposed on the spreading soil in the second step. An important feature of the analysis identified by Boulanger et al. (2007) is that the restraining force mobilized at a given amount of free-field ground displacement is not equal to the restraining force that exists during the entire earthquake. Rather, the restraining force begins at zero and eventually reaches its final value at the end of lateral spreading. Hence, Boulanger et al. (2007) suggest taking the running average of the relation between restraining force and free-field ground displacement to use in combination with the Newmark sliding block analysis in the second step.

The second step involves a sequence of slope stability analyses to find the yield acceleration of the embankment associated with various levels of restraining force, and a Newmark sliding block analysis to identify the ground displacement associated with that yield acceleration. The restraining forces can be represented by directly imposing the distribution of forces in the p-y springs on the slope, or by representing the distribution as a resultant force acting at the centroid of the distribution. The limit equilibrium analysis is conducted for a unit thickness (i.e. out of the plane of the problem), and the restraining force must therefore be multiplied by an appropriate thickness of the embankment to obtain units of force. Boulanger et al. (2007) found that using a width equal to only the width of the pile group is inadequate because stresses attenuate geometrically in the embankment, and recommend using the full crest width plus half of the side slope mass to determine an appropriate equivalent width.

After performing both steps, the mobilized force versus ground displacement is plotted on the same figure as the restraining force versus Newmark displacement, and the intersection of this plot is the displacement-compatible solution. An example of the pinning procedure is performed for the three different global load cases 1, 2 and 3 for the bridge in the example problem. Step 1 of the pinning procedure was therefore already completed in previous sections, and step 2 was completed using slope stability analyses in the Rocscience program Slide 5.0 combined with a Newmark sliding block analysis for a ground motion recorded at Port Island scaled to peak ground accelerations of 0.2g, 0.3g and 0.4g. Obviously, the amplitude of Newmark displacements also depend on the frequency content and duration of the ground motion, but those effects were ignored for this analysis.

The soil properties used for the slope stability analyses are summarized in Figure 2.26. The embankment was 6 meters tall. The clay crust and the liquefied sand layers were 3 and 2 meters tall, respectively. The equivalent width of the embankment was calculated to be $18.2m$ using recommendations by Boulanger et al. (2007) and the length of backfill embankment for the slope stability analyses was limited to $30m$ (5 times the height of the embankment). The yield acceleration (i.e. a_y) of the embankment with no pinning force present was calculated to be $0.0615g$ using Spencer's method (Figure 2.27).

Figure 2.28 shows the distribution of the forces on the abutment piles at the end of the load case 1. The distribution was represented as the resultant acting at a depth of $4.35m$. The location of the equivalent force is assumed to be constant for different values of the resisting force, even though the location somewhat varies by the magnitude and the distribution of the forces behind the wall for every load case.

Figure 2.29 shows the results of the pinning analyses for load cases 1, 2 and 3. As can be seen in Figure 2.29, the amount of restraining force mobilized at the abutment depends on the pattern of lateral spreading displacements imposed on the bridge. The softest response is load case 1, where the entire left side of the bridge is being pushed by lateral spreading soil. This load case is the least effective at pinning the spreading embankment. The stiffest response is load case 2, where symmetrical lateral spreading demands are imposed in opposite directions, while inertia load is applied from left to right. This load case is the most effective at pinning the spreading embankment because the superstructure acts as a strut. Load case 3 which has inertia demand out-of-phase from the lateral spreading demands is more effective than load case 1, in pinning the embankment displacements, but less effective than load case 2.

Furthermore, the pinning is more effective for stronger motions. Figure 2.30 shows the reduction in the ratio of the pinning-compatible displacements to free-field displacements, which is the intersection of the two steps of the pinning analysis for different values of ground displacements. The reduction in lateral spreading displacement demands becomes more significant, consistently for all load cases, as the free-field displacement (or peak ground acceleration) increases.

On average the pinning compatible displacement is about 3/4 of the free-field ground displacement for these load cases. The pinning procedure outlined in this section can easily be repeated for other bridges and load cases with only a modest increase in effort from a design perspective. However, the procedure is onerous for the large number of analyses performed in this dissertation because it would require repeating the slope stability analysis and repeating the global equivalent static analysis for each of the thousands of simulations. Hence, in chapter 4 the displacements at the abutments were decreased by 25% from their estimated free-field values to approximately incorporate the influence of pinning. This reduction is important because demands on the bridge are ultimately related to free-field lateral spreading ground displacement, which is a convenient metric that can be estimated using a number of different approaches. A reduction was not required for the pile group supporting the piers because the extent of lateral spreading soil was assumed to be very large for these components such that the free-field demand was appropriate.

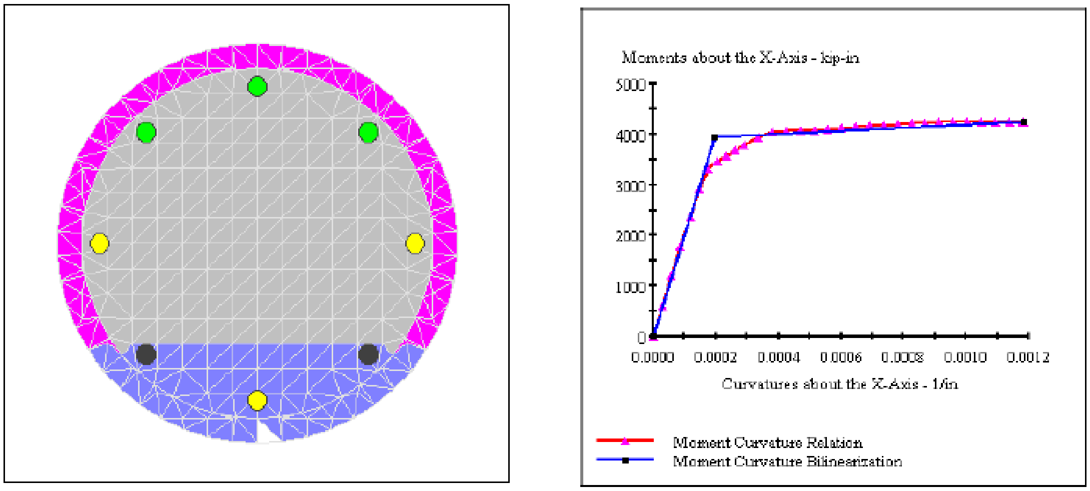

Figure 2.1: Fiber-section of a 24" CIDH pile model and the corresponding moment curvature relation

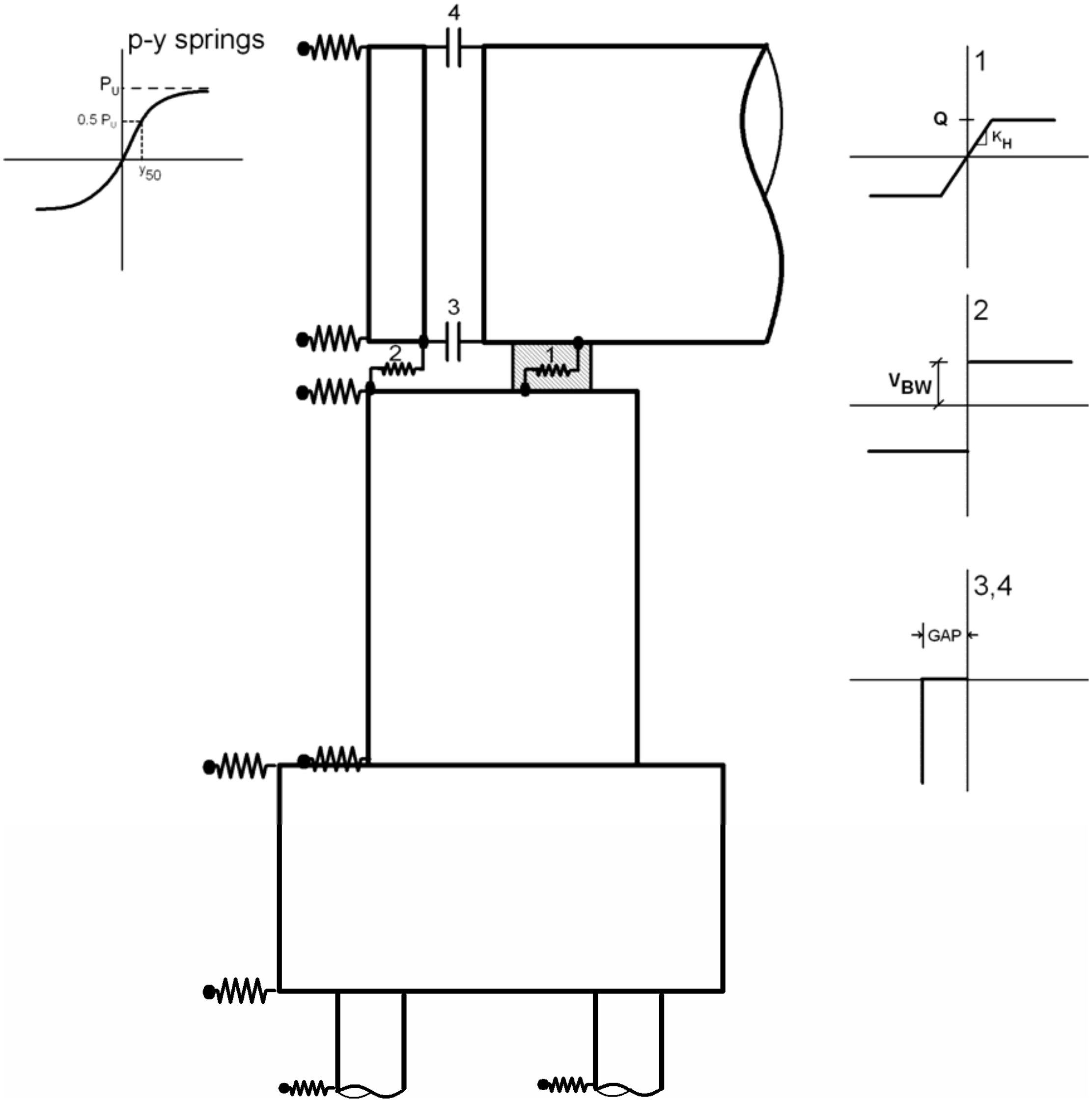

Figure 2.2: Schematic of a seat-type abutment of the bridge and the corresponding interface springs

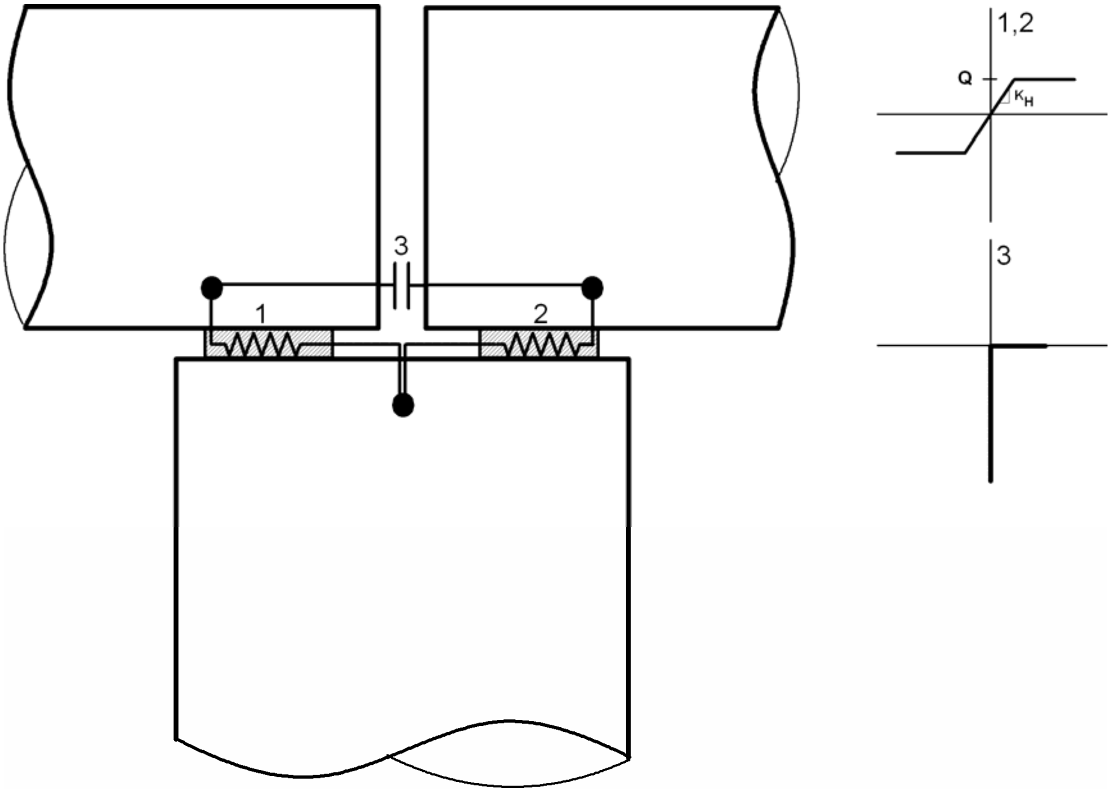

Figure 2.3: Schematic of a simply-supported bridge superstructure and the corresponding interface springs at the top of a pier

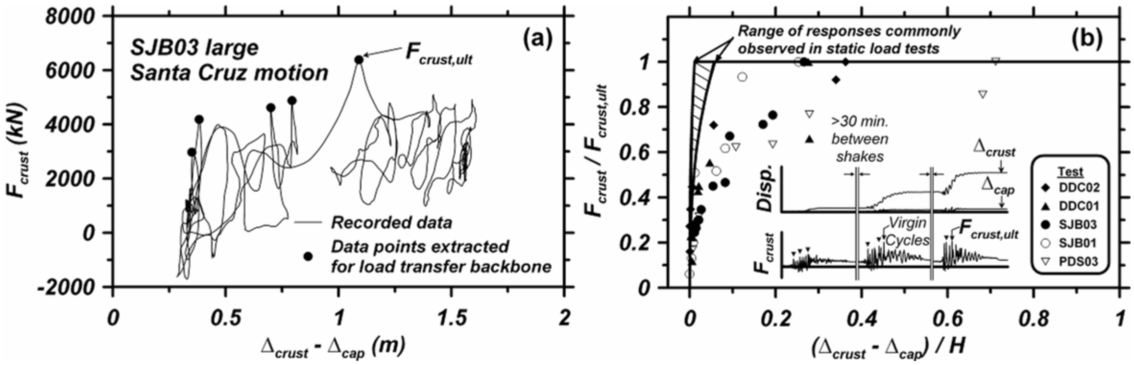

Figure 2.4: Load transfer in non-liquefiable crust, (a) Recorded load-deflection data from centrifuge models, (b) Normalized back-bone load transfer relations (Brandenberg et al. 2007)

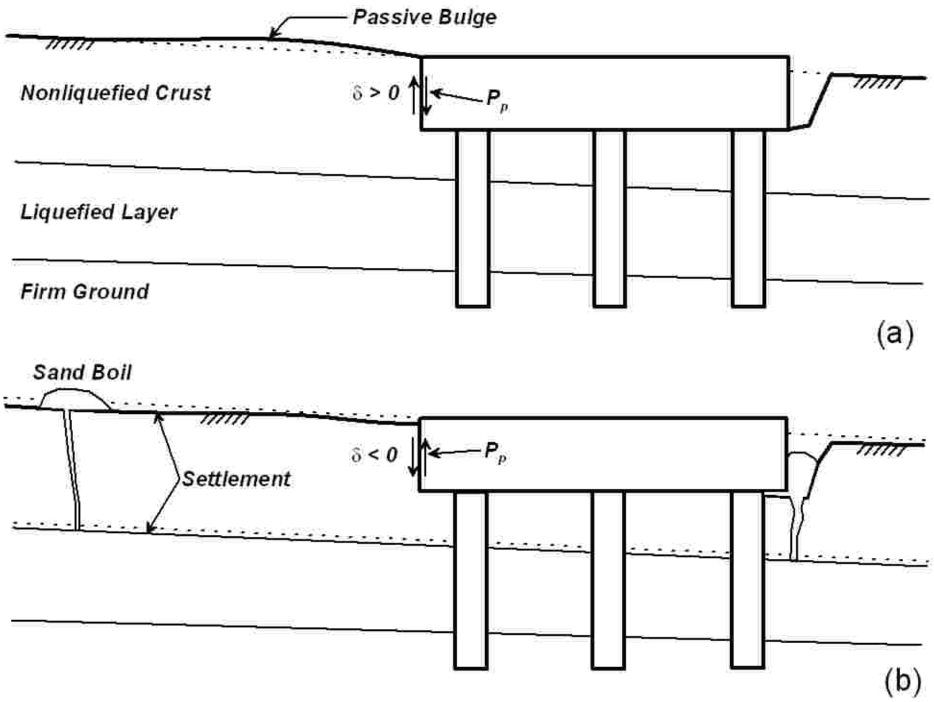

Figure 2.5: Schematic of (a) traditional passive pressure development with δ > 0, and (b) downdrag passive pressure development with δ < 0 due to settlement of nonliquefied crust (Courtesy of Scott J. Brandenberg).

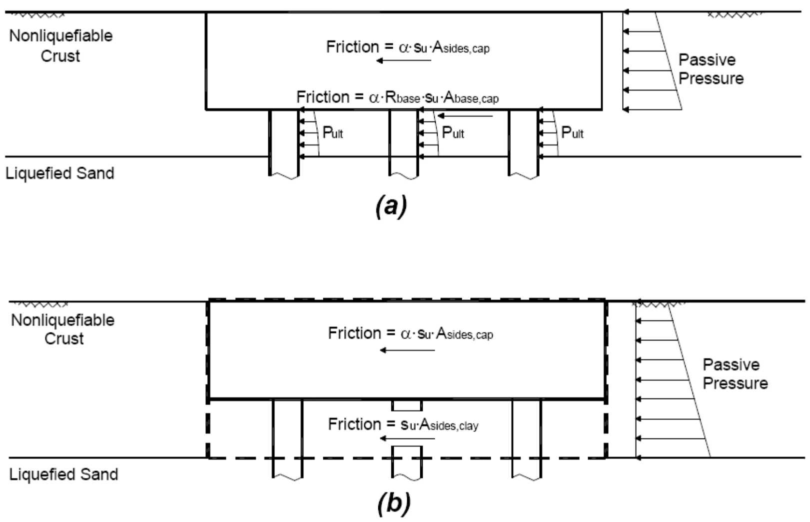

Figure 2.6: Mechanisms of spreading in nonliquefiable crust, a) Flowing mechanism, b) Equivalent Block mechanism (Courtesy of Scott J. Brandenberg)

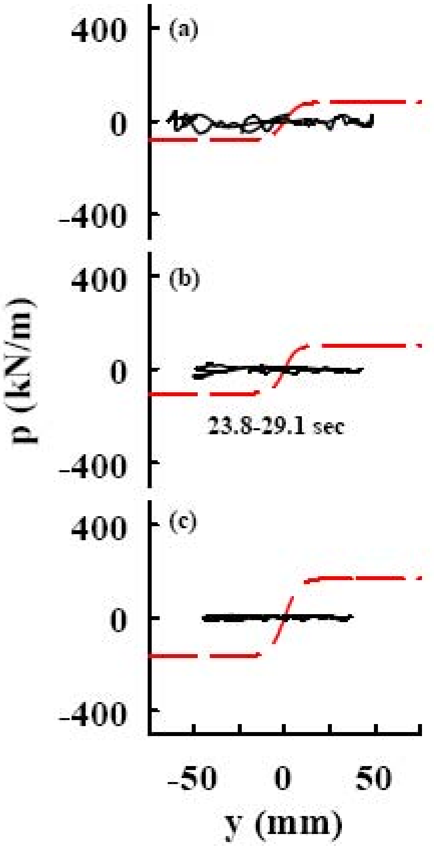

Figure 2.7: p-y loops in liquefying loose sand (Dr = 35 %) at depths a) 2D b) 3D, and c) 4D (D = 0.67 m). Dashed lines per API (1993). (Wilson et al. 2000)

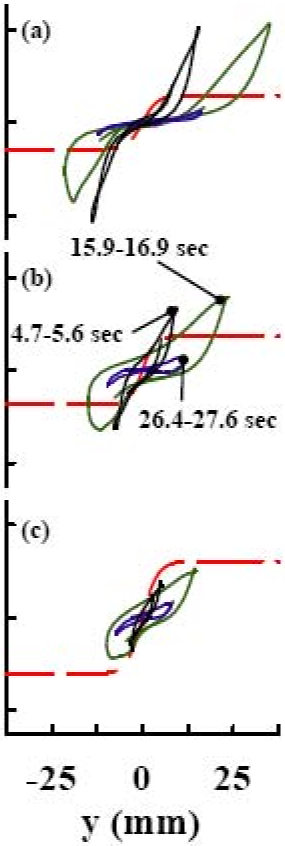

Figure 2.8: p-y loops in liquefying medium sand (Dr = 55 %) at depths a) 2D b) 3D, and c) 4D (D = 0.67 m). Dashed lines per API (1993). (Wilson et al. 2000)

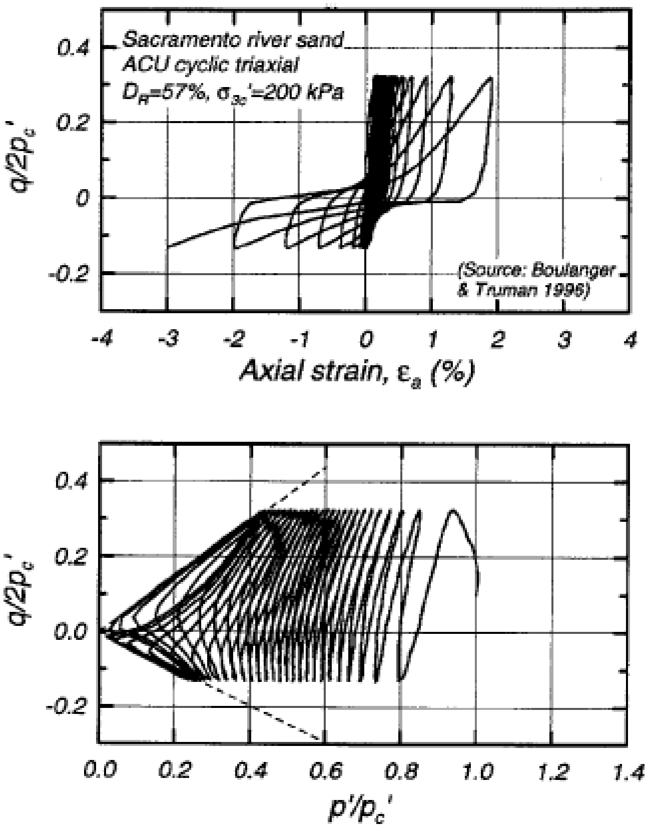

Figure 2.9: Stress-strain response and effective stress path for Sacramento River sand during undrained cyclic triaxial loading (Boulanger and Idriss 2006)

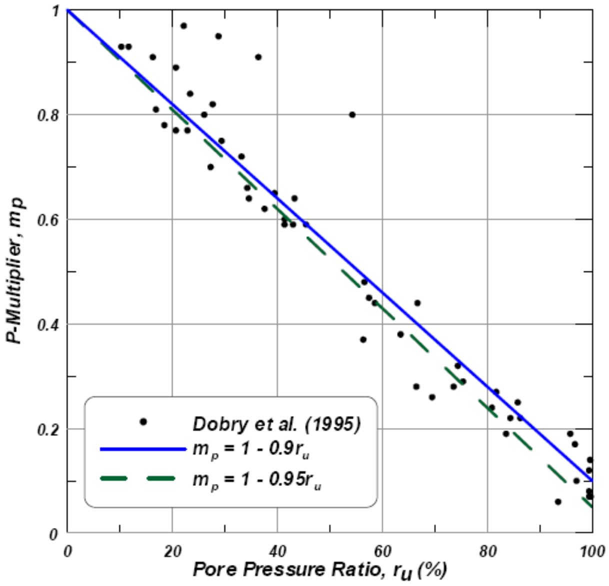

Figure 2.10: Effect of peak free-field excess pore pressure ratio on the ultimate capacity of p-y materials in liquefied sand (Dobry et al. 1995).

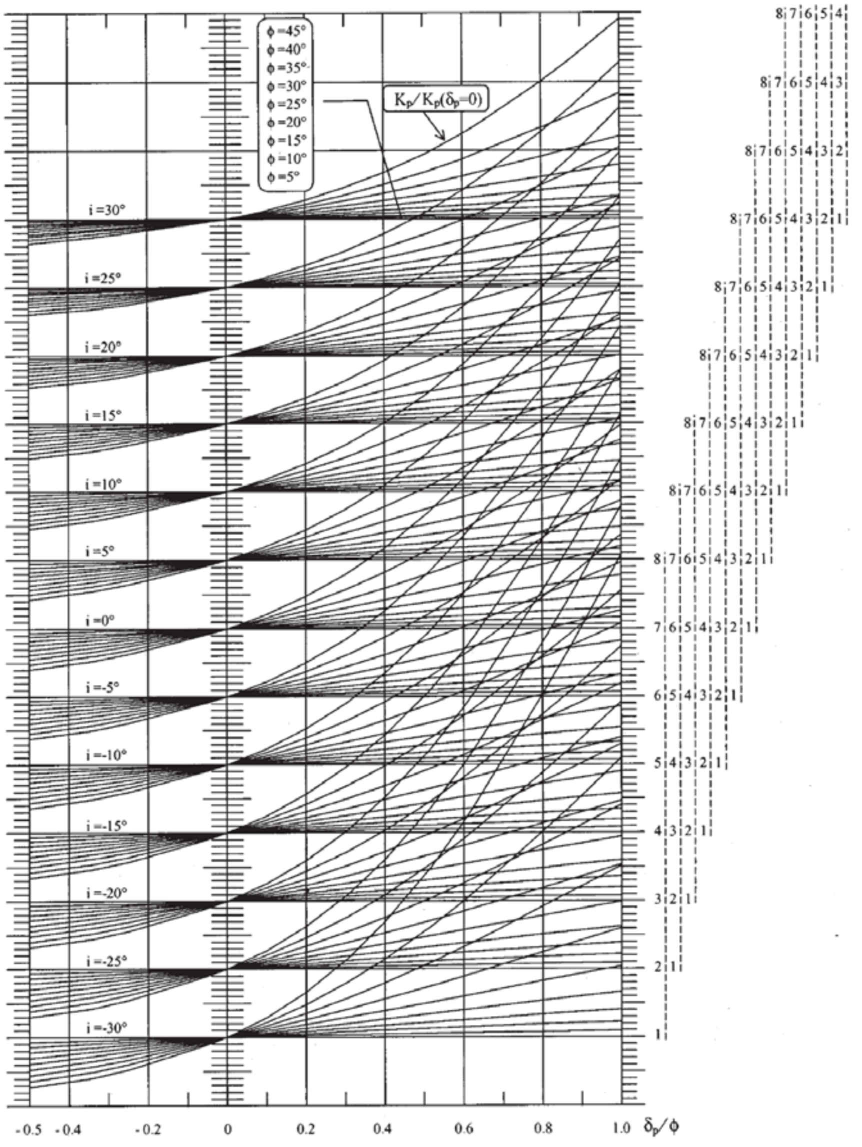

Figure 2.11: ratio of K_p(rough wall) to K_p(smooth wall) for different values of friction angle and back fill inclination (Zhu and Qian, 2000)

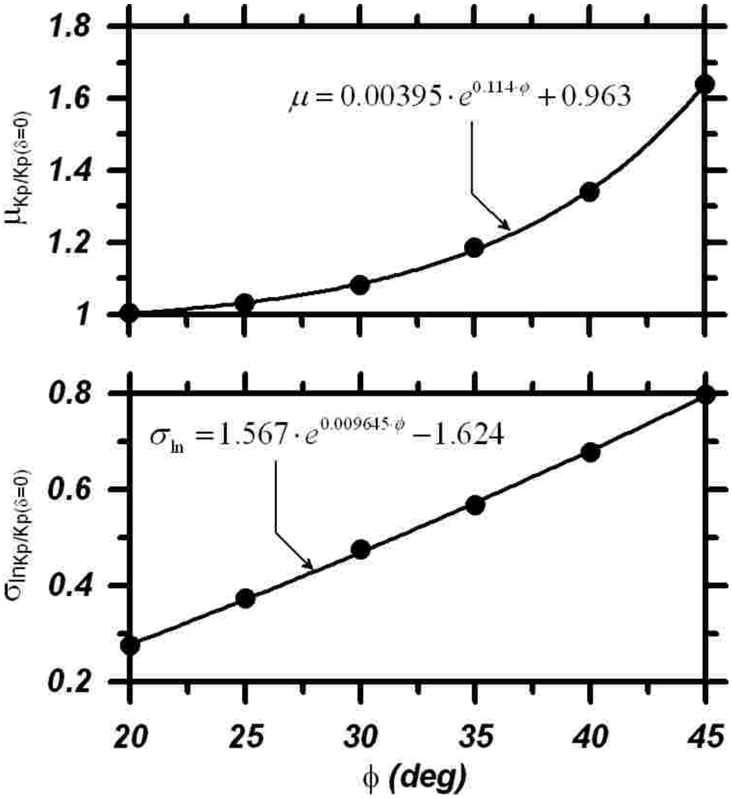

Figure 2.12: Mean and standard deviation of K_p / $K_p(\delta=0)$ versus friction angle.

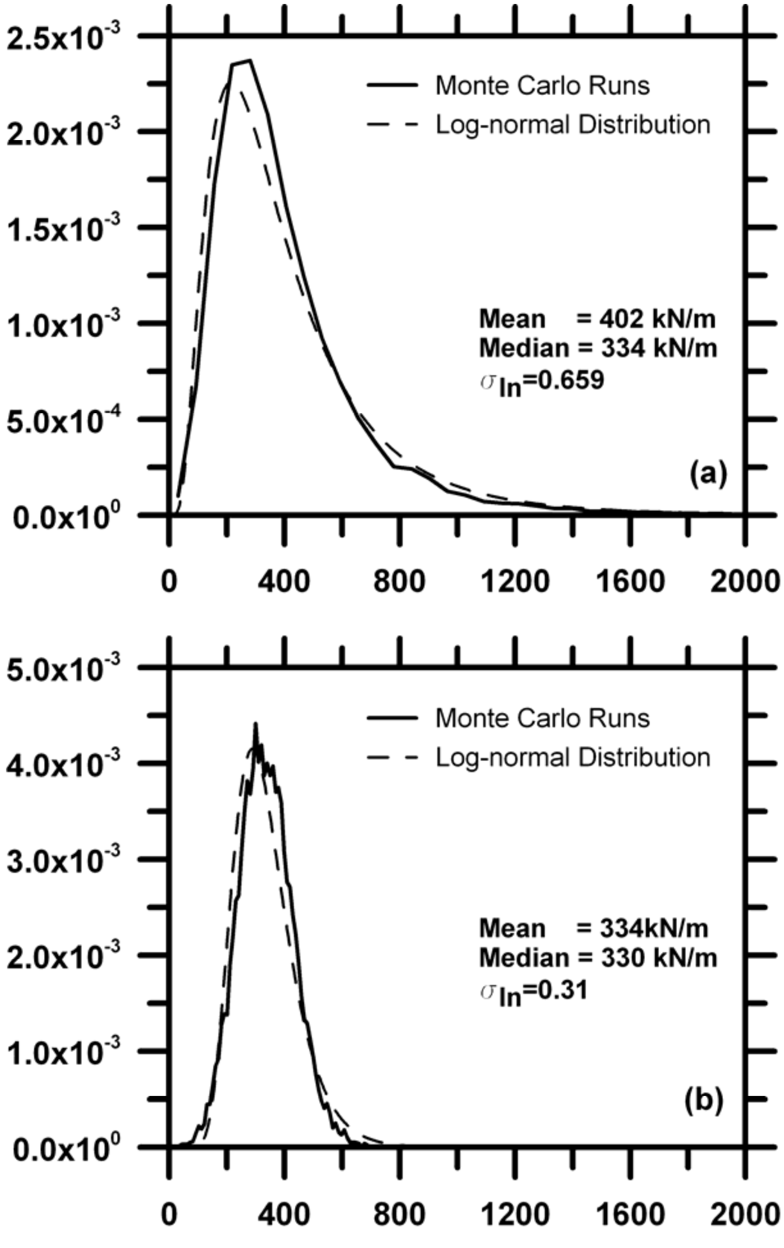

Figure 2.13: Distribution of the passive force based on the Monte Carlo analyses using (a) Log-spiral theory with variations on δ, (b) Rankine theory without wall friction

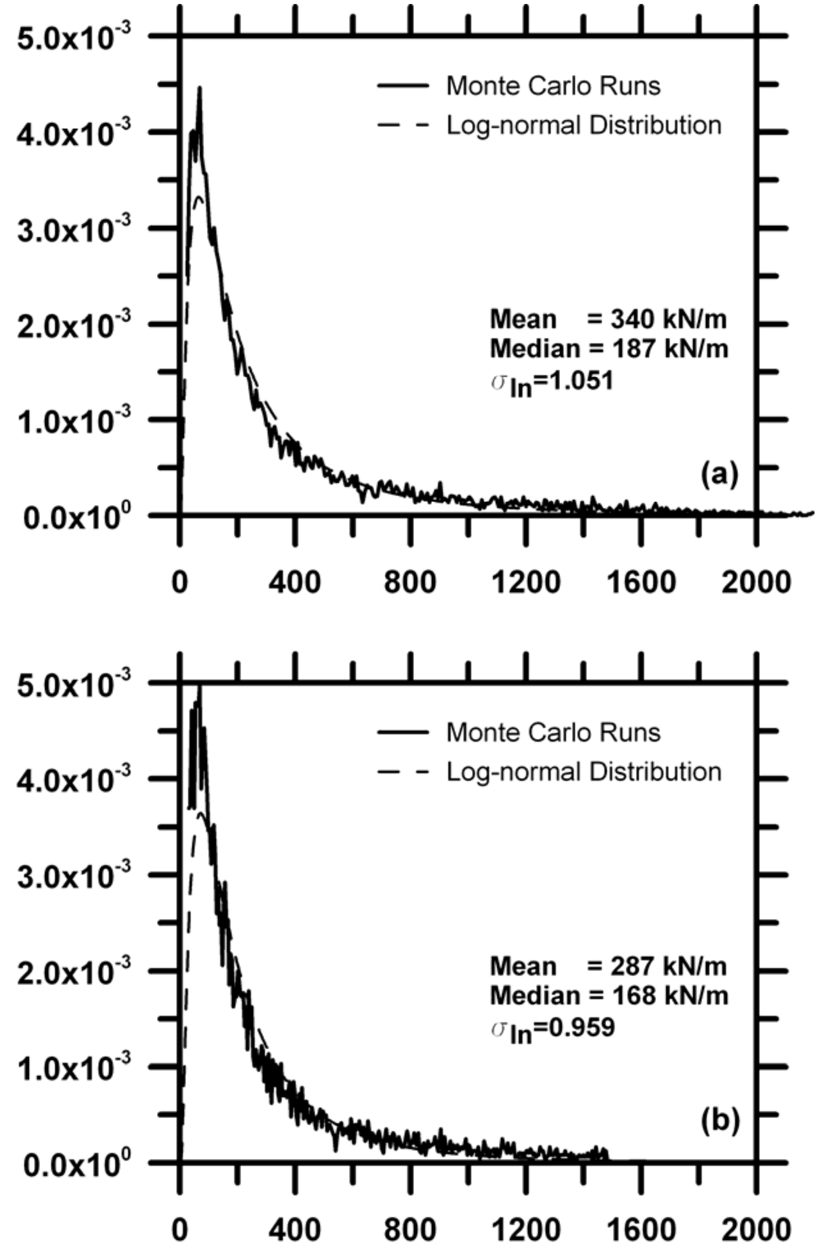

Figure 2.14: Distribution of the passive force based on the Monte Carlo analyses using Coulomb-type planar failure surface, (a) with variation of seismic horizontal coeffient, (b)

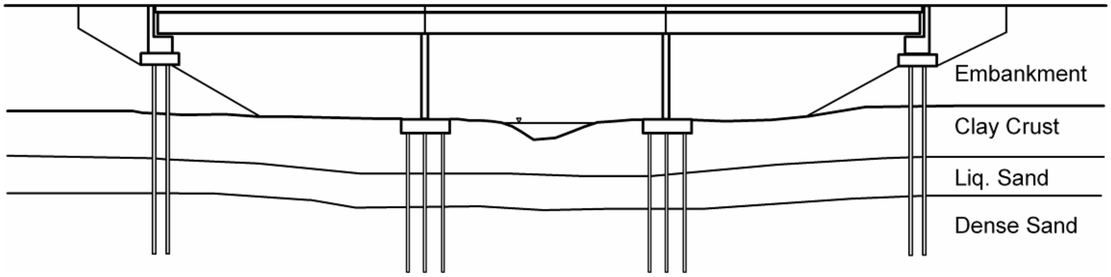

Figure 2.15: Schematic of the Three-Span Simply-supported Bridge with Seat-type Abutments

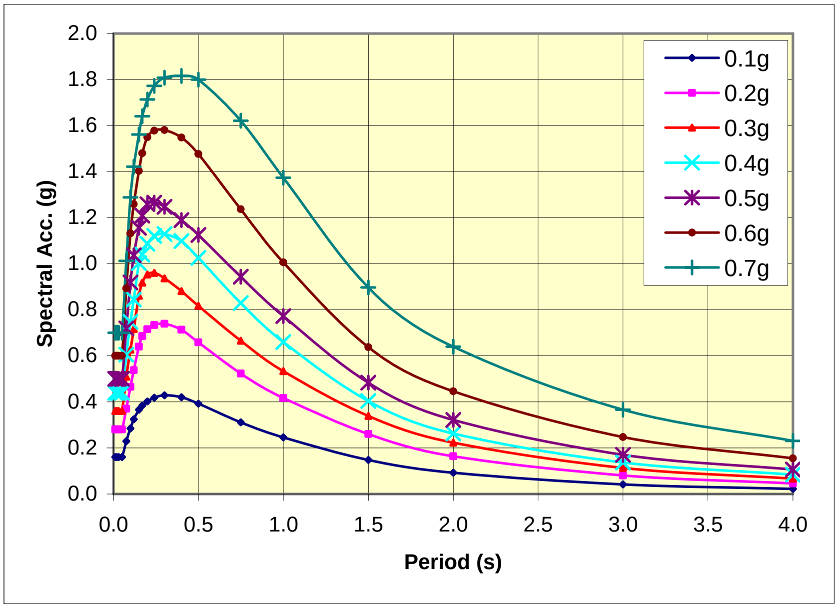

Figure 2.16: CALTRANS Acceleration Response Spectra for 5 % damping for Magnitude 7.25 ± 0.25 in Site Class D

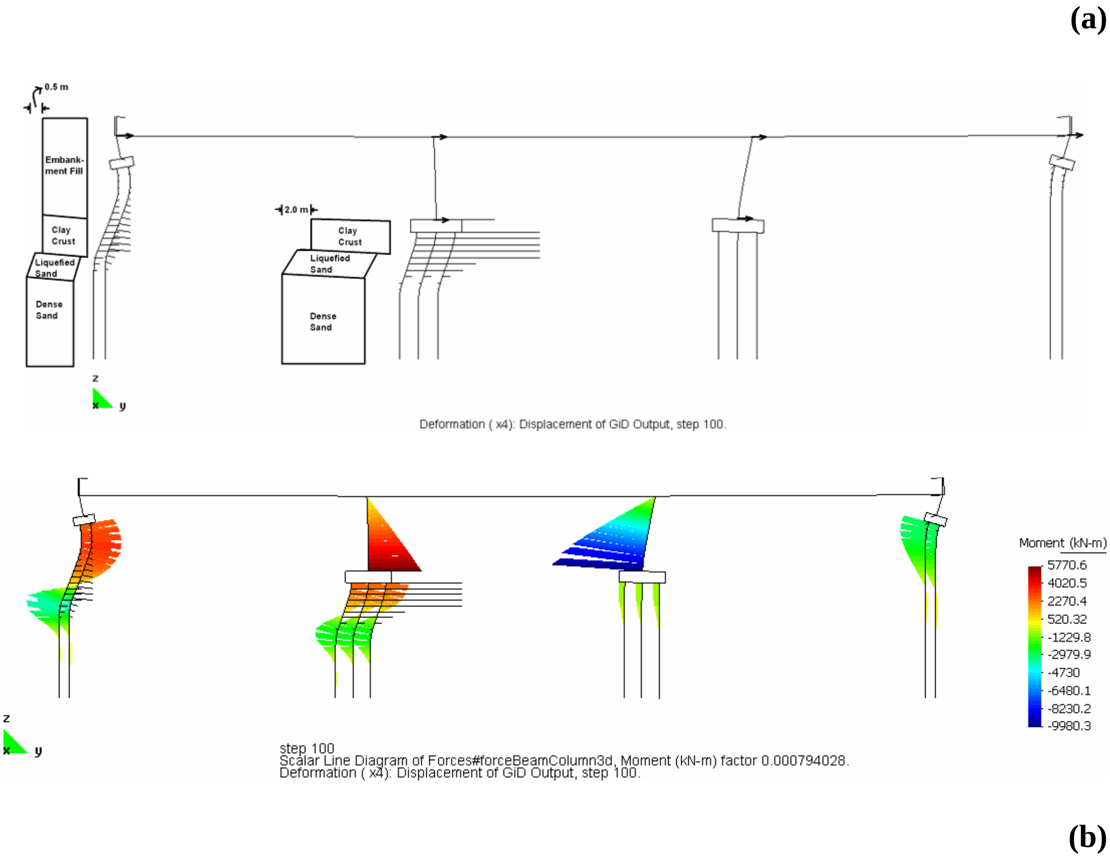

Figure 2.17: Global Analysis Load Case 1; a) Load Pattern and Deformed Mesh; b) Deformed Mesh and Moment Distribution in nonlinear beam column elements (Deformations amplified by a factor of 4.0)

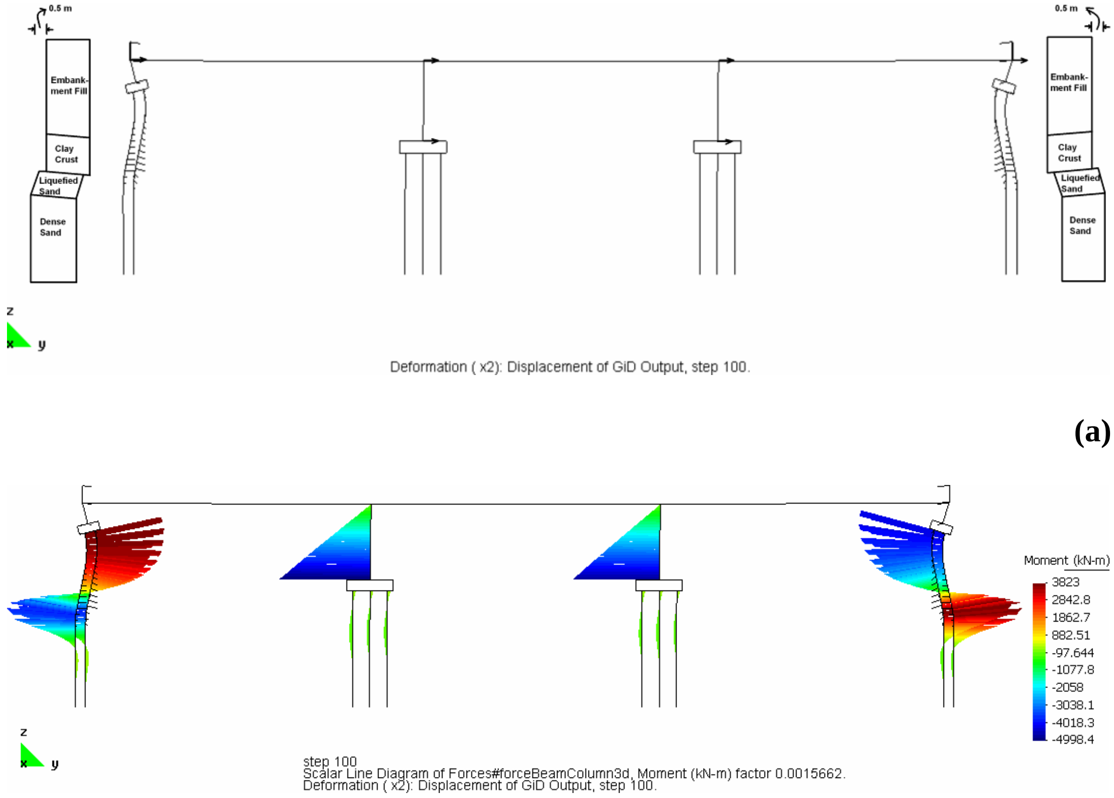

Figure 2.18: Global Analysis Load Case 2; a) Load Pattern and Deformed Mesh; b) Deformed Mesh and Moment Distribution in nonlinear beam column elements (Deformations amplified by a factor of 2.0)

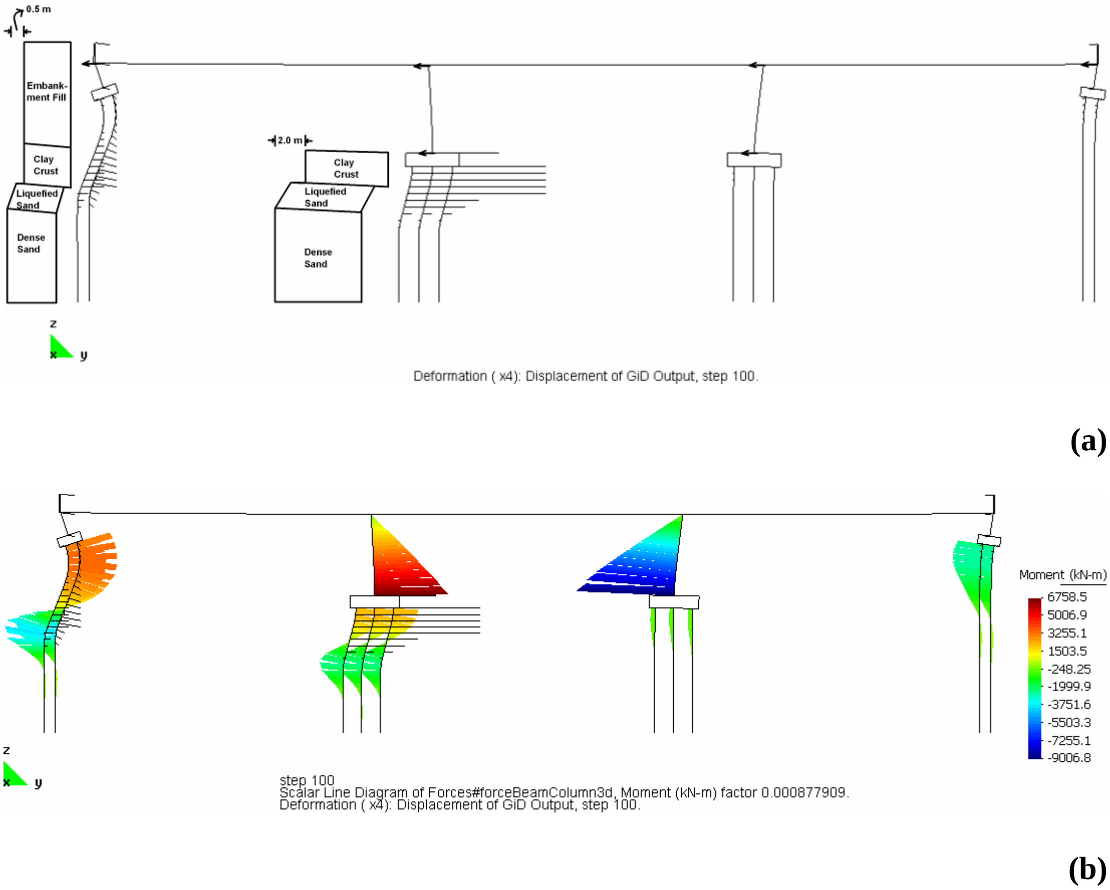

Figure 2.19: Global Analysis Load Case 3; a) Load Pattern and Deformed Mesh; b) Deformed Mesh and Moment Distribution in nonlinear beam column elements (Deformations amplified by a factor of 4.0)

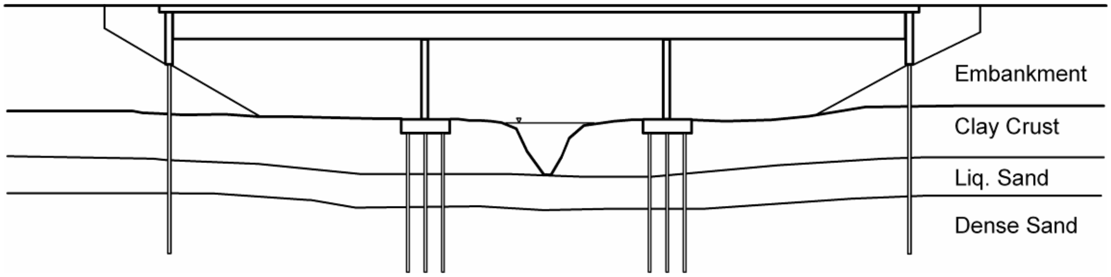

Figure 2.20: Schematic of the Three-Span Continuous Bridge with Monolithic Abutments

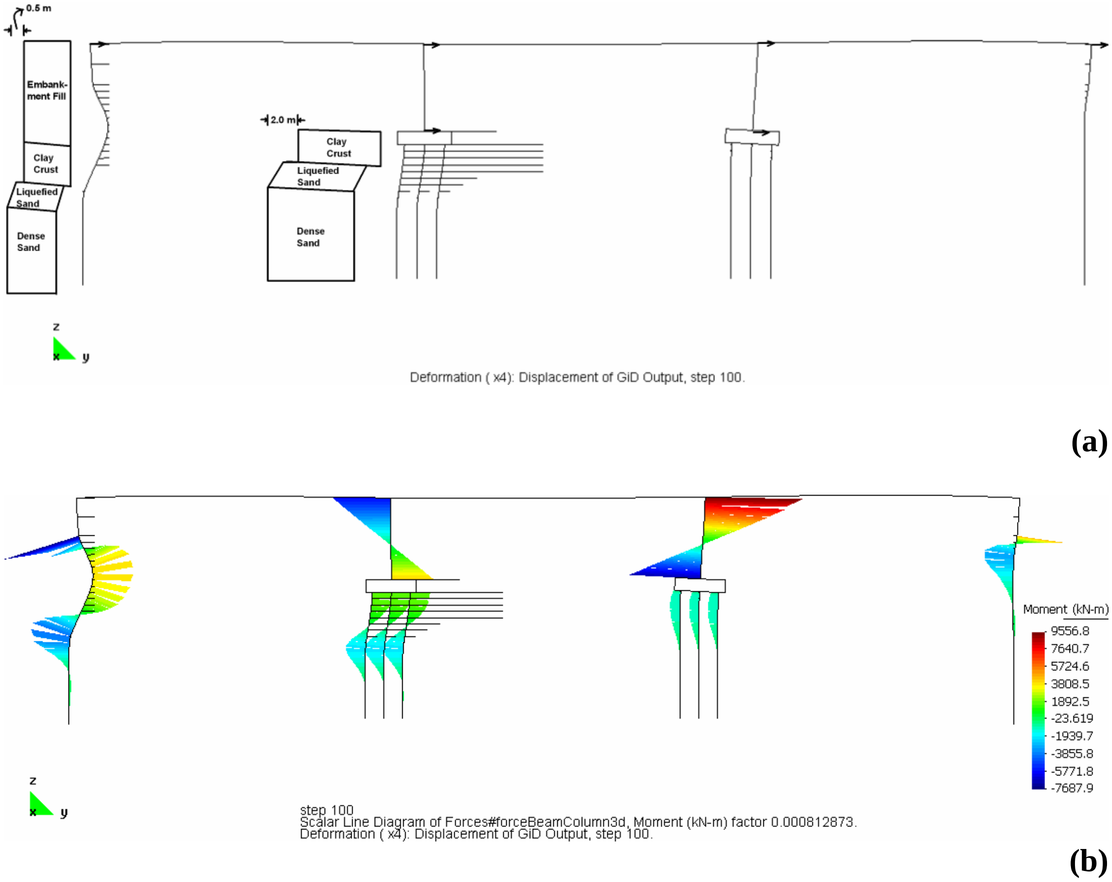

Figure 2.21: Global Analysis Load Case 4 (Continuous Bridge with Monolithic Abutments; a) Load Pattern and Deformed Mesh; b) Deformed Mesh and Moment Distribution in nonlinear beam column elements (Deformations amplified by a factor of 4.0)

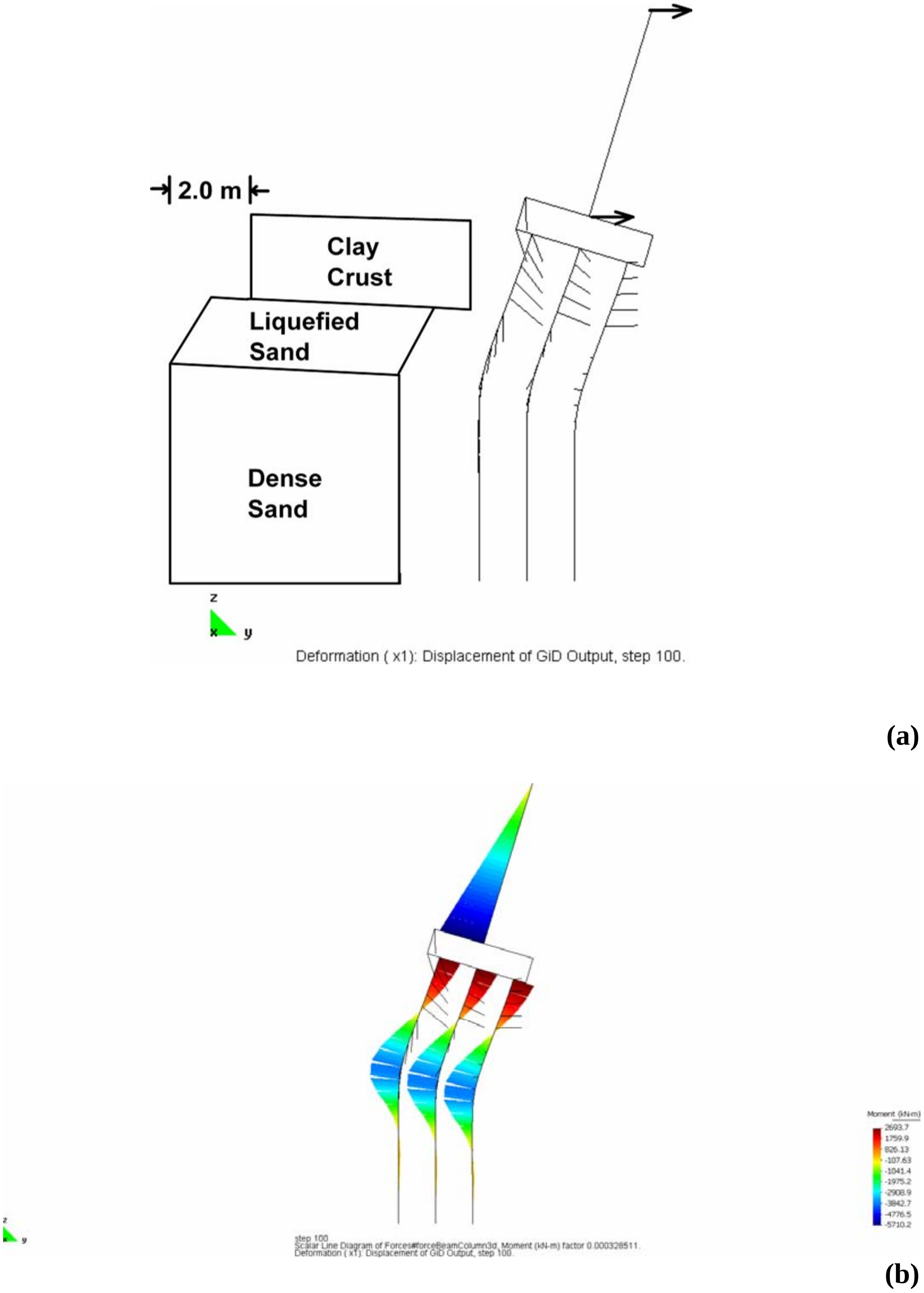

Figure 2.22: Local Analysis 1; a) Load Pattern and Deformed Mesh; b) Deformed Mesh and Moment Distribution

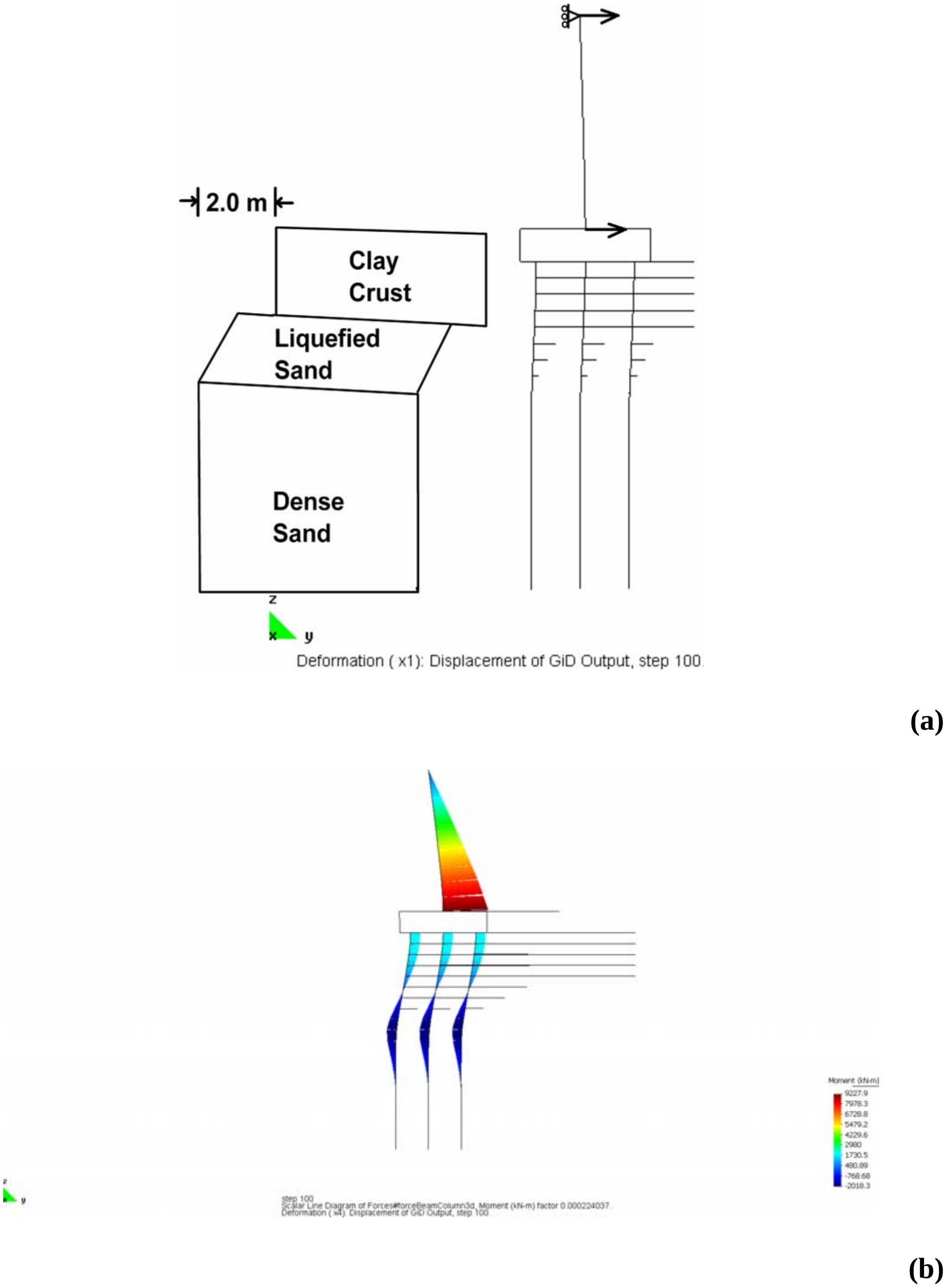

Figure 2.23: Local Analysis 2; a) Load Pattern and Deformed Mesh; b) Deformed Mesh and Moment Distribution

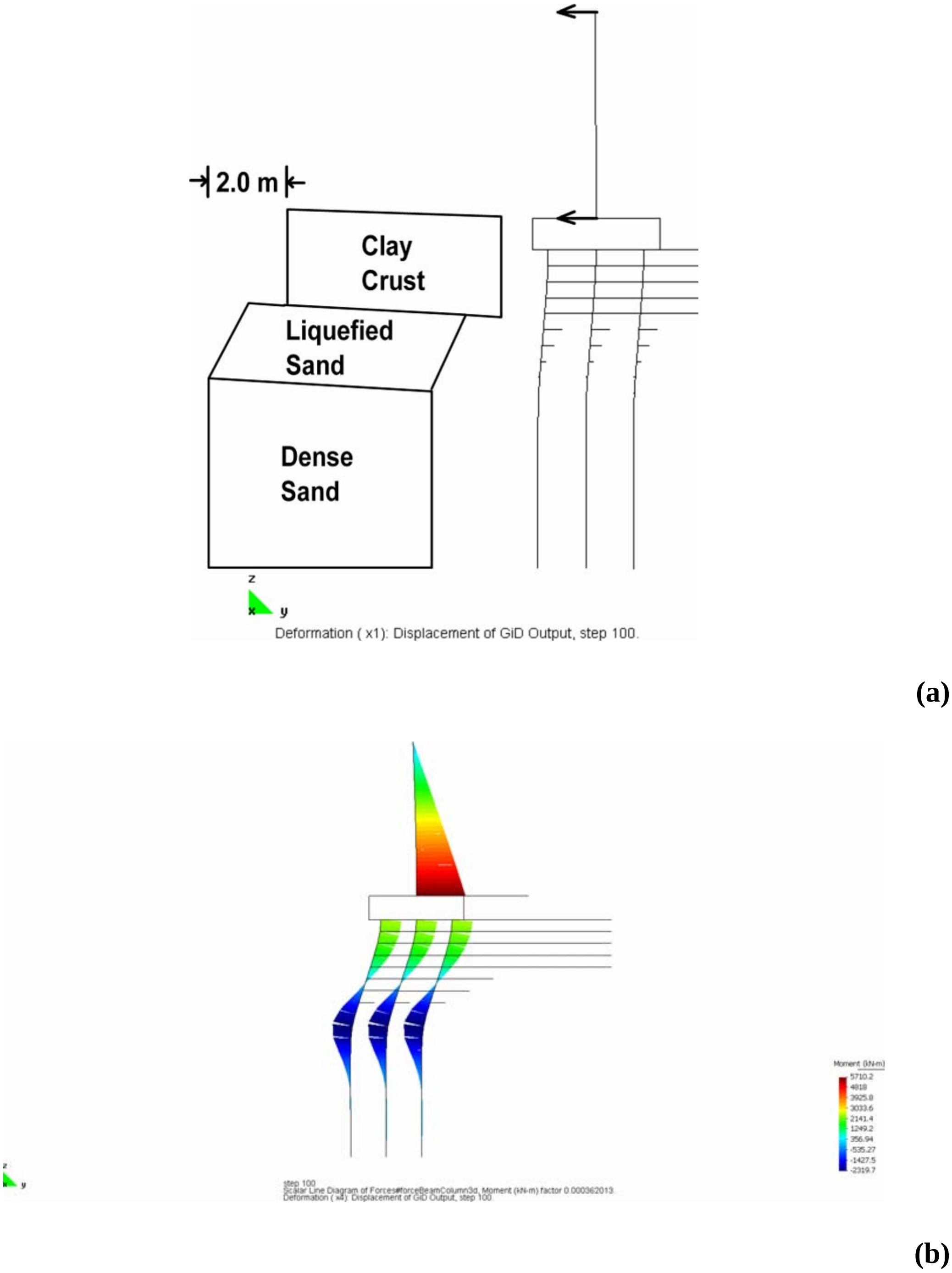

Figure 2.24: Local Analysis 3; a) Load Pattern and Deformed Mesh (Deformations × 1); b) Deformed Mesh and Moment Distribution (Deformations × 4)

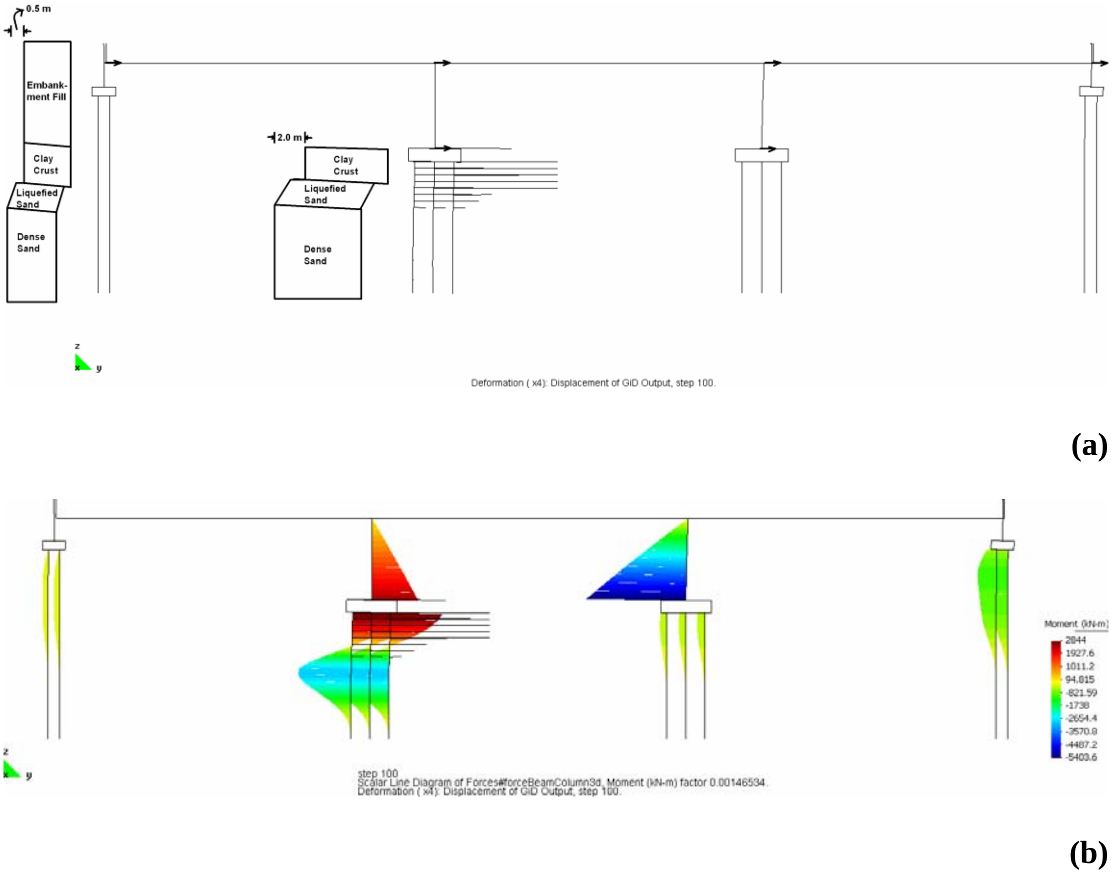

Figure 2.25: Global Analysis Load Case 5 with CISS piles; a) Load Pattern and Deformed Mesh; b) Deformed Mesh and Moment Distribution in nonlinear beam column elements (Deformations amplified by a factor of 4.0)

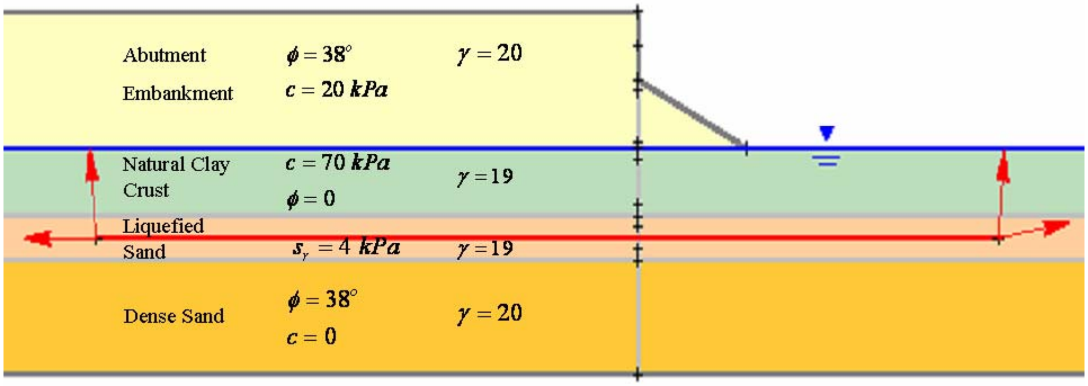

Figure 2.26: Soil Profile and its Properties used in the Pinning Analysis of Abutments

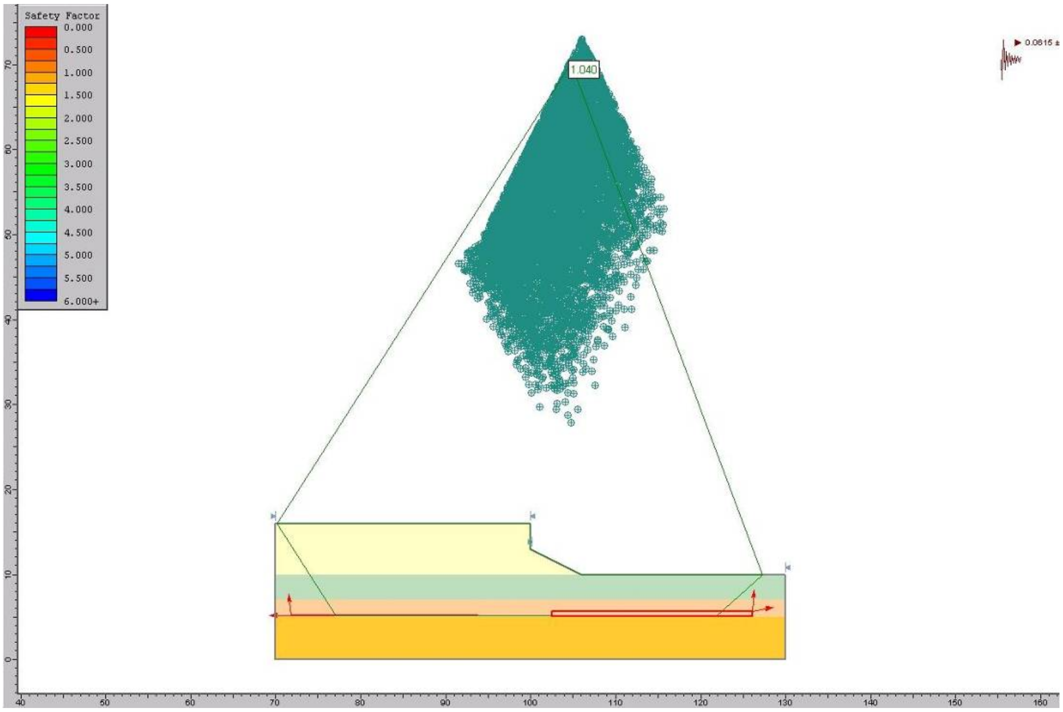

Figure 2.27: Slope Stability Analyses Performed using Slide 5.0 and the Associated Failure Surface for yield acceleration of $a_y = 0.0615g$

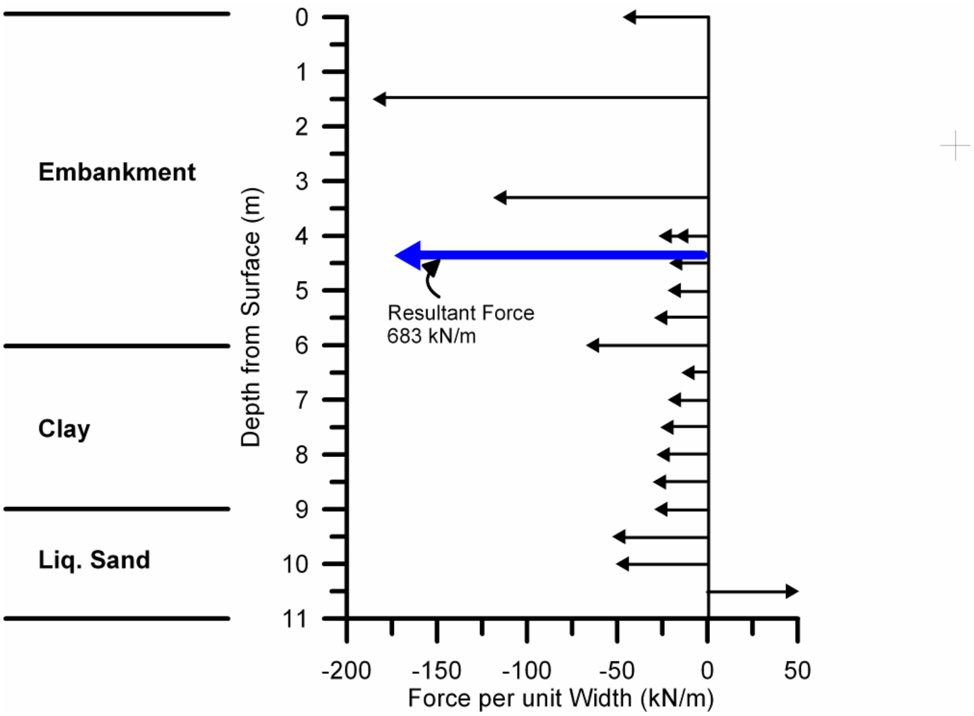

Figure 2.28: Distribution of Forces behind the Abutment Wall at the End of the Load Case 1 Analysis

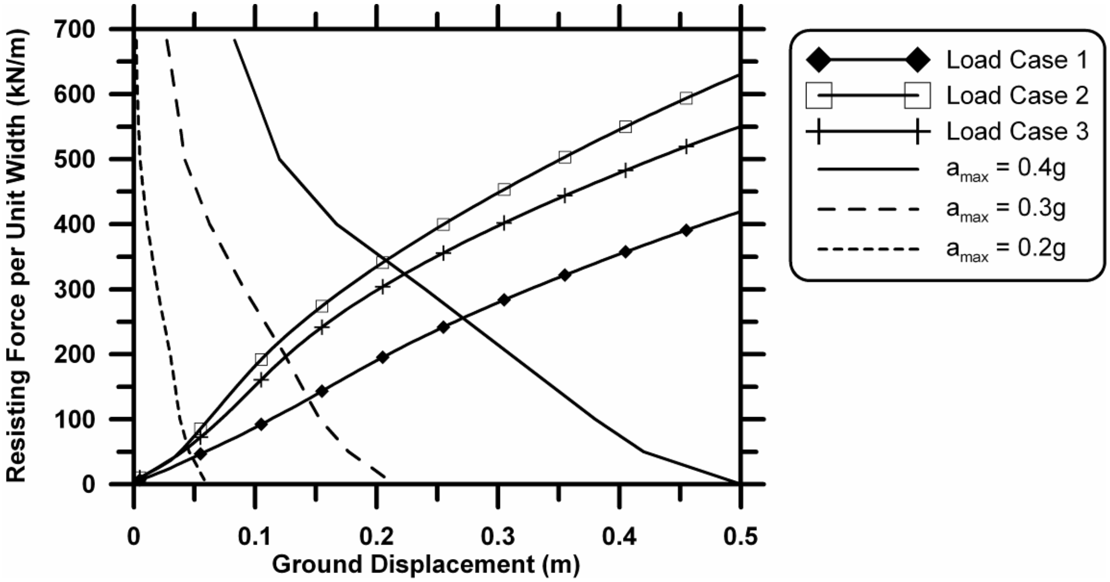

Figure 2.29: Results of the Pinning Analyses for Different Load Cases 1, 2, 3 at different peak ground motion levels for Kobe Motion Recorded at Port Island

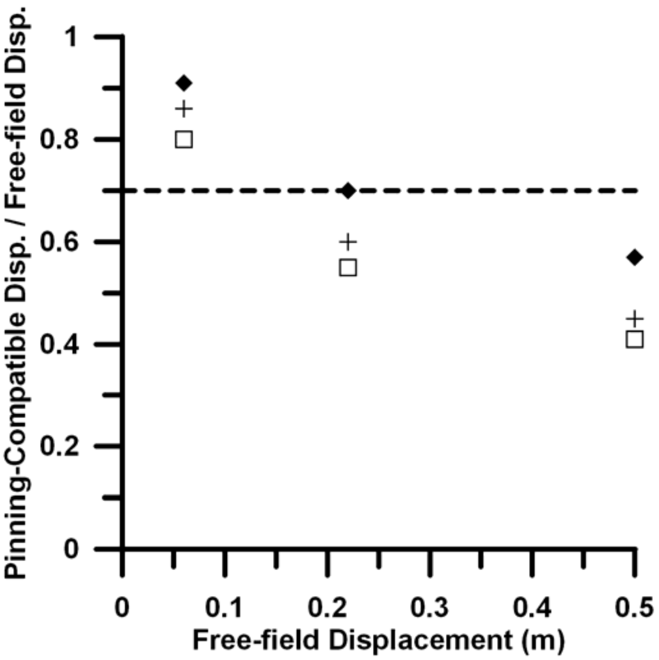

Figure 2.30: Ratio of Pinning Compatible Displacement to Free-field Ground Displacements at Different Values of Free-field Ground Displacement

3 Input Parameters Selection

A number of different possible approaches exist for characterizing the potential for liquefaction-induced damage to the more than 12,000 Caltrans-owned bridges. The most robust approach would involve a systematic individual evaluation of every single bridge using the current state-of-the-art analysis procedures. This approach is essentially impossible because it would require too much time and money and also wasteful because many bridges may be rendered unsusceptible to liquefaction without requiring a formal detailed analysis (e.g., bridges that map in non-liquefiable geologic units would not need to be analyzed). Another approach would analyze a smaller, statistically representative sample of the total bridge population, and extrapolate findings to the remaining bridges that were left unanalyzed. While this approach appears more reasonable, a statistically representative sample would need to capture the various combinations of structural configurations and soil conditions that exist for the entire bridge population, which would still involve an unreasonably large effort. Furthermore, obtaining as-built bridge drawings from the Caltrans database is time-consuming.

The approach adopted in this study was to use a small set of as-built drawings combined with information in the National Bridge Inventory (NBI) to guide adoption of a simple classification system based on structural properties such as vintage, type of connection between piers and abutments, number of pier columns per bent, and type of foundation. Structural properties such as span length and pier height were varied within each class to represent the variations identified in the NBI. A generic three-span bridge configuration was used throughout the analyses. Soil conditions for the liquefiable soil profiles were based on the USGS database of cone penetrometer soundings in the San Francisco Bay area. The structural and geotechnical input parameters were represented as probability density functions. In some cases a large amount of data was available to define these input distributions (e.g., the NBI had maximum span length for all Caltrans bridges), while in other cases very little data was available. Communication with Caltrans bridge designers and judgment was used when the available data was insufficient to accurately define distributions and correlations among the inputs.

After defining distributions and correlation coefficients for all of the input parameters, individual realizations were obtained by randomly picking discrete input parameter values from their underlying distributions, and constructing a numerical model of the bridge. The task of automatically constructing a numerical model based on random inputs was facilitated by the scripting capabilities of the TCL language that is used to control OpenSees. Thousands of realizations were obtained by the Monte Carlo method to integrate the input variables. The remainder of this chapter presents the manner in which the distributions and correlations for the input parameters were defined.

3.1 Generic Bridge Configuration

Figure 3.1 shows the generic 3-span template that was used throughout this study. This template was selected because it is the simplest configuration that permits study of the different types of loading conditions studied. For example, lateral spreading could occur at the left embankment and pier, but not at the right embankment and pier, or it could occur on both sides of the bridge toward the center. Fewer spans might limit the possible load combinations, while additional spans would probably not add significant information to the study. All of the spans have the same length and the two piers have equal heights. The abutments and piers are supported on pile groups. The pile groups with 15" diameter Precast piles had 20 piles in a group (4x5 configuration), while the pile groups with larger 24" diameter CIDH and CISS piles had 12 piles per group (3x4 configuration). The deck width was assigned a fixed value of 12.2*m* (i.e. 40 feet) which is typical of two-lane highway super-structure deck width. Dead loads were estimated using deck section weight calculations based on 16 pre-1971 as-built bridge drawings and the dead load values were subsequently used to size the piers.

3.2 Structural Classification

Figure 3.2 is a flowchart depicting the structural classification system adopted in this study. The bridges are classified based on vintage, structure type, number of columns per bent, and pile types, as discussed in detail in the sections that follow.

3.2.1 Vintage

The structural properties of a bridge are strongly related to the year in which the bridge was designed because design codes have evolved and improved over the years. Based on personal communication with Caltrans bridge designers, certain landmark dates are associated with major changes in bridge structural design codes. The most significant changes were introduced after the 1971 San Fernando earthquake and after the 1994 Northridge earthquake. Piers for bridges designed prior to 1971 generally had poor shear (transverse) reinforcement, and therefore did not exhibit much ductility. After 1971 more shear reinforcement was required in bridge piers to improve ductility. Code revisions following the Northridge earthquake involved primarily structural detailing and connections. Modeling connection detail was beyond the scope of this project, and this code revision was therefore not reflected in the classification system. Older vintage bridges tend to be supported on small-diameter pile foundations that have very little lateral capacity because the focus of design was on supporting the vertical load demands. Newer vintage bridges, however, are often supported on bigger diameter piles, such as Cast in Drilled Hole (CIDH), Cast in Steel Shell (CISS), and steel pipe piles, which exhibit significantly improved lateral load stiffness and capacity. This is reflected in the classification system, where various different pile types are assigned to newer vintage bridges. Various types of piles were also encountered in the as-builts for the older vintage bridges, but the different types of piles exhibited equally poor lateral load carrying capacity and varying the properties of the piles was deemed unnecessary.

3.2.2 Structural Connection Type

The connection between the superstructure and the abutments and piers effects the distribution of shear and bending moment demands to the various bridge components. The types of abutments considered in this study are seat-type, where the superstructure rests on top of a bearing attached to the abutment, and monolithic, where the abutment provides a moment-resisting connection to the superstructure. A gap is typically present between the superstructure and abutment backwall for seat-type abutments. Superstructures were considered either continuous, where the entire superstructure is a monolithic member, or as simply supported where the superstructure is composed of multiple segments. Connections between the superstructure and the tops of the piers were modeled as either pinned or resting on an elastomeric bearing for the simply-supported bridges. In this study, the bridges are categorized into three major classes of continuous bridges with monolithic abutments, simply-supported bridges with seat-type abutments and continuous bridges with seat-type abutments.

3.2.3 Number of Pier Columns per Bent

The number of pier columns per bent was adopted as a criterion for classifying bridges in this study because multi-column bents tend to have higher moment and shear capacities compared with their single-column counterparts.

Bridges with continuous superstructures and multi-column bents are designed with a pin connection at their connection to the pile cap as opposed to a fixed connection in single-columns piers. Therefore, continuous bridges with multi-column piers are more flexible. This translates to major differences in the fragility of different components of these two types of piers.

However, for simply-supported bridges the only difference in the number of pier columns is attributed to the marginal increase in the moment and shear capacities from single-column to multi-column piers. For single-column bridges the difference between a single-column and multi-column bent is more important for transverse loading than for longitudinal loading since a multi-column bent forms a frame that can be much stiffer than a single-column.

3.2.4 Pile Type

The type of piles used in the bridge foundation has a significant effect on its performance under liquefaction and lateral spreading demands. Older bridges (i.e. Pre-1971) mostly had small diameter (14" to 16" diameter) piles that were primarily designed for axial load bearing, without much consideration for lateral loading. They would generally be considered unsuitable for bridges located in liquefiable soils based on today's design standards, but are nevertheless important to model for characterizing performance of the older vintage bridges.

A broader range of pile types appears in the Post-1971 bridges. Three individual pile types were considered for the newer vintage bridges, including 15" diameter precast concrete piles, 24" diameter Cast-in-Drilled-Hole (CIDH) reinforced concrete piles and 24" diameter Cast-in-Steel-Shell (CISS) piles. These larger diameter CIDH and

CISS piles are being more widely used in newer bridges, especially when the potential of liquefaction and lateral spreading is present at the site of the bridge. Even larger-diameter drilled shafts are often used in new bridge designs, but these large shafts were not considered in this study.

3.3 Selection of Bridge Input Parameter Distributions

Selection of statistical distributions for, and correlations among, input parameters for this study was based on (1) a set of 16 as-built drawings of bridges built before 1971 and 4 as-built drawings of bridges constructed after 1971 provided by Tom Shantz from Caltrans, (2) the National Bridge Inventory, (3) personal communication with Caltrans bridge designers, (4) geotechnical information from the USGS database of cone penetration test records in the San Francisco Bay Area, and (5) engineering judgment when adequate information was unavailable.

3.3.1 Span Lengths

The maximum span length of bridges is listed in the National Bridge Inventory database. Figure 3.3 shows the histograms of the maximum span lengths for both the Pre-1971 and Post-1971 California bridges according to the NBI database. The newer bridges tend to have longer span lengths and also longer maximum span lengths. The distribution of maximum span length has some probability mass lumped at short span lengths, which are probably associated with short single-span crossings, and are therefore inappropriate for use in our three-span template. The remaining part of the distribution can be reasonably approximated by a normal distribution. The Pre-1971 bridges were generated with spans sampled from a truncated normal distribution with mean of 21.6 m, standard deviation of 13.3 m, and truncation limits of 10*m* and 60*m*, while Post-1971 bridges had span lengths sampled from a truncated normal distribution with mean of 35.8*m* and standard deviation of 17.7*m* and the same truncation limits. The distribution was truncated to prevent analysis of very short or very long spans.

3.3.2 Pier Heights

The National Bridge Inventory lists Minimum Vertical Underclearance for some bridges that cross other roads or railways, and Minimum Navigational Vertical Clearance is listed for some of river-crossing. However, the NBI does not directly report pier height. As a result the distribution of the pier heights was based on the limited number of drawings provided by Caltrans combined with judgment. A truncated normal distribution was assumed for pier height, with a mean of 6.5*m* and a standard deviation of 1.65*m* and truncation limits of 2*m*. The truncation limit was used to prevent analysis of unrealistically short piers.

3.3.3 Superstructure Weight

The distribution of the superstructure weight is important for the gravity analysis of the bridge, as well as for establishing the inertia demand on the bridge. My fellow graduate student in the structures program Mr. Yili Huo, calculated the deck stress (dead weight per tributary length per width of the deck) for the 16 pre-1971 as built drawings that were provided from Caltrans as is summarized in Table 3.1. Based on Table 3.1 the distribution of the deck dead weight per area was assumed to be normally distributed with a mean of 9.1 kN/m^2 and a standard deviation of 1.5 kN/m^2. The weight of the superstructure was correlated with the size of the piers, as described in the next section.

Table 3.1: Dead Weight per Unit Area for the available pre-1971 Caltrans drawings *

Bridge Number	Deck width B (m)	Equal-weight concrete area A (m2)	Weight per Trib. length W (kN/m)	Ratio W/B (kN/m2)
1	16.5	6.65	166.3	10.1
2	8.5	3.57	89.3	10.5
3	11.9	5.55	138.8	11.7
4	12.28	5.33	133.4	10.9
5	48.8	29.40	735.0	15.1
6	51.2	11.64	291.0	5.7
7	10.0	3.02	75.4	7.5
8	9.4	4.05	101.3	10.8
9	10.4	3.38	84.5	8.1
10	24.4	10.31	257.5	10.6
11	9.1	2.98	74.4	8.2
12	11.2	2.74	68.5	6.1
13	9.75	3.32	82.9	8.5
14	12.2	3.88	97.1	7.95
15	10.4	2.71	67.7	6.5
16	11.6	3.54	88.4	7.62

* Reproduced with permission of Mr. Yili Huo

3.3.4 Pier Column Moment and Shear Capacity

The size of the piers is well correlated with the dead load acting on the pier and the axial load ratio (i.e. the ratio of the axial load to axial capacity of pier). Axial load ratio of the piers can vary from less than 1% (e.g. some pier walls) to more than 10%

(e.g. some single-column piers). The as-built drawings were utilized to estimate distributions of axial load ratio. In general, axial load ratios were larger for the single-column bents and smaller for the multi-column bents. The mean axial load ratios were estimated to be 0.06 for the single-column piers and 0.04 and 0.03 for 2-column and 3-column piers with standard deviations of 0.007, 0.006 and 0.005 for single column, 2-column and 3-column piers, respectively. These axial load ratios were used to size the piers based on the weight per area of the columns, which embedded correlation between span length and pier column capacity. The gross areas of the piers were calculated by dividing the total axial capacity per column (back calculated from the axial load ratio) divided by the compressive strength of concrete ($f'c$).

After sizing the pier diameter, the flexural capacity was computed based on analysis performed by Mr. Yili Huo under supervision of Prof. Zhang. They performed numerous Monte Carlo moment-curvature analyses of the sections in OpenSees with representative distributions of steel strength (f_y), compressive strength of concrete ($f'c$), section effective depth (d), longitudinal reinforcement ratio (ρ) confined to unconfined concrete strength ratio ($\frac{f'c_{confined}}{f'c_{unconfined}}$) for both the pre-1971 and post-1971 eras, and came up with a convenient way of characterizing the moment capacity of the pier based on a few fundamental properties of a section and a normalized relationship of the yield moment of a column as is stated in Equation 3.1:

$$M_y' = \frac{M_y}{f'c.A_g.d.\left[1+(n-1)\rho\right]} \tag{3.1}$$

Where, M_y = the yield moment of the column

` A_g = the gross area of the column

d = the effective depth of the section

$n = \frac{E_s}{E_c}$ (i.e. the ratio of the modulus of elasticity of steel to concrete)

ρ = longitudinal reinforcement ratio

and, M_y' = the normalized yield moment of the column

The normalized yield moment, M_y' was found to be log-normally distributed with medians and dispersions listed in Table 3.2. Mr. Yili Huo also recorded the yield curvature values from the moment-curvature analyses and found regressions relationships between the yield moments of the sections and their corresponding yield curvature as are listed in Table 3.2. Yield curvature is an important parameter, since the curvature ductility of the piers is an important demand measure on the piers of the columns.

Table 3.2: The median and dispersion of the normalized yield moment and the relationships between yield curvature and yield moment for circular and rectangular sections for both Pre-1971 and Post-1971 eras.*

Section Shape	Vintage	Log-Normal Distribution of $M_y^{'}$		Relationship of yield curvature, ϕ_y and yield moment, M_y
		λ	ξ	
Circular Sections	Pre-1971	-2.65	0.24	$\phi_y = 0.00866e^{\left(-\frac{M_y}{679.0}\right)} + 0.00257$
	Post-1971	-2.42	0.23	$\phi_y = 0.00532e^{\left(-\frac{M_y}{795.2}\right)} + 0.00211$
Rectangular Sections	Pre-1971	-2.73	0.22	$\phi_y = 0.0123e^{\left(-\frac{M_y}{956.6}\right)} + 0.00332$
	Post-1971	-2.48	0.22	$\phi_y = 0.00711e^{\left(-\frac{M_y}{1145.8}\right)} + 0.00268$

* Reproduced with permission of Mr. Yili Huo

Using the normalized relationship of Eq. 3.1 and following the representative distributions of its parameters, I regenerated random numbers belonging to those distributions and found the relationship between the yield moment of the columns and their diameter (or the smaller dimension for the rectangular sections).

The regression formula is as follows:

$$\ln(My) = A_1 + A_2 \times \ln(D) \tag{3.2}$$

Where, $\ln(My)$ = is the natural log of the median of the yield moment for a column with a diameter or (smaller dimension) of D

$\ln(D)$ = is the natural log of the smaller dimension of the column

A_1 and A_2 = fitting parameters

The yield moment of the piers are log-normally distributed with medians found from Equation 3.1 and with fitting parameters and dispersions listed in Table 3.3. Eq. 3.2 was easy to implement using the TCL scripting capabilities.

Table 3.3: The fitting parameters for the natural log of medians of pier yield moments and the dispersion of the yield moments for circular and rectangular sections for both Pre-1971 and Post-1971 eras.

Vintage	Column Shape	Number of Columns per Pier	Fitting Parameters for ln(My)		Dispersion, ξ
			A_1	A_2	
Pre-1971	Circular	1	7.5559	2.3272	0.355
		2	8.1377	2.3713	0.358
		3	8.5011	2.3672	0.357
	Rectangular	1	7.8237	2.2632	0.356
		2	8.4064	2.3160	0.360
		3	8.7643	2.3166	0.359
Post-1971	Circular	1	7.9747	2.3700	0.344
		2	8.5589	2.4089	0.347
		3	8.9220	2.4153	0.348
	Rectangular	1	8.2881	2.3261	0.356
		2	8.8742	2.3693	0.359
		3	9.2358	2.3729	0.359

Mr. Yili Huo also provided me with a normalized relationship for shear capacity of the piers as is stated in Equation 3.3.

$$V'_d = \frac{V_d}{A_e\sqrt{f'_c}\left(5.65 + \frac{f_{yh}\rho_t}{2\sqrt{f'_c}}\right)} \tag{3.3}$$

Where, V_d = shear capacity of the piers

A_e = Effective area of the pier (approximated as 0.8 times the gross area of the pier)

f'_c = compressive strength of concrete (must be in units of kPa)

f_{yh} = strength of transverse steel

ρ_t = the transverse reinforcement ratio

And, V'_d = the normalized shear capacity of piers

The normalized shear capacity of the piers , V'_d was found to be normally distributed with mean and standard deviations listed in Table 3.4.

Table 3.4: The mean and standard deviation of the normalized shear capacity of the pier for both Pre-1971 and Post-1971 eras (reproduced with permission of Mr. Yili Huo).

Section Shape	Vintage	Normal Distribution of V'_d	
		μ	σ
Circular Sections	Pre-1971	1.087	0.018
	Post-1971	1.189	0.034
Rectangular Sections	Pre-1971	1.028	0.009
	Post-1971	1.054	0.013

Similar to the case with yield moment of columns, using the normalized relationship of Eq. 3.3 I regenerated random numbers belonging to the distributions of the parameters in Eq. 3.3 and found the relationship between the shear capacity of the piers and the column diameter (or the smaller dimension for the rectangular sections). The regression formula follows:

$$\ln(V_d) = B_1 + B_2 \times \ln(D) \tag{3.4}$$

Where, $\ln(V_d)$ = the natural log of the median of the shear capacity

And, B_1 and B_2 = the fitting parameters

Table 3.5 summarizes the fitting parameters for the natural log of the medians for a pier with diameter (or smaller dimension) of D, and the dispersion associated with the log-normal distributions.

Table 3.5: The fitting parameters for the natural log of medians of pier shear capacity and the dispersion of the shear capacity for circular and rectangular sections for both Pre-1971 and Post-1971 eras.

Vintage	Column Shape	Number of Columns per Pier	Fitting Parameters for ln(Vd)		Dispersion, ξ
			B_1	B_2	
Pre-1971	Circular	1	6.8585	1.7329	0.150
		2	7.5078	1.7480	0.151
		3	7.8990	1.7437	0.150
	Rectangular	1	7.3097	1.6414	0.188
		2	7.9494	1.6613	0.189
		3	8.3344	1.6545	0.188
Post-1971	Circular	1	7.3371	1.8367	0.232
		2	8.0016	1.8512	0.232
		3	8.3997	1.8457	0.232
	Rectangular	1	7.7733	1.7220	0.246
		2	8.4257	1.7375	0.246
		3	8.8152	1.7313	0.246

Using the abovementioned relationships, the yield moment and the shear capacity of the piers of the bridges used in the analyses were chosen from realistic distributions consistent with their size, which itself was correlated with the dead load that was being supported by them. These capacities were checked with the capacities calculated for the deterministic piers from as-built drawings, and agreed well with those deterministic values.

Table 3.6 summarizes the median and dispersions of the Moment and Shear Capacities for Single-Column and Multi-Column bridges belonging to both Pre-1971 and Post-1971 eras. The capacities for the multi-column bents represent the sum of capacities of the columns in the bent.

Table 3.6: The fitting parameters for the natural log of medians of pier shear capacity and the dispersion of the shear capacity for circular and rectangular sections for both Pre-1971 and Post-1971 eras.

Vintage	Column Type	Moment Median and Dispersion		Shear Median and Dispersion	
		λ $(kN.m)$	ξ	λ (kN)	ξ
Pre-1971	Single-Column	4040	0.77	1763	0.52
	Multi-Column	5982	0.79	3115	0.54
Post-1971	Single-Column	8478	0.78	3774	0.57
	Multi-Column	11970	0.81	6475	0.61

3.3.5 Bearings Parameters

Bridges with seat-type abutments were assumed to be supported on elastomeric bearings using the structural elements detailed in Chapter 2. Connections between the pier top and the superstructure were assumed to be either on elastomeric bearings, pin connections (i.e. grouted dowels), or a concrete-to-concrete seat, with 1/3 of the analyses receiving each type of connection. Data were unavailable to select these values and assignment of equal percentages is admittedly subjective. However, it is believed that these three types of connection essentially cover a wide range of possibilities as far as the connection of the spans at the top of the piers.

Properties of the elastomeric bearings were based primarily on the as-built drawings. Strain mobilized in an elastomeric bearing is a function of the bearing displacement and the height of the bearing. Table 3.7 summarizes the breakdown of the bearing heights that were used for the elastomeric bearings in bridges belonging to both the Pre-1971 and Post-1971 eras. The values selected were based on the available as-built drawings.

Table 3.7: The Breakdown of Elastormeric Bearing Heights for Pre-1971 and Post-1971 Bridges

Bearing Thickness (in Inches)	Pre-1971	Post-1971
1	25%	N/A
1.5	25%	N/A
2	50%	50%
3	N/A	50%

To compute the load-deformation characteristics of the bearings, their stiffness and ultimate capacity had to be estimated. The capacity of the elastomeric bearings was set to 35% weight acting on the bearing, per recommendations of SDC 2006. The yield displacement of the bearing was computed using Eq. 3.5, and depends on the shear modulus of the bearing material, bearing thickness, and vertical stress acting on the bearing. In modern design of the bearings, the total surface area of the bearing pads are selected so that the vertical stress on the bearings does not exceed 100 psi (i.e. 690 kPa), significantly. Vertical stresses on the bearings were calculated for the available as-built drawings. According to the available drawings the distribution of the vertical stresses on the bearings was assumed to be normally distributed with means and standard deviations summarized in Table 3.8.

Table 3.8 Mean and Standard Deviation of Vertical Stress on the Elastomeric Bearings for Pre-1971 and Post-1971 bridges.

Bearing Vertical Stress	Pre-1971	Post-1971
Mean	690 kPa (100 psi)	1035 kPa (150 psi)
Standard Deviation	103 kPa (15 psi)	173 kPa (25 psi)

The yield displacement could be calculated using the following mathematical manipulations:

$$U_y = \frac{Q}{K_H} = \frac{Q}{\left(\frac{G.A}{t_r}\right)} = \frac{\cancel{Q}}{\frac{G}{t_r}.\frac{\cancel{Q}}{\sigma_v}} = \frac{t_r.\sigma_v}{G} \tag{3.5}$$

Where, U_y = yield displacement of the bearing

t_r = the total thickness of the bearing pad

σ_v = the vertical stress on the bearing

G = the shear modulus of rubber (~ 1 MPa)

The load-deformation of the bearing could be entirely known in the analyses using the three parameters of bearing ultimate capacity (Q), total bearing pad height (t_r)

and the vertical stress acting on the bearing (σ_v). The load-deformation behavior was assumed to be elastic perfectly-plastic.

An elastic perfectly-plastic material was also used for the analyses with the concrete-to-concrete interface, and the stiffness of the linear portion of the load-deformation was set to a large value making the load-deformation essentially rigid-plastic. Using the same elastic perfectly-plastic material for all types of bearings was convenient to implement in OpenSees, even though some bearing types were essentially rigid-plastic. For the analyses where the dowels were used to connect the superstructure to the pier, the capacity of the load-deformation (i.e. plastic capacity value) was set to the shear capacity of the dowels, with stiffness set very high making the response rigid-plastic. Shear capacity of the dowels was based on observations from the as-built drawings combined with judgment.

3.3.6 Pile Strengths

Figure 3.4 shows a few examples of the piles that were commonly used in California bridges. Lateral loading of piles were rarely considered in the typical pre-1971 bridges and the type of piles encountered in the as-built drawings of those bridges were generally 15" diameter piles of varying strengths that were not designed to resist lateral loading, and would generally yield fairly quickly under demands of lateral spreading. Therefore, for all of the classes of the pre-1971 bridges, only one type of precast piles was considered in the analyses. The strength and the yield curvature of the Pre-1971 piles are listed in Table 3.9.

Three different types of piles were considered for the bridges that were built after 1971. A variety of the 14" to 16" precast concrete piles with different configurations were modeled using Xtract. Based on those Xtract section analyses, the yield moment of these small-diameter newer precast concrete piles were assigned a log-normal distribution, while a normal distribution with very small variation was assigned to their yield curvatures. 24"CIDH and 24"CISS piles were also considered in the analyses of the post-1971 bridges. These piles are typically much stronger that the small-diameter piles and are more commonly used in the design of modern bridges. The yield moment and yield curvature of these piles were also performed in Xtract, however the values were not varied in the analyses.

Table 3.9: Yield Moment and Yield Curvature for Piles used in the Analyses

Vintage	Pile Type	Mean or Median Moment (*kN.m*)	Dispersion	Mean Yield Curvature (*1/m*)	Standard Devation
Pre-1971	15"Precast	84	N/A	0.011	N/A
Post-1971	15"Precast	180 (Median)	0.25	0.0123	0.0005
	24"CIDH	400	N/A	0.0069	N/A
	24"CISS	1977	N/A	0.0069	N/A

3.4 Selection of Geotechnical Input Parameter Distributions

Geotechnical parameters defined in the analyses in this dissertation include the strength and thicknesses of the soil layers, the load-transfer between soil and embedded bridge components, and the lateral spreading deformation profile. Each of these inputs is discussed in the sections that follow.

3.4.1 Thickness of Natural Crust, Liquefied Sand, and Approach Embankments

The thickness and variation of the natural crust and thickness of the liquefiable sand were selected primarily based on the distribution of CPT logs for East Bay in Northern California available on the USGS website (http://earthquake.usgs.gov/regional/nca/cpt/). Figure 3.4 developed by a fellow graduate student Minxing Zhao, depicts distributions of thickness and average CPT tip resistance in nonliquefied crust layers. Nonliquefied crust material was separated into fine-grained and coarse-grained soils.The thickness of the crust materials can go even beyond 10*m* in some cases, but lateral spreading and other surface manifestations of liquefaction are typically limited to shallower layers (e.g., Ishihara 1985). Hence, the thickness of the crust was assumed to be uniformly distributed between zero and 6*m*.

The histogram of the liquefied sands thickness can be roughly approximated by log-normal distributions. Based on this histogram, the thickness of the liquefied sand layer was assumed to be log-normally distributed with a median of 3m and dispersion of 0.7 (i.e. $\ln(2)$).

The distribution of thickness of the embankment was rather subjective. It was assumed that the thickness of the embankment would vary uniformly between 3*m* and 9*m*.

3.4.2 Undrained Shear Strength of Cohesive Nonliquefied Crust Material

The undrained shear strength of clayey crust soils was estimated from the average CPT cone tip resistance values summarized in Figure 3.4. of the median value of cone tip resistance (q_t) is about 3.0 MPa, which corresponds to an undrained shear strength of 200 kPa according to Equation 3.6:

$$S_u = \frac{q_t - \sigma_v}{N_{kt}} \tag{3.6}$$

Where, q_t = the tip resistance of the cone

σ_v = total vertical stress

N_{kt} = Empirical Value between 10 and 20, with 15 as an average

However, this undrained shear strength is larger than would be anticipated for near-shore sediments. Hence, judgment was used to reduce the median value of undrained shear strength to 70 kPa, which is consistent with strengths that would be anticipated for a desiccated crust above the ground water table.

The distribution of the strength was assumed to be log-normally distributed with $\sigma_{\ln}$ = 0.75.

3.4.3 Lateral Loads from Embankment Soils

The embankment load consists of two components: the passive pressures behind the abutment wall and the load mobilized by the piles supporting the abutment walls. Passive pressure was computed using Rankine earth pressure theory, and was assumed to be log-normally distributed with $\sigma_{\ln}$ = 0.75. The large standard deviation is caused by uncertainty in the interface friction (as discussed in Chapter 2). The embankment backfill was assumed to have a baseline friction angle of $\phi = 38^o$ and baseline apparent cohesion of $c = 20kPa$.

The ultimate values of lateral loads on the piles (p_{ult}) were computed using the API (1993) sand p-y curves using the baseline set of soil properties, the distribution was assumed log-normal with $\sigma_{\ln}$ = 0.75. For convenience, these distributions were implemented by computing the median value of passive pressure or p_{ult} using the baseline set of input parameters, and subsequently multiplying by a p-multiplier with median value of 1.0 and $\sigma_{\ln}$ = 0.75. Note that this is different than assuming that the fundamental soil properties are random variables and subsequently computing p_{ult}. Directly assigning a median and standard deviation to crust load rather than the fundamental soil properties is based on the analysis in Chapter 2 that quantified the influence of interface friction angle uncertainty on passive pressure.

3.4.4 Subgrade reaction in Liquefied Sand

Soil-structure interaction in the liquefied sand was modeled by applying a p-multiplier to the drained p-y curve to reduce its capacity. The distribution of the p-multipliers in the sand was chosen based on the recommendations of Brandenberg (2005) (Table 2.1). For loose sandy material $\left[(N_1)_{60-CS} < 8\right]$ Brandenberg recommends using a p-multiplier between 0.0 and 0.1. Therefore, for the analyses performed in this document, the p-multiplier of liquefied sand was assigned a truncated normal distribution with a mean of 0.05 and a standard deviation of 0.025, truncated at values below 0.01.

The example problem presented below explains why the p-multipler approach is recommended and utilized in the analyses:

The p-y behavior of liquefied sand back-calculated from full-scale field test and small-scale centrifuge tests exhibit a concaved upward response attributed to the dilatancy of the sand, as shown by many studies (e.g. Wilson et al. 2000, Rollins et al. 2005). Despite widespread acknowledgment that p-y behavior in liquefied ground can exhibit this type of behavior due to dilatancy, static analysis approaches traditionally have utilized a p-multiplier approach in which the p-y behavior is modeled as being artificially soft and weak. The reluctance to model concave up behavior in static lateral spreading analysis procedures is due to a mismatch in the assumed ground displacement profile and the strength of the p-y behavior. The basic idea is that a sand that is weak enough to exhibit large shear strains that manifest as lateral spreading should also be weak as it flows around a pile. Assuming a sand is weak enough to exhibit large shear strains (say 50%) but at the same time exert a large downslope force on a pile due to lateral spreading seems to be inconsistent. A more likely scenario is that the sand may transiently exhibit pore pressure reduction during shaking due to dilatancy, and the increment of shear strain mobilized during this cycle would be very small since the soil would be transiently stiff. As pore pressures rise back to 1 and the soil re-liquefies, it would then strain again and flow past the pile.

It is interesting to note that the studies that have shown large subgrade reaction forces mobilized by liquefied sand have also shown that these subgrade reaction forces act to resist downslope displacement of the pile. Rollins et al. (2005) showed that large forces could be mobilized in static load tests in blast-induced liquefied soil, and that the sand could provide significant stiffness to react against the actuator. Wilson et al. (2000) showed that liquefied sand could provide significant resistance to inertia-driven downslope pile displacement. Brandenberg et al. (2005) showed that liquefied sand could provide a large upslope resisting force against the combined effects of inertia and lateral spreading of an overlying clay layer. Never has a study shown that liquefied sand can mobilize a large downslope driving force against a pile during periods of dilatancy-induced pore pressure decreases, presumably because the dilatant sand does not exhibit large strain increments during the instants when pore pressures transiently drop. Therefore, in static analysis procedures, imposing large shear strains in a liquefied sand layer combined with a concave up dilatant p-y material is inappropriate, and would result in overestimation of the demands on the pile.

To clarify this matter, an example problem is presented here that shows the expected response of a single 24” CIDH pile under lateral spreading demands of liquefied sand (without a crust) against the pile, using a few cases of a hardening p-y behavior as well as the recommended approach which is applying a p-multiplier to the traditional strain-softening response as presented by API (1993) p-y curves.

The pile is modeled to behave elastically with stiffness equal to the initial (pre-yield) stiffness of the pile obtained using section analysis of the pile in Xtract, with properties as was shown in Table 2.6.

The hardening shape of the p-y behavior as observed in Wilston et al. (2000) was modeled using PyLiq2 Material in OpenSees by applying effective stresses in the form of a second-order polynomial, as follows:

$$\sigma_v\,' = \left(\frac{y}{y_{\max}}\right)^2 .\sigma_{vf}\,' \tag{3.7}$$

in which:

$$\sigma_{vf}\,' = F.\sigma_{vi}\,' \tag{3.8}$$

Where, F = the ratio of the ultimate effective stress to the initial effective stress prior to liquefaction

And where,

y = lateral displacement

$y_{\max}$ = maximum value of lateral displacement

Centrifuge test performed by Wilson et al. (2000) showed that the ultimate load may be smaller or larger than the ultimate load as predicted by API (1993) curves. For the purpose of this example, the analyses were performed with *F* values equal to 2, 1 and 0.5.

In this example, lateral spreading is happening over 5*m* of liquefied sand (with no nonliquefied crust) overlying denser sands (Figure 3.6). The extent of lateral spreading displacement at the surface is 0.5*m* and the strain is constant in the liquefied sand. Soil properties of the layers are summarized in Table 3.10.

Table 3.10: Properties of the soil layers used in the example analyses

Layer	Depth to top of the layer (*m*)	$\gamma\ (kN/m^3)$	ϕ'	$\eta_h\ (kN/m^3)$
Loose sand	0	18	32	9,500
Dense sand	5	18	38	32,600

Figure 3.7 shows the effective stress as a function of displacement ratio for cases with final effective stresses double, same and half the initial effective stress, as well as the nonliquefied effective stress at the middle of the liquefied sand layer (depth = 2.5*m*) with an effective stress of 20 kN/m^2. Figure 3.8 shows the p-y behavior in the middle of the liquefied sand layer (2.5*m*) for the three hardening cases as well as for the traditional API and the recommended approach (p-multiplier approach).

Analyses were performed for four different p-y behaviors as shown in Figure 3.8 with the first three using the polynomial hardening curves with ultimate loads equal to 2, 1 and 0.5 times the API ultimate load, respectively. The last analysis is however performed using a softened p-y curve with a p-multipler of 0.05 applied to the traditional API p-y curve. Figure 3.9 shows the predicted soil and pile displacements as well as the subgrade reaction and moment distribution along the pile for different cases of this example analysis. As can be seen in Figure 3.9 the hardening shape of the p-y curves predicts significant displacements of the 24” CIDH piles under a modest lateral spreading displacement of 0.5m, in which the top of the pile displaces 0.35*m*, 0.25*m* and 0.15*m* for load cases 1, 2, and 3, respectively. Also, the mobilized moment in the pile for the hardening load cases far exceeds the moment capacity of the pile (M_y ~ 400 *kN.m*), which would have resulted in significant curvature ductility in the pile had it been modeled, nonlinearly. Such high displacement level of a large diameter 24” CIDH pile under only 0.5*m* of lateral spreading and in the absence of a nonliquefiable crust is not in agreement of the expected response of these piles based on case history evaluation and model test studies. The p-multipler approach (i.e. load case 4) predicts a pile displacement of 0.02m, which is deemed more reasonable.

3.4.5 Stiffness of Load Transfer in the Crust and Embankment

The stiffness of the load transfer in the nonliquefied crust in a liquefied site, is significantly (i.e. an order of magnitude) softer that the stiffness of soils in nonliquefied ground. Following the model presented by Brandenberg et al. (2007), the load transfer response was calculated for load transfer between the abutment and the approach embankment, and between the pile cap and spreading crust layer. The baseline value of y_{50} were 0.20*m* for the abutments and 0.05*m* for the pile caps.. The y_{50} value was assigned a truncated normal distribution with a COV of 0.5, truncated at 0.005*m* at piers and at 0.020*m* for the abutments.

3.4.6 Characterization of Axial Capacity

Axial capacity of the foundation comes from the t-z springs along the length of the piles, and the q-z springs at the tip of the piles. While the t-z relations are known for the nonliquefied ground, little is known about the t-z relations in the liquefied sites. Given the lack of information, the p-multipliers were also applied to the t-z relations. The baseline axial capacity of the bridge in any foundation component is simply the sum of the t-z springs and the q-z springs in the piles. In order to account for the variability of axial capacity, axial capacity multipliers were applied to the baseline values of the t-z and q-z springs. Similar to the p-multipliers in the liquefied sand, a truncated normal distribution with a mean of 1.0, a standard deviation of 0.5 (i.e. COV = 0.5) and a truncation value of 0.01 was applied to the multiplier of t-z and q-z springs.

3.4.7 Horizontal Variation of Lateral Spreading Surface Displacements

Lateral spreading ground surface displacements are known to exhibit significant horizontal variability throughout a spread feature (e.g., Faris, 2004). The size of a lateral spread can be large or small relative to a bridge, and it is conceivable that ground displacements be large at some components and zero at others, or be nearly the same at multiple components. In order to capture the horizontal variability in the patterns of lateral spreading ground surface displaceemnt, the left side (i.e. the left abutment and the left pier) and the right side (i.e. the right abutment and the right pier) of the bridge were treated as separate spread features. Within the spread features, the spreading is randomized but correlated so that the ratio of the displacements of the two components in the spread feature (e.g. ratio of displacement of the left pier to the displacement of the left abutment) follows a lognormal distribution with a median of 1.0 and a dispersion of ln(3). Furthermore, 1/3 of the load cases involved lateral spreading only on the left side of the bridge (left abutment and the left intermediate pier), 1/3 with spreading only on the right side (right abutment and the right intermediate pier) and 1/3 with spreading on both sides. Ground displacements were randomly selected at each component in accordance with these statistics, and subsequently scaled so that the maximum ground displacement applied in all of the analyses was set to 2.0*m*. Ground displacements at the abutments were subsequently reduced by 25% to account for the pinning effect, based on the results of the pinning analyses as explained in Chapter 2.

3.4.8 Vertical Ground Deformation Profile

The vertical profile of ground deformation is also highly uncertain. Studies with a permeable nonliquefied crust layer were associated with a continuous displacement profile (e.g., Abdoun et al. 2003), whereas studies with a low-permeability crust have exhibited a displacement discontinuity at the interface (e.g., Malvick 2008, Brandenberg et al. 2005). The ground surface displacement can therefore be attributed to a combination of shear strains in the various soil layers (mostly in the liquefied layer) and interface slip as the crust spreads on top of the liquefied layers. For simplicity in this study, shear strains in the nonliquefied layers were assumed to be zero, with the ground surface displacement entirely attributed to a combination of shear strain in the liquefied sand and interface slip. The amount of slip at the interface was represented by the ratio of displacement at the top of the liquefied layer to the displacement of the nonliquefied crust layer. This ratio was assumed uniformly distributed between 0 and 1. The shear strain in the loose sand layer was set to provide the remaining fraction of ground surface displacement.

3.5 Characterization of Inertia Demands on the Bridge

Lateral spreading ground displacement during liquefaction can happen during ground shaking, while it is also possible that the lateral spreading would occur after the ground shaking has finished. Therefore, inertia demands were applied concurrently with lateral spreading displacement only in 50% of the analyses within each class, while for the other 50% of the analyses, no inertia was present during the analysis. When inertia was present in the analyses the inertia demand on the bridge was applied as a force equal to the product of the mass and spectral acceleration for liquefaction, as mentioned in Chapter 2. The natural period of the bridge was computed based on the mass of the superstructure and the fixed-base stiffness of the piers. Spectral accelerations were picked from the Caltrans Seismic Design Criteria acceleration response spectra for Site Class D, and moment magnitude 7.25 ± 0.25. Peak ground acceleration was assumed to be either 0.2g, 0.3g or 0.4g since response spectra are available for these PGA's. The response spectra for peak rock acceleration of $0.1g$ was believed to be small enough not to cause liquefaction and/or liquefaction-induced lateral spreading, and therefore was not used in the analyses. Once the spectral acceleration for nonliquefaction was selected, the spectral acceleration for liquefaction was calculated using liquefaction modifiers recommended by Boulanger et al. 2007 stated in Chapter 2. The inertia force was linearly increased simultaneously with ground displacements, and reached its peak value when the ground displacement reached $0.5m$. Inertia force was kept constant as ground deformation was increased beyond 0.5 m. This approach was consistent with the expected maximum transient ground deformation during a single inertia cycle based on centrifuge test observations.

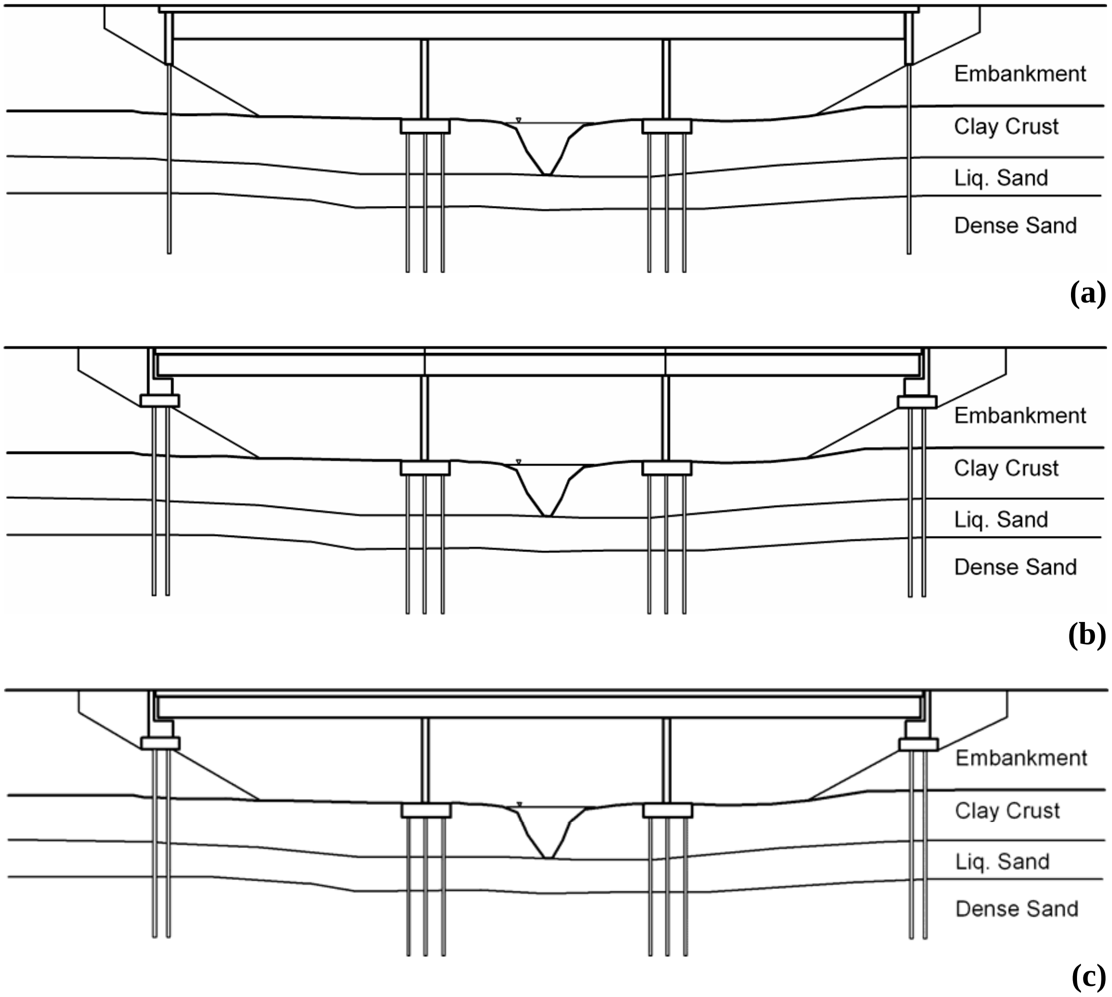

Figure 3.1: Template of the bridges for modeling and analyses; a) Bridges with Continuous Super-Structure and Monolithic Abutments, b) Bridges with Simply-Supported Super-Structure and Seat-Type Abutments. c) Bridges with Continuous Super-Structure and Seat-Type Abutments.

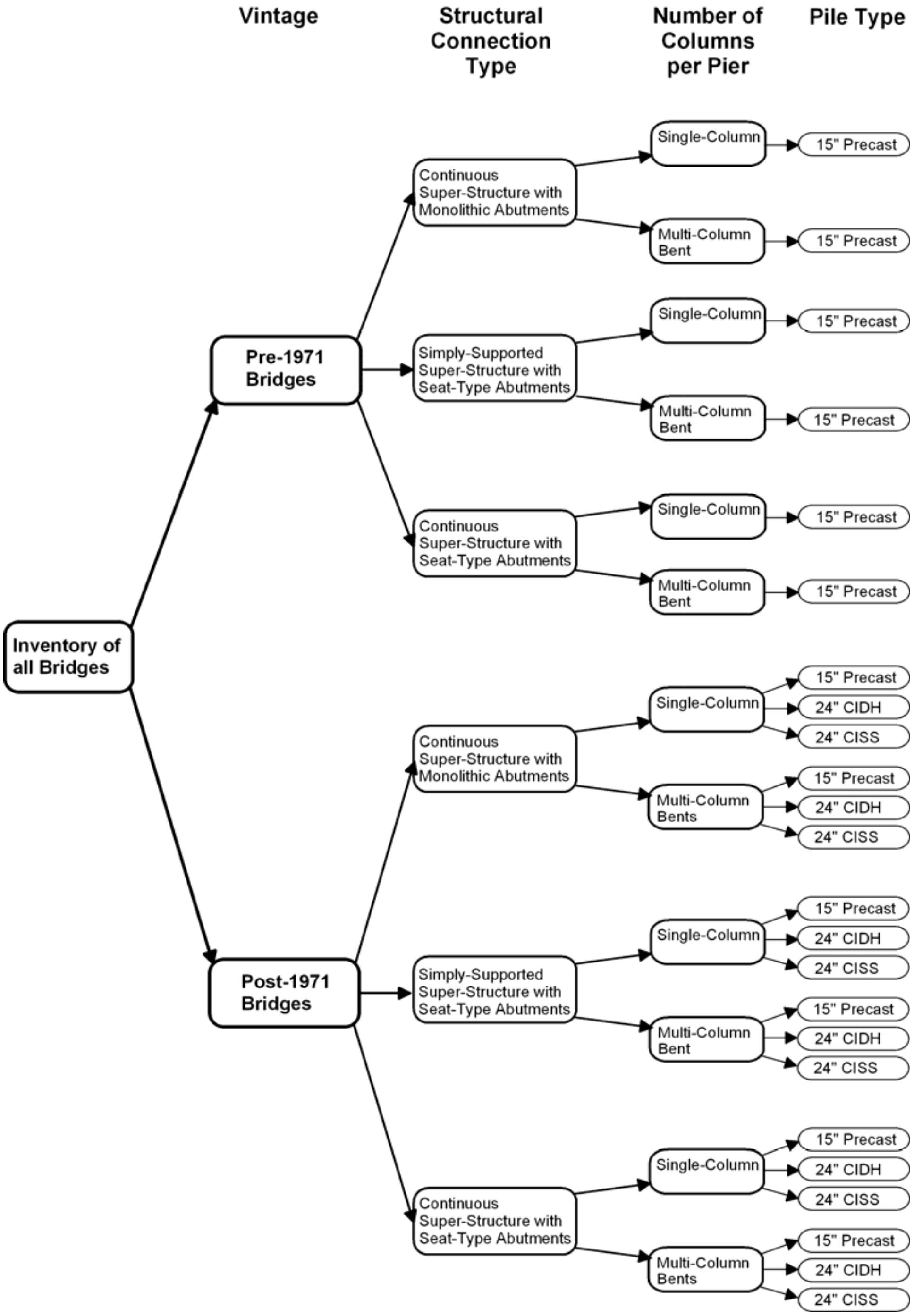

Figure 3.2: Classification of Bridges based on Vintage, Structure Type, Number of Piers and Type of Piles

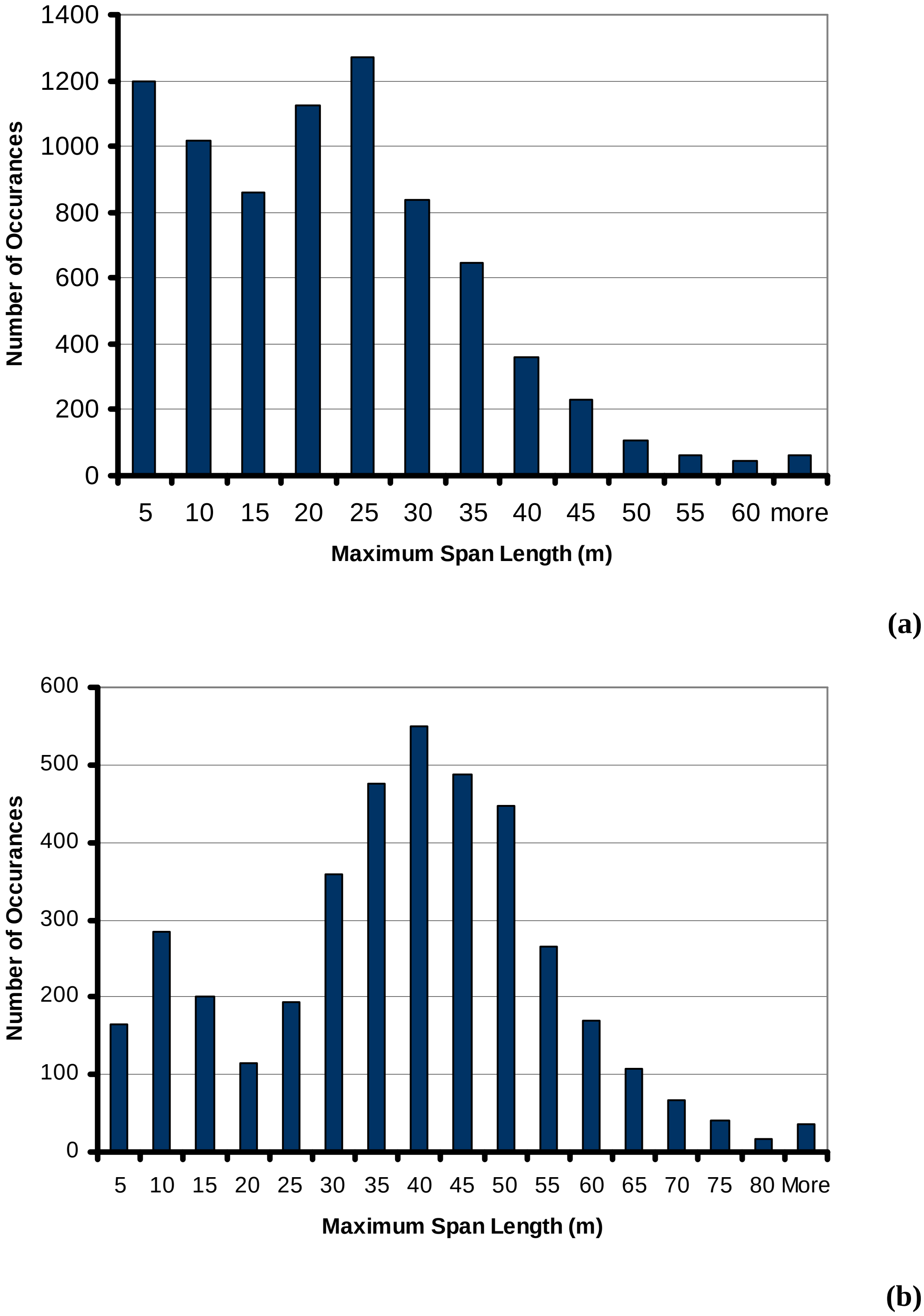

Figure 3.3: Histograms of Maximum Span Length of Bridges from NBI database; (a) Pre-1971, (b) Post-1971

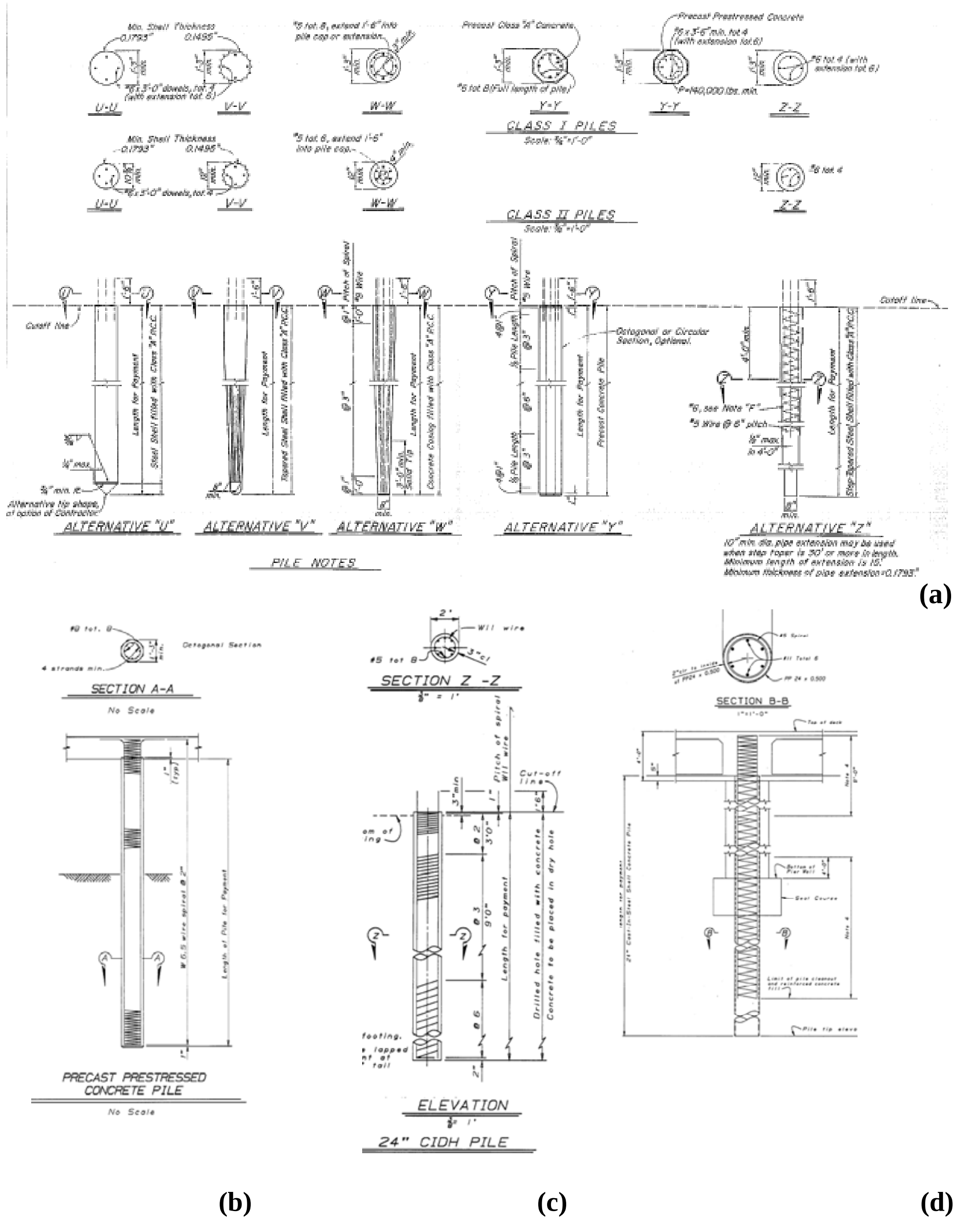

Figure 3.4: Examples of piles specification from as-built drawings for (a) 15" Precast Concrete Piles typically used in Pre-1971 Bridges, (b) Post-1971 15" Precast, (c) Post-1971 24" CIDH, (d) Post-1971 24" CISS.

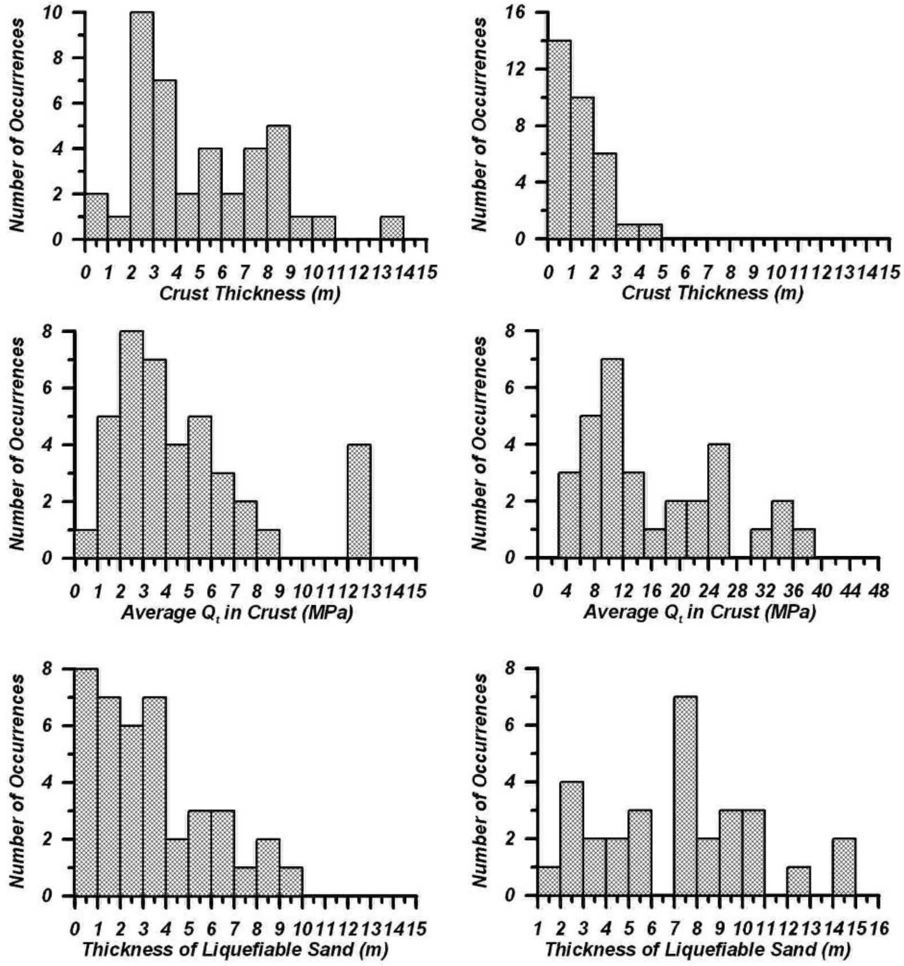

a) Fine-Grained Crust Material b) Coarse-Grained Crust Material

Figure 3.5: Distribution of crust and liquefiable layer thickness based on USGS CPT Logs for East Bay in Northern California

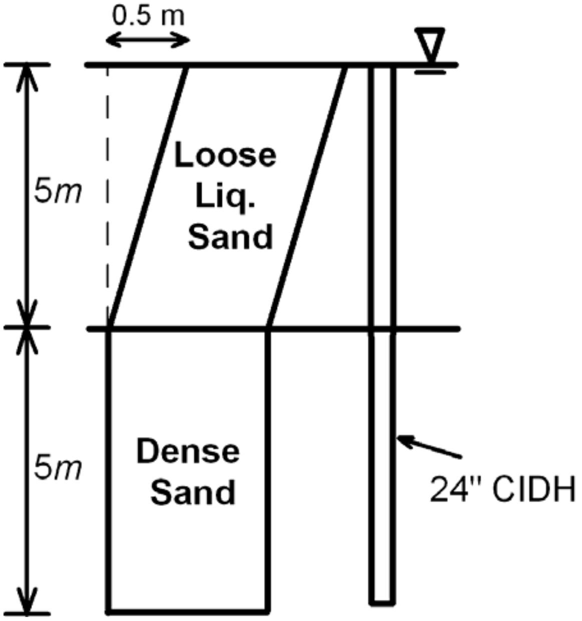

Figure 3.6: Soil and lateral spreading profile used in the example analyses.

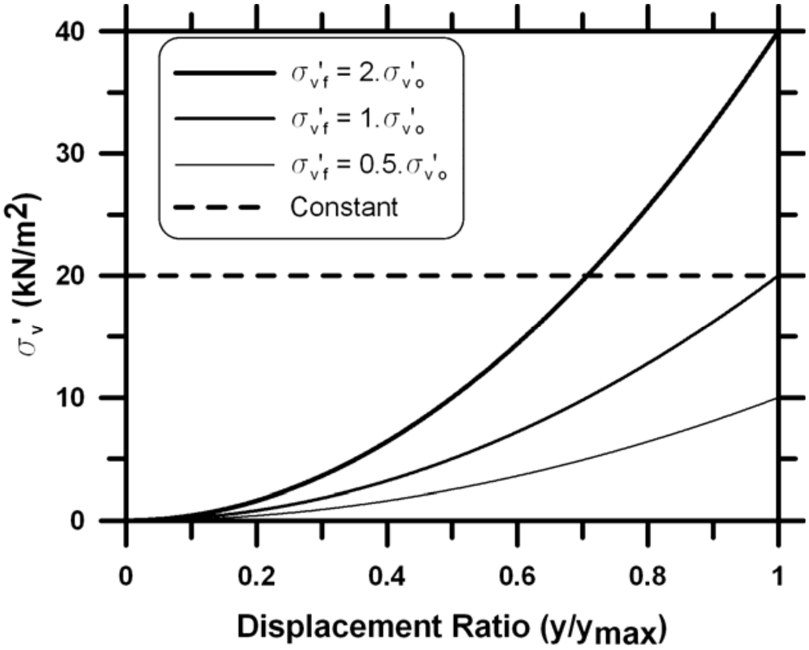

Figure 3.7: Effective stress relations used in the example analyses calculated at the center of the liquefied sand layer

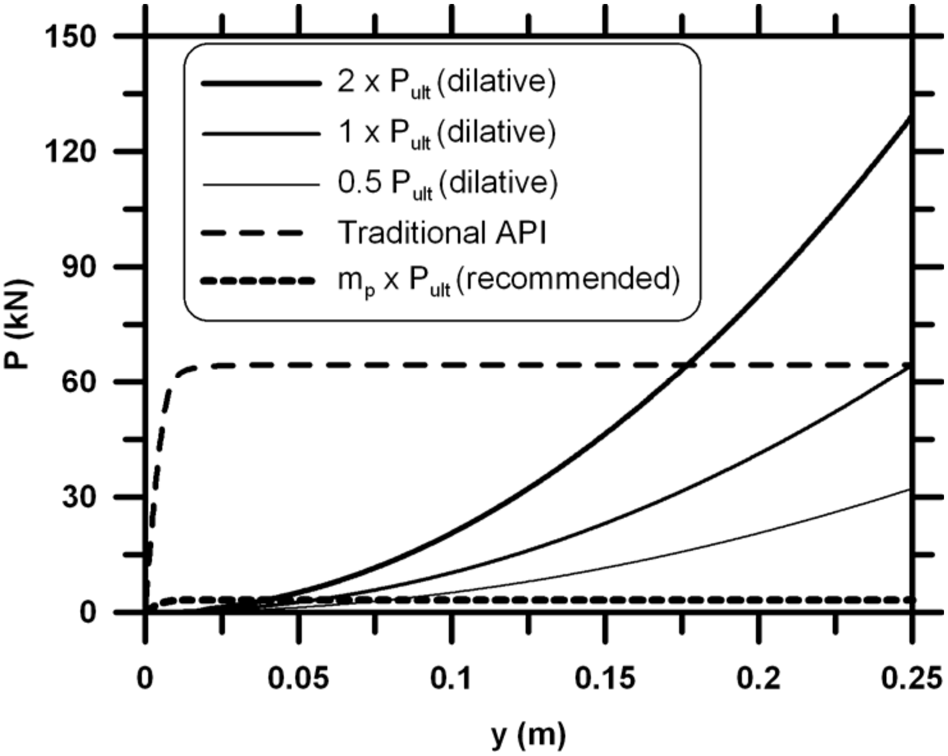

Figure 3.8: p-y curves used in the example analyses at the center of the liquefied sand layer

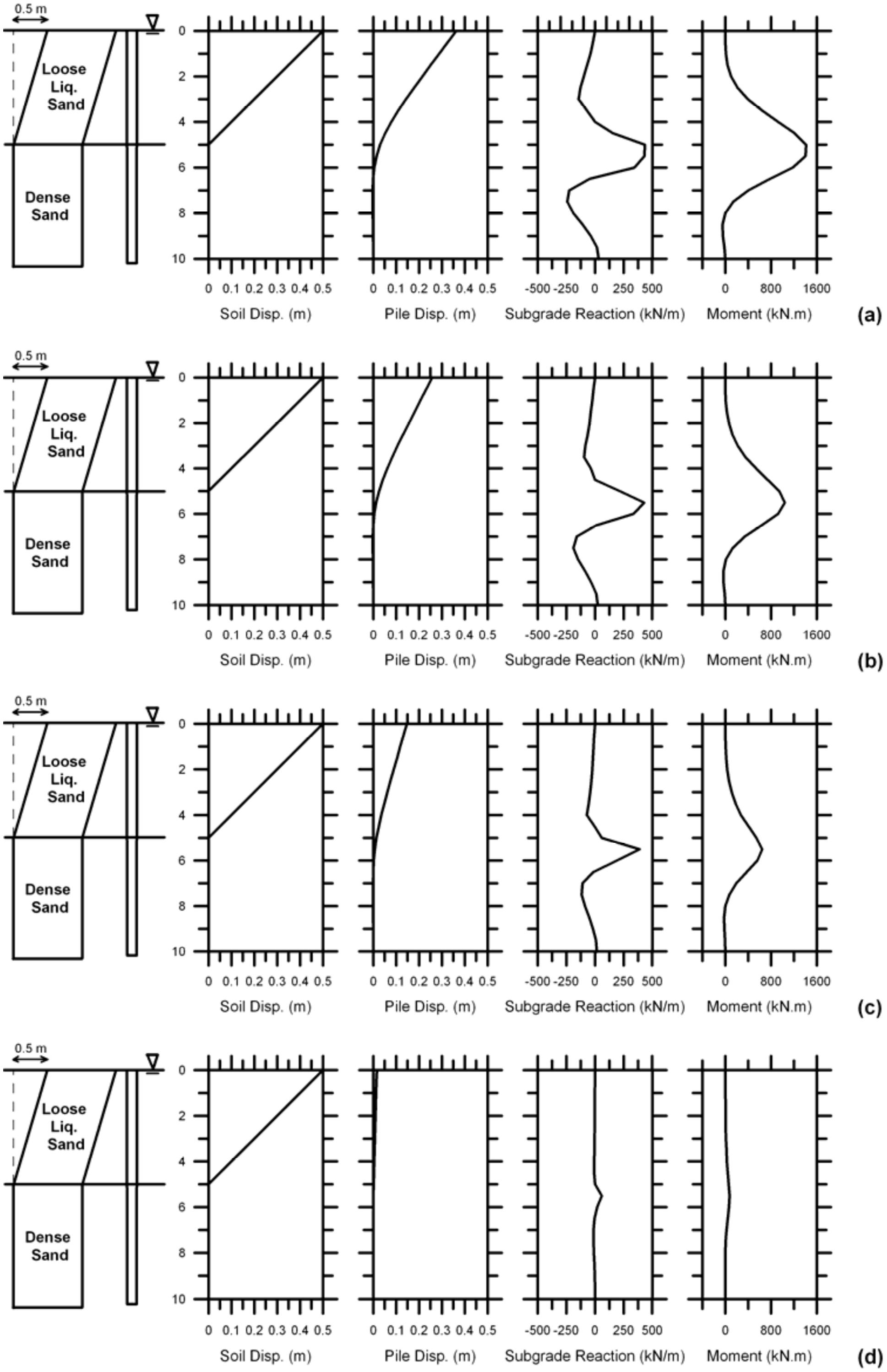

Figure 3.9: Soil and pile displacement and subgrade reaction and moment distribution for (a) $P_{ult} = 2 \times P_{ult\_API}$ (b) $P_{ult} = 1 \times P_{ult\_API}$ (c) $P_{ult} = 0.5 \times P_{ult\_API}$ and (d) $m_p = 0.05$

4 Fragility of Bridges to Lateral Spreading

4.1 Performance-based Earthquake Engineering and Fragility Functions

The Pacific Earthquake Engineering Research Center developed a performance-based earthquake engineering methodology defined by the triple integral in Equation. 4.1.

$$P(DV > dv) = \int_{dm}\int_{edp}\int_{im} G_{DV|DM}(dv \mid dm).\mid dG_{DM|EDP}(dm \mid edp)\mid . \mid dG_{EDP|IM}(edp \mid im)\mid . \mid dG_{IM}(im)\mid \tag{4.1}$$

Where, DV = the decision variable

DM = the damage measure

EDP = the engineering demand parameter

dv = the value of decision variable

dm = the value of the damage measure

edp = the value of the engineering demand parameter

im = the value of the intensity measure

To solve the triple integral, probabilistic relations are needed to define EDP given IM, DM given EDP, and DV given DM. Fragility functions typically quantify the probability of exceeding a DM given an EDP (e.g. Porter et al. 2007), though the term has also been applied to functions that represent probability of exceeding an EDP given an IM (Mackie and Stojadinovic, 2005) or probability of exceeding a DM given an IM (HAZUS 1999). Fragility functions are therefore a critical component of performance-based earthquake engineering. Fragility functions can also be represented as surfaces when expressed over some range of IM and EDP values, and these functions have been called "demand fragility surfaces" by Mackie and Stojadinovic (2005).

This chapter focuses on producing demand fragility surfaces characterizing probability of exceeding common EDP's for bridges (i.e. pier column curvature ductility, abutment displacement, pile cap displacement) as functions of free-field permanent ground surface displacement, which is deemed to be the most important and useful IM to characterize liquefaction-induced lateral spreading. The fragility demand surfaces are produced numerically using thousands of realizations of a finite element model in which the inputs were randomly selected as detailed in Chapter 3 (i.e. Monte Carlo simulation). Correlation among EDP values is important for estimating DM using the demand fragility surfaces, so correlation coefficients among EDP's is also presented. Finally, disaggregation of the results is used to identify the input parameters that most significantly contribute to the demand fragility surfaces.

4.2 Generation of Demand Fragility Surfaces

Demand fragility surfaces were generated using Monte Carlo simulations involving thousands of realizations of a Nonlinear Equivalent Static Global Analysis. Input parameters were randomly selected from their assigned distributions (discussed in chapter 3) using the uniform random number generator in TCL combined with a Box-Muller transform (Box and Muller 1958) for any variables that are not uniformly distributed (i.e. for variables with normal and log-normal distributions). During the analyses the free-field lateral ground displacement was increased incrementally and the values of the IM (i.e. the maximum free-field ground surface displacement among the various bridge components) were recorded when specified levels of several EDP's were mobilized. Tables 4.1, 4.2 and 4.3 present the EDP's that were monitored during the analyses for continuous bridges with monolithic abutments, simply-supported bridges with seat-type abutments and continuous bridges with seat-type abutments, respectively, and ground displacements were recorded when the EDP first reached the "Initial Value" and subsequently at each "Incremental Value" thereafter. The analysis proceeded until the maximum free-field ground displacement reached 2.0*m* or until a limiting demand on a bridge pier was reached defined as either exceeding a curvature ductility of 11 in one of the pier columns or exceeding the shear capacity of a pier column. These limits were established (1) based on the assumption that this level of mobilized EDP in the pier column would constitute serious damage and continuing the analysis would have little physical meaning, and

(2) numerical convergence became difficult at such large levels of structural nonlinearity.

Table 4.1: Engineering Demand Parameters and their Recorder Values for Continuous Bridges with Monolithic Abutments

Engineering Demand Parameter	Performance Group	Initial Value	Incremental Value	Unit
Curvature Ductility in Piers	Pier 2 Curvature Ductility	1	1	NA
	Pier 3 Curvature Ductility	1	1	NA
Pile Cap Displacement	Pier 2 Pile Cap Displacment	0.025	0.025	(m)
	Pier 2 Pile Cap Displacment	0.025	0.025	(m)
Pile Cap Rotation	Pier 2 Pile Cap Rotation	0.5	0.5	%
	Pier 3 Pile Cap Rotation	0.5	0.5	%
Abutment Displacement	Abutment 1 Displacement	0.025	0.025	(m)
	Abutment 4 Displacement	0.025	0.025	(m)
Abutment Rotation	Abutment 1 Rotation	0.5	0.5	%
	Abutment 4 Rotation	0.5	0.5	%
Pier Pile Curvature Ductility	Pier 2 Piles Curvature Ductility	1	2	NA
	Pier 3 Piles Curvature Ductility	1	2	NA
Abutment Pile Curvature Ductility	Abutment 1 Piles Curvature Ductility	1	2	NA
	Abutment 4 Piles Curvature Ductility	1	2	NA

Table 4.2: Engineering Demand Parameters and their Recorder Values for Simply-Supported Bridges with Seat-Type Abutments

Engineering Demand Parameter	Performance Group	Initial Value	Incremental Value	Unit
Curvature Ductility in Piers	Pier 2 Curvature Ductility	1	1	NA
	Pier 3 Curvature Ductility	1	1	NA
Pile Cap Displacement	Pier 2 Pile Cap Displacement	0.025	0.025	(m)
	Pier 2 Pile Cap Displacement	0.025	0.025	(m)
Pile Cap Rotation	Pier 2 Pile Cap Rotation	0.5	0.5	%
	Pier 3 Pile Cap Rotation	0.5	0.5	%
Abutment Displacement	Abutment 1 Displacement	0.025	0.025	(m)
	Abutment 4 Displacement	0.025	0.025	(m)
Abutment Rotation	Abutment 1 Rotation	0.5	0.5	%
	Abutment 4 Rotation	0.5	0.5	%
Pier Pile Curvature Ductility	Pier 2 Piles Curvature Ductility	1	2	NA
	Pier 3 Piles Curvature Ductility	1	2	NA
Abutment Pile Curvature Ductility	Abutment 1 Piles Curvature Ductility	1	2	NA
	Abutment 4 Piles Curvature Ductility	1	2	NA
Strains in Bearings	Strain in Abutment 1	50	50	%
	Strain in Pier 2	50	50	%
	Strain in Pier 3	50	50	%
	Strain in Abutment 4	50	50	%
Unseating	Unseating in any Pier or Abutment	0.38	NA	(m)

Table 4.3: Engineering Demand Parameters and their Recorder Values for Continuous Bridges with Seat-Type Abutments

Engineering Demand Parameter	Performance Group	Initial Value	Incremental Value	Unit
Curvature Ductility in Piers	Pier 2 Curvature Ductility	1	1	NA
	Pier 3 Curvature Ductility	1	1	NA
Pile Cap Displacement	Pier 2 Pile Cap Displacement	0.025	0.025	(m)
	Pier 2 Pile Cap Displacement	0.025	0.025	(m)
Pile Cap Rotation	Pier 2 Pile Cap Rotation	0.5	0.5	%
	Pier 3 Pile Cap Rotation	0.5	0.5	%
Abutment Displacement	Abutment 1 Displacement	0.025	0.025	(m)
	Abutment 4 Displacement	0.025	0.025	(m)
Abutment Rotation	Abutment 1 Rotation	0.5	0.5	%
	Abutment 4 Rotation	0.5	0.5	%
Pier Pile Curvature Ductility	Pier 2 Piles Curvature Ductility	1	2	NA
	Pier 3 Piles Curvature Ductility	1	2	NA
Abutment Pile Curvature Ductility	Abutment 1 Piles Curvature Ductility	1	2	NA
	Abutment 4 Piles Curvature Ductility	1	2	NA
Strains in Bearings	Strain in Abutment 1	50	50	%
	Strain in Abutment 4	50	50	%
Unseating	Unseating in any Abutment	0.38	NA	(m)

Once the analyses finished, the free-field ground displacements required to mobilize a given EDP value were sorted in increasing order, and plotted as a histogram reflecting the cumulative probability mass function. The probability mass assigned to each discrete analysis was equal to 1/N, where N was the number of analyses in a given data set (typically 1000). Separate cumulative probability mass functions were developed for each EDP type (e.g., pier curvature ductility), each EDP value within that type (e.g., curvature ductility of 1, 2, 3, …) and for each class of bridge. The process is best demonstrated through an example:

Table 4.4 shows the exercise of generating the fragility function for maximum curvature ductility of 7 in any of the piers of the set of analyses of post-1971 simply-supported bridges with seat-type abutments and single-column piers.

Table 4.4: Generation of Fragility Function for Curvature Ductility of 7 in Post-1971 Simply-Supported Bridges with Seat-type abutments and Single-column Piers

Sorted Δ_{FF}	**Probability Mass Dist.**	**Cumulative Prob. Mass**
0.044	0.001105	0
0.049	0.001105	1.11E-03
0.053	0.001105	2.21E-03
0.054	0.001105	3.32E-03
0.055	0.001105	4.42E-03
0.057	0.001105	5.53E-03
0.058	0.001105	6.63E-03
:	:	:
:	:	:
:	:	:
1.838	0.001105	0.393
1.905	0.001105	0.394

The first column is the array of free-field ground displacements required to mobilize a maximum curvature ductility of 7 in the piers. The probability mass of all of the analyses are the same as listed in the second column. If none of the analyses were terminated due to long computation time, the probability mass of the analyses would have been 1/1000 = 0.001. However, in this set 95 analyses were terminated before finishing, and thus the total number of analyses was N = 905 and the probability mass of each analysis was 1/905 = 0.001105. The third column is the sum of the probabilities (cumulative probability) of the analyses in the set.

Figure 4.1a shows the histogram of the probability mass distributions of free-field displacements to reach curvature ductility of 7 presented in Table 4.4. It is evident from the figure that the probability distribution follows the shape of a log-normal distribution. The cumulative distribution of the actual data is shown on Figure 4.1b with the corresponding log-normal distribution superimposed on the distribution of the data. As can be seen in the figure the log-normal distribution fits the data very well.

Cumulative probability density functions for typical random variables range from 0 to 1. The fragility function shown in Figure 4.1 however does not reach an ultimate value of 1 but rather reaches a value of only 0.4 as ground displacement reaches 2 m. The cause of this behavior is that the structure is strong enough to resist the ultimate lateral spreading loads in some cases, and lateral spreading can never mobilize some EDP levels, even if the free-field ground displacement was increased to infinity. For example, if the pile group is very stiff and strong and limits pile cap displacement to only a few centimeters, very little damage may be induced in the pier column regardless of how large the free-field ground displacement becomes. Hence, the fragility functions in this dissertation are mixed random variables with some probability mass lumped at infinite ground displacement.

4.3 Fitting Fragility Surfaces to the Data

The fragility function in the previous section was generated numerically by summing the probability mass of each discrete case, but making use of this large amount of information is not very convenient. A more convenient representation of the fragility function can be obtained by fitting a functional form to the discrete data. The form of the fragility functions in this study were well-approximated as log-normal distributions, hence this form was selected. One option would be to specify a median and standard deviation for each value of EDP for each analysis case, but this would result in a very large number of constants. The approach adopted in this study was to utilize six constants to fully define the demand fragility surface. Each of the six constants is presented by example in the following paragraphs

For a simply-supported bridge with seat-type abutments and single-column piers belonging to the post-1971 era, ten different Engineering Demand Parameters are recorded, as listed in Table 4.2. The fragility results of two of the engineering demand parameters, Pile Cap Displacement and Pier Curvature Ductility are shown in Figure 4.3. The fragility functions at every EDP value could be defined by a median λ, a standard deviations of natural logarithms of the data ξ, and an additional scalar value representing the limiting value of cumulative probability (i.e. the amount of probability mass included in the finite range of free-field ground displacement, also equal to 1 minus the probability mass lumped at a ground displacement of infinity). This would involve specifying 80 different constants for cap displacement and 11 different constants for pier curvature ductility. Repeating this process for the other EDPs in Tables 4.1, 4.2 and 4.3 and for all for all of the classes of bridges would result in an unmanageable representation of the fragility functions. The alternative approach adopted in this study is to use linear regression to define the medians, standard deviations, and peak probabilities as functions of EDP. Linear regression requires specification of a slope and an intercept value, hence two constants each are required for median, standard deviation, and maximum probability and the entire demand fragility surface can therefore be defined by six constants. Figure 4.3 shows the linear regressions of the natural logarithms of median, standard deviation and peak probability for pile cap displacement of the abovementioned class of bridges. It can be seen from the figure that all three parameters can be represented fairly well using a linear regression versus logarithms of the EDP values, though there is some misfit particularly at lower values of EDP. Some misfit must be accepted as a tradeoff for the convenience of expressing the demand fragility surfaces using a manageable set of constants. The formulas for the three lines can be summarized as follows:

$$\lambda = A + B \times \ln(edp) \tag{4.6}$$

$$\xi = C + D \times \ln(edp) \tag{4.7}$$

$$\mathrm{p}_{max} = E + F \times \ln(edp) \leq 1.0 \tag{4.8}$$

Where, λ = logarithm of median of the log-normal distribution

ξ = standard deviation of natural logs of data (dispersion)

p_{max} = maximum probability at 2m of ground displacement at each EDP value

The form of Eq. 4.8 permits $\mathrm{p}_{max} > 1$, which is a violation of probability theory. This can be seen in the misfit in Fig. 4.4 at low edp values where the data lie below the linear trend. The data are all below a cumulative probability of 1.0, but the linear trend extends above 1.0. Hence, $\mathrm{p}_{\mathrm{max}}$ was truncated to have a maximum value of 1.0. For some EDP's a log-transformation of the edp values did not produce a linear fit, and a better linear fit was obtained based on the values of the variables themselves. Hence, $\mathrm{p}_{\mathrm{max}}$ for some EDPs was defined as follows:

$$\mathrm{p}_{max} = E + F \times edp \leq 1.0 \tag{4.9}$$

By utilizing the equations of the lines presented in equations 4.6 through 4.9 for every value of IM (i.e. ground displacement) and every value of EDP (edp), the probability of exceedance can be calculated using equation 4.10:

$$P(EDP < edp \mid IM = im) = \underbrace{\Phi\left(\frac{\ln(im) - (A + B \times \ln(edp))}{(C + D \times \ln(edp))}\right)}_{\text{Standard Normal Cumulative Distribution}} . \underbrace{\left(E + F \times \ln(edp)\right)}_{\text{Peak Probability at edp value}} \tag{4.10}$$

or using equation 4.11 for Curvature Ductilies in piers, abutment piles and piles in pile groups supporting the pier, as follows:

$$P(EDP < edp \mid IM = im) = \underbrace{\Phi\left(\frac{\ln(im) - (A + B \times \ln(edp))}{(C + D \times \ln(edp))}\right)}_{\text{Standard Normal Cumulative Distribution}} . \underbrace{\left(E + F \times edp\right)}_{\text{Peak Probability at edp value}} \tag{4.11}$$

Where, Φ = the standard normal cumulative distribution function

Eqs. 4.10 and 4.11 provide a convenient means of specifying the entire demand fragility surface using only six variables. In few occasions the misfit of the surface, generated values for probability of exceeding certain engineering demand parameters above 1 or below 0. Since these values were statistically meaningless, the values of probabilities of exceedance were truncated between 0 and 1. Figure 4.4 shows demand fragility surfaces plotted along with the discreet data for pile cap displacement and pier curvature ductility in the above-mentioned class of bridges. The degree of misfit between the data and the surface in Figure 4.4 is characteristic of the misfit for other EDPs. As can be seen in the figure, the probability of exceedance of pile cap displacement at low edp value of 0.025*m* exceeds 1 due to the misfit of the fragility surface. Thus the fragility surface was truncated at 1.

4.4 Fragility Surface Results

Using the fitting method explained above, fragility surfaces were created for all recorded engineering demand parameters for all classes of bridges that were analyzed in the analyses, except for un-seating in the case of simply-supported bridges, since no incremental values were available for un-seating. Tables 4.5 through 4.28 summarize the parameters for fitting the fragility surfaces for all 24 different classes of bridges analyzed as well as the appropriate equation to be used for each EDP for fitting the fragility surface. In addition to the parameters, the coefficient of the determination (R^2) value associated with each of the fitting lines is presented, here. From the R^2 values it is evident that the surfaces fitted to the data, match the data values fairly well, since most of the R^2 values are above 0.9. The lowest R^2 values are on the order of 0.8, indicating that the fitted surface agrees reasonably well with the discrete data. Plots of the fitted fragility surfaces for different engineering demand parameters for all the classes of bridges analyzed are summarized in Figures 4.5 through 4.28.

Table 4.5: Fragility Surfaces Parameters for Post-1971 Simply-Supported Bridges with Seat-type Abutments and Single-Column Piers and 24” CIDH piles

Engineering Demand Parameter	**Parameters**						**Coefficient of Determination**			**Eq.**
	A	B	C	D	E	F	R^2_{λ}	R^2_{ξ}	$R^2_{Prob.}$	No.
Abutment Displacement (m)	0.617	0.787	0.183	-0.191	0.174	-0.273	0.965	0.952	0.967	4.10
Abutment Rotation (%)	1.025	0.541	0.171	-0.103	0.073	-0.193	0.999	0.94	0.929	4.10
Pile Cap Displacement (m)	0.227	0.694	0.193	-0.232	0.22	-0.237	0.997	0.981	0.983	4.10
Pile Cap Rotation (%)	1.438	0.532	-0.142	-0.196	-0.312	-0.157	0.999	0.97	0.953	4.10
Pier Curvature Ductility	-1.257	0.413	0.852	-0.137	0.403	-0.024	0.939	0.964	0.99	4.11
Pier Piles Curvature Ductility	-1.893	0.62	0.99	-0.19	0.849	-0.034	0.991	0.921	0.985	4.11
Abutment Piles Curvature Ductility	-1.896	0.525	0.809	-0.086	0.985	-0.019	0.987	0.974	0.998	4.11
Strain in Abutment Bearings	-0.439	0.271	0.715	-0.165	0.308	-0.057	0.987	0.993	0.922	4.10
Strain in Pier Bearings	-0.887	0.41	0.697	-0.144	0.362	-0.053	0.994	0.998	0.995	4.10

Table 4.6: Fragility Surfaces Parameters for Post-1971 Simply-Supported Bridges with Seat-type Abutments and Multi-Column Piers and 24” CIDH piles

Engineering Demand Parameter	**Parameters**						**Coefficient of Determination**			**Eq.**
	A	B	C	D	E	F	R^2_{λ}	R^2_{ξ}	$R^2_{Prob.}$	No.
Abutment Displacement (m)	0.604	0.786	0.178	-0.19	0.235	-0.263	0.957	0.928	0.954	4.10
Abutment Rotation (%)	1.047	0.551	0.199	-0.095	0.099	-0.192	1	0.927	0.916	4.10
Pile Cap Displacement (m)	0.23	0.681	0.193	-0.237	0.255	-0.236	0.996	0.979	0.973	4.10
Pile Cap Rotation (%)	1.44	0.542	-0.18	-0.205	-0.331	-0.175	0.999	0.953	0.979	4.10
Pier Curvature Ductility	-0.876	0.357	0.771	-0.135	0.287	-0.021	0.968	0.953	0.976	4.11
Pier Piles Curvature Ductility	-1.883	0.622	1.006	-0.193	0.862	-0.031	0.986	0.919	0.989	4.11
Abutment Piles Curvature Ductility	-1.924	0.526	0.789	-0.072	1.015	-0.018	0.987	0.96	0.995	4.11
Strain in Abutment Bearings	-0.475	0.291	0.688	-0.156	0.359	-0.057	0.998	0.992	0.938	4.10
Strain in Pier Bearings	-0.873	0.422	0.693	-0.152	0.395	-0.048	0.997	0.998	0.972	4.10

Table 4.7: Fragility Surfaces Parameters for Post-1971 Simply-Supported Bridges with Seat-type Abutments and Single-Column Piers and 24” CISS piles

Engineering Demand Parameter	**Parameters**						**Coefficient of Determination**			**Eq.**
	A	B	C	D	E	F	R^2_{λ}	R^2_{ξ}	$R^2_{Prob.}$	No.
Abutment Displacement (m)	0.495	0.765	0.162	-0.205	0.258	-0.25	0.969	0.939	0.961	4.10
Abutment Rotation (%)	1.347	0.55	0.016	-0.149	-0.516	-0.29	0.991	0.948	0.99	4.10
Pile Cap Displacement (m)	0.224	0.617	0.209	-0.237	0.092	-0.166	0.995	0.983	0.919	4.10
Pile Cap Rotation (%)	1.55	0.504	-0.281	-0.206	-0.396	-0.181	0.995	0.947	0.881	4.10
Pier Curvature Ductility	-1.275	0.38	0.832	-0.104	0.385	-0.026	0.974	0.903	0.967	4.11
Pier Piles Curvature Ductility	-0.829	0.483	0.942	-0.301	0.253	-0.023	0.93	0.948	0.76	4.11
Abutment Piles Curvature Ductility	-1.167	0.507	0.833	-0.19	0.803	-0.039	0.984	0.955	0.965	4.11
Strain in Abutment Bearings	-0.645	0.338	0.645	-0.14	0.55	-0.085	0.984	0.997	0.989	4.10
Strain in Pier Bearings	-0.931	0.393	0.693	-0.105	0.319	-0.088	0.998	0.992	0.99	4.10

Table 4.8: Fragility Surfaces Parameters for Post-1971 Simply-Supported Bridges with Seat-type Abutments and Multi-Column Piers and 24” CISS piles

Engineering Demand Parameter	**Parameters**						**Coefficient of Determination**			**Eq.**
	A	B	C	D	E	F	R^2_{λ}	R^2_{ξ}	$R^2_{Prob.}$	No.
Abutment Displacement (m)	0.521	0.764	0.165	-0.203	0.278	-0.241	0.966	0.94	0.966	4.10
Abutment Rotation (%)	1.354	0.548	-0.003	-0.152	-0.507	-0.286	0.988	0.948	0.983	4.10
Pile Cap Displacement (m)	0.262	0.585	0.218	-0.236	0.085	-0.17	0.992	0.979	0.939	4.10
Pile Cap Rotation (%)	1.416	0.466	-0.014	-0.142	-0.417	-0.194	0.981	0.99	0.938	4.10
Pier Curvature Ductility	-1.076	0.366	0.773	-0.086	0.261	-0.019	0.956	0.953	0.977	4.11
Pier Piles Curvature Ductility	-0.689	0.379	0.845	-0.196	0.27	-0.025	0.984	0.983	0.792	4.11
Abutment Piles Curvature Ductility	-1.182	0.526	0.81	-0.193	0.81	-0.039	0.982	0.955	0.976	4.11
Strain in Abutment Bearings	-0.612	0.334	0.66	-0.148	0.571	-0.086	0.989	0.992	0.943	4.10
Strain in Pier Bearings	-0.868	0.409	0.671	-0.119	0.335	-0.102	0.998	0.988	0.986	4.10

Table 4.9: Fragility Surfaces Parameters for Post-1971 Simply-Supported Bridges with Seat-type Abutments and Single-Column Piers and 15” Precast Piles

Engineering Demand Parameter	**Parameters**						**Coefficient of Determination**			**Eq.**
	A	B	C	D	E	F	R^2_{λ}	R^2_{ξ}	$R^2_{Prob.}$	No.
Abutment Displacement (m)	0.575	0.798	0.198	-0.172	0.064	-0.294	0.972	0.912	0.98	4.10
Abutment Rotation (%)	0.927	0.558	0.241	-0.076	0.127	-0.181	0.998	0.943	0.933	4.10
Pile Cap Displacement (m)	0.241	0.779	0.171	-0.235	0.175	-0.291	0.998	0.979	0.945	4.10
Pile Cap Rotation (%)	1.554	0.607	-0.123	-0.191	-0.336	-0.193	0.999	0.987	0.988	4.10
Pier Curvature Ductility	-1.236	0.397	0.84	-0.132	0.387	-0.023	0.938	0.935	0.992	4.11
Pier Piles Curvature Ductility	-2	0.601	0.942	-0.155	0.899	-0.036	0.989	0.944	0.994	4.11
Abutment Piles Curvature Ductility	-1.996	0.471	0.773	-0.075	0.97	-0.019	0.989	0.989	0.998	4.11
Strain in Abutment Bearings	-0.772	0.375	0.66	-0.107	0.173	-0.038	0.988	0.984	0.897	4.10
Strain in Pier Bearings	-0.835	0.371	0.688	-0.117	0.358	-0.068	0.98	0.985	0.452	4.10

Table 4.10: Fragility Surfaces Parameters for Post-1971 Simply-Supported Bridges with Seat-type Abutments and Multi-Column Piers and 15” Precast Piles

Engineering Demand Parameter	**Parameters**						**Coefficient of Determination**			**Eq.**
	A	B	C	D	E	F	R^2_{λ}	R^2_{ξ}	$R^2_{Prob.}$	No.
Abutment Displacement (m)	0.586	0.797	0.206	-0.171	0.099	-0.295	0.967	0.895	0.971	4.10
Abutment Rotation (%)	0.87	0.551	0.233	-0.073	0.225	-0.162	0.998	0.929	0.919	4.10
Pile Cap Displacement (m)	0.251	0.747	0.186	-0.238	0.182	-0.283	0.997	0.982	0.963	4.10
Pile Cap Rotation (%)	1.539	0.603	-0.106	-0.19	-0.345	-0.211	0.999	0.959	0.996	4.10
Pier Curvature Ductility	-0.921	0.387	0.724	-0.115	0.224	-0.015	0.955	0.976	0.99	4.11
Pier Piles Curvature Ductility	-1.95	0.595	0.949	-0.15	0.898	-0.036	0.991	0.928	0.989	4.11
Abutment Piles Curvature Ductility	-2.038	0.496	0.749	-0.063	0.985	-0.016	0.99	0.993	0.997	4.11
Strain in Abutment Bearings	-0.63	0.314	0.701	-0.125	0.212	-0.051	0.97	0.966	0.931	4.10
Strain in Pier Bearings	-0.859	0.405	0.704	-0.133	0.36	-0.064	0.985	0.994	0.399	4.10

Table 4.11: Fragility Surfaces Parameters for Pre-1971 Simply-Supported Bridges with Seat-type Abutments and Single-Column Piers and 15” Precast Piles

Engineering Demand Parameter	**Parameters**						**Coefficient of Determination**			**Eq.**
	A	B	C	D	E	F	R^2_{λ}	R^2_{ξ}	$R^2_{Prob.}$	No.
Abutment Displacement (m)	0.606	0.819	0.168	-0.169	0.016	-0.292	0.975	0.947	0.989	4.10
Abutment Rotation (%)	0.852	0.562	0.172	-0.082	0.108	-0.178	0.989	0.984	0.938	4.10
Pile Cap Displacement (m)	0.234	0.8	0.178	-0.225	0.147	-0.301	0.999	0.977	0.945	4.10
Pile Cap Rotation (%)	1.57	0.619	-0.125	-0.184	-0.265	-0.141	0.998	0.983	0.967	4.10
Pier Curvature Ductility	-1.624	0.487	0.842	-0.096	0.672	-0.028	0.955	0.895	0.996	4.11
Pier Piles Curvature Ductility	-2.356	0.63	0.944	-0.12	0.974	-0.035	0.987	0.911	0.998	4.11
Abutment Piles Curvature Ductility	-2.337	0.501	0.743	-0.059	0.949	-0.016	0.987	0.981	0.995	4.11
Strain in Abutment Bearings	-1.477	0.781	0.847	-0.233	0.261	-0.125	0.735	0.824	0.614	4.10
Strain in Pier Bearings	-1.144	0.415	0.814	-0.148	0.282	-0.021	0.996	0.991	0.972	4.10

Table 4.12: Fragility Surfaces Parameters for Pre-1971 Simply-Supported Bridges with Seat-type Abutments and Multi-Column Piers and 15” Precast Piles

Engineering Demand Parameter	**Parameters**						**Coefficient of Determination**			**Eq.**
	A	B	C	D	E	F	R^2_{λ}	R^2_{ξ}	$R^2_{Prob.}$	No.
Abutment Displacement (m)	0.616	0.805	0.204	-0.154	0.033	-0.307	0.966	0.884	0.978	4.10
Abutment Rotation (%)	0.825	0.547	0.226	-0.076	0.143	-0.183	0.997	0.957	0.892	4.10
Pile Cap Displacement (m)	0.225	0.797	0.18	-0.226	0.191	-0.318	0.998	0.965	0.927	4.10
Pile Cap Rotation (%)	1.556	0.63	-0.065	-0.178	-0.273	-0.165	0.999	0.933	0.994	4.10
Pier Curvature Ductility	-1.345	0.451	0.824	-0.142	0.486	-0.024	0.944	0.958	0.996	4.11
Pier Piles Curvature Ductility	-2.384	0.654	0.954	-0.122	1.013	-0.032	0.986	0.874	0.996	4.11
Abutment Piles Curvature Ductility	-2.281	0.507	0.756	-0.065	0.981	-0.014	0.99	0.996	0.998	4.11
Strain in Abutment Bearings	-1.317	0.726	0.882	-0.264	0.255	-0.114	0.721	0.81	0.633	4.10
Strain in Pier Bearings	-1.107	0.402	0.826	-0.162	0.372	-0.038	0.996	0.991	0.945	4.10

Table 4.13: Fragility Surfaces Parameters for Post-1971 Continuous Bridges with Monolithic Abutments and Single-Column Piers and 24" CIDH piles

Engineering Demand Parameter	**Parameters**						**Coefficient of Determination**			**Eq.**
	A	B	C	D	E	F	R^2_{λ}	R^2_{ξ}	$R^2_{Prob.}$	No.
Abutment Displacement (m)	0.674	0.526	0.28	-0.104	-0.249	-0.276	0.95	0.965	0.969	4.10
Abutment Rotation (%)	2.256	0.726	-0.123	-0.167	-1.017	-0.355	0.993	0.959	0.997	4.10
Pile Cap Displacement (m)	0.496	0.654	0.237	-0.219	-0.239	-0.291	0.994	0.979	0.983	4.10
Pile Cap Rotation (%)	1.274	0.467	-0.057	-0.174	-0.854	-0.277	0.992	0.932	0.977	4.10
Pier Curvature Ductility	-1.621	0.44	0.967	-0.095	0.897	-0.054	0.91	0.89	0.93	4.11
Pier Piles Curvature Ductility	-1.568	0.504	1.102	-0.226	0.363	-0.022	0.938	0.953	0.845	4.11
Abutment Piles Curvature Ductility	-1.619	0.298	0.923	-0.094	0.713	-0.023	0.99	0.923	0.923	4.11

Table 4.14: Fragility Surfaces Parameters for Post-1971 Continuous Bridges with Monolithic Abutments and Multi-Column Piers and 24" CIDH piles

Engineering Demand Parameter	**Parameters**						**Coefficient of Determination**			**Eq.**
	A	B	C	D	E	F	R^2_{λ}	R^2_{ξ}	$R^2_{Prob.}$	No.
Abutment Displacement (m)	0.917	0.608	0.124	-0.152	-0.190	-0.295	0.982	0.994	0.997	4.10
Abutment Rotation (%)	2.439	0.759	-0.015	-0.142	-1.085	-0.383	0.991	0.974	0.992	4.10
Pile Cap Displacement (m)	0.478	0.732	0.340	-0.185	-0.048	-0.305	0.984	0.979	0.938	4.10
Pile Cap Rotation (%)	1.016	0.423	0.328	-0.089	-0.409	-0.170	0.997	0.971	0.997	4.10
Pier Curvature Ductility	-1.454	0.428	0.941	-0.107	0.889	-0.045	0.932	0.864	0.823	4.11
Pier Piles Curvature Ductility	-1.592	0.538	1.006	-0.184	0.785	-0.045	0.985	0.924	0.950	4.11
Abutment Piles Curvature Ductility	-1.979	0.375	0.818	-0.072	0.927	-0.017	0.987	0.863	0.974	4.11

Table 4.15: Fragility Surfaces Parameters for Post-1971 Continuous Bridges with Monolithic Abutments and Single-Column Piers and 24” CISS piles

Engineering Demand Parameter	Parameters						Coefficient of Determination			Eq.
	A	B	C	D	E	F	R^2_{λ}	R^2_{ξ}	$R^2_{Prob.}$	No.
Abutment Displacement (m)	0.81	0.563	0.169	-0.138	-0.274	-0.286	0.959	0.981	0.959	4.10
Abutment Rotation (%)	2.227	0.719	-0.157	-0.174	-0.977	-0.351	0.995	0.951	0.996	4.10
Pile Cap Displacement (m)	0.568	0.629	0.266	-0.218	-0.264	-0.268	0.992	0.95	0.939	4.10
Pile Cap Rotation (%)	1.796	0.52	-0.015	-0.144	-0.86	-0.264	0.988	0.892	0.921	4.10
Pier Curvature Ductility	-1.542	0.429	0.994	-0.102	0.875	-0.056	0.901	0.905	0.949	4.11
Pier Piles Curvature Ductility	-0.989	0.542	1.083	-0.283	0.099	-0.0098	0.906	0.722	0.583	4.11
Abutment Piles Curvature Ductility	-1.147	0.384	0.765	-0.138	0.597	-0.031	0.997	0.977	0.868	4.11

Table 4.16: Fragility Surfaces Parameters for Post-1971 Continuous Bridges with Monolithic Abutments and Multi-Column Piers and 24” CISS piles

Engineering Demand Parameter	Parameters						Coefficient of Determination			Eq.
	A	B	C	D	E	F	R^2_{λ}	R^2_{ξ}	$R^2_{Prob.}$	No.
Abutment Displacement (m)	0.870	0.589	0.037	-0.199	-0.233	-0.297	0.988	0.979	0.986	4.10
Abutment Rotation (%)	2.191	0.700	-0.208	-0.191	-0.920	-0.351	0.999	0.978	0.994	4.10
Pile Cap Displacement (m)	0.407	0.682	0.312	-0.197	-0.147	-0.274	0.987	0.985	0.993	4.10
Pile Cap Rotation (%)	1.391	0.517	0.095	-0.141	-0.769	-0.277	0.994	0.989	0.994	4.10
Pier Curvature Ductility	-1.292	0.381	0.918	-0.094	0.837	-0.052	0.929	0.895	0.940	4.11
Pier Piles Curvature Ductility	-0.828	0.439	0.849	-0.187	0.232	-0.029	0.929	0.982	0.887	4.11
Abutment Piles Curvature Ductility	-1.099	0.377	0.775	-0.144	0.658	-0.030	0.998	0.981	0.894	4.11

Table 4.17: Fragility Surfaces Parameters for Post-1971 Continuous Bridges with Monolithic Abutments and Single-Column Piers and 15” Precast

Engineering Demand Parameter	**Parameters**						**Coefficient of Determination**			**Eq.**
	A	B	C	D	E	F	R^2_{λ}	R^2_{ξ}	$R^2_{Prob.}$	No.
Abutment Displacement (m)	0.87	0.619	0.214	-0.127	-0.203	-0.27	0.986	0.977	0.993	4.10
Abutment Rotation (%)	2.237	0.702	0.046	-0.133	-0.961	-0.332	0.985	0.948	0.978	4.10
Pile Cap Displacement (m)	0.753	0.822	0.292	-0.185	-0.201	-0.348	0.997	0.982	0.968	4.10
Pile Cap Rotation (%)	2.107	0.709	0.112	-0.143	-1.078	-0.371	0.998	0.989	0.983	4.10
Pier Curvature Ductility	-1.746	0.45	0.999	-0.112	0.94	-0.05	0.898	0.824	0.847	4.11
Pier Piles Curvature Ductility	-1.677	0.572	0.967	-0.139	0.677	-0.04	0.982	0.981	0.88	4.11
Abutment Piles Curvature Ductility	-2.388	0.394	0.898	-0.094	0.919	-0.015	0.974	0.864	0.985	4.11

Table 4.18: Fragility Surfaces Parameters for Post-1971 Continuous Bridges with Monolithic Abutments and Multi-Column Piers and 15” Precast

Engineering Demand Parameter	**Parameters**						**Coefficient of Determination**			**Eq.**
	A	B	C	D	E	F	R^2_{λ}	R^2_{ξ}	$R^2_{Prob.}$	No.
Abutment Displacement (m)	0.858	0.596	0.203	-0.128	-0.160	-0.295	0.973	0.966	0.994	4.10
Abutment Rotation (%)	2.511	0.752	-0.098	-0.160	-0.983	-0.352	0.990	0.974	0.991	4.10
Pile Cap Displacement (m)	0.563	0.784	0.333	-0.191	0.018	-0.301	0.987	0.962	0.915	4.10
Pile Cap Rotation (%)	0.805	0.394	0.295	-0.107	-0.399	-0.177	0.994	0.994	0.996	4.10
Pier Curvature Ductility	-1.464	0.421	0.961	-0.127	0.852	-0.043	0.929	0.857	0.837	4.11
Pier Piles Curvature Ductility	-1.444	0.533	0.983	-0.183	0.739	-0.042	0.981	0.956	0.929	4.11
Abutment Piles Curvature Ductility	-2.344	0.396	0.884	-0.085	0.980	-0.012	0.982	0.820	0.996	4.11

Table 4.19: Fragility Surfaces Parameters for Pre-1971 Continuous Bridges with Monolithic Abutments and Single-Column Piers and 15” Precast Piles

Engineering Demand Parameter	**Parameters**						**Coefficient of Determination**			**Eq.**
	A	B	C	D	E	F	R^2_{λ}	R^2_{ξ}	$R^2_{Prob.}$	No.
Abutment Displacement (m)	0.735	0.55	0.263	-0.113	-0.188	-0.189	0.964	0.834	0.939	4.10
Abutment Rotation (%)	2.125	0.649	-0.238	-0.196	-0.738	-0.228	0.984	0.898	0.902	4.10
Pile Cap Displacement (m)	0.753	0.906	0.256	-0.206	-0.295	-0.337	0.992	0.944	0.973	4.10
Pile Cap Rotation (%)	2.342	0.797	0.018	-0.176	-0.893	-0.284	0.946	0.949	0.99	4.10
Pier Curvature Ductility	-2.356	0.519	1.044	-0.092	0.96	-0.048	0.906	0.778	0.86	4.11
Pier Piles Curvature Ductility	-2.2	0.542	1.056	-0.139	0.672	-0.038	0.985	0.887	0.913	4.11
Abutment Piles Curvature Ductility	-3.078	0.435	0.794	-0.066	0.88	-0.016	0.98	0.872	0.994	4.11

Table 4.20: Fragility Surfaces Parameters for Pre-1971 Continuous Bridges with Monolithic Abutments and Multi-Column Piers and 15” Precast Piles

Engineering Demand Parameter	**Parameters**						**Coefficient of Determination**			**Eq.**
	A	B	C	D	E	F	R^2_{λ}	R^2_{ξ}	$R^2_{Prob.}$	No.
Abutment Displacement (m)	0.845	0.574	0.167	-0.143	-0.184	-0.230	0.986	0.980	0.986	4.10
Abutment Rotation (%)	2.201	0.643	-0.038	-0.151	-0.836	-0.262	0.991	0.973	0.931	4.10
Pile Cap Displacement (m)	0.340	0.769	0.320	-0.204	-0.116	-0.330	0.999	0.995	0.927	4.10
Pile Cap Rotation (%)	0.558	0.353	0.250	-0.115	-0.311	-0.116	0.970	0.973	0.981	4.10
Pier Curvature Ductility	-1.988	0.483	1.025	-0.129	0.935	-0.038	0.893	0.920	0.672	4.11
Pier Piles Curvature Ductility	-1.999	0.522	1.061	-0.143	0.819	-0.042	0.965	0.948	0.958	4.11
Abutment Piles Curvature Ductility	-2.725	0.366	1.034	-0.110	0.940	-0.012	0.981	0.914	0.991	4.11

Table 4.21: Fragility Surfaces Parameters for Post-1971 Continuous Bridges with Seat-type Abutments and Single-Column Piers and 24” CIDH Piles

Engineering Demand Parameter	**Parameters**						**Coefficient of Determination**			**Eq.**
	A	B	C	D	E	F	R^2_{λ}	R^2_{ξ}	$R^2_{\text{Prob.}}$	No.
Abutment Displacement (m)	0.528	0.762	0.166	-0.188	-0.001	-0.265	0.959	0.911	0.956	4.10
Abutment Rotation (%)	0.899	0.525	0.168	-0.101	-0.280	-0.242	0.998	0.894	0.972	4.10
Pile Cap Displacement (m)	0.616	0.795	0.233	-0.187	-0.125	-0.290	0.996	0.941	0.962	4.10
Pile Cap Rotation (%)	2.077	0.667	-0.001	-0.138	-0.627	-0.226	0.982	0.951	0.921	4.10
Pier Curvature Ductility	-1.791	0.472	0.860	-0.082	0.832	-0.039	0.902	0.872	0.998	4.11
Pier Piles Curvature Ductility	-1.773	0.579	0.869	-0.099	0.689	-0.041	0.989	0.936	0.900	4.11
Abutment Piles Curvature Ductility	-1.940	0.493	0.777	-0.072	0.866	-0.028	0.993	0.917	0.987	4.11
Strain in Abutment Bearings	-0.724	0.337	0.749	-0.192	0.194	-0.035	0.995	0.997	0.977	4.10

Table 4.22: Fragility Surfaces Parameters for Post-1971 Continuous Bridges with Seat-type Abutments and Multi-Column Piers and 24” CIDH Piles

Engineering Demand Parameter	**Parameters**						**Coefficient of Determination**			**Eq.**
	A	B	C	D	E	F	R^2_{λ}	R^2_{ξ}	$R^2_{\text{Prob.}}$	No.
Abutment Displacement (m)	0.578	0.777	0.165	-0.190	0.059	-0.290	0.960	0.937	0.976	4.10
Abutment Rotation (%)	0.958	0.532	0.166	-0.099	-0.179	-0.244	0.998	0.918	0.948	4.10
Pile Cap Displacement (m)	0.388	0.749	0.185	-0.233	0.059	-0.264	0.993	0.918	0.944	4.10
Pile Cap Rotation (%)	0.962	0.405	0.188	-0.138	-0.143	-0.080	0.990	0.979	0.832	4.10
Pier Curvature Ductility	-1.567	0.461	0.834	-0.101	0.814	-0.031	0.914	0.855	0.997	4.11
Pier Piles Curvature Ductility	-1.827	0.633	0.857	-0.153	0.858	-0.045	0.981	0.960	0.981	4.11
Abutment Piles Curvature Ductility	-1.896	0.493	0.790	-0.079	0.959	-0.026	0.989	0.962	0.997	4.11
Strain in Abutment Bearings	-0.625	0.325	0.729	-0.187	0.272	-0.055	0.989	0.993	0.949	4.10

Table 4.23: Fragility Surfaces Parameters for Post-1971 Continuous Bridges with Seat-type Abutments and Single-Column Piers and 24” CISS Piles

Engineering Demand Parameter	**Parameters**						**Coefficient of Determination**			**Eq.**
	A	B	C	D	E	F	R^2_{λ}	R^2_{ξ}	$R^2_{\text{Prob.}}$	No.
Abutment Displacement (m)	0.444	0.752	0.162	-0.197	0.098	-0.241	0.970	0.928	0.970	4.10
Abutment Rotation (%)	1.337	0.552	0.123	-0.123	-0.505	-0.249	0.995	0.860	0.962	4.10
Pile Cap Displacement (m)	0.677	0.770	0.220	-0.192	-0.147	-0.222	0.973	0.779	0.890	4.10
Pile Cap Rotation (%)	1.765	0.576	0.342	-0.063	-0.678	-0.223	0.990	0.525	0.839	4.10
Pier Curvature Ductility	-1.763	0.466	0.840	-0.090	0.771	-0.047	0.900	0.841	0.987	4.11
Pier Piles Curvature Ductility	-1.134	0.427	0.887	-0.189	0.195	-0.037	0.990	0.990	0.955	4.11
Abutment Piles Curvature Ductility	-1.354	0.553	0.789	-0.162	0.564	-0.028	0.984	0.957	0.905	4.11
Strain in Abutment Bearings	-0.880	0.394	0.664	-0.155	0.384	-0.070	0.986	0.998	0.953	4.10

Table 4.24: Fragility Surfaces Parameters for Post-1971 Continuous Bridges with Seat-type Abutments and Multi-Column Piers and 24” CISS Piles

Engineering Demand Parameter	**Parameters**						**Coefficient of Determination**			**Eq.**
	A	B	C	D	E	F	R^2_{λ}	R^2_{ξ}	$R^2_{\text{Prob.}}$	No.
Abutment Displacement (m)	0.485	0.750	0.163	-0.197	0.172	-0.260	0.966	0.952	0.984	4.10
Abutment Rotation (%)	1.343	0.542	0.144	-0.112	-0.544	-0.287	0.989	0.947	0.986	4.10
Pile Cap Displacement (m)	0.384	0.712	0.198	-0.234	0.015	-0.204	0.993	0.953	0.910	4.10
Pile Cap Rotation (%)	1.396	0.529	-0.007	-0.160	-0.440	-0.195	0.986	0.936	0.883	4.10
Pier Curvature Ductility	-1.543	0.458	0.797	-0.099	0.793	-0.046	0.929	0.781	0.990	4.11
Pier Piles Curvature Ductility	-1.035	0.611	0.935	-0.314	0.197	-0.019	0.936	0.917	0.736	4.11
Abutment Piles Curvature Ductility	-1.225	0.517	0.762	-0.149	0.726	-0.036	0.985	0.942	0.945	4.11
Strain in Abutment Bearings	-0.738	0.356	0.633	-0.126	0.528	-0.100	0.996	0.984	0.927	4.10

Table 4.25: Fragility Surfaces Parameters for Post-1971 Continuous Bridges with Seat-type Abutments and Single-Column Piers and 15” Precast Piles

Engineering Demand Parameter	**Parameters**						**Coefficient of Determination**			**Eq.**
	A	B	C	D	E	F	R^2_{λ}	R^2_{ξ}	$R^2_{\text{Prob.}}$	No.
Abutment Displacement (m)	0.588	0.812	0.196	-0.156	-0.027	-0.277	0.970	0.913	0.970	4.10
Abutment Rotation (%)	0.851	0.555	0.229	-0.073	-0.101	-0.212	0.998	0.866	0.955	4.10
Pile Cap Displacement (m)	0.576	0.832	0.214	-0.184	-0.080	-0.294	0.998	0.946	0.959	4.10
Pile Cap Rotation (%)	2.339	0.771	0.106	-0.114	-0.933	-0.328	0.981	0.584	0.983	4.10
Pier Curvature Ductility	-1.801	0.481	0.814	-0.065	0.892	-0.041	0.924	0.676	0.993	4.11
Pier Piles Curvature Ductility	-1.873	0.538	0.884	-0.119	0.730	-0.040	0.983	0.967	0.922	4.11
Abutment Piles Curvature Ductility	-2.065	0.451	0.727	-0.043	0.876	-0.022	0.992	0.951	0.983	4.11
Strain in Abutment Bearings	-0.857	0.435	0.703	-0.170	0.165	-0.040	0.994	0.990	0.960	4.10

Table 4.26: Fragility Surfaces Parameters for Post-1971 Continuous Bridges with Seat-type Abutments and Multi-Column Piers and 15” Precast Piles

Engineering Demand Parameter	**Parameters**						**Coefficient of Determination**			**Eq.**
	A	B	C	D	E	F	R^2_{λ}	R^2_{ξ}	$R^2_{\text{Prob.}}$	No.
Abutment Displacement (m)	0.604	0.803	0.182	-0.165	0.014	-0.290	0.968	0.942	0.983	4.10
Abutment Rotation (%)	0.932	0.573	0.226	-0.072	0.042	-0.200	0.995	0.873	0.923	4.10
Pile Cap Displacement (m)	0.282	0.727	0.250	-0.202	0.053	-0.284	0.985	0.954	0.936	4.10
Pile Cap Rotation (%)	0.792	0.375	0.171	-0.159	-0.152	-0.097	0.996	0.953	0.902	4.10
Pier Curvature Ductility	-1.709	0.493	0.804	-0.087	0.808	-0.028	0.904	0.880	0.997	4.11
Pier Piles Curvature Ductility	-1.807	0.557	0.899	-0.142	0.856	-0.044	0.991	0.972	0.968	4.11
Abutment Piles Curvature Ductility	-2.079	0.482	0.750	-0.059	0.948	-0.018	0.985	0.991	0.992	4.11
Strain in Abutment Bearings	-0.695	0.351	0.704	-0.176	0.179	-0.044	0.995	0.999	0.963	4.10

Table 4.27: Fragility Surfaces Parameters for Pre-1971 Continuous Bridges with Seat-type Abutments and Single-Column Piers and 15” Precast Piles

Engineering Demand Parameter	Parameters						Coefficient of Determination			Eq.
	A	B	C	D	E	F	R^2_{λ}	R^2_{ξ}	$R^2_{\text{Prob.}}$	No.
Abutment Displacement (m)	0.705	0.761	0.170	-0.165	-0.084	-0.164	0.989	0.771	0.774	4.10
Abutment Rotation (%)	1.779	0.876	0.205	-0.067	-0.434	-0.254	0.985	0.652	0.982	4.10
Pile Cap Displacement (m)	0.681	0.978	0.130	-0.217	-0.080	-0.229	0.988	0.858	0.858	4.10
Pile Cap Rotation (%)	2.843	0.932	0.494	-0.033	-0.766	-0.238	0.944	0.242	0.969	4.10
Pier Curvature Ductility	-2.477	0.535	0.774	-0.037	0.905	-0.038	0.895	0.543	0.998	4.11
Pier Piles Curvature Ductility	-2.390	0.543	0.878	-0.087	0.676	-0.038	0.988	0.861	0.917	4.11
Abutment Piles Curvature Ductility	-2.510	0.485	0.659	-0.026	0.709	-0.023	0.983	0.702	0.938	4.11
Strain in Abutment Bearings	-1.775	0.939	0.832	-0.174	0.177	-0.107	0.777	0.986	0.570	4.10

Table 4.28: Fragility Surfaces Parameters for Pre-1971 Continuous Bridges with Seat-type Abutments and Multi-Column Piers and 15” Precast Piles

Engineering Demand Parameter	Parameters						Coefficient of Determination			Eq.
	A	B	C	D	E	F	R^2_{λ}	R^2_{ξ}	$R^2_{\text{Prob.}}$	No.
Abutment Displacement (m)	0.708	0.745	0.156	-0.169	-0.089	-0.249	0.990	0.790	0.939	4.10
Abutment Rotation (%)	1.774	0.858	0.160	-0.080	-0.342	-0.280	0.981	0.826	0.975	4.10
Pile Cap Displacement (m)	0.280	0.824	0.275	-0.172	0.008	-0.300	0.997	0.956	0.927	4.10
Pile Cap Rotation (%)	0.800	0.428	0.180	-0.189	-0.058	-0.034	0.979	0.934	0.893	4.10
Pier Curvature Ductility	-2.191	0.565	0.734	-0.035	0.956	-0.021	0.906	0.700	0.988	4.11
Pier Piles Curvature Ductility	-2.336	0.584	0.837	-0.094	0.940	-0.044	0.986	0.942	0.987	4.11
Abutment Piles Curvature Ductility	-2.358	0.481	0.721	-0.053	0.909	-0.022	0.987	0.963	0.992	4.11
Strain in Abutment Bearings	-1.591	0.847	0.836	-0.194	0.247	-0.125	0.768	0.834	0.657	4.10

While evaluating the fragility of bridges requires establishing component-level damage models which relate the damage in a component to the mobilized demand in the other components, as well as establishing overall bridge-level damage models that integrate the damage in different components into an overall damage to the bridge, the trends of relative performance of different classes of bridges can be determined by comparing the fragility surfaces of different components within each class with other bridge classes. Some of the trends observed from the fragility surfaces presented here are summarized, as follows:

4.4.1 Effect of Vintage on the Fragility of the Bridge

Bridges built prior to 1971 have piers with poor transverse reinforcement and lower yield moment (and shear capacity) relative to the new vintage bridges. The relatively weak piers result in pier curvature ductility fragility surfaces that have a much higher probability of exceedance at almost all values of curvature ductility and free-field ground displacement relative to their newer vintage counterparts.

The older vintage bridges also tend to have poor quality piles that were not designed with much consideration for lateral load capacity. However, the effect of pile type on the foundation demand parameters is not evident for the pre-1971 bridges.

4.4.2 Effect of Structure Type on the Fragility of the Bridge

The differences in structure types in the classes analyzed here are divided in to the differences at the pier top and bottom connections and the differences in the type of abutments (monolithic vs. seat-type).

Piers of the simply-supported bridges are free about rotation (pinned) at the top of the pier. Consequently the top of the pier is not a moment-bearing connection and the piers are more flexible relative to a continuous bridge with double fixity (i.e single-column) at the top and bottom connections. This flexibility in bridges with simply-supported superstructures results in decreased curvature demand in the piers of the bridge, relative to the bridges with doubly-fixed continuous superstructure.

However, the flexibility of the pier has the negative effect of allowing for more pile cap displacements and rotations and abutment displacements and rotations, which subsequently causes additional demand in the piles supporting both the pile caps and the abutment walls.

As a result, while the simply-supported bridges tend to perform better at the pier and superstructure level, they perform more poorly at the foundation level relative to the continuous bridges with doubly-fixed piers. Therefore, the overall relative fragility of the bridges based on structural configuration, depends on the component-level and bridge-level damage models (i.e. whether damage to piers is more/less acceptable than damage to the foundation).

Continuous bridges with multi-column bents unlike continuous bridges with single-column piers are designed with a pin connection at the pile cap level. As a result, while continuous bridges with multi-column bents have moment-bearing connections at the superstructure level, their connection at the pile cap is free about rotation. Therefore, these types of piers are less stiff (more flexible) which mobilize less curvature demand at the pier level, but allow for more displacements at the foundation level.

The fragility surfaces between two classes of continuous bridges with monolithic and seat-type abutments are similar except at the abutments. Typically seat-type abutments allow for more displacements because in cases where the back-wall breaks due to lateral displacements at the abutments, barely any pinning resistance is provided by the superstructure of the bridge to the stem-wall at the abutments and thus, the stem-wall could displace more freely, especially if the supporting piles at the abutments are significantly damaged. Seat-type abutments in simply-supported bridges also allow for more displacements at the abutments.

4.4.3 Effect of Number of Columns per Pier on the Fragility of the Bridge

As stated in Chapter 3, the bridges with multiple column piers tend to have a modest increase in their yield moment capacity (and also shear capacity) relative to the bridges with single column piers.

As a result, in simply-supported bridges that have single-fixity in piers, it is expected that the piers of the bridges with multi-column bents would perform slightly better than their single-column counterparts in terms of the mobilized curvature ductility. This effect is evident by comparing of the bridges in classes that are the same except in the number of columns per piers (e.g., by comparing Figs. 4.5 and 4.6). However, more damage in one component usually translates to less damage in the other components. Therefore, among simply-supported bridges while bridges with multi-column bents tend to have better performance in piers, they have an increased demand in almost every other component of the bridge. Consequently, the fragility surfaces for components in the foundation (e.g., pile cap displacement and rotation) and the abutments (e.g., abutment displacement and rotation) in multi-column piers are higher than the fragility surfaces of single-column piers, because they are transferring more demand to those components.

For Continuous bridges, since multi-columns piers are designed with a pinned connection at pile cap and therefore are more flexible (less stiff), they resist less demand at the pier and allow for more displacements of the pile caps. However, since the connection at the pile cap is free about rotation, the rotation of the pier does not translate very effectively to the pile cap. Consequently for multi-column piers while pile cap displacements are generally larger than for the single-columns, the rotations are typically smaller.

On the other hand, even though continuous bridges have double-fixity in single-column piers and single-fixity in the multi-column bents, due to excessive displacements of the pile cap, the mobilized curvature ductility is often higher in multi-column bents than in single-column piers. Thus, multi-column continuous bridges are more fragile than the single-column continuous bridges, regardless of their abutment type.

4.4.4 Effect of Pile Types on the Fragility of the Bridge

The effect of the pile type is most clear for the classes of the bridges with 24"CISS piles. The bridges with 24"CISS piles exhibited significantly lower curvature demands in the piles due to the high flexural capacity introduced by the steel shell. As a result, these piles also provided significant reductions in displacements and rotations at the pile caps and abutments.

The 24” CIDH piles also provided some marginal improvement over the 15” precast piles, but the improvement in performance is not very large. The cause of this small increment in improvement is that the 24" CIDH piles still exhibited considerable yielding in response to the lateral spreading demands. This indicates that (1) increasing pile capacity may provide little return on investment if the piles still yield and displace with the ground, (2) increasing pile capacity may provide significant improvements in performance if the piles can withstand the lateral spreading demands without significant yielding, and (3) increasing pile capacity beyond the 24" CISS piles could provide a large increment of improvement for bridge performance.

4.5 Correlation Tables

It is intuitive that demand in one component of a bridge would be correlated to demand in other components. For example, pile cap displacement would be correlated with pile cap rotation and with demand in the piles supporting the pile group. Correlation can also be more indirect, wherein demands in one component are transferred to another component by axial stresses in the superstructure. Quantifying the correlation among EDPs is important for appropriately preserving the statistics of the analyses when the demand fragility surfaces are used.

Correlation coefficients were computed from the sample of EDP values at a free-field ground displacement of 0.8*m* for each class of bridge. The coefficients were found to be basically independent of vintage and pile type. However, the correlation coefficients between the different EDPs were different for different structural types of bridges, because the load transfer between different components of the bridge depends on the way the loads are transferred among different components of the bridge. For continuous bridges, since the connection of the pier to the pile cap for multi-column bents is different (i.e. pinned) from single-column piers (i.e. fixed), the load transfer among components are different for single-column and multi-column piers. Tables 4.29 and 4.30 show the correlation tables for the continuous bridges with monolithic abutments with single-column and multi-column piers, respectively, while Tables 4.31 and 4.32 show the correlation tables for the continuous bridges with seat-type abutments with single-column and multi-column piers, respectively.

Since the connection type of the piers for the simply-supported bridges is the same for the single-column and multi-column piers the correlation tables of single-column and multi-column piers are essentially the same and is shown in a single table (Table 4.33).

Low values of correlation coefficient (i.e. those with absolute value less than 0.3) were set to zero based on the observation that small random samples of uncorrelated variables may still exhibit some correlation despite the fact that the population of the variables is uncorrelated.

Table 4.29: Correlation Tables for Continuous Bridges with Monolithic Abutments and Single-Column Piers

	Abutment Disp.	**Abutment Rotation**	**Cap Disp.**	**Cap Rotation**	**Pier Curvature Ductility**
Abutment Disp.	**1**	**0.45**	**0.6**	**0.6**	**0.35**
Abutment Rotation	**0.45**	**1**	**0**	**0**	**0**
Cap Disp.	**0.6**	**0**	**1**	**0.7**	**0.4**
Cap Rotation	**0.6**	**0**	**0.7**	**1**	**0.5**
Pier Curvature Ductility	**0.35**	**0**	**0.4**	**0.5**	**1**

Table 4.30: Correlation Tables for Continuous Bridges with Monolithic Abutments and Multi-Column Piers

	Abutment Disp.	**Abutment Rotation**	**Cap Disp.**	**Cap Rotation**	**Pier Curvature Ductility**
Abutment Disp.	**1**	**0.45**	**0.45**	**0**	**0**
Abutment Rotation	**0.45**	**1**	**0**	**0**	**0**
Cap Disp.	**0.45**	**0**	**1**	**0.50**	**0.45**
Cap Rotation	**0**	**0**	**0.50**	**1**	**0**
Pier Curvature Ductility	**0**	**0**	**0.45**	**0**	**1**

Table 4.31: Correlation Tables for Continuous Bridges with Seat-Type and Single-Column Piers

	Abutment Disp.	**Abutment Rotation**	**Cap Disp.**	**Cap Rotation**	**Pier Curvature Ductility**	**Abutment Bearing Strain**
Abutment Disp.	**1**	**0**	**0.50**	**0.50**	**0**	**0.80**
Abutment Rotation	**0**	**1**	**0**	**0**	**0**	**0**
Cap Disp.	**0.50**	**0**	**1**	**0.65**	**0.35**	**0**
Cap Rotation	**0.50**	**0**	**0.65**	**1**	**0.50**	**0**
Pier Curvature Ductility	**0**	**0**	**0.35**	**0.50**	**1**	**0**
Abutment Bearing Strain	**0.80**	**0**	**0**	**0**	**0**	**1**

Table 4.32: Correlation Tables for Continuous Bridges with Seat-Type and Multi-Column Piers

	Abutment Disp.	**Abutment Rotation**	**Cap Disp.**	**Cap Rotation**	**Pier Curvature Ductility**	**Abutment Bearing Strain**
Abutment Disp.	**1**	**0**	**0.40**	**0**	**0**	**0.75**
Abutment Rotation	**0**	**1**	**0**	**0**	**0**	**0**
Cap Disp.	**0.40**	**0**	**1**	**0.50**	**0.45**	**0**
Cap Rotation	**0**	**0**	**0.50**	**1**	**0**	**0**
Pier Curvature Ductility	**0**	**0**	**0.45**	**0**	**1**	**0**
Abutment Bearing Strain	**0.75**	**0**	**0**	**0**	**0**	**1**

Table 4.33: Correlation Tables for the Simply-Supported Bridges with Seat-Type Abutments

	Abutment Disp.	**Abutment Rotation**	**Cap Disp.**	**Cap Rotation**	**Pier Curvature Ductility**	**Abutment Bearing Strain**	**Pier Bearing Strain**
Abutment Disp.	**1**	**0.35**	**0**	**0**	**0**	**0.7**	**0**
Abutment Rotation	**0.35**	**1**	**0**	**0**	**0**	**0**	**0**
Cap Disp.	**0**	**0**	**1**	**0.5**	**0.35**	**0**	**0.65**
Cap Rotation	**0**	**0**	**0.5**	**1**	**0**	**0**	**0**
Pier Curvature Ductility	**0**	**0**	**0.35**	**0**	**1**	**0**	**0**
Abutment Bearing Strain	**0.7**	**0**	**0**	**0**	**0**	**1**	**0**
Pier Bearing Strain	**0**	**0**	**0.65**	**0**	**0**	**0**	**1**

As can be seen in Table 4.29 most of the EDPs are correlated with each other for continuous bridges with single-column piers, which depicts that the demands are transferred from one component and one EDP to other ones, especially once the ground displacement increases. By comparing Tables 4.29 and 4.30, it is evident that correlations are weaker for continuous bridges with multi-columns since the connection at the pile cap is pinned and the load transfer does not occur between the pier foundation elements, as effectively. Another interesting feature of Table 4.30 is that rotation of the pile caps is basically uncorrelated to abutment displacements and curvature ductilities in the piers, since the rotation of the pier does not cause rotation of the pile cap since the connection is pinned.

Tables 4.31 and 4.32 show the same trend for the continuous bridges with seat-type abutments as the continuous bridges with monolithic abutments (Tables 4.29 and 4.30). Just as in continuous bridges with monolithic abutments, the correlation coefficients become weaker for bridges with multi-column bents for the continuous bridges with seat-type abutments.

As can be seen in Table 4.33, for the simply-supported bridges many of the EDPs have low correlation coefficients (shown as zero, here), which means that they are uncorrelated. This is an interesting feature of the simply-supported bridges. What it implies is that in simply-supported bridge, especially in the ones supported on bearing at the top of the piers, the damage in one component does not translate to the other components as effectively as in continuous bridges.

Correlation coefficients were found to depend on the level of ground displacement selected. Tables 4.34 through 4.35 show how the correlation coefficients vary for the Post-1971 simply-supported bridges with seat-type abutments and single-column piers supported on 24” CIDH piles and the Post-1971 continuous bridges with monolithic abutments and single-column piers supported on 24” CIDH piles . The correlation coefficients generally increase with an increase in free-field ground displacement. For example, pier curvature ductility is uncorrelated with pile cap displacement when the free-field ground displacement is only 0.2*m*, probably because very few piers yielded at this low demand level and inertia force played an important role. However, the correlation coefficient increases to 0.4 when the ground displacement reaches 0.8*m*, indicating that the increased demand has caused more of the piers to yield due to large foundation displacements. An interesting feature in Table 4.34 is the increasing correlation between abutment displacements and strains in the abutment bearings as the ground displacement increases. The abutment displacements are almost uncorrelated with abutment bearings strains at low displacements, since low free-field ground displacements have not yet closed the gap between the superstructure and abutment backwall, and strain in the bearings is dominated by inertia forces. However, larger free-field ground displacements cause the gap to close, eventually breaking the abutment backwall and causing the stemwall to displace beneath the superstructure, thereby inducing strain in the bearings. Hence, strain in the bearings becomes closely correlated with abutment stemwall displacement at large free-field ground displacements.

Table 4.34: The correlation tables for the Post-1971 simply-supported bridges with seat-type abutments and single column piers supported on 24” CIDH piles

Ground Displacement: 0.2

	Abutment Disp.	Abutment Rot.	Cap Disp.	Cap Rot.	Pier Curvature Ductility	Abutment Bearing Strain	Pier Bearing Strain
Abutment Disp.	1	0.405	0	0	0	0.364	0
Abutment Rot.	0.405	1	0	0	0	0	0
Cap Disp.	0	0	1	0.491	0	0	0.559
Cap Rot.	0	0	0.491	1	0	0	0
Pier Curvature Ductility	0	0	0	0	1	0	0
Abutment Bearing Strain	0.364	0	0	0	0	1	0
Pier Bearing Strain	0	0	0.559	0	0	0	1

Ground Displacement: 0.5

	Abutment Disp.	Abutment Rot.	Cap Disp.	Cap Rot.	Pier Curvature Ductility	Abutment Bearing Strain	Pier Bearing Strain
Abutment Disp.	1	0.393	0	0	0	0.698	0
Abutment Rot.	0.393	1	0	0	0	0	0
Cap Disp.	0	0	1	0.504	0.338	0	0.646
Cap Rot.	0	0	0.504	1	0	0	0
Pier Curvature Ductility	0	0	0.338	0	1	0	0
Abutment Bearing Strain	0.698	0	0	0	0	1	0
Pier Bearing Strain	0	0	0.646	0	0	0	1

Ground Displacement: 0.8

	Abutment Disp.	Abutment Rot.	Cap Disp.	Cap Rot.	Pier Curvature Ductility	Abutment Bearing Strain	Pier Bearing Strain
Abutment Disp.	1	0.305	0	0	0	0.76	0
Abutment Rot.	0.305	1	0	0	0	-0.312	0
Cap Disp.	0	0	1	0.5	0.394	0	0.724
Cap Rot.	0	0	0.5	1	0	0	0
Pier Curvature Ductility	0	0	0.394	0	1	0	0
Abutment Bearing Strain	0.76	-0.312	0	0	0	1	0
Pier Bearing Strain	0	0	0.724	0	0	0	1

Table 4.35: The correlation tables for the Post-1971 conntinuous bridges with monolithic abutments and single column piers supported on 24” CIDH piles

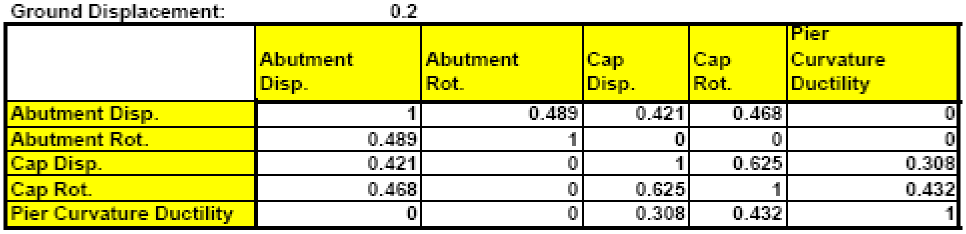

Ground Displacement: 0.2

	Abutment Disp.	Abutment Rot.	Cap Disp.	Cap Rot.	Pier Curvature Ductility
Abutment Disp.	1	0.489	0.421	0.468	0
Abutment Rot.	0.489	1	0	0	0
Cap Disp.	0.421	0	1	0.625	0.308
Cap Rot.	0.468	0	0.625	1	0.432
Pier Curvature Ductility	0	0	0.308	0.432	1

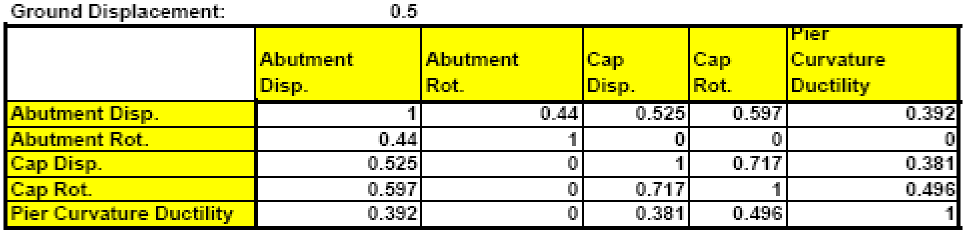

Ground Displacement: 0.5

	Abutment Disp.	Abutment Rot.	Cap Disp.	Cap Rot.	Pier Curvature Ductility
Abutment Disp.	1	0.44	0.525	0.597	0.392
Abutment Rot.	0.44	1	0	0	0
Cap Disp.	0.525	0	1	0.717	0.381
Cap Rot.	0.597	0	0.717	1	0.496
Pier Curvature Ductility	0.392	0	0.381	0.496	1

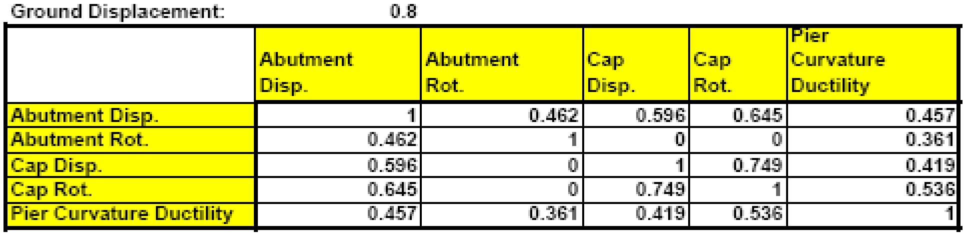

Ground Displacement: 0.8

	Abutment Disp.	Abutment Rot.	Cap Disp.	Cap Rot.	Pier Curvature Ductility
Abutment Disp.	1	0.462	0.596	0.645	0.457
Abutment Rot.	0.462	1	0	0	0.361
Cap Disp.	0.596	0	1	0.749	0.419
Cap Rot.	0.645	0	0.749	1	0.536
Pier Curvature Ductility	0.457	0.361	0.419	0.536	1

4.6 Disaggregation of Input Parameters

In order to evaluate the relative importance of the input parameters in the performance of the bridge, the ground displacements required to exceed an EDP value for a certain engineering demand parameter can be plotted versus the values of each of the input parameters in the analyses. Figure 4.29 shows an example of dissagregation of input parameters for the general class of post-1971 simply-supported bridges. In this case, the ground displacement required to reach or exceed curvature ductility of 7 in the piers, is plotted on the y-axes. As can be seen in the figure, the trend lines of the free-field displacements versus the input parameters are more or less flat, which means that the median value of free-field displacement is essentially insensitive to the values within the range specified by the distribution of the input parameters. While the disaggregation results vary from one class to another, and also vary depending on what EDP is investigated and at what value of the EDP the disaggregation is performed, there is not a parameter with a very strong trend in the input parameters. This is partly due to the fact that the Monte Carlo analyses are performed with many input parameters that may counter balance each other, and partly due to the fact that the ground displacement patterns are essentially random, and different types of spreading patterns apply different levels of damage to different components of the bridge and therefore the response of the bridge is strongly related to the spreading demand pattern being applied.

Based on the information presented in this chapter, it is evident that the relative performance of different components of the bridge depends on the class of the bridge (e.g. simply-supported bridges have more abutment displacements and pile cap displacements relative to the continuous bridge, while the continuous bridges have more fragile piers). However, the overall fragility of the bridge depends on the acceptable levels of damage for different components of the bridge, since it is clear from the demand fragility surfaces that for all classes of bridges analyzed here, significant damage is expected in some of the components. The evaluation of the overall fragility of the bridge requires having damage models that quantify the level of damage on the demand level mobilized in every component.

4.7 Example of Application of Fragility Surfaces

This section demonstrates how the performance-based earthquake engineering can be applied to predict liquefaction-induced damage to bridges. An example problem consisting of a site with a corresponding seismic hazard curve and disaggregation is combined with a liquefiable soil profile to compute a hazard curve defining mean annual rate of exceedance of lateral spreading ground displacement. The ground displacement hazard curve is combined with the fragility functions generated in this dissertation, to compute mean annual rate of exceedance of various bridge engineering demand parameters due to liquefaction and lateral spreading.

4.7.1 Site and Seismic Hazard Analysis

A site in Santa Monica, CA, (118.492°W, 34.015°N) was selected for this example problem. This is the same Santa Monica site analyzed by Kramer and Mayfield (2007), which provides a convenient means of validating the liquefaction hazard curve with their results. A probabilistic seismic hazard analysis was performed using OpenSHA (Field et al. 2003), with Vs_{30} = 300 m/s. The seismic hazard curve and magnitude disaggregation are shown in Figures 4.30 and 4.31. The soil profile at the site consists of a 2*m* thick nonliquefied crust with unit weight $\gamma = 18$ kN/m^3 lies over a clean liquefiable sand with $(N_1)_{60} = 10$. The ground gently slopes at an angle of $\beta = 2°$ and can be reasonably represented as an infinite slope.

4.7.2 Liquefaction Triggering Evaluation

The next step in the analysis is computing the annual rate of exceedance of triggering of liquefaction. To simplify, the mean hazard curve from Figure 4.30 will be used. Kramer and Mayfield (2007) outlined a framework for computing annual rate of non-exceedance of liquefaction that is adopted in this study. The approach is based on the probabilistic liquefaction triggering framework developed by Cetin et al. (2004), using the regression constants that account for measurement/estimation errors. Eq. 4.12 defines probability of factor of safety against liquefaction (FS_L) dropping below a value (FS_L^*) given $(N_1)_{60}$, fines content FC cyclic stress ratio CSR_{eq} moment magnitude M_w and vertical effective stress σ_{vo}'.

$$P\left[FS_L < FS_L^* \mid PGA, M_w\right] = \Phi\left[-\frac{(N_1)_{60}(1+0.004FC) - 13.79\ln CSR_{eq} - 29.06\ln M_w - 3.82\ln(\sigma_{vo}^{'}/p_a) + 0.06FC + 15.25}{4.21}\right] \tag{4.12}$$

The cyclic stress ratio is defined as $CSR_{eq} = 0.65(PGA/g)(\sigma_v/\sigma_{vo}')r_d$, where the stress reduction factor r_d was treated deterministically (Golesorkhi 1989). Uncertainty in r_d is anticipated to have negligible effect on the hazard analysis since the site is so shallow and r_d is near unity. Peak horizontal ground acceleration (PGA) is not sufficient to characterize liquefaction triggering, and magnitude appears as well due to the influence of duration and frequency content. Hence, the hazard calculation must be integrated over PGA and M_w, which requires the disaggregation shown in Figure 4.31. Eq. 4.13 defines the probability of non-exceedance of factor of safety against liquefaction, where the summations indicate discrete numerical integration over an adequate range of PGA and M_w values using the binning method wherein the probability density functions are divided into small slices for numerical integration (after Kramer and Mayfield 2007).

$$\Lambda_{FS_L^*} = \sum_{j=1}^{N_{M_w}} \sum_{i=1}^{N_{PGA}} P\left[FS_L < FS_L^* \mid PGA_i, M_{w_j}\right] \Delta\lambda_{PGA,M_w} \tag{4.13}$$

Figure 4.32 shows the mean annual rate of non-exceedance of factor of safety against liquefaction, which is similar to the Santa Monica site presented by Kramer and

Mayfield (see Fig. 9 in their paper). The return period for $FS_L<1$ is about 100 years (i.e. $\Lambda=0.01\ yr^{-1}$).

4.7.3 Ground Displacement Evaluation

The next step in the procedure is computing the mean annual rate of exceedance of lateral spreading ground displacement for this site. A number of methods for estimating lateral spreading displacements exist, and including multiple approaches is important for quantifying the effects of epistemic uncertainty. However, for simplicity only a single approach is utilized in this paper, though the methodology can easily be extended to other methods. The approach by Bray and Travasarou (2007) for computing permanent ground displacements is combined with the approach by Olson and Stark (2002) for estimating undrained residual strength of liquefied sand. For $(N_1)_{60}$ = 10, the mean value of $s_r/\ {}_v$’ = 0.1 based on the Olson and Stark suggestion, hence ${}_{sr}$ = $0.1(2m)(18kN/m^3) = 3.6kPa$. Furthermore, the standard deviation is ${}_{sr}$ = $0.025(2m)(18kN/m^3) = 0.9kPa$. The static driving shear stress is ${}_{stat}$ = $(2m)(18kN/m^3)\sin(2°) = 1.3kPa$. If the static driving shear stress exceeds the undrained residual strength, then a flow slide occurs and ground displacement is large. Assuming that s_r is log-normally distributed, the probability of a flow slide can be computed using Eq. 4.14, where □ is the standard normal cumulative distribution function.

$$P\left[FlowSlide\,|\,Liq\right]=\Phi\left[\frac{\ln\tau_{stat}-\ln s_r}{\sqrt{1-\frac{\sigma_{sr}{}^2}{\mu_{sr}{}^2}}}\right] \tag{4.14}$$

For cases when a flow slide does not occur, the lateral spreading ground displacement is be computed using the methodology of Bray and Travasarou (2007) defined in Eq. 4.15, where k_y is the yield acceleration. For an infinite slope, $k_y = (s_r - \tau_{stat})/\gamma H\cos\beta$.

$$\begin{aligned} &P(D=0)=1-\Phi\left(-1.76-3.22\ln(k_y)+3.52\ln(PGA)\right) \\ &P(D>d\,|\,D>0)=1-\Phi\left(\frac{\ln(d)-\ln(\hat{d})}{0.66}\right) \\ &\ln(\hat{d})=-0.22-2.83\ln(k_y)-0.333(\ln(k_y))^2+0.566\ln(k_y)\ln(PGA) \\ &\qquad +3.04\ln(PGA)-0.244(\ln(PGA))^2+0.278(M_w-7) \end{aligned} \tag{4.15}$$

The probability of lateral spreading ground displacement exceeding some value, *d*, conditioned on the occurrence of liquefaction is given in Eq. 4.16, where the summation indicates numerical integration by the binning method over the random variable k_y, which depends on random variable s_r.

$$\begin{aligned} &P(D>d\,|\,Liq)=\sum_{i=1}^{N_{ky}}[1-P(D=0)][P(D>d\,|\,D>0)][1-P(FlowSlide\,|\,Liq)]\Delta k_y + \\ &P(FlowSlide\,|\,Liq) \end{aligned} \tag{4.16}$$

The mean annual rate of exceedance of free-field lateral spreading ground displacement is computed by inserting the conditional probability defined in Eq. 4.16

in the hazard integral, as defined in Eq. 4.17.

$$\lambda_D = \sum_{j=1}^{N_M} \sum_{i=1}^{N_{PGA}} P(D > d \mid Liq) P(Liq \mid PGA, M_w) \Delta\lambda_{PGA,M_w} \tag{4.17}$$

Figure 4.33 shows the lateral spreading ground displacement hazard curve for the example problem, which was computed using 30 bins for PGA and k_y, and 17 bins for magnitude, for a total of 15,300 computations. Also shown in Figure 4.33 are several values of ground displacement computed deterministically by taking the PGA associated with some hazard level combined with the modal magnitude (M_w = 6.5 in this case), mean k_y value, and mean lateral spreading displacement value computed using Eq. 4.15. In this case the deterministic approach underestimates the true ground displacement hazard primarily because (1) the modal magnitude was used and higher magnitudes contribute to larger displacements according to a nonlinear relation, and (2) the mean value of the liquefied undrained strength was used and lower undrained strengths produce larger displacements according to a nonlinear relation. Kramer and Mayfield (2007) also showed how inconsistencies between the probabilistic and deterministic approaches to liquefaction triggering evaluation arise due to nonlinearities in the equations, and the mismatch depends on the slope of the hazard curve. These observations indicate that the return period associated with a design level ground motion may not be the same as the return period for a deterministically-computed engineering response parameter, and utilizing the performance-based approach is the only way to provide consistency.

4.7.4 Bridge Engineering Demand Parameter Evaluation

Example demand fragility surfaces are shown in Figure 4.34 for bridges constructed after 1971 with simply-supported spans, seat-type abutments, and 24” Cast in Drilled Hole deep foundations supporting the pile caps and abutments.

The conditional probabilities defined in the demand fragility surfaces were inserted into the hazard integral to define the mean annual rate of exceedance of the three EDP values (Eq. 4.18).

$$\lambda_{EDP} = \sum_{j=1}^{N_M} \sum_{i=1}^{N_{PGA}} P(EDP > edp \,|\, D) P(D > d \,|\, Liq) P(Liq \,|\, PGA, M_w) \Delta\lambda_{PGA,M_w} \tag{4.18}$$

The EDP hazard curves are plotted in Figure 4.35. The 10% in 50 year EDP values (λ = 2.1x10^{-3} yr^{-1} and return period = 475yr) are pile cap displacement = 0.18*m*, the pier column remains elastic, and abutment displacement = 0.15*m*. These EDP hazard curves provide for better decision-making compared with the standard-of-practice approach of selecting a probabilistic ground motion and performing engineering calculations deterministically.

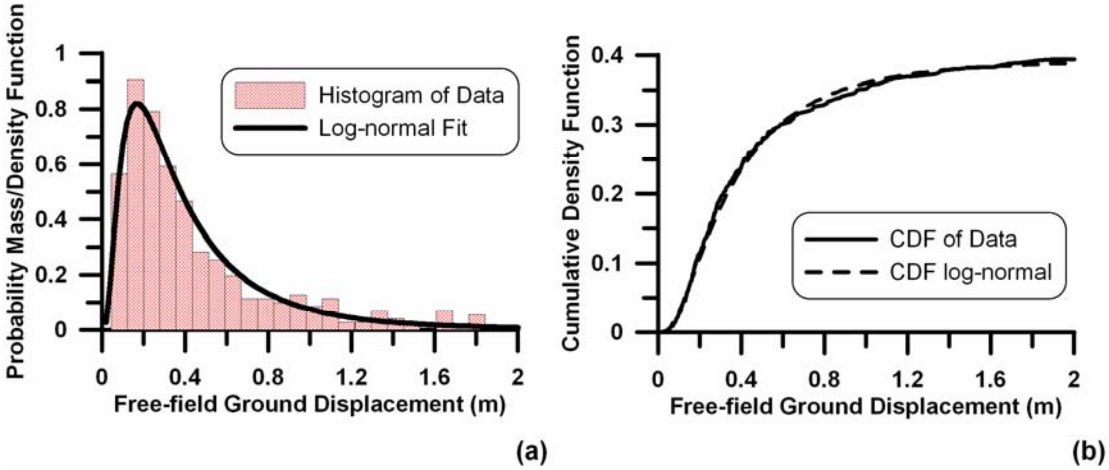

Figure 4.1: Generation of fragility function for pier curvature ductility of 7, for post-1971 simply-supported bridges with seat-type abutments and single-column piers, (a) probability mass function; (b) cumulative density function

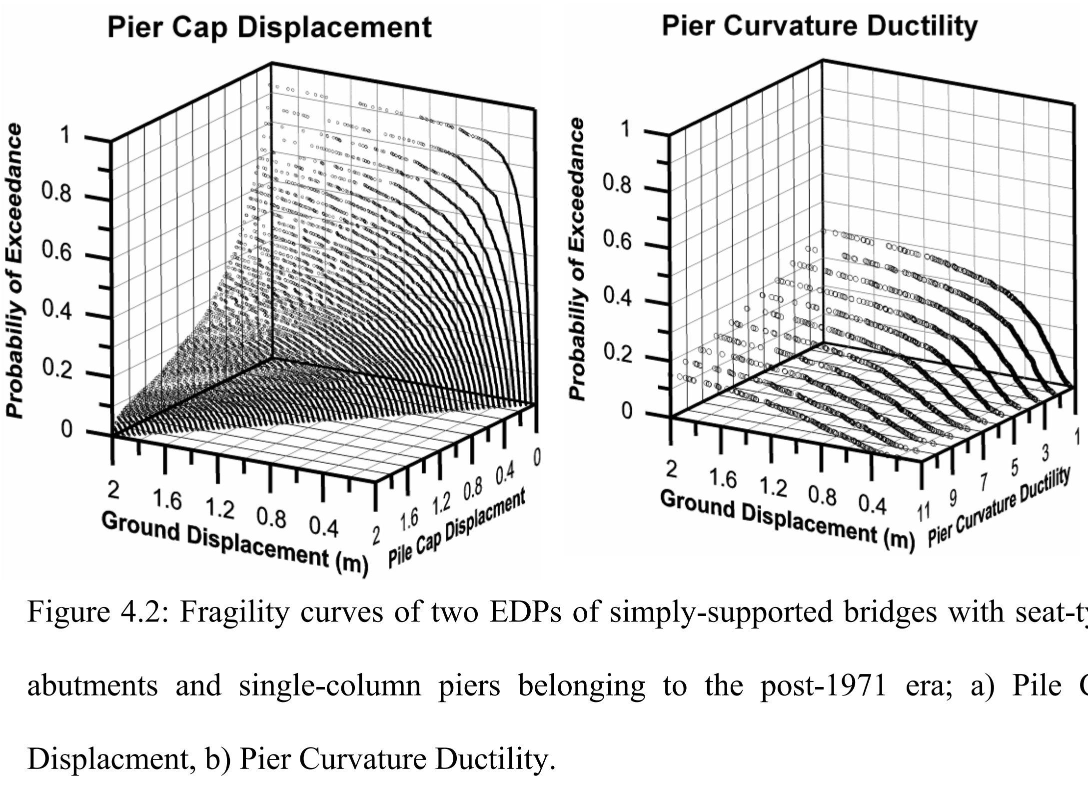

Figure 4.2: Fragility curves of two EDPs of simply-supported bridges with seat-type abutments and single-column piers belonging to the post-1971 era; a) Pile Cap Displacment, b) Pier Curvature Ductility.

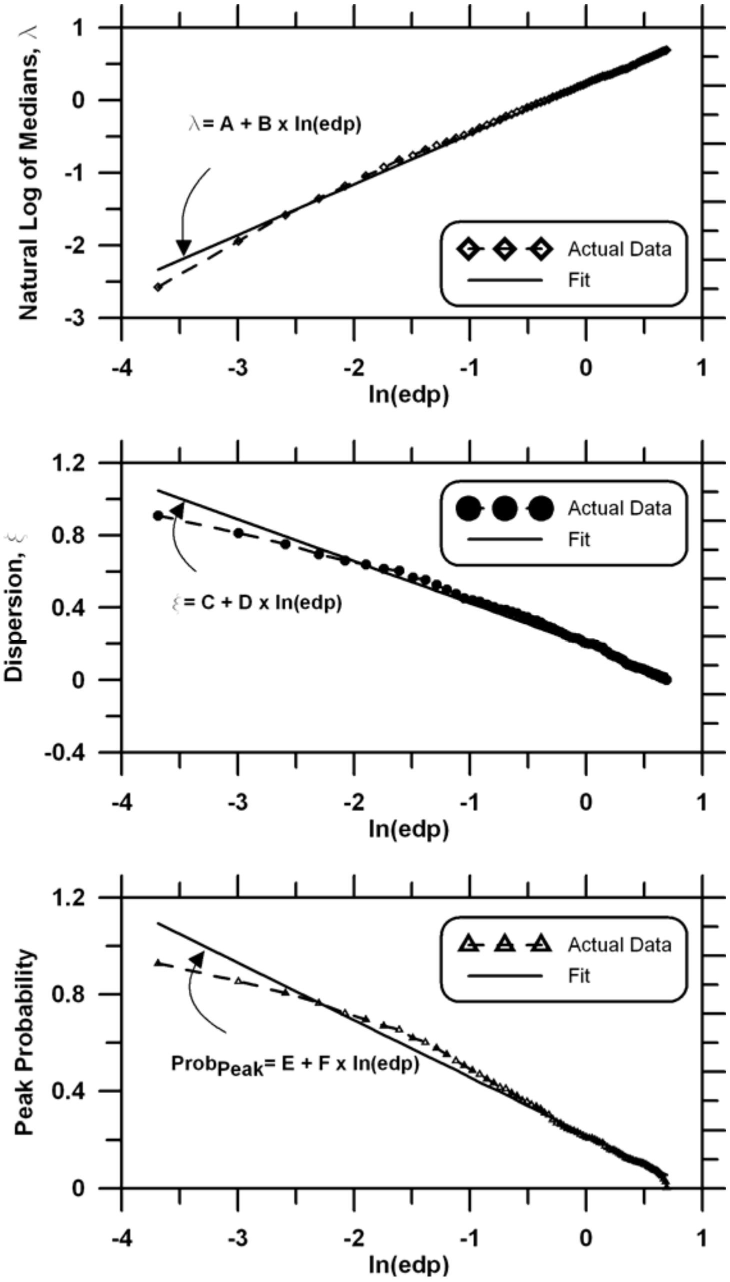

Figure 4.3: Linear regression of the values of fragility curve parameters; a) Logarithm of Medians, b) Dispersion (standard deviation of logarithms of data), c) Maximum probability for simply-supported bridges with seat-type abutments and single-column piers belonging to the post-1971

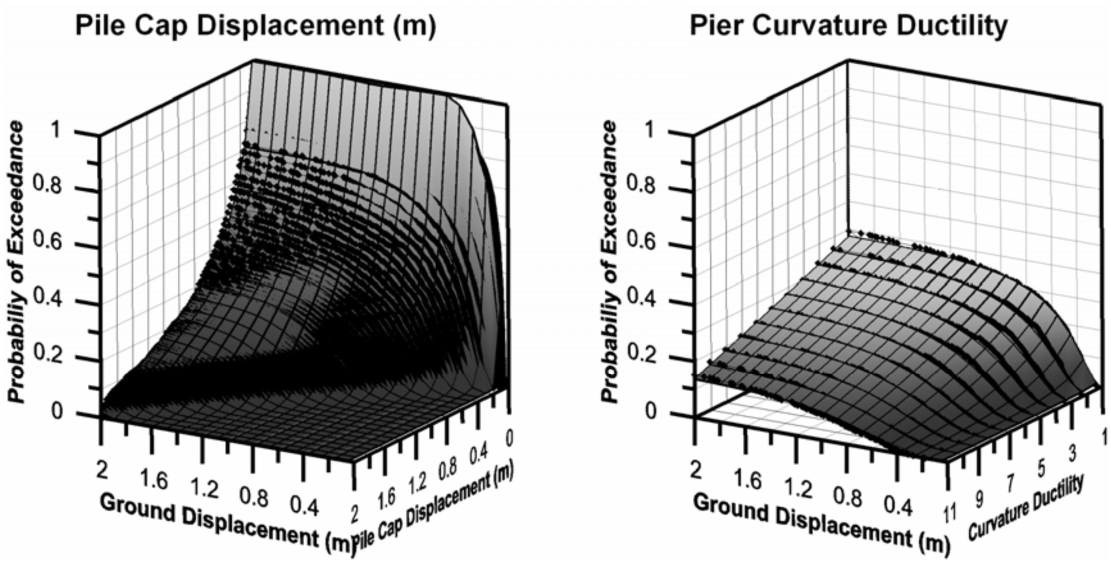

Figure 4.4: Demand fragility surfaces plotted along with the discreet date for, (a) Pile Cap Displacement, (b) Pier Curvature Ductility, for simply-supported bridges with seat-type abutments and single-column piers belonging to the post-1971

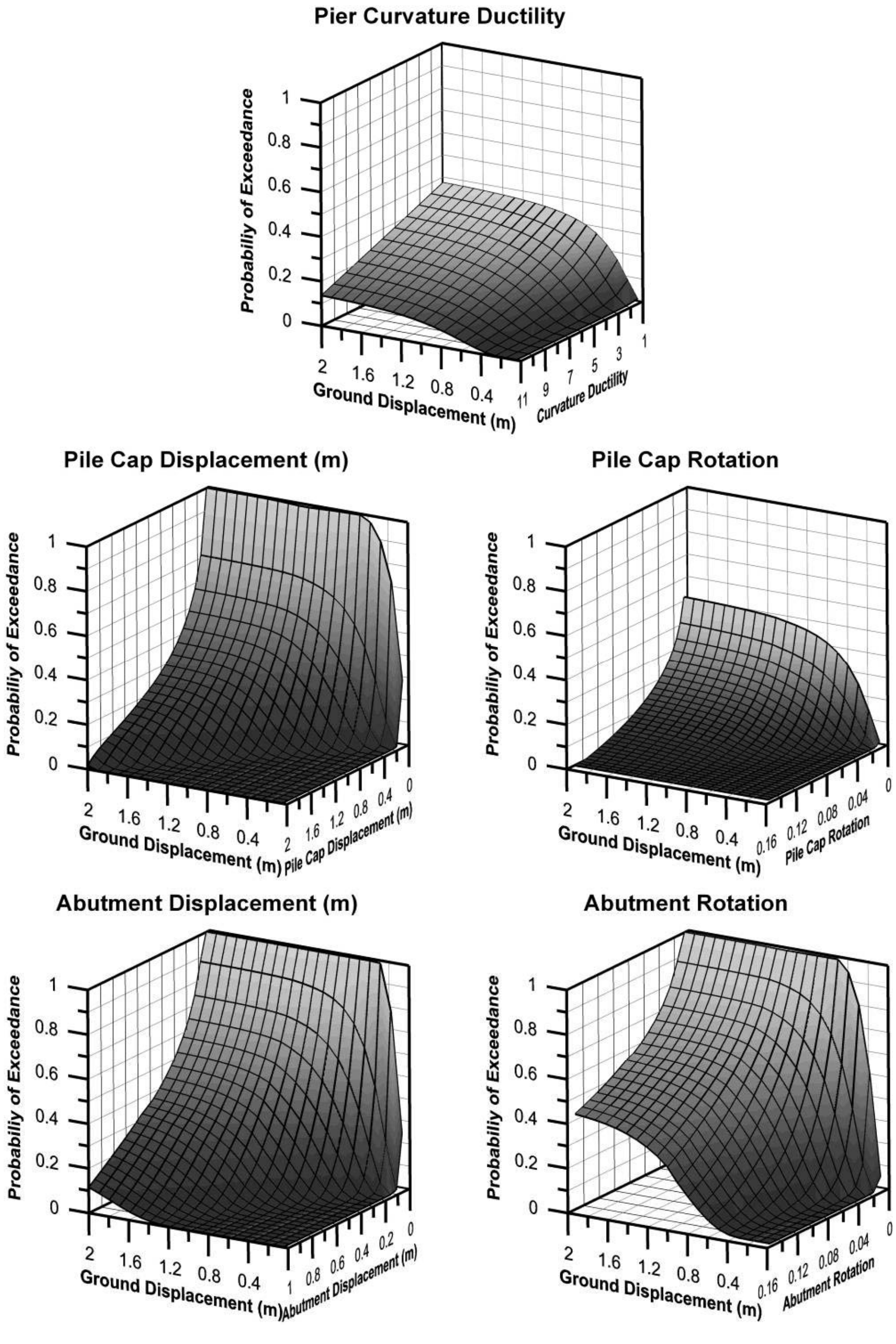

Figure 4.5: Fragility Surfaces for Post-1971 Simply-Supported Bridges with Seat-type Abutments and Single-Column Piers and 24” CIDH piles

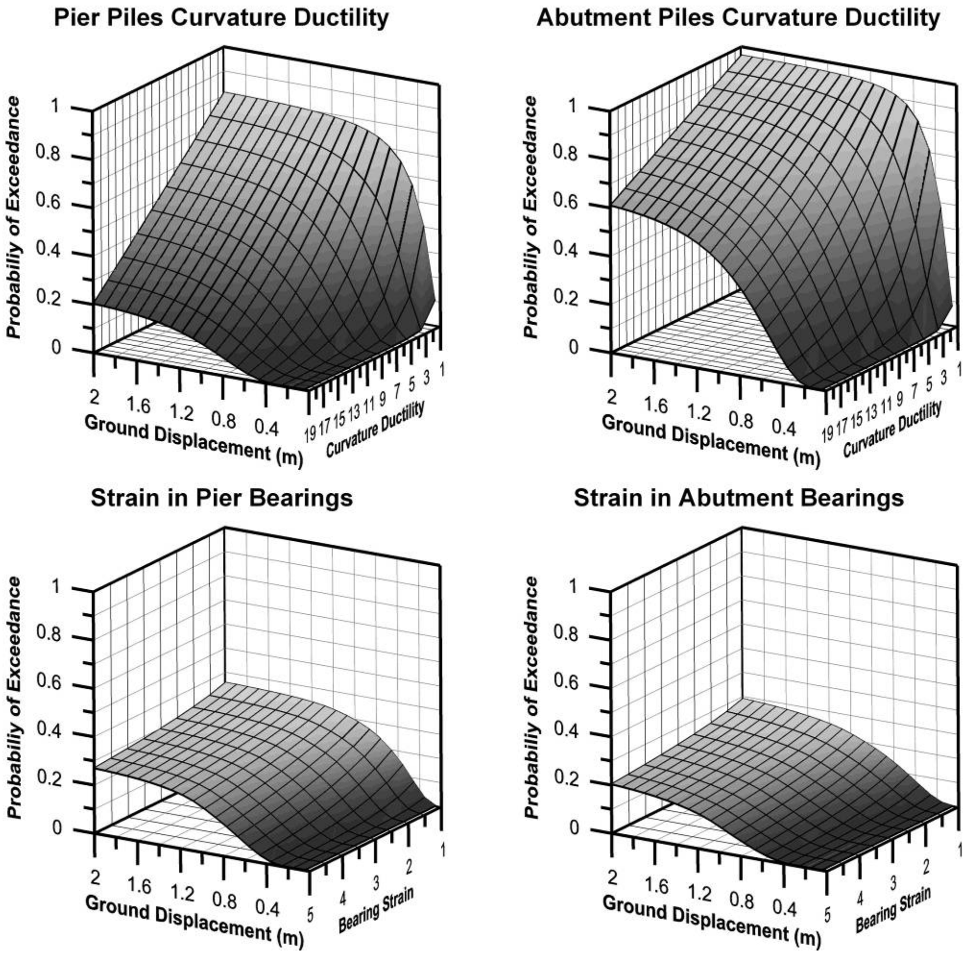

Figure 4.5: - Continued

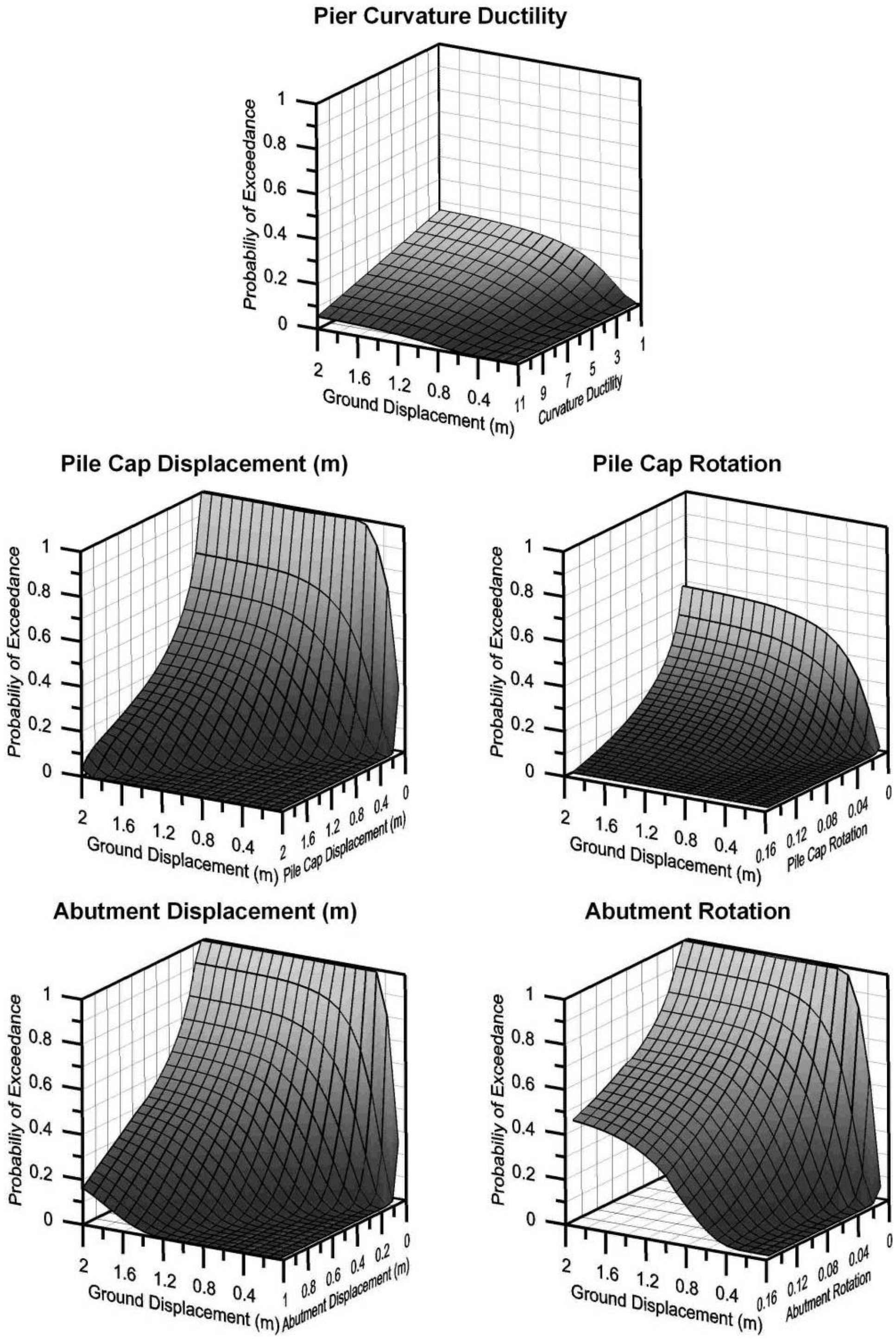

Figure 4.6: Fragility Surfaces for Post-1971 Simply-Supported Bridges with Seat-type Abutments and Multi-Column Piers and 24” CIDH piles

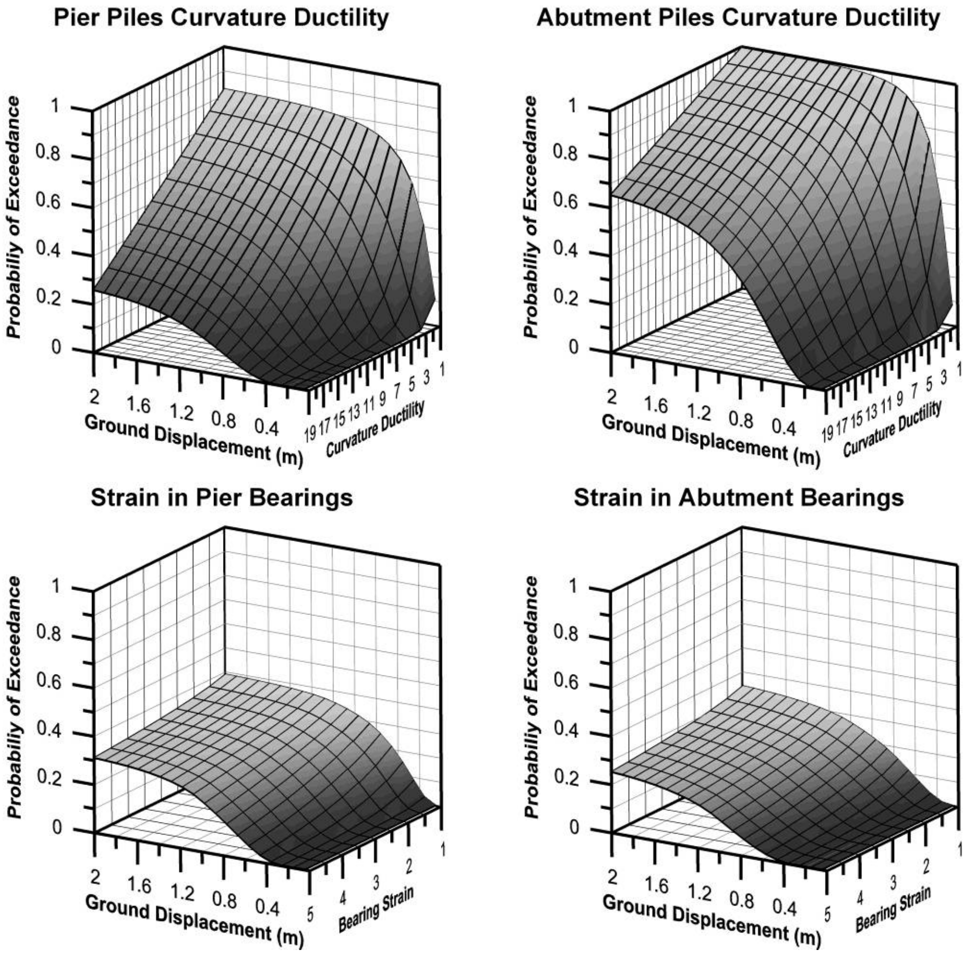

Figure 4.6: - Continued

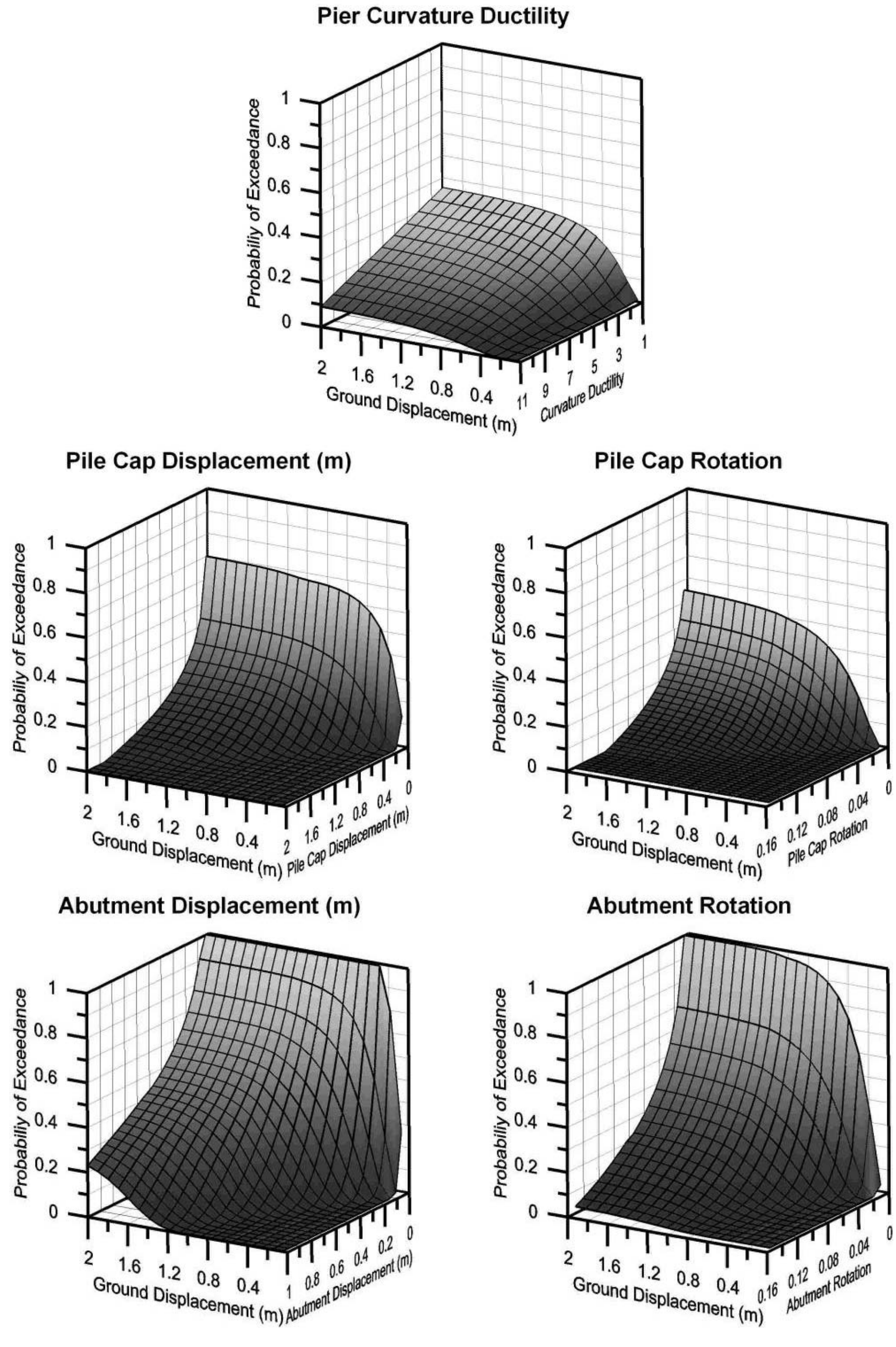

Figure 4.7: Fragility Surfaces for Post-1971 Simply-Supported Bridges with Seat-type Abutments and Single-Column Piers and 24" CISS piles

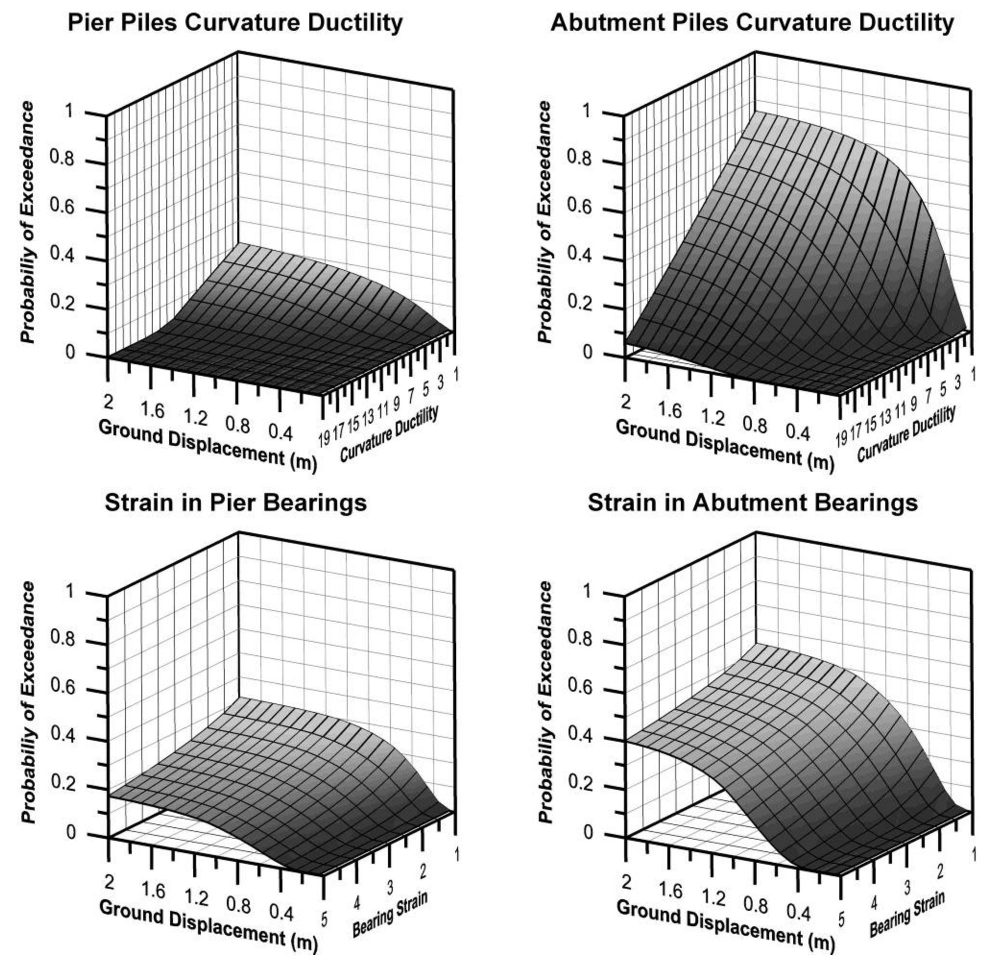
Pier Piles Curvature Ductility

Abutment Piles Curvature Ductility

Strain in Pier Bearings

Strain in Abutment Bearings

Figure 4.7: - Continued

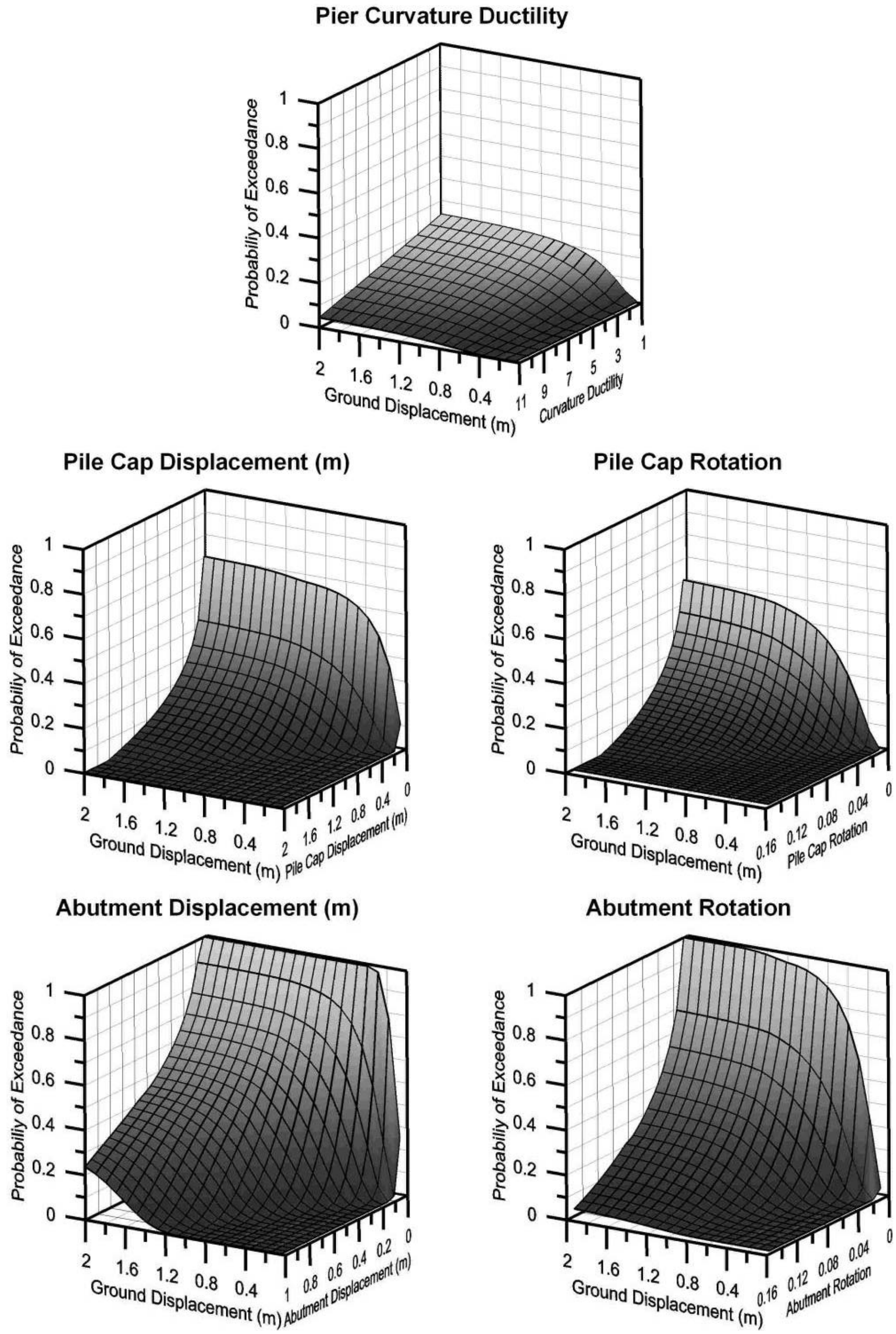

Figure 4.8: Fragility Surfaces for Post-1971 Simply-Supported Bridges with Seat-type Abutments and Multi-Column Piers and 24” CISS piles

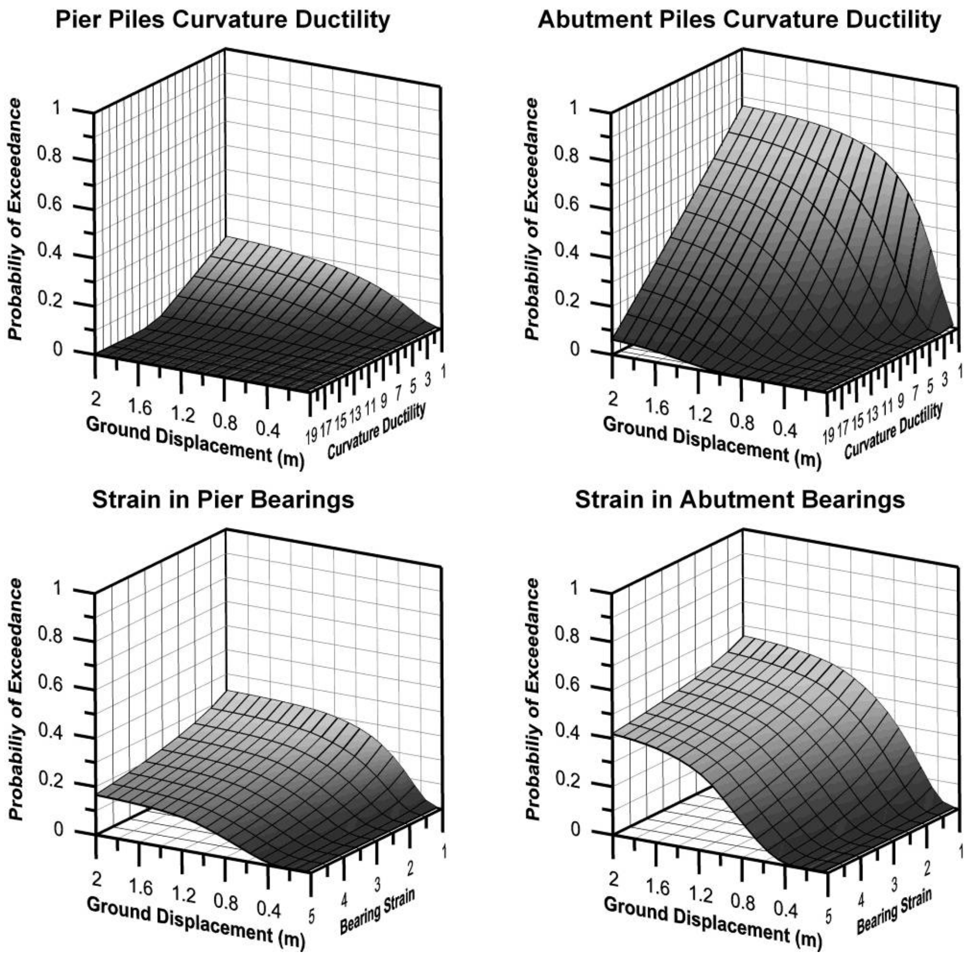

Pier Piles Curvature Ductility

Abutment Piles Curvature Ductility

Strain in Pier Bearings

Strain in Abutment Bearings

Figure 4.8: -Continued

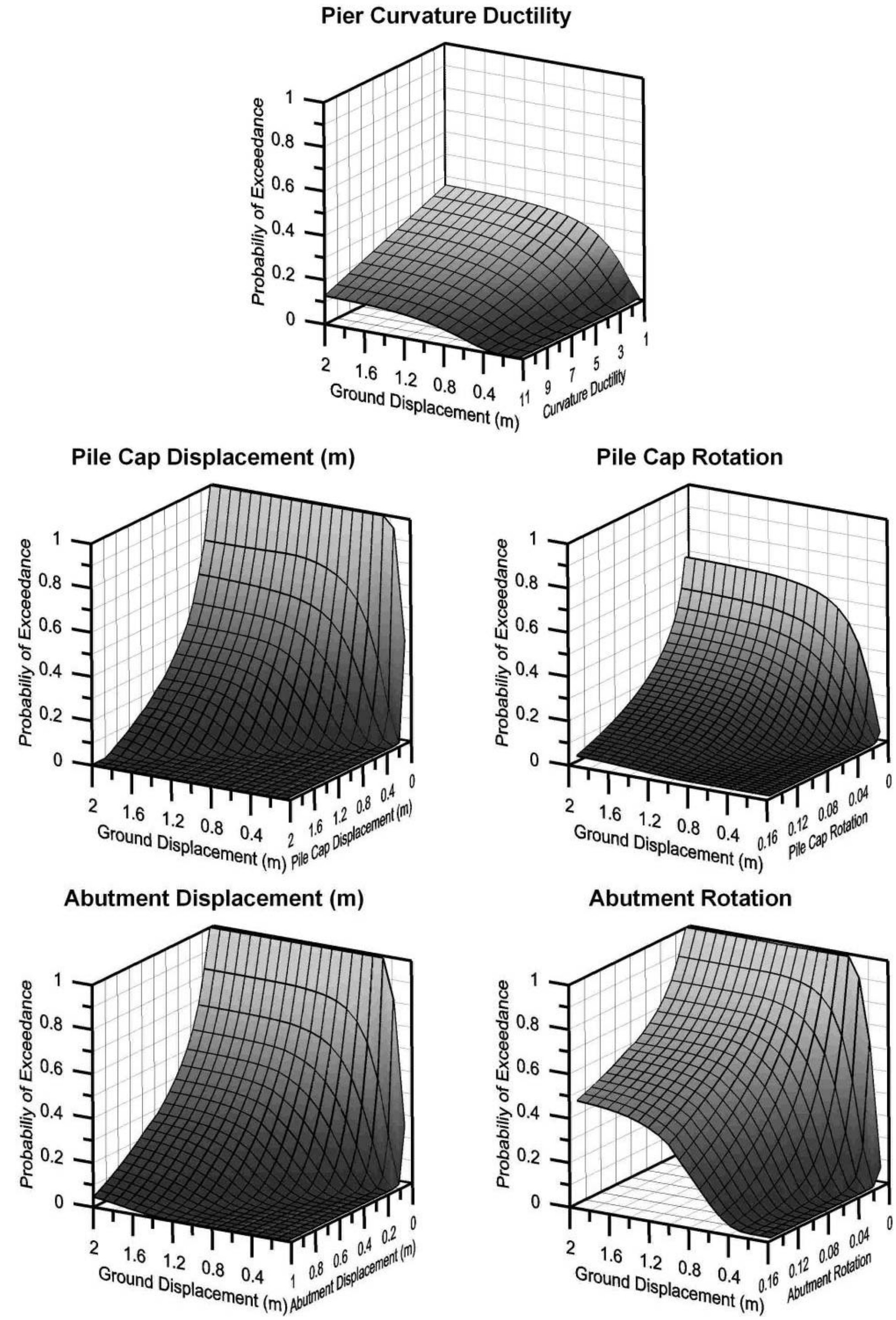

Pier Curvature Ductility

Pile Cap Displacement (m)

Pile Cap Rotation

Abutment Displacement (m)

Abutment Rotation

Figure 4.9: Fragility Surfaces for Post-1971 Simply-Supported Bridges with Seat-type Abutments and Single-Column Piers and 15” Precast Piles

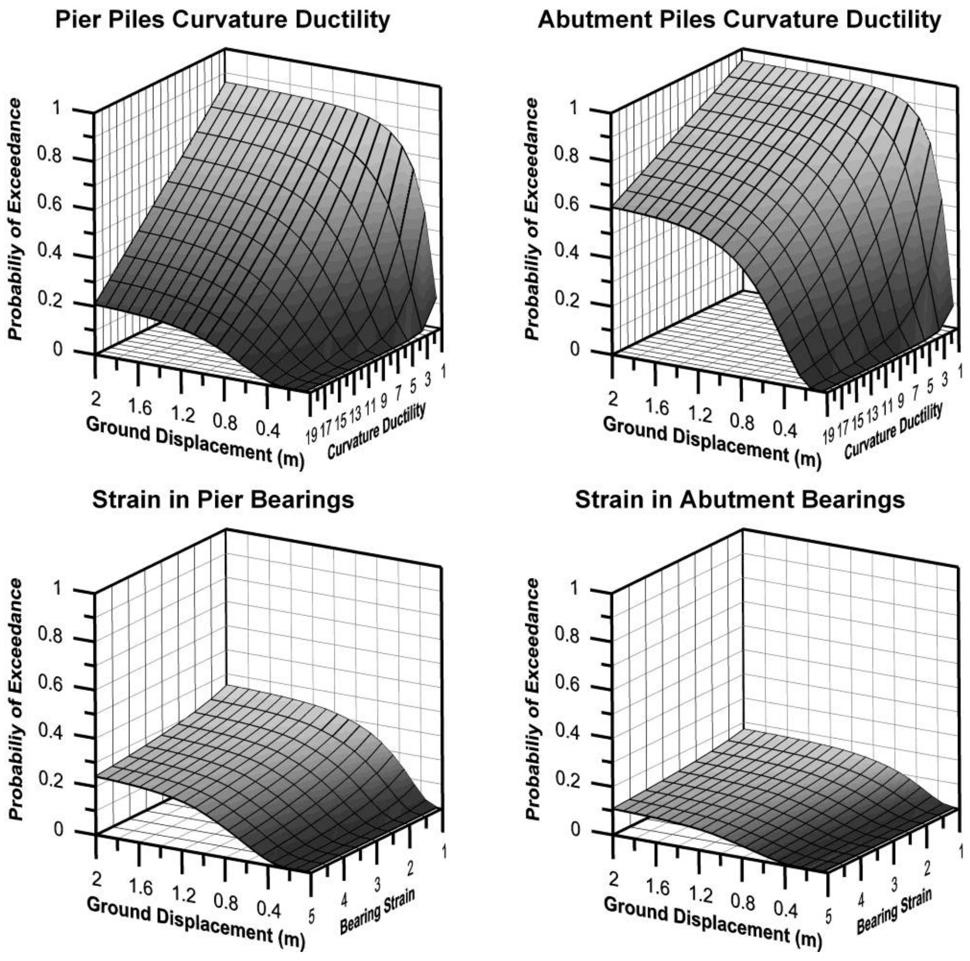

Figure 4.9: -Continued

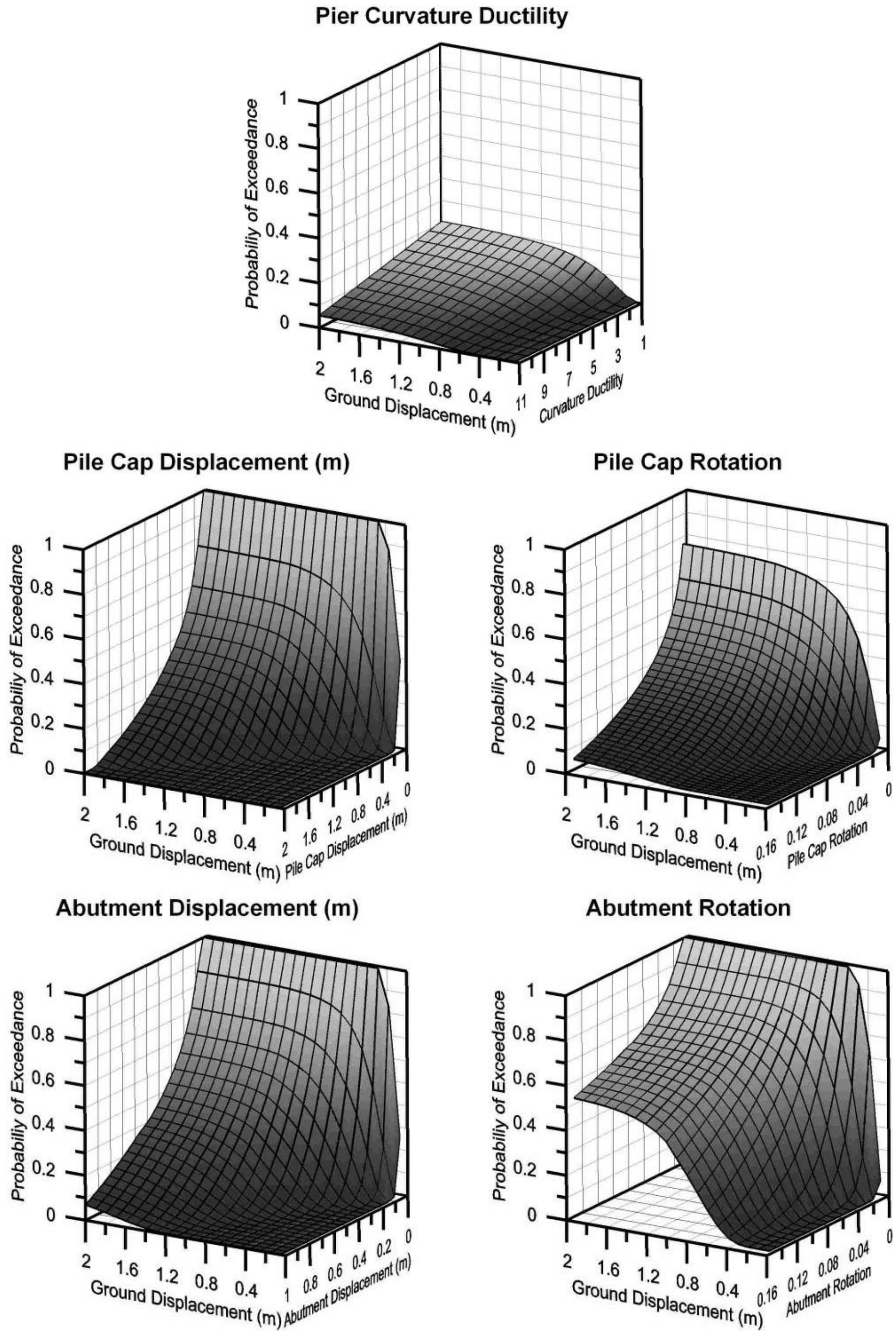

Figure 4.10: Fragility Surfaces for Post-1971 Simply-Supported Bridges with Seat-type Abutments and Multi-Column Piers and 15” Precast Piles

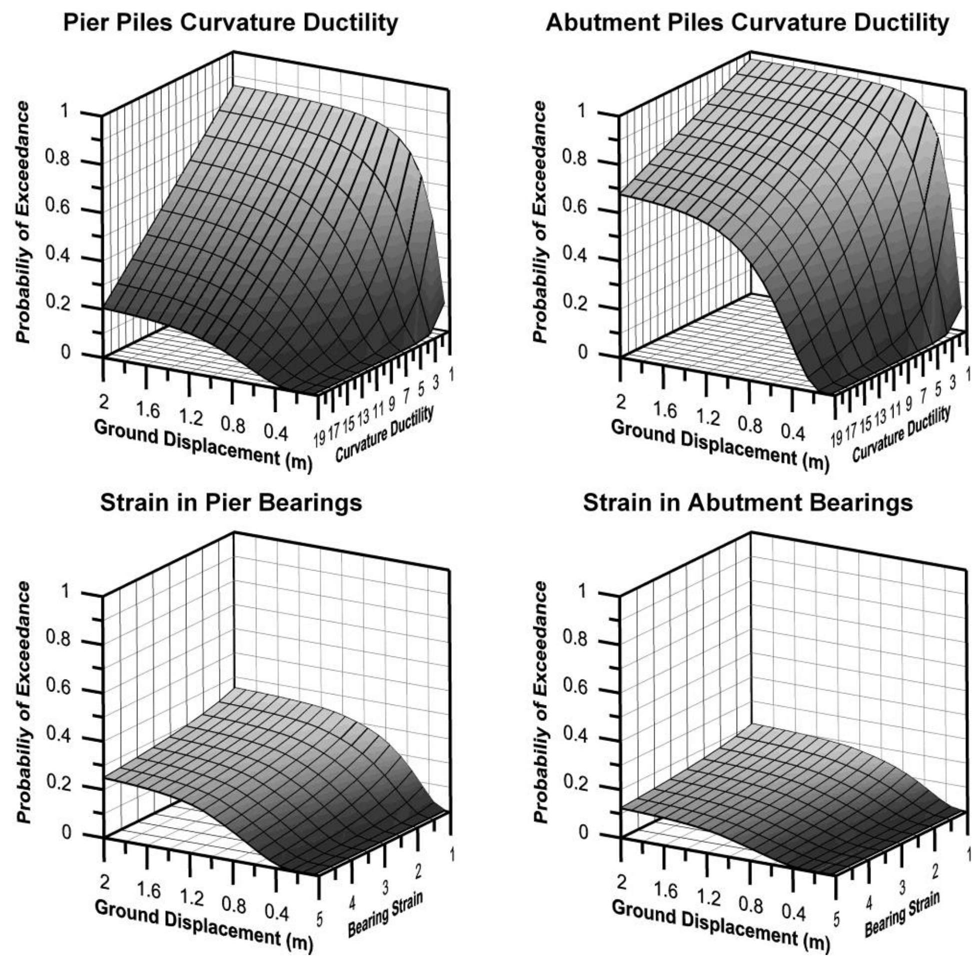

Figure 4.10: -Continued

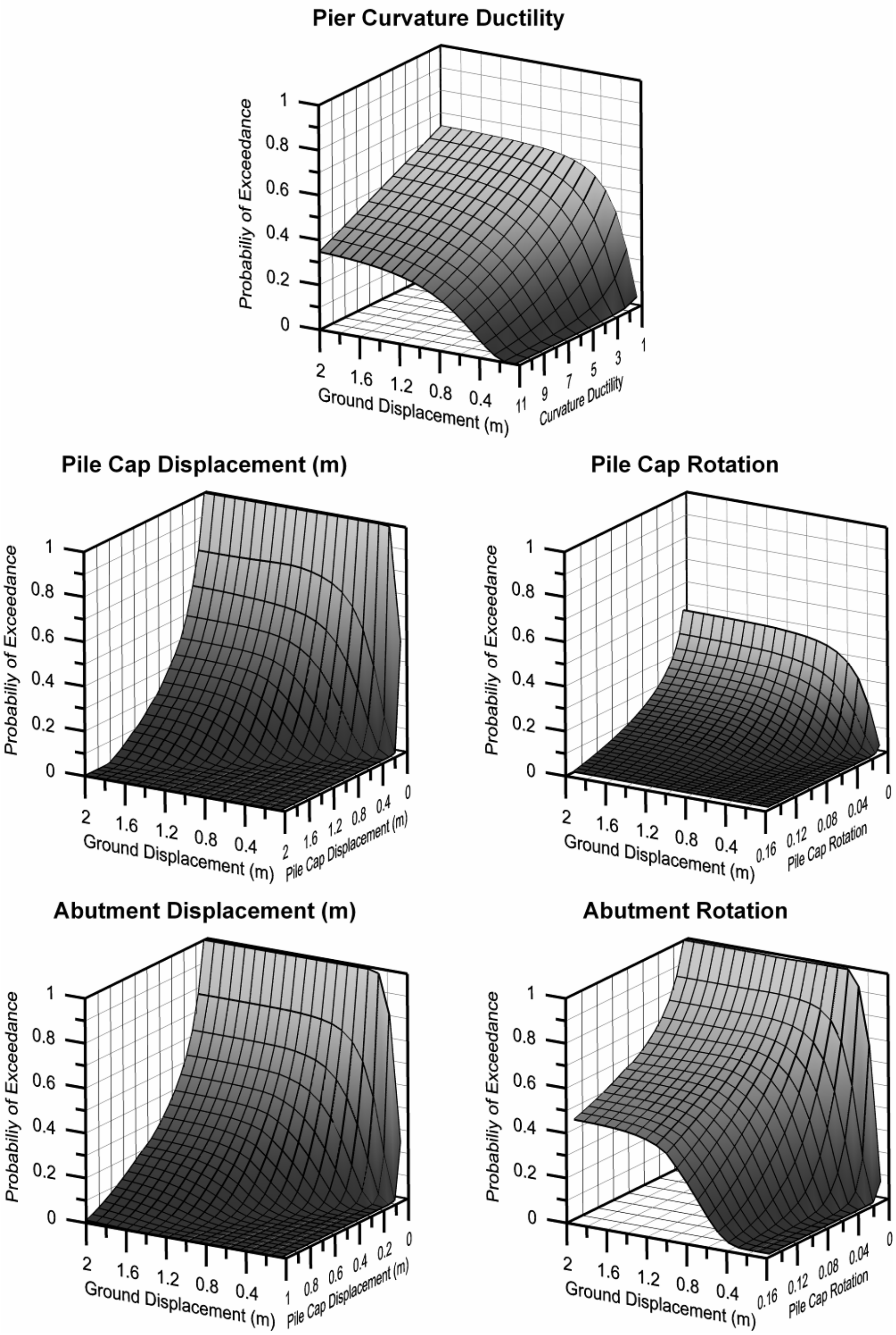

Pier Curvature Ductility

Pile Cap Displacement (m)

Pile Cap Rotation

Abutment Displacement (m)

Abutment Rotation

Figure 4.11: Fragility Surfaces for Pre-1971 Simply-Supported Bridges with Seat-type Abutments and Single-Column Piers and 15” Precast Piles

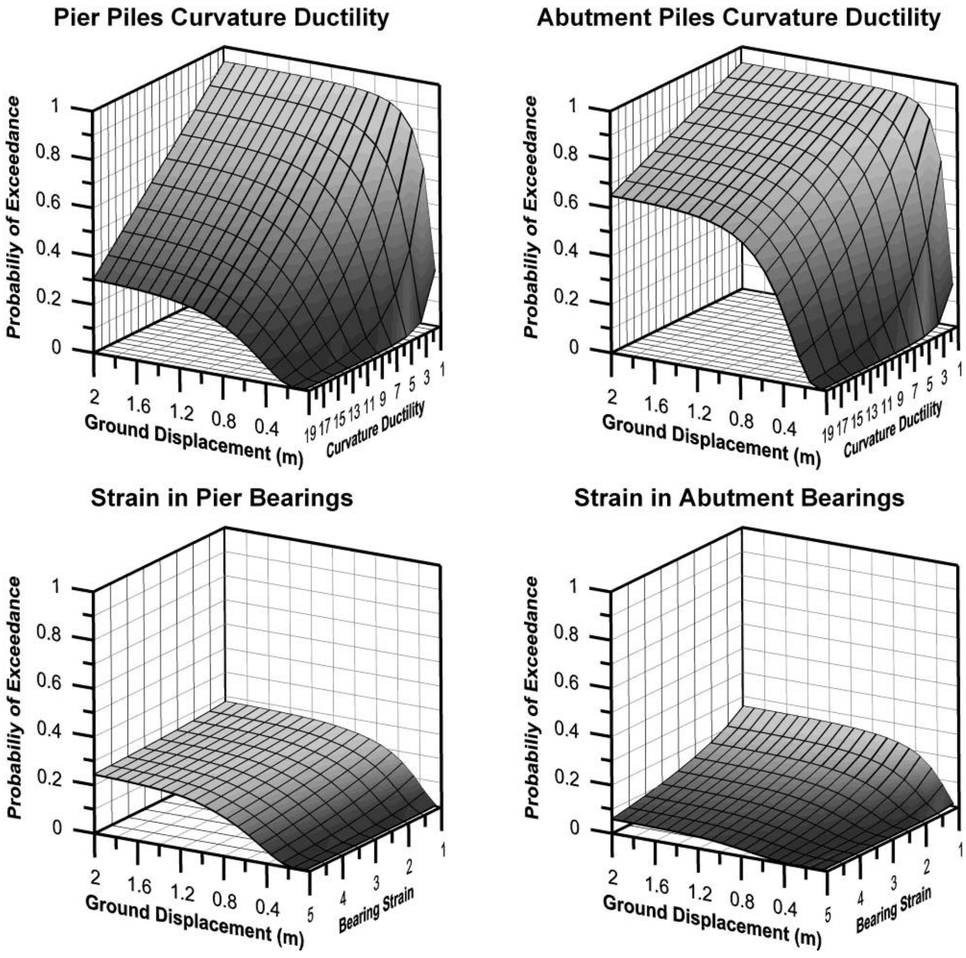

Figure 4.11: -Continued

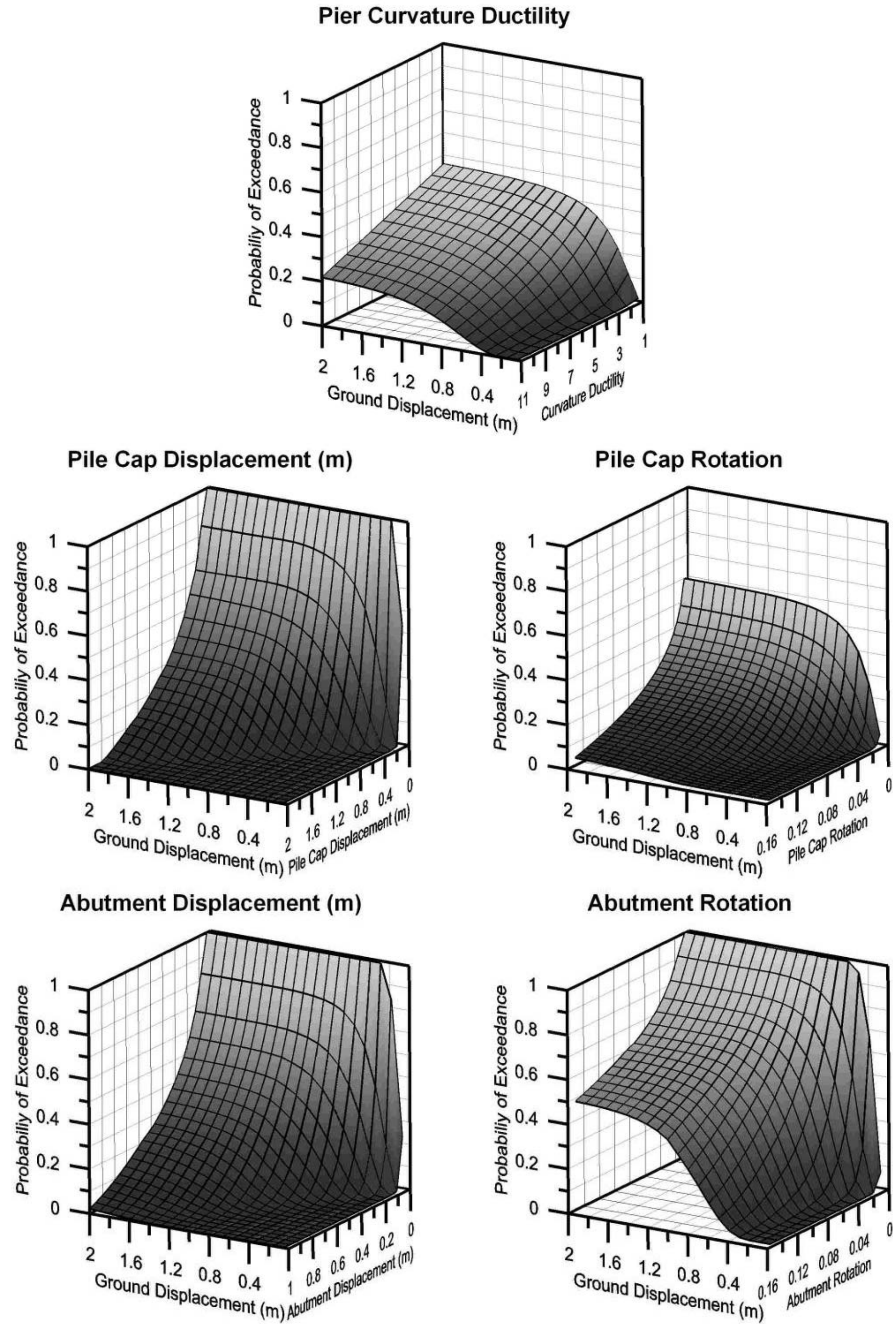

Figure 4.12: Fragility Surfaces for Pre-1971 Simply-Supported Bridges with Seat-type Abutments and Multi-Column Piers and 15” Precast Piles

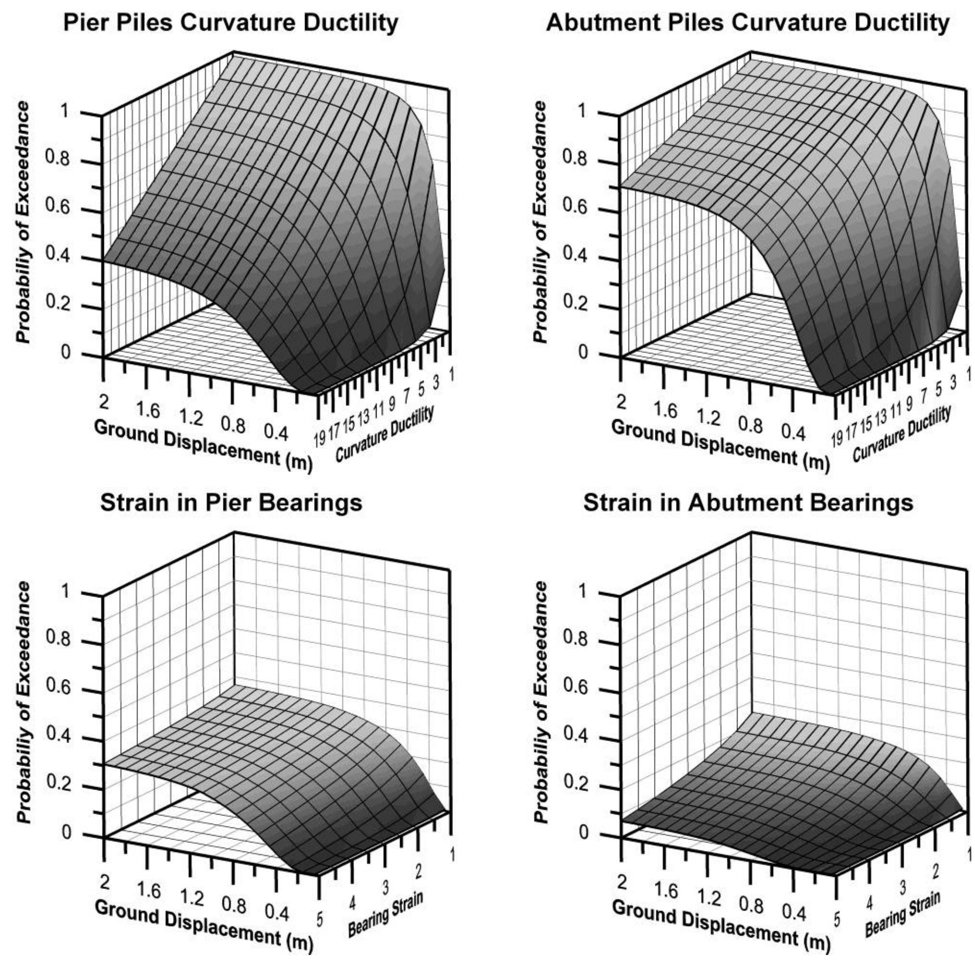

Figure 4.12: -Continued

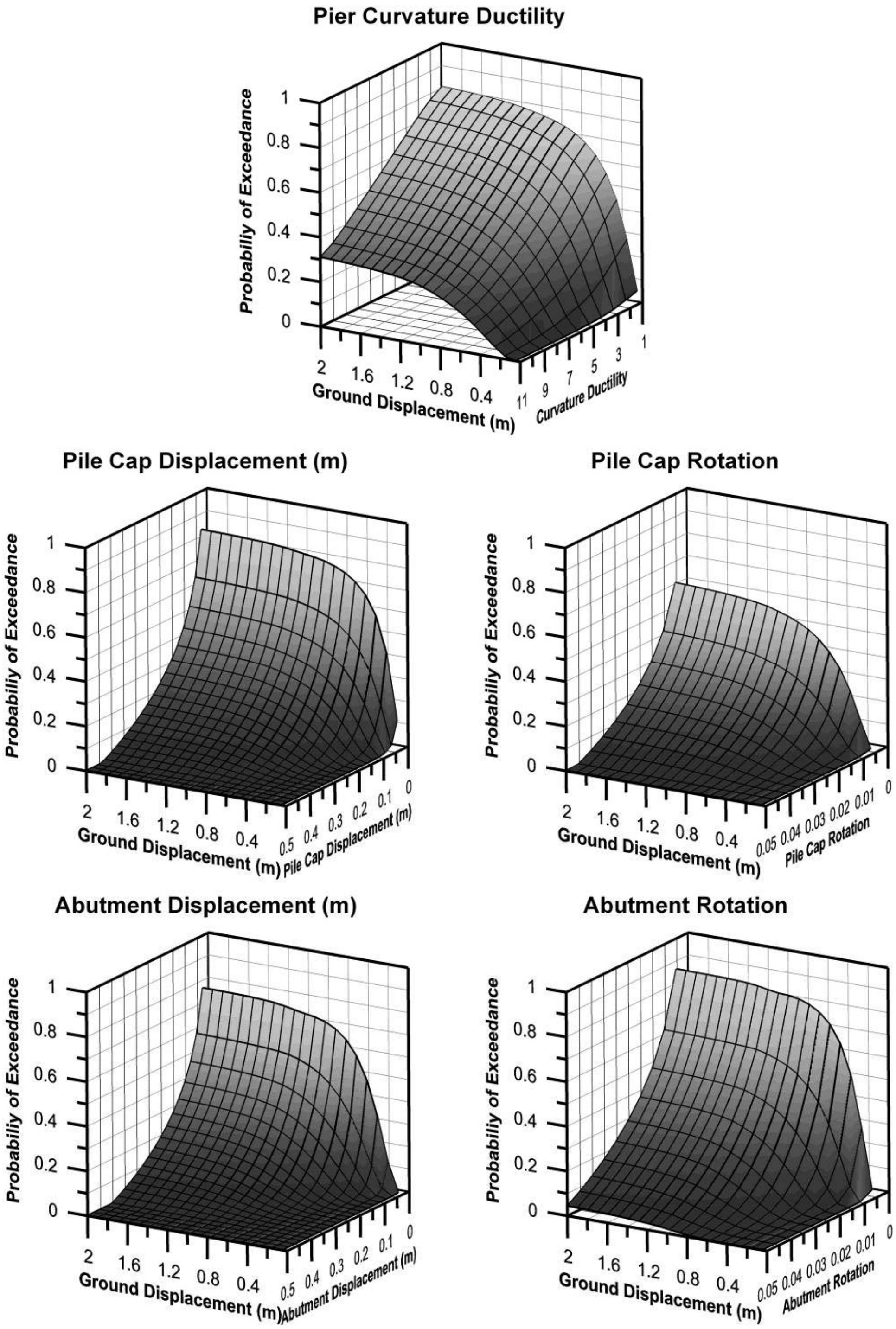

Figure 4.13: Fragility Surfaces for Post-1971 Continuous Bridges with Monolithic Abutments and Single-Column Piers and 24” CIDH piles

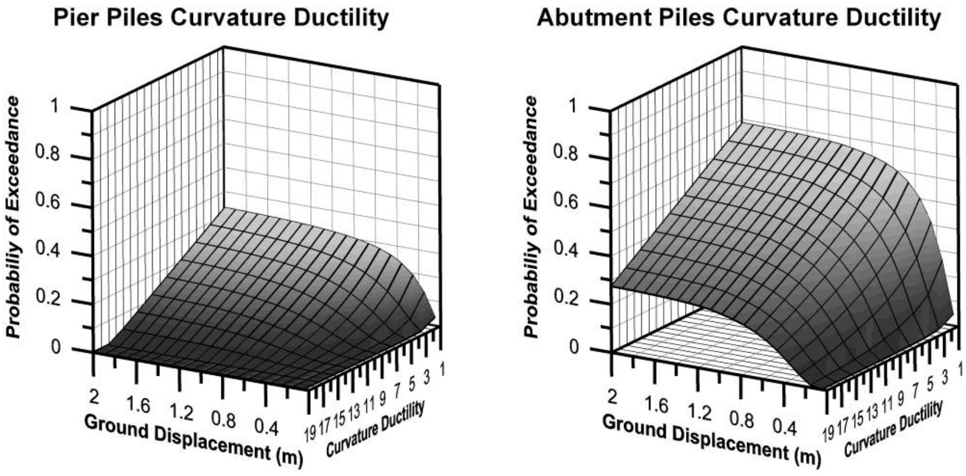

Figure 4.13: -Continued

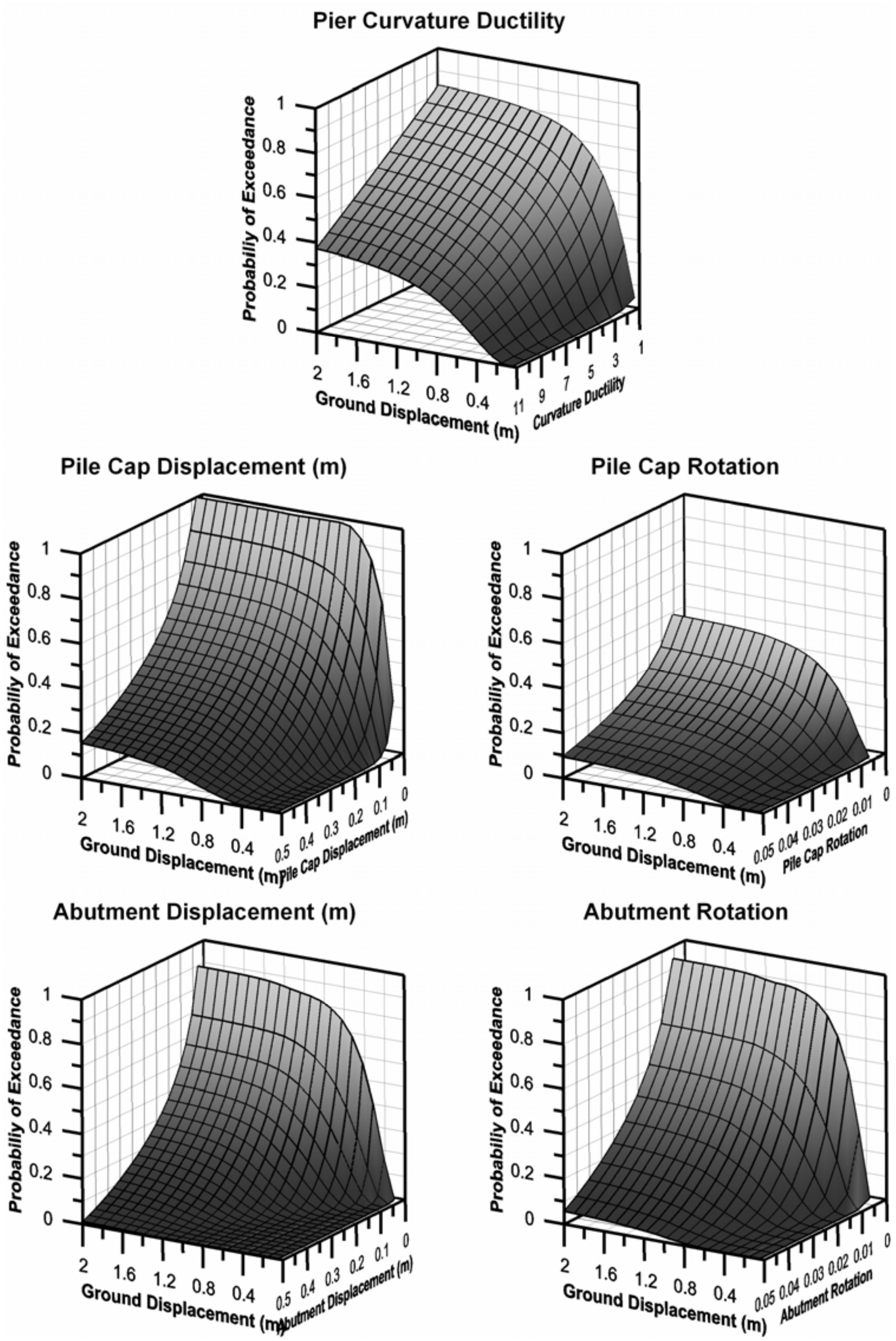
Pier Curvature Ductility

Pile Cap Displacement (m)

Pile Cap Rotation

Abutment Displacement (m)

Abutment Rotation

Figure 4.14: Fragility Surfaces for Post-1971 Continuous Bridges with Monolithic Abutments and Multi-Column Piers and 24” CIDH piles

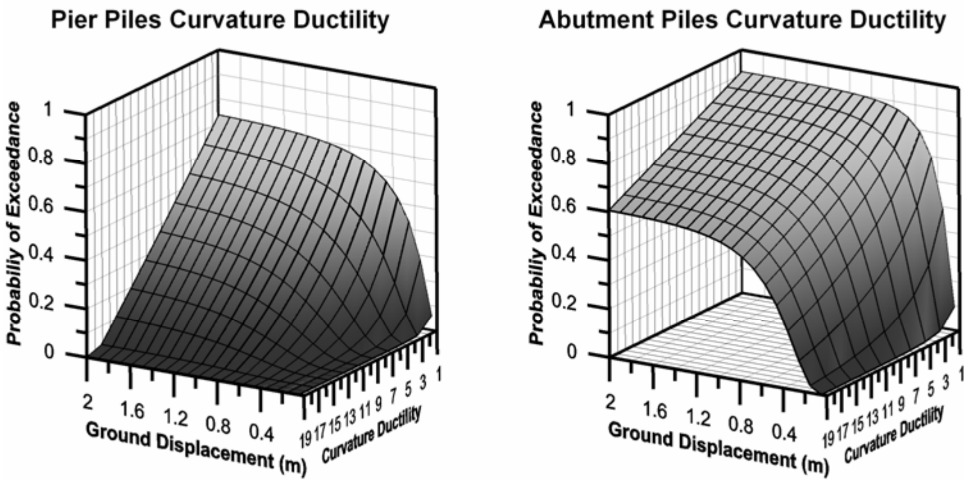
Pier Piles Curvature Ductility

Abutment Piles Curvature Ductility

Figure 4.14: -Continued

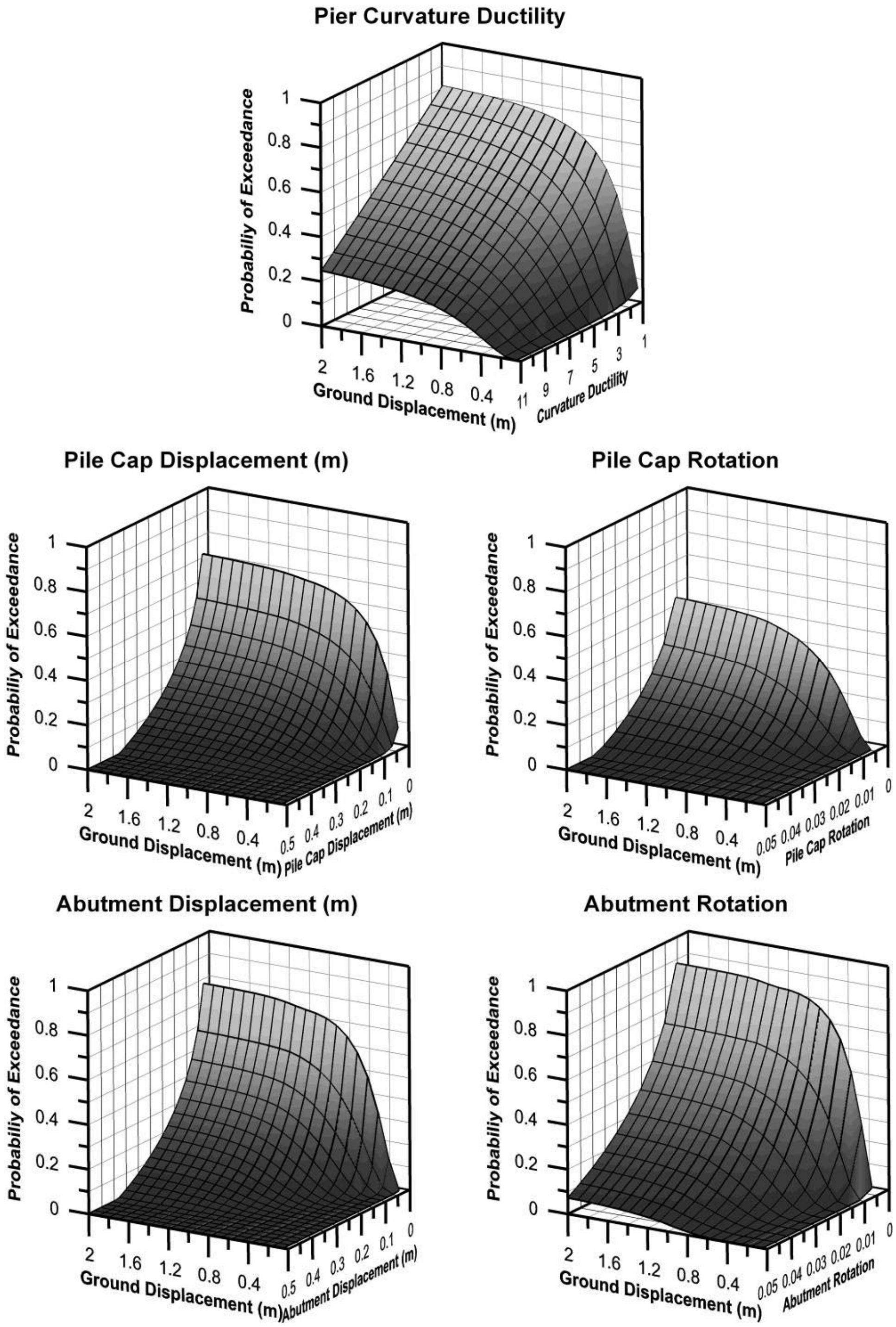

Pier Curvature Ductility

Pile Cap Displacement (m)

Pile Cap Rotation

Abutment Displacement (m)

Abutment Rotation

Figure 4.15: Fragility Surfaces for Post-1971 Continuous Bridges with Monolithic Abutments and Single-Column Piers and 24" CISS piles

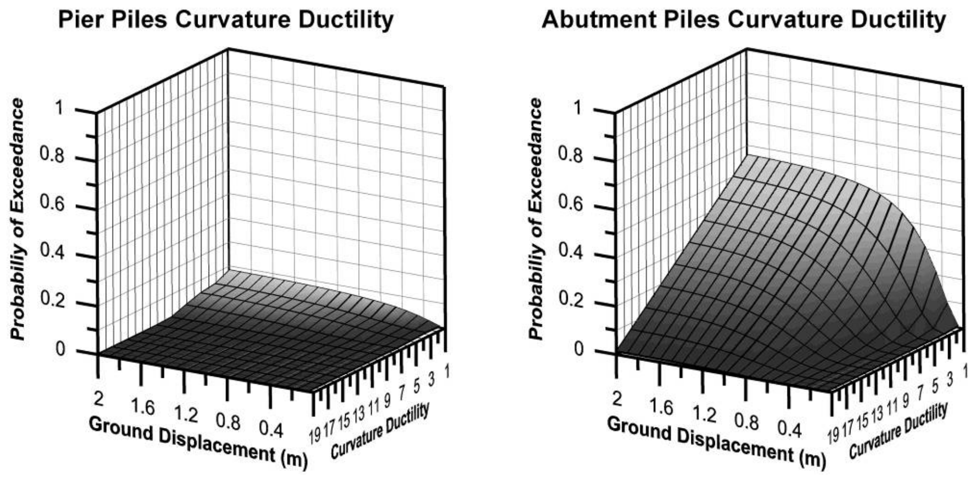

Figure 4.15: -Continued

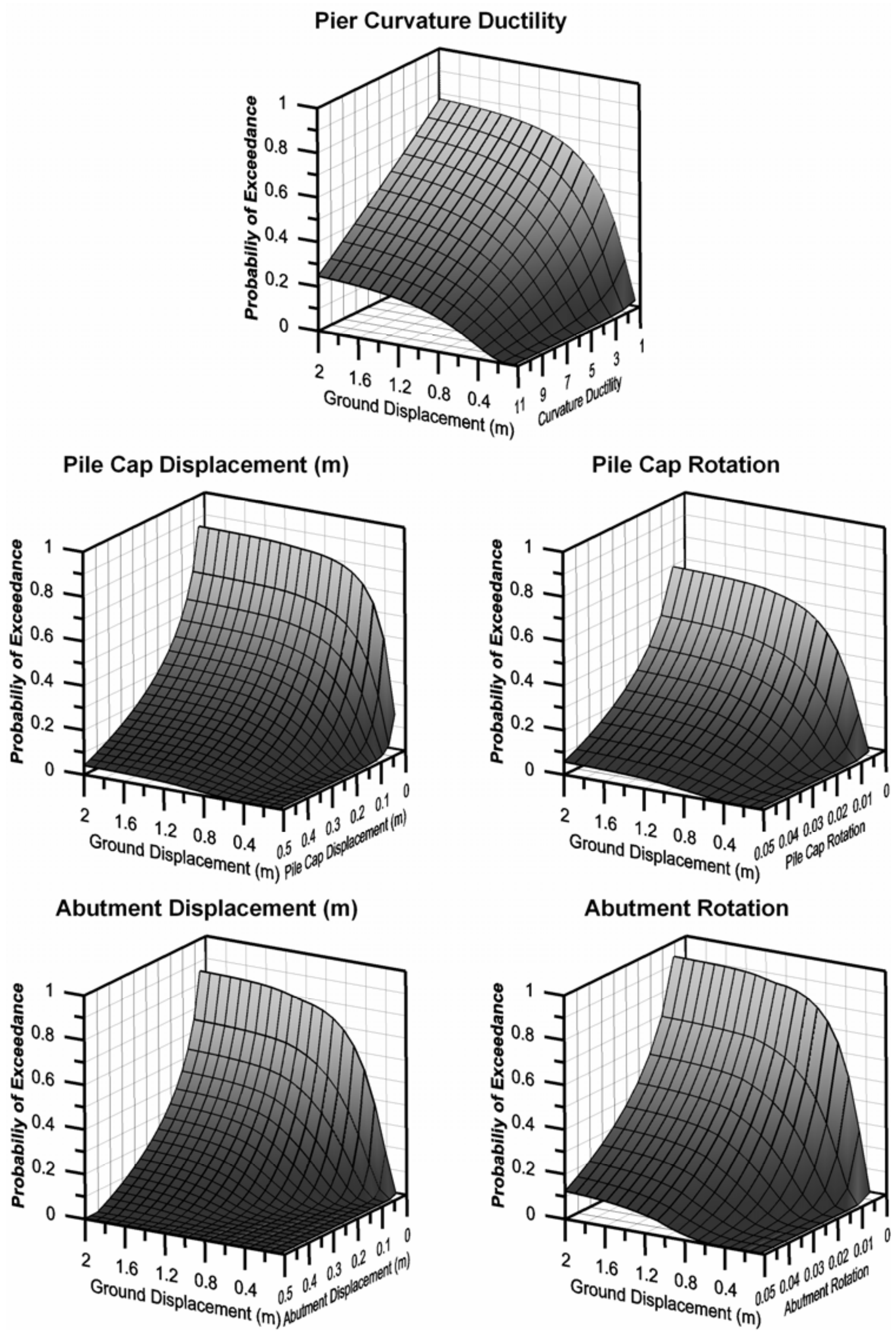

Figure 4.16: Fragility Surfaces for Post-1971 Continuous Bridges with Monolithic Abutments and Multi-Column Piers and 24” CISS piles

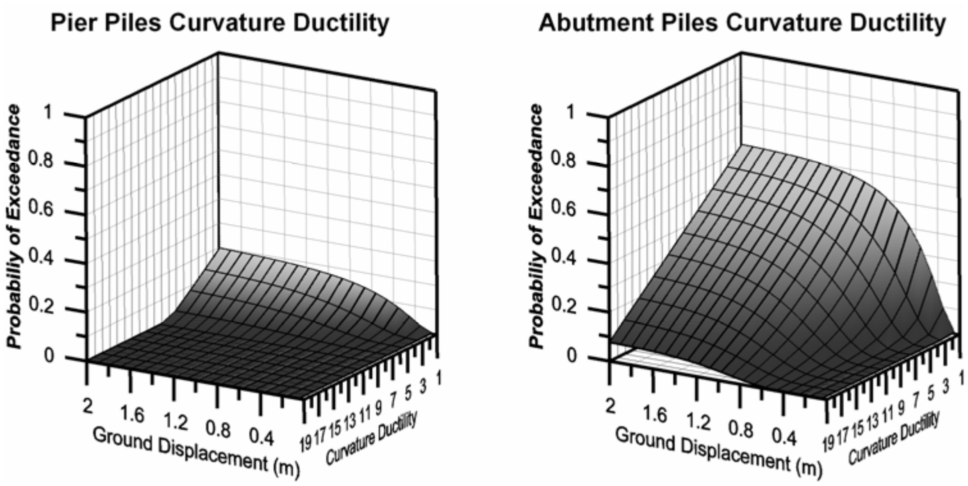
Pier Piles Curvature Ductility

Abutment Piles Curvature Ductility

Figure 4.16: -Continued

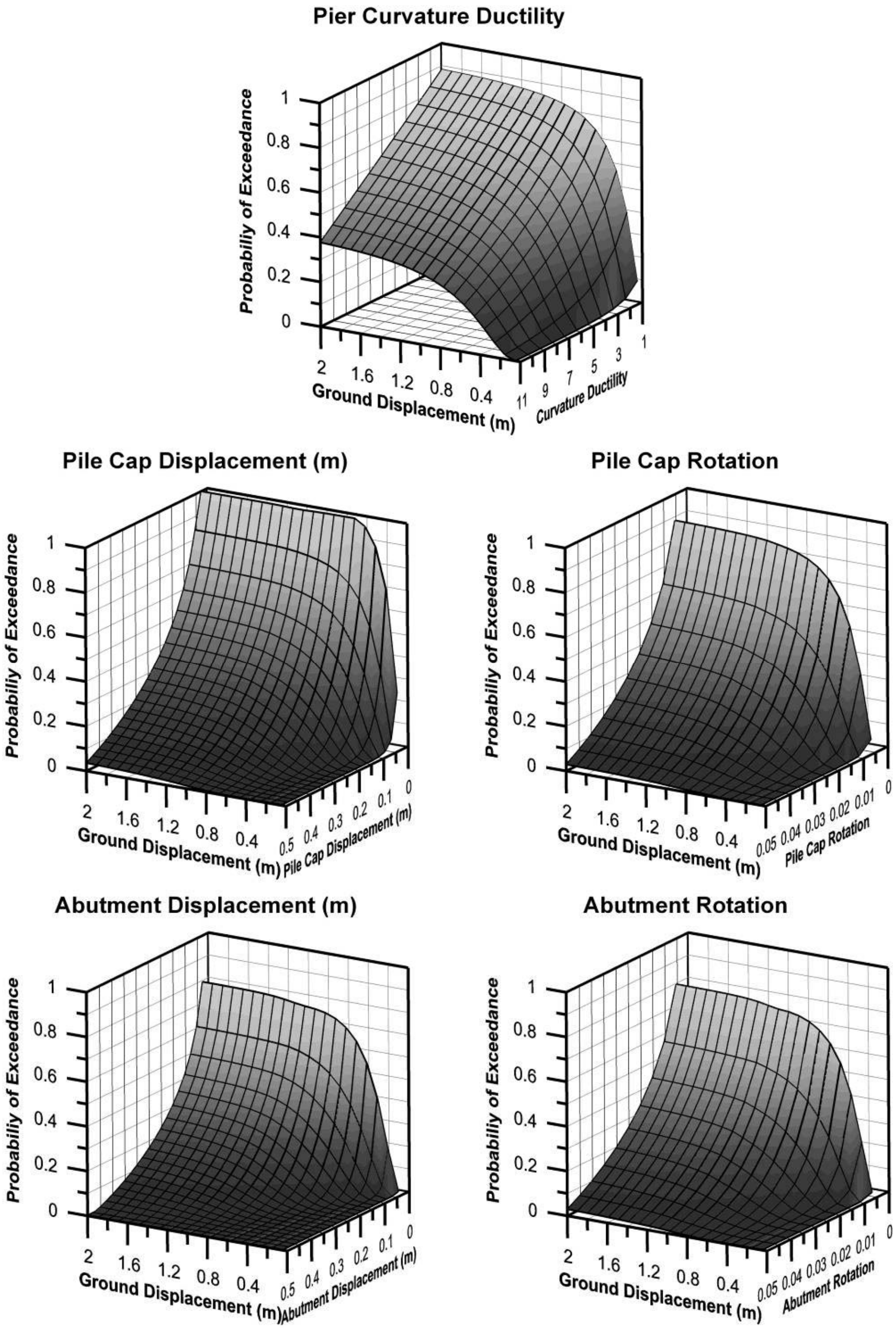

Figure 4.17: Fragility Surfaces for Post-1971 Continuous Bridges with Monolithic Abutments and Single-Column Piers and 15” Precast

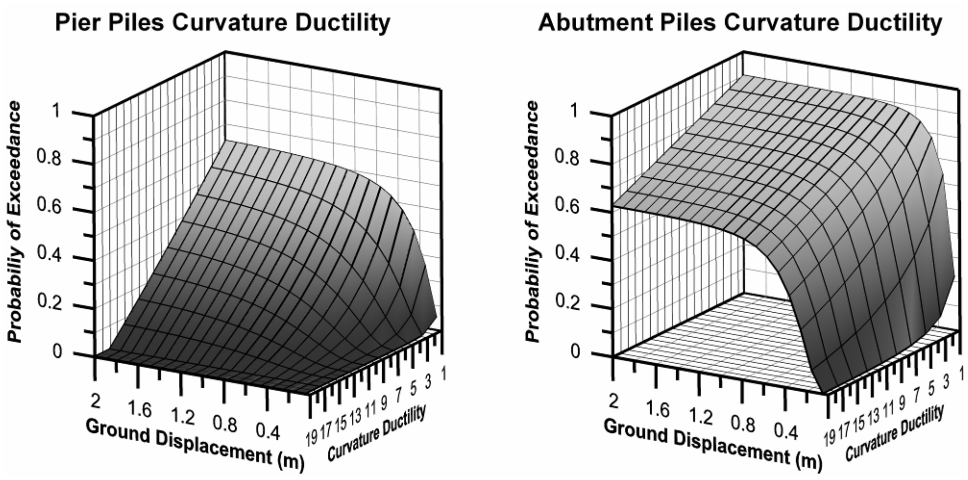
Pier Piles Curvature Ductility

Abutment Piles Curvature Ductility

Figure 4.17: -Continued

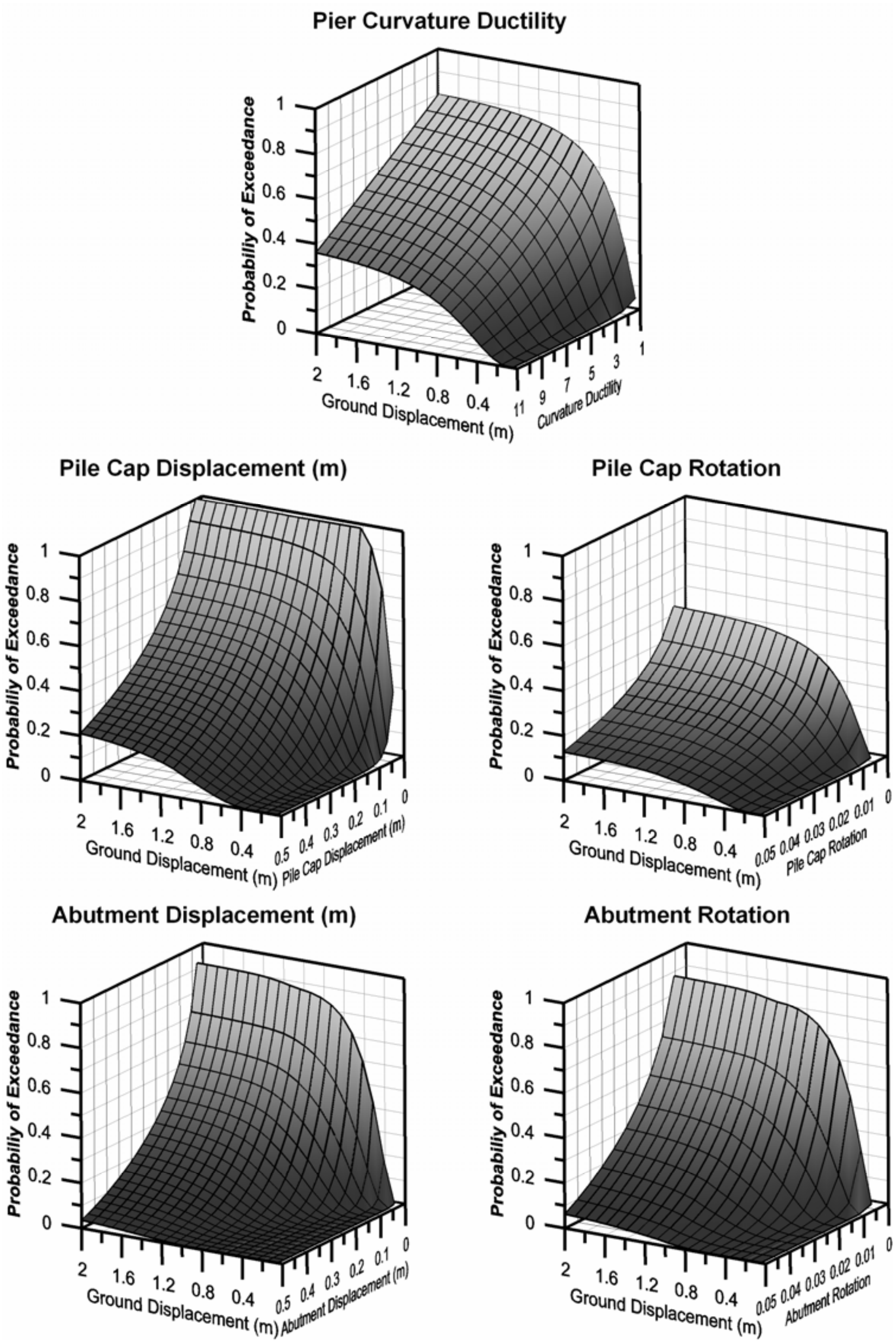

Pier Curvature Ductility

Pile Cap Displacement (m)

Pile Cap Rotation

Abutment Displacement (m)

Abutment Rotation

Figure 4.18: Fragility Surfaces for Post-1971 Continuous Bridges with Monolithic Abutments and Multi-Column Piers and 15” Precast

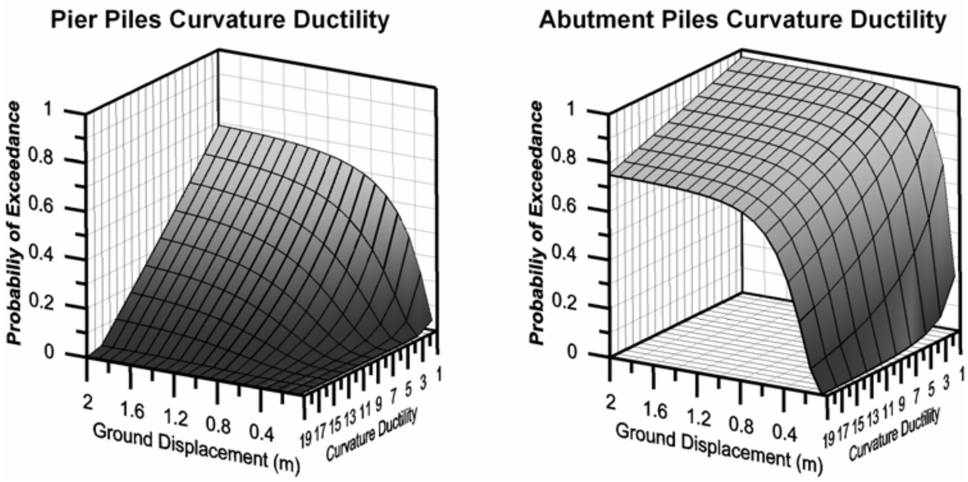

Figure 4.18: -Continued

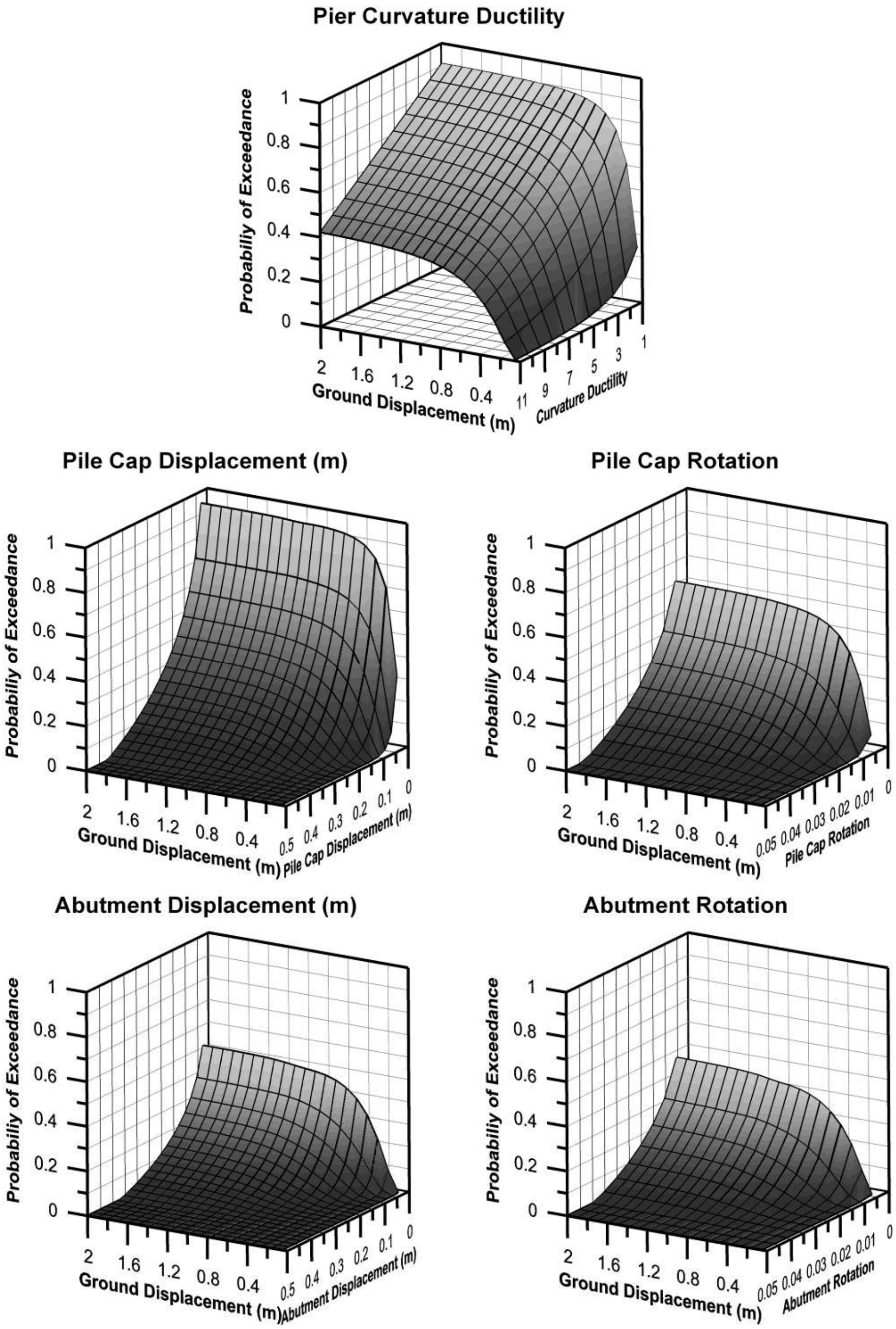

Figure 4.19: Fragility Surfaces for Pre-1971 Continuous Bridges with Monolithic Abutments and Single-Column Piers and 15” Precast Piles

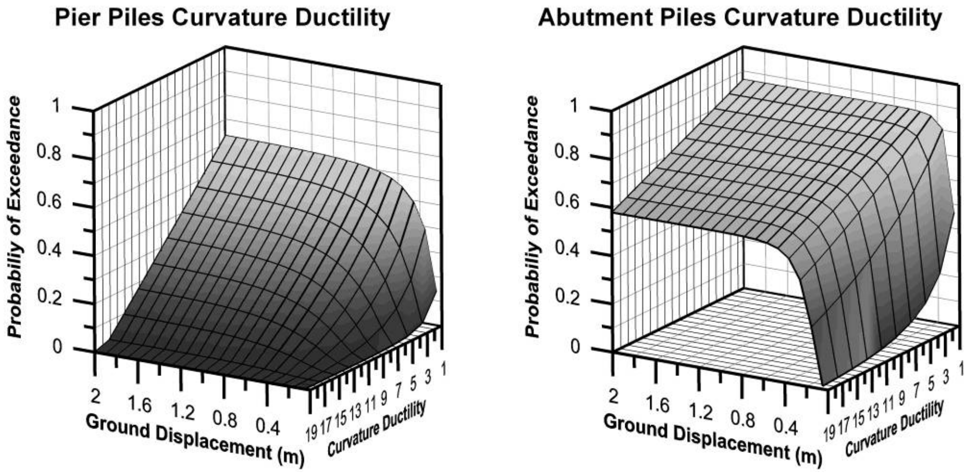

Pier Piles Curvature Ductility

Abutment Piles Curvature Ductility

Figure 4.19: -Continued

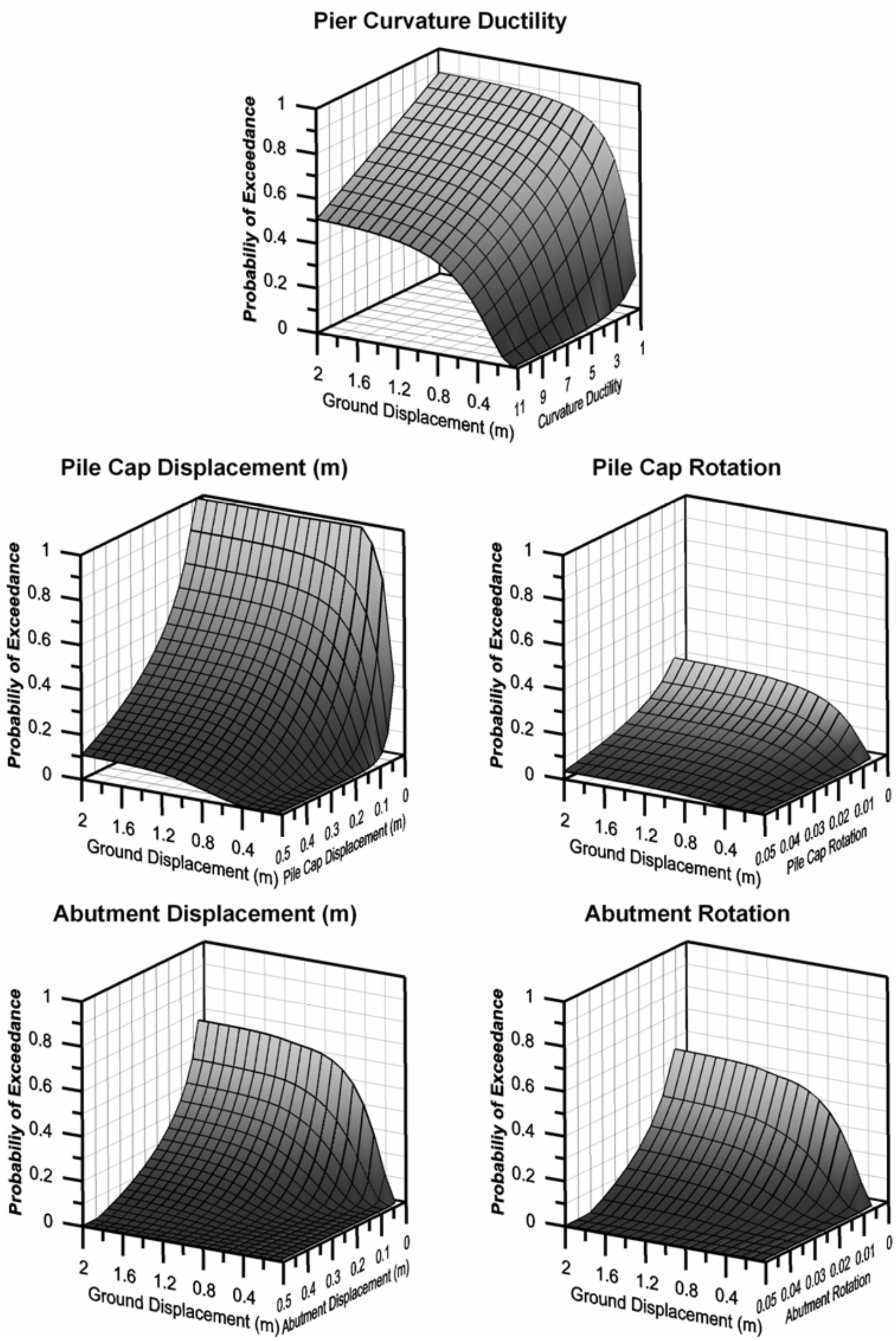

Figure 4.20: Fragility Surfaces for Pre-1971 Continuous Bridges with Monolithic Abutments and Multi-Column Piers and 15” Precast Piles

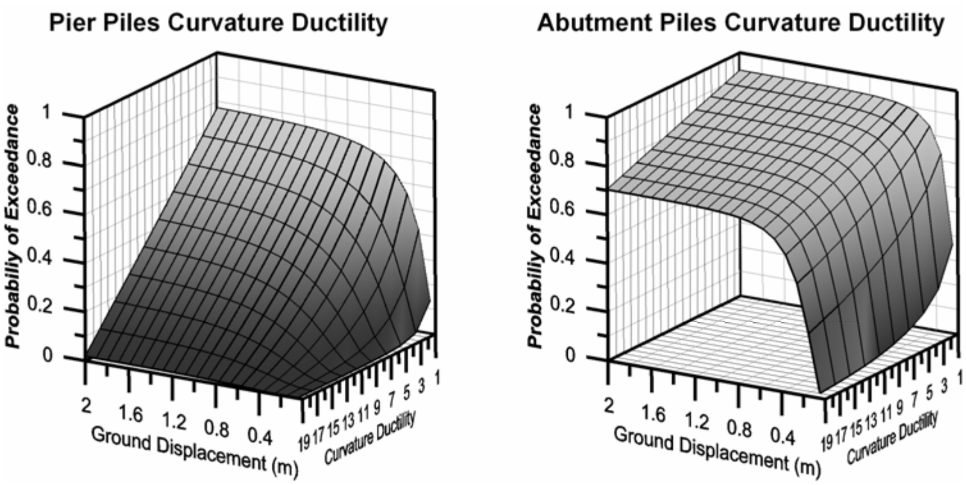

Figure 4.20: -Continued

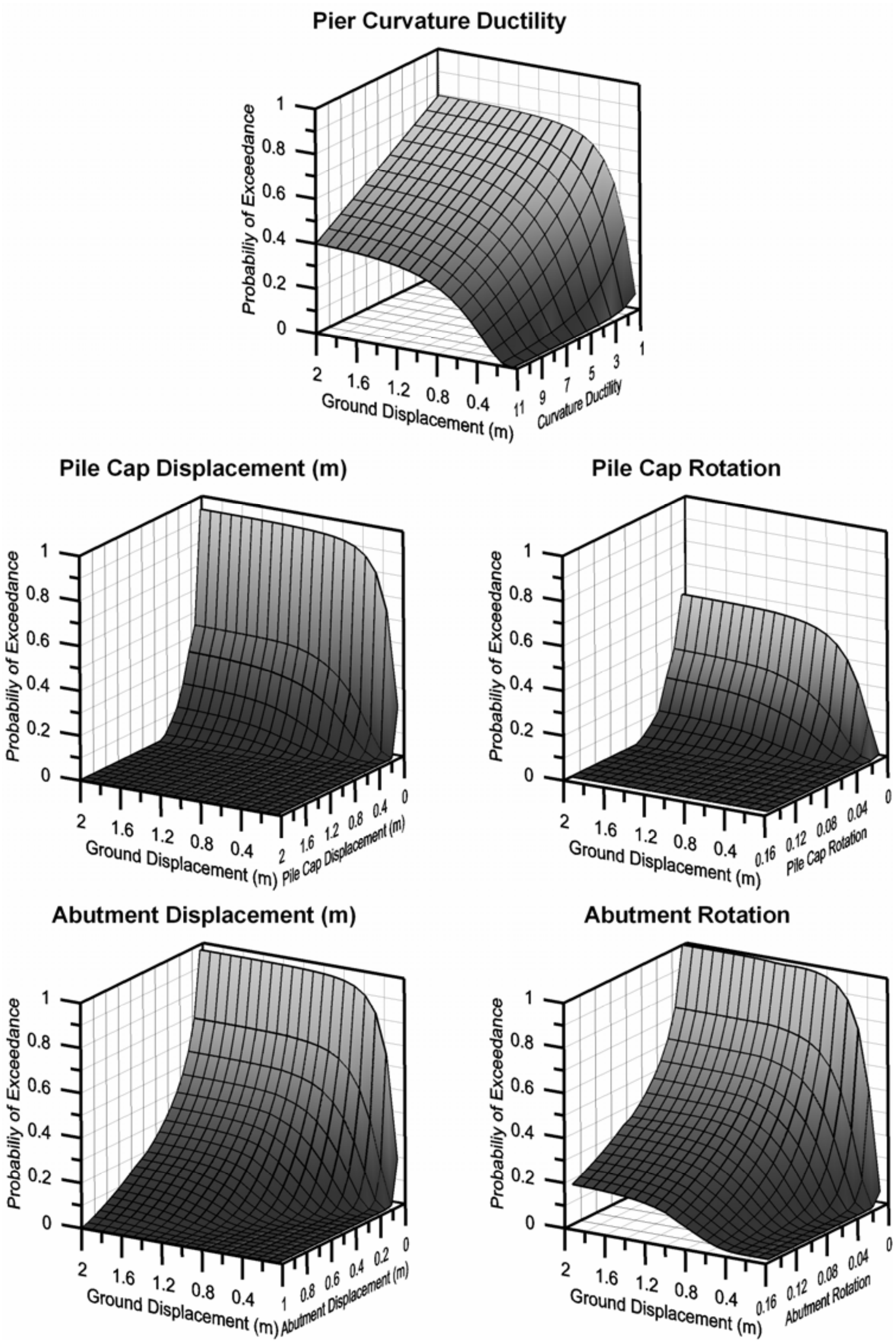

Figure 4.21: Fragility Surfaces for Post-1971 Continuous Bridges with Seat-type Abutments and Single-Column Piers and 24” CIDH piles

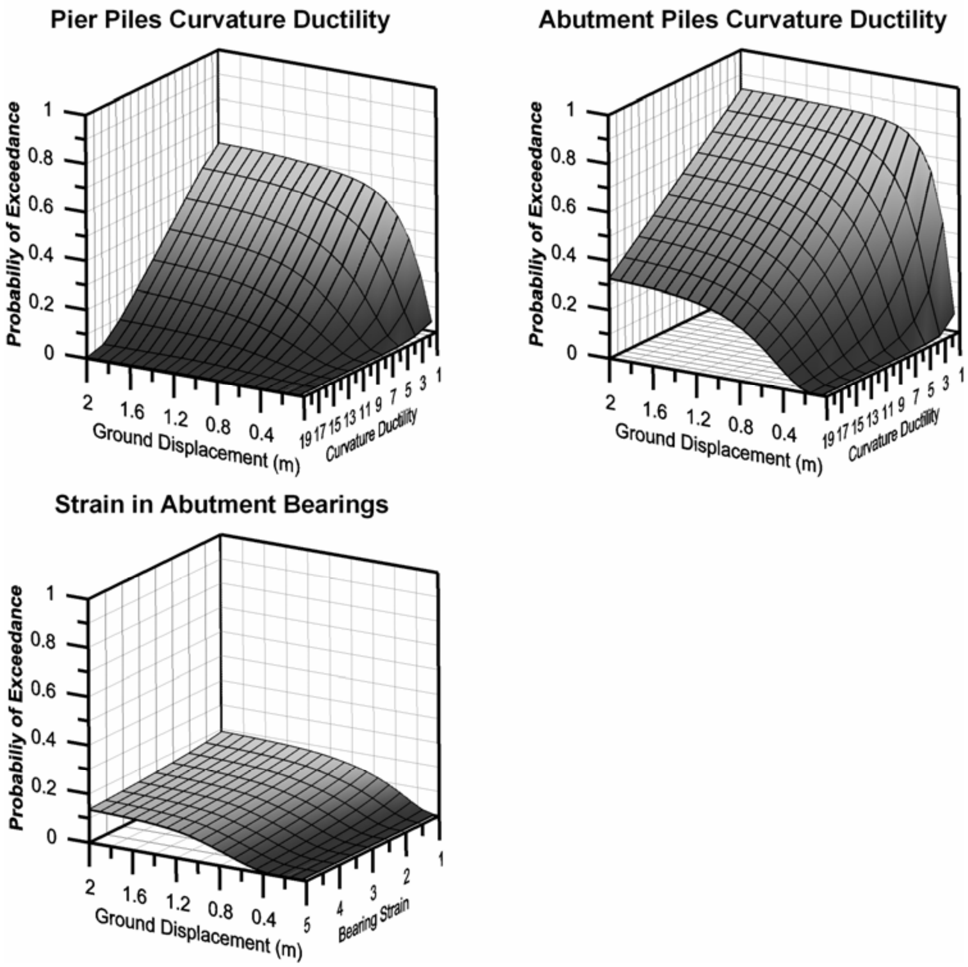

Figure 4.21: -Continued

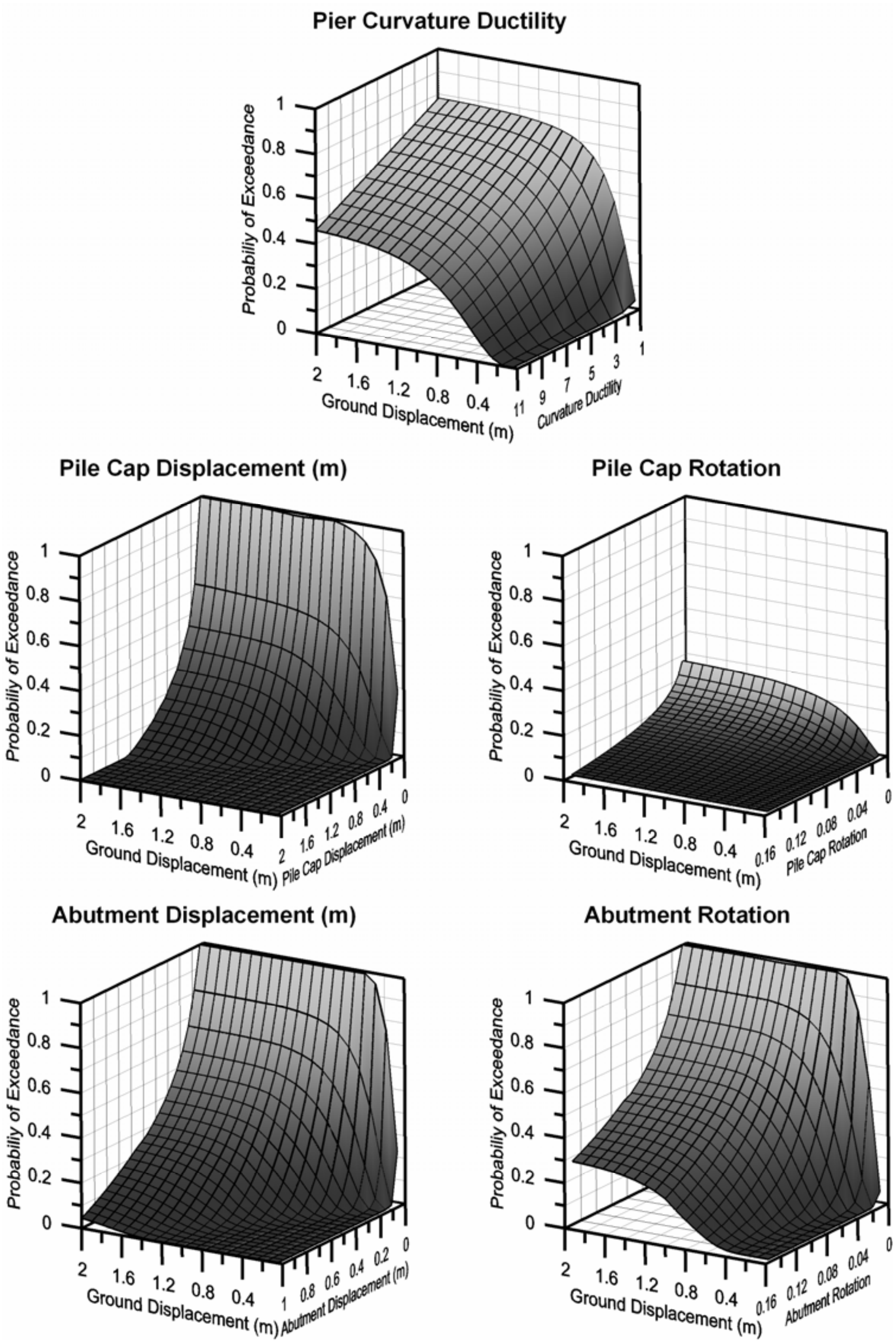

Figure 4.22: Fragility Surfaces for Post-1971 Continuous Bridges with Seat-type Abutments and Multi-Column Piers and 24” CIDH piles

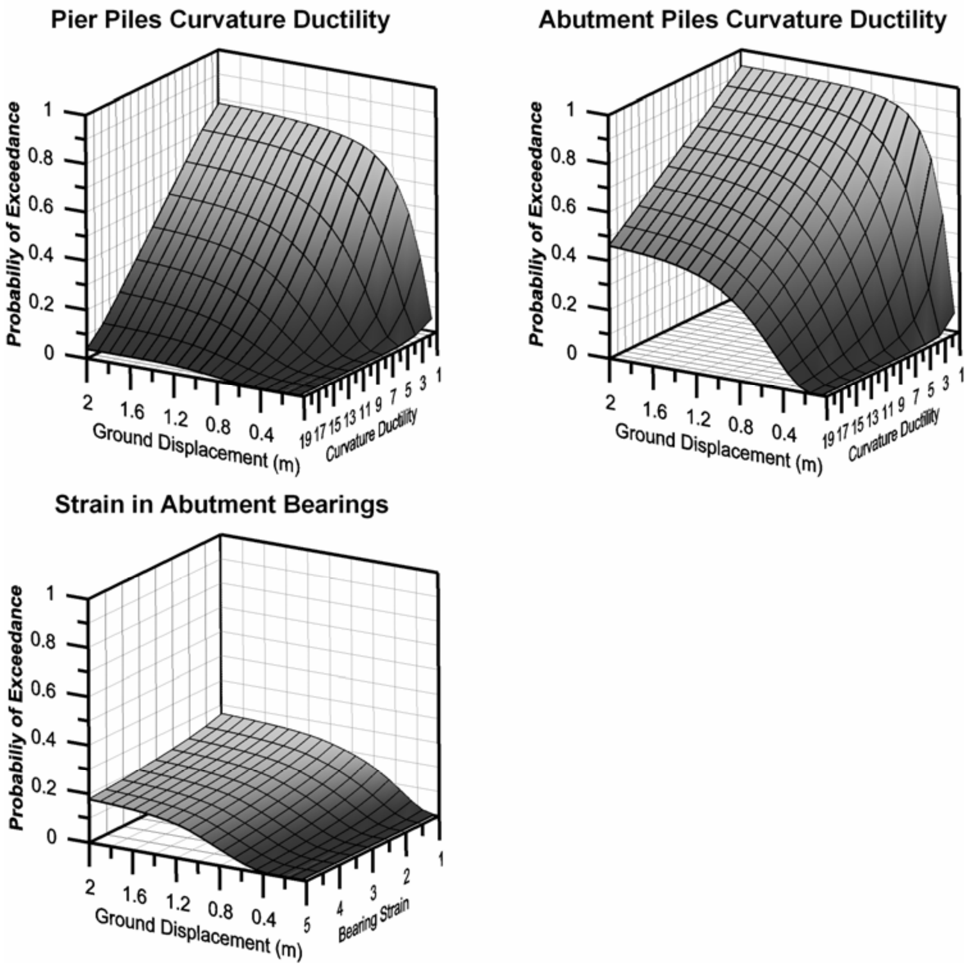

Figure 4.22: -Continued

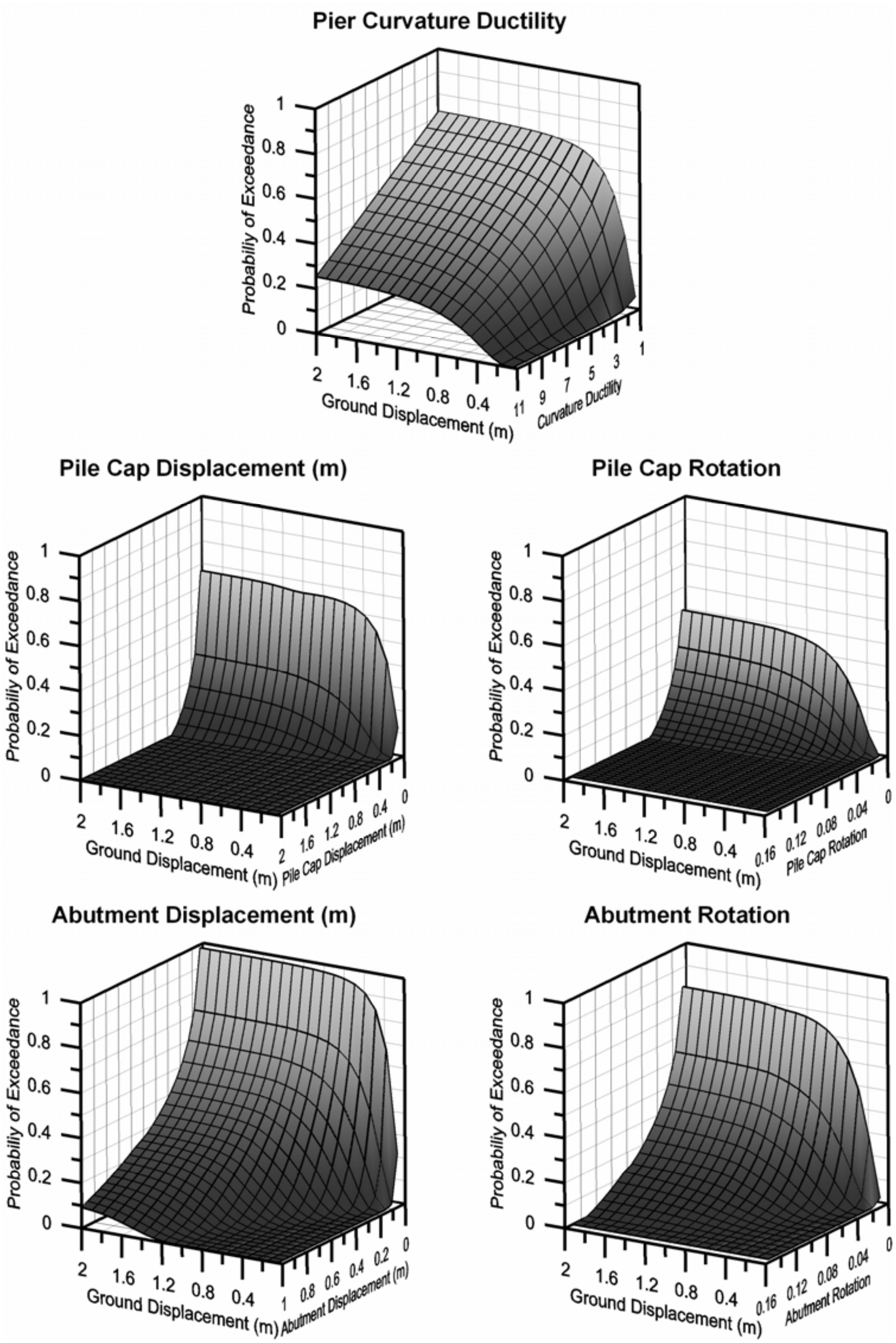

Figure 4.23: Fragility Surfaces for Post-1971 Continuous Bridges with Seat-type Abutments and Single-Column Piers and 24” CISS piles

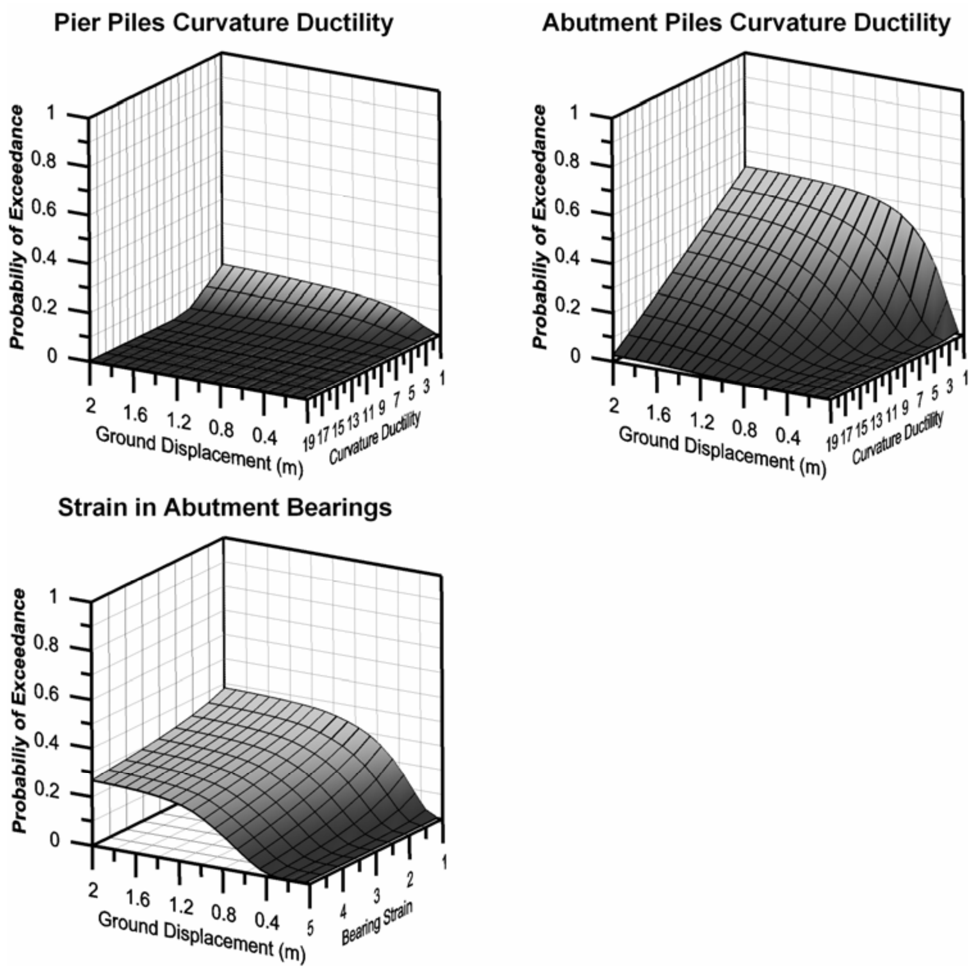

Pier Piles Curvature Ductility

Abutment Piles Curvature Ductility

Strain in Abutment Bearings

Figure 4.23: -Continued

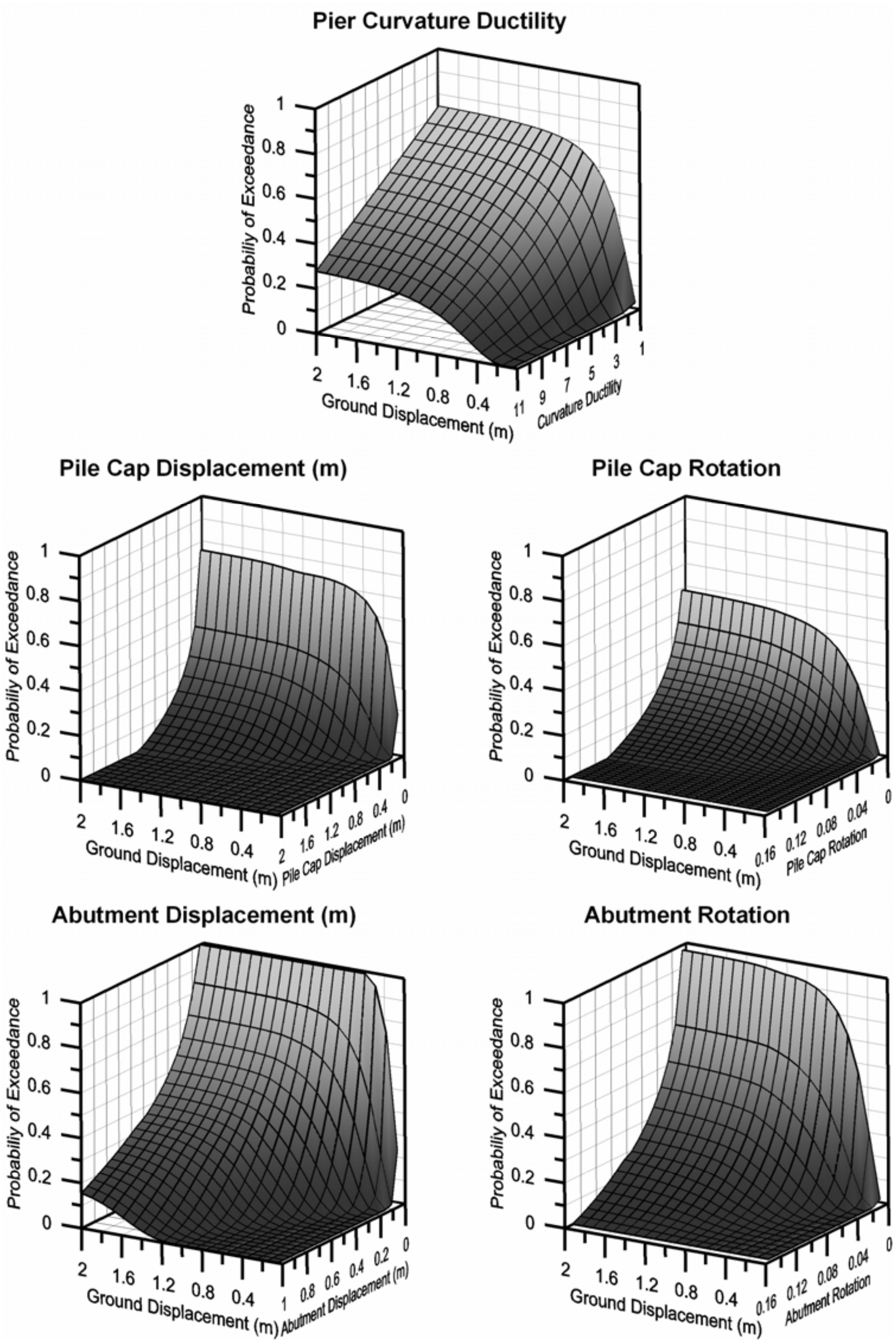
Pier Curvature Ductility

Pile Cap Displacement (m)

Pile Cap Rotation

Abutment Displacement (m)

Abutment Rotation

Figure 4.24: Fragility Surfaces for Post-1971 Continuous Bridges with Seat-type Abutments and Multi-Column Piers and 24” CISS piles

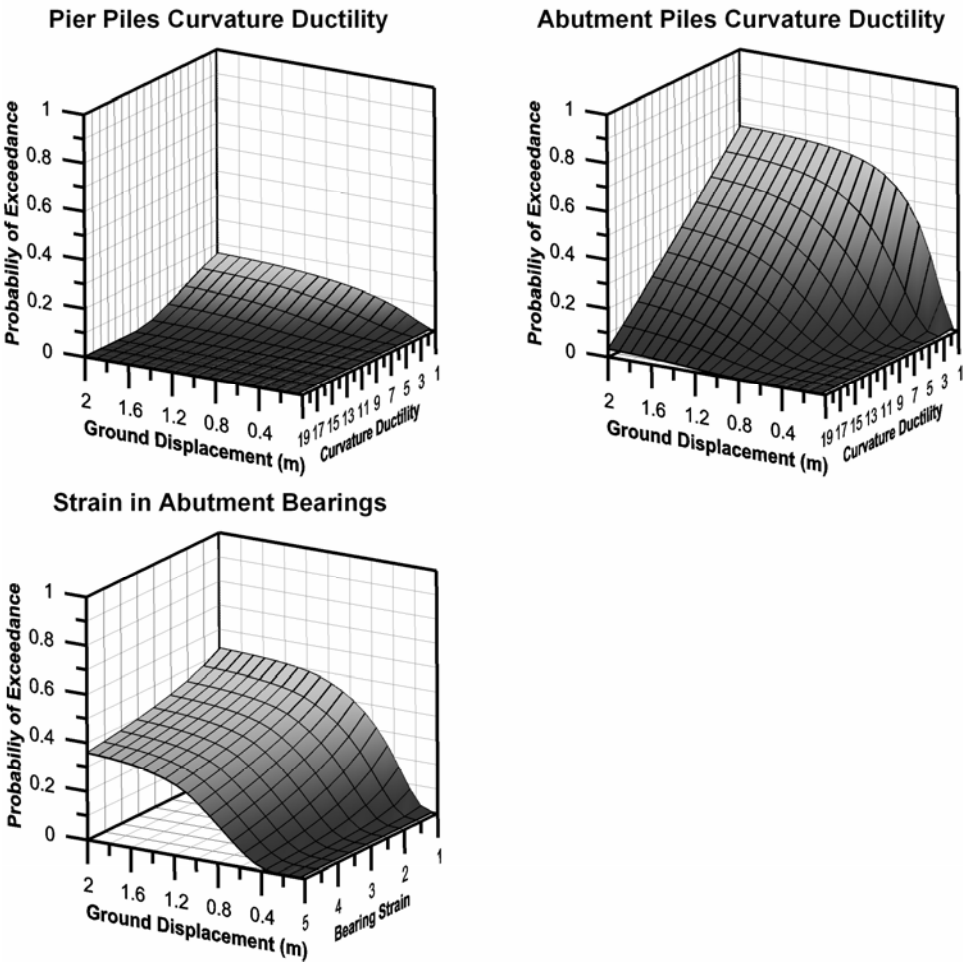

Figure 4.24: -Continued

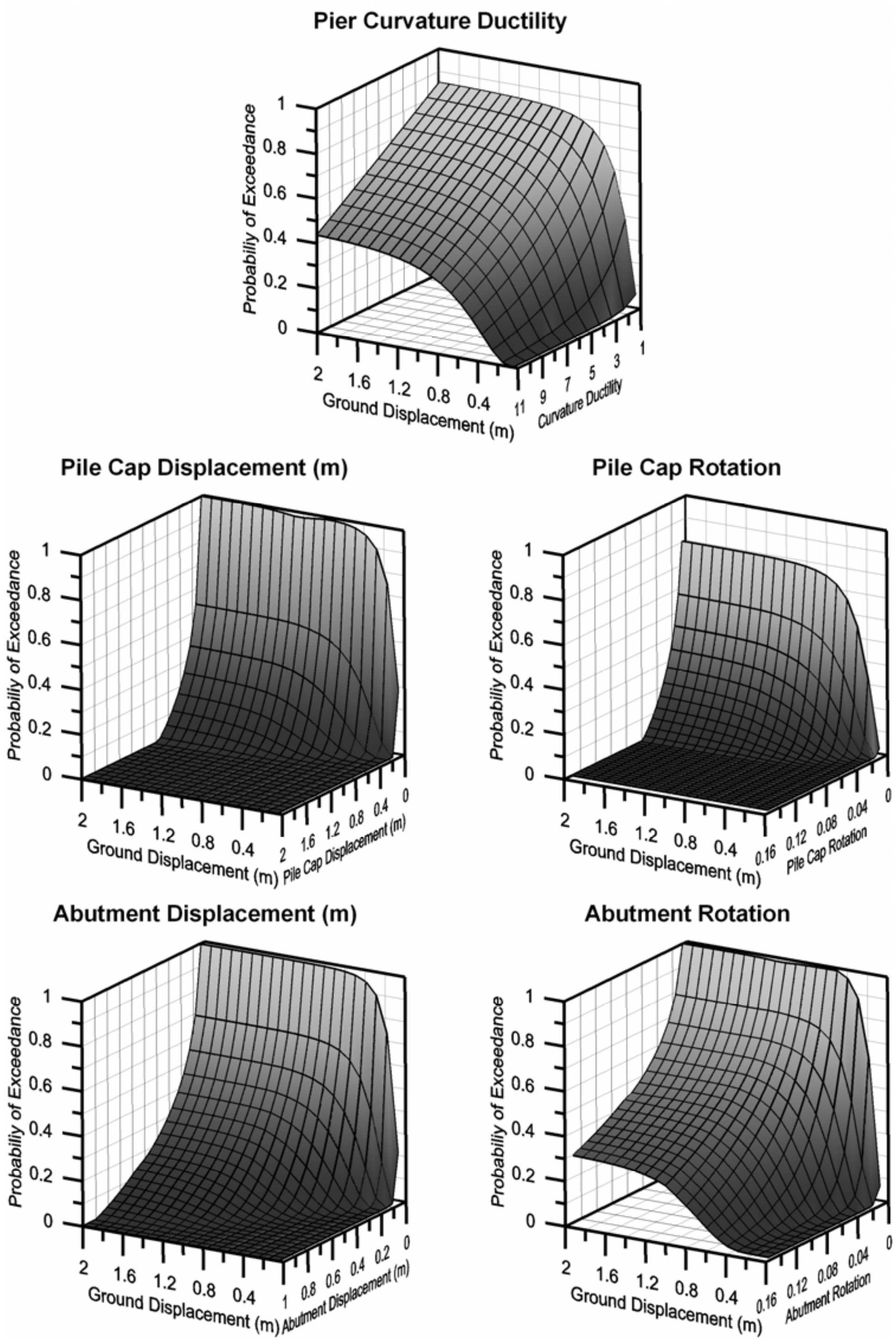

Figure 4.25: Fragility Surfaces for Post-1971 Continuous Bridges with Seat-type Abutments and Single-Column Piers and 15” Precast

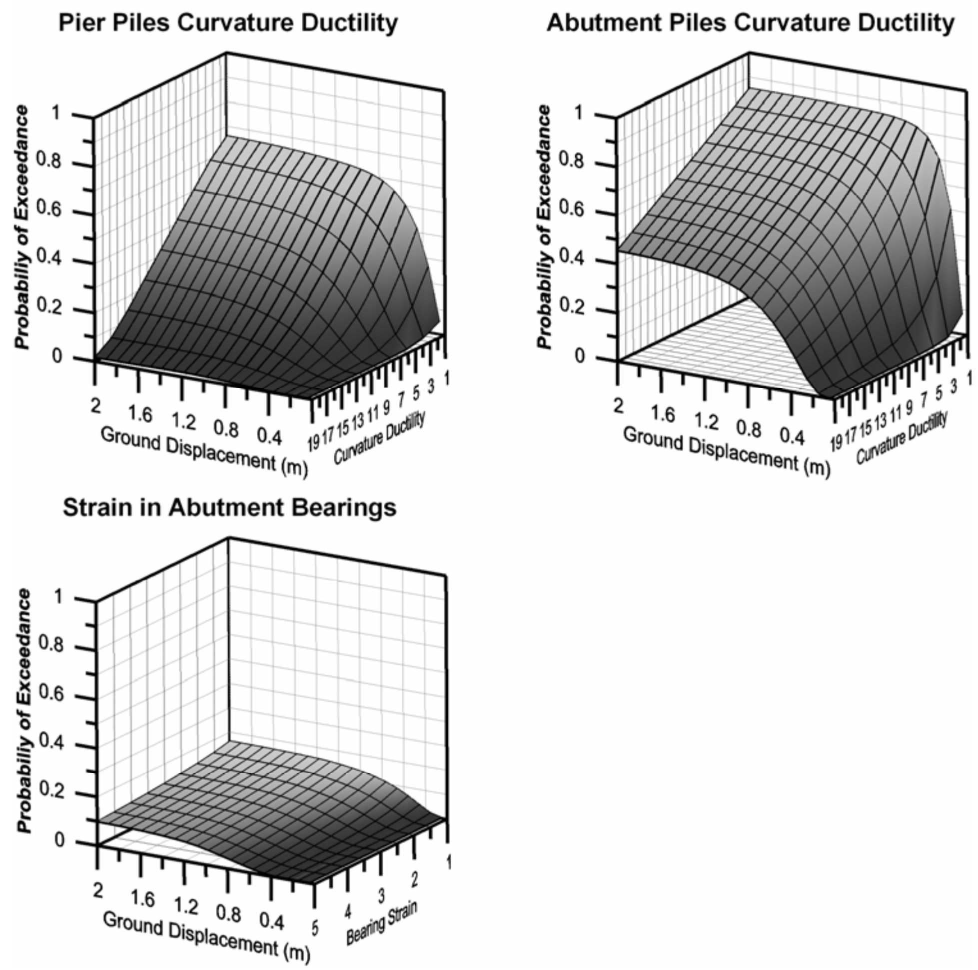

Figure 4.25: -Continued

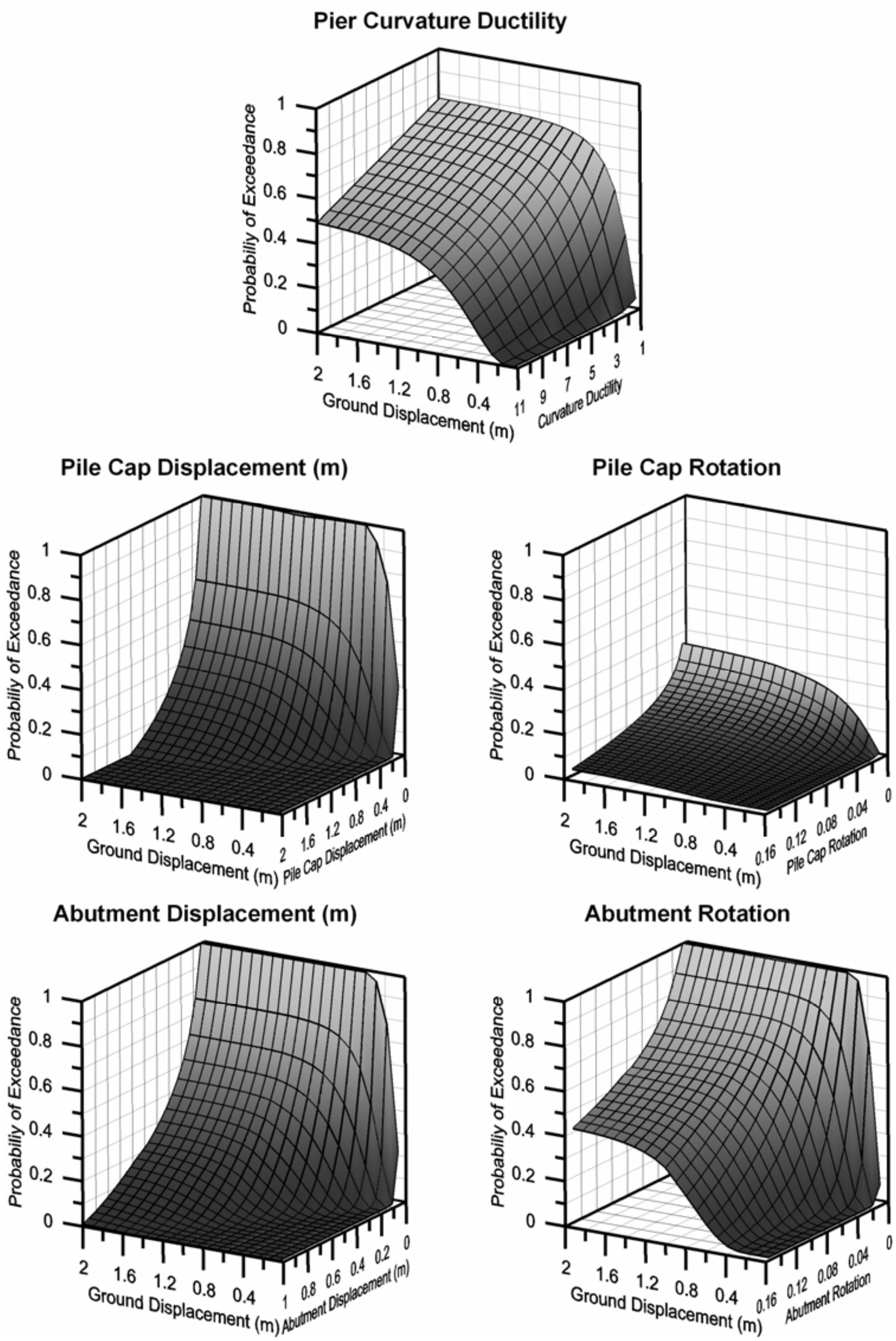
Pier Curvature Ductility

Pile Cap Displacement (m)

Pile Cap Rotation

Abutment Displacement (m)

Abutment Rotation

Figure 4.26: Fragility Surfaces for Post-1971 Continuous Bridges with Seat-type Abutments and Multi-Column Piers and 15” Precast

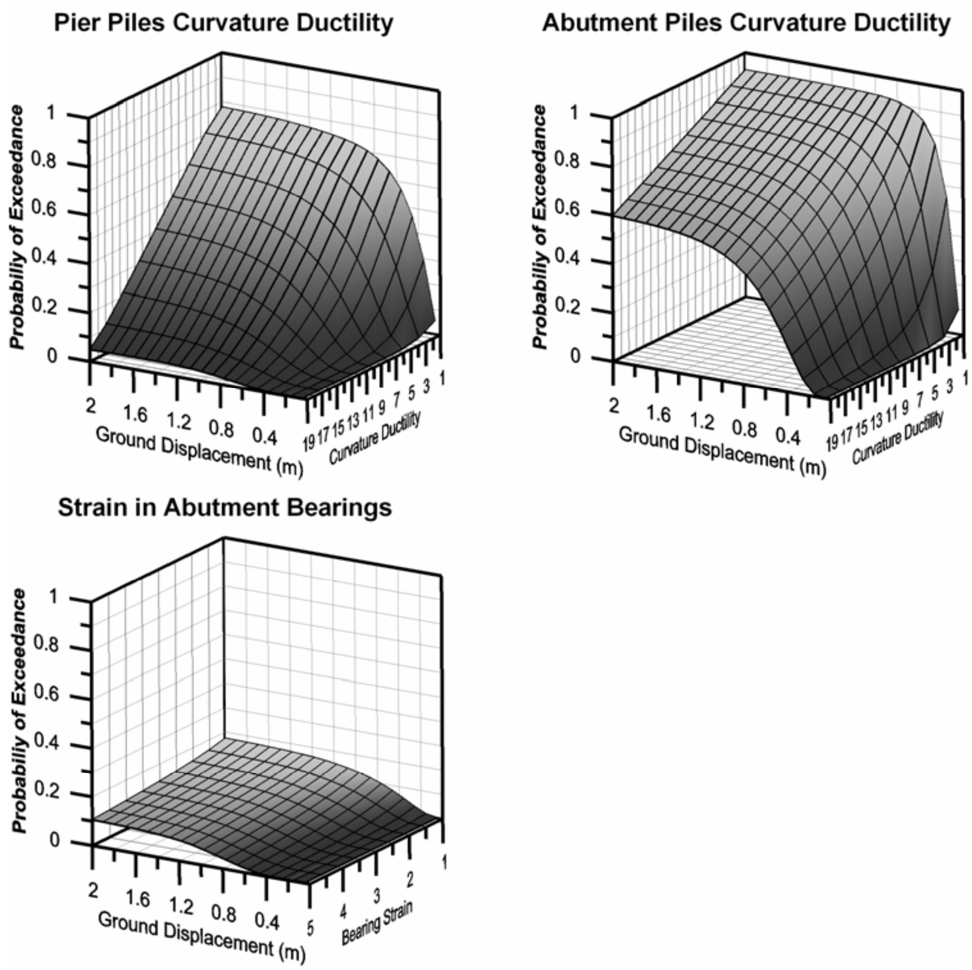
Pier Piles Curvature Ductility

Abutment Piles Curvature Ductility

Strain in Abutment Bearings

Figure 4.26: -Continued

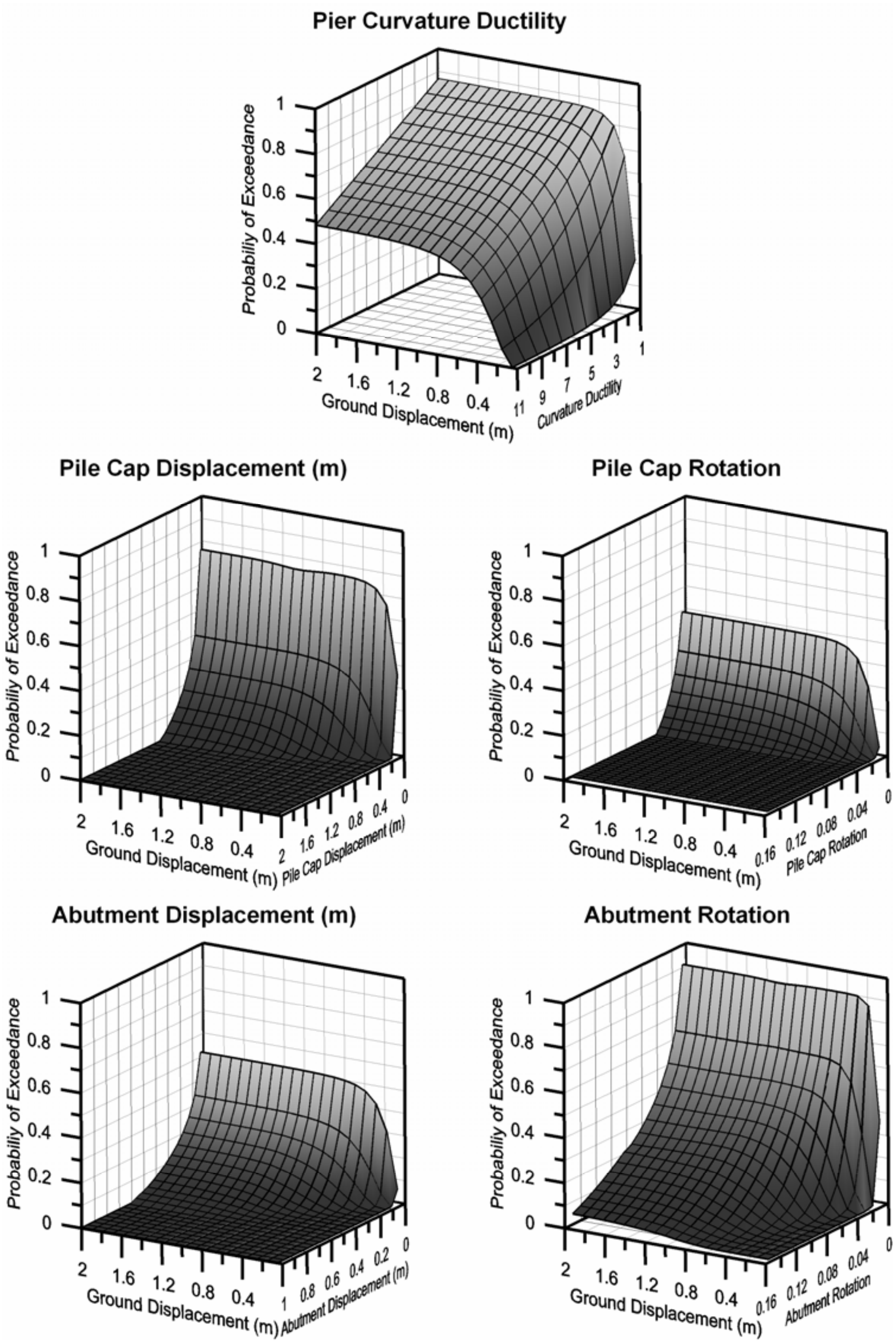

Figure 4.27: Fragility Surfaces for Pre-1971 Continuous Bridges with Seat-type Abutments and Single-Column Piers and 15” Precast

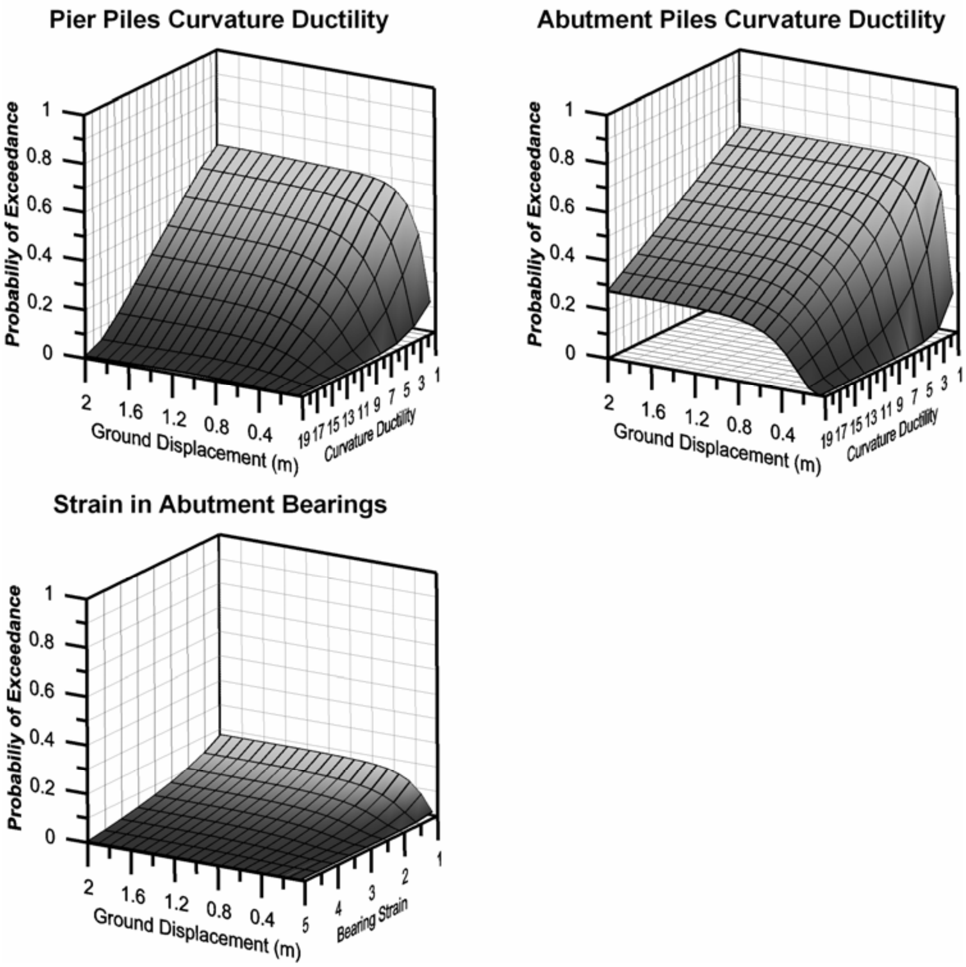

Figure 4.27: -Continued

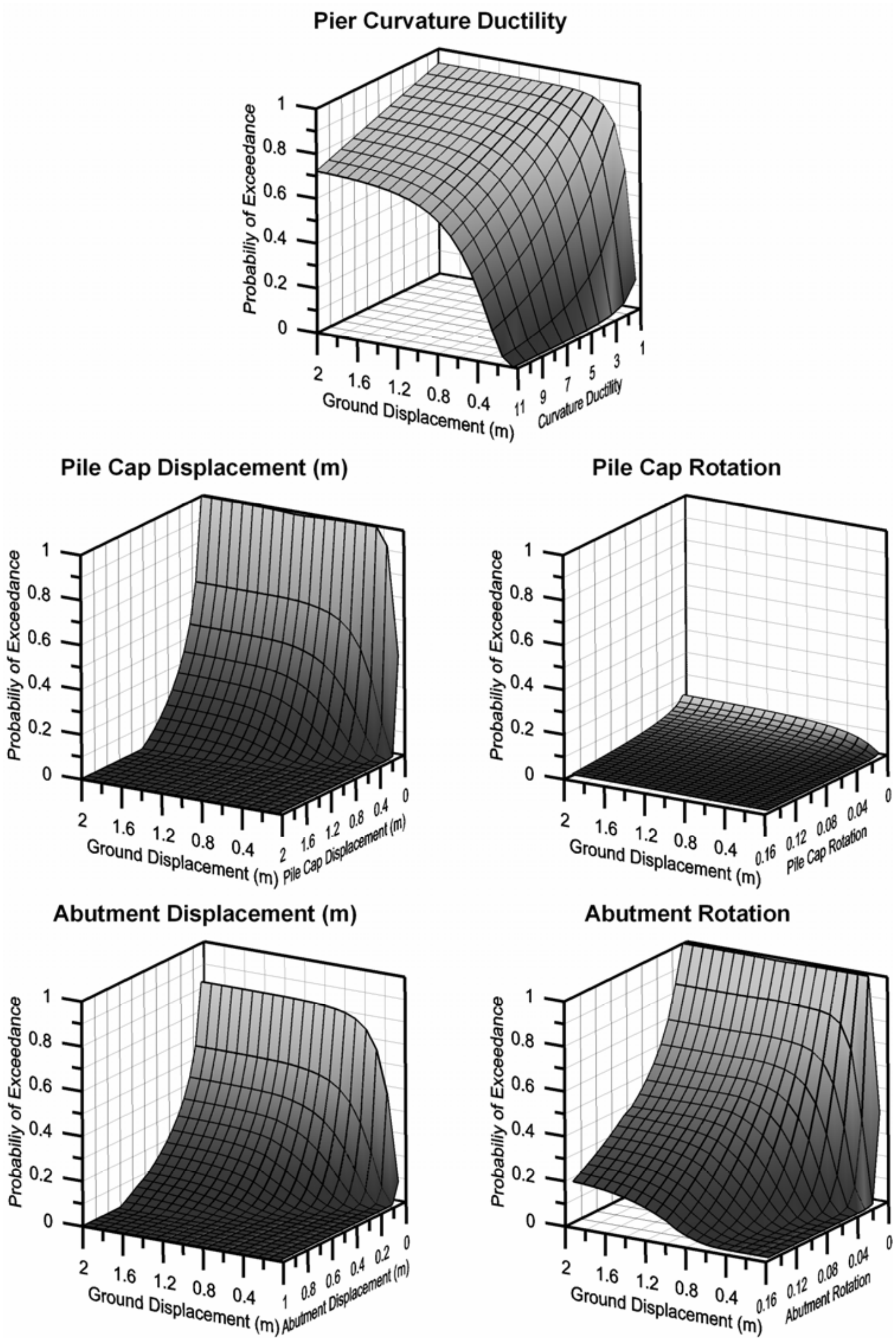

Pier Curvature Ductility

Pile Cap Displacement (m)

Pile Cap Rotation

Abutment Displacement (m)

Abutment Rotation

Figure 4.28: Fragility Surfaces for Pre-1971 Continuous Bridges with Seat-type Abutments and Multi-Column Piers and 15” Precast

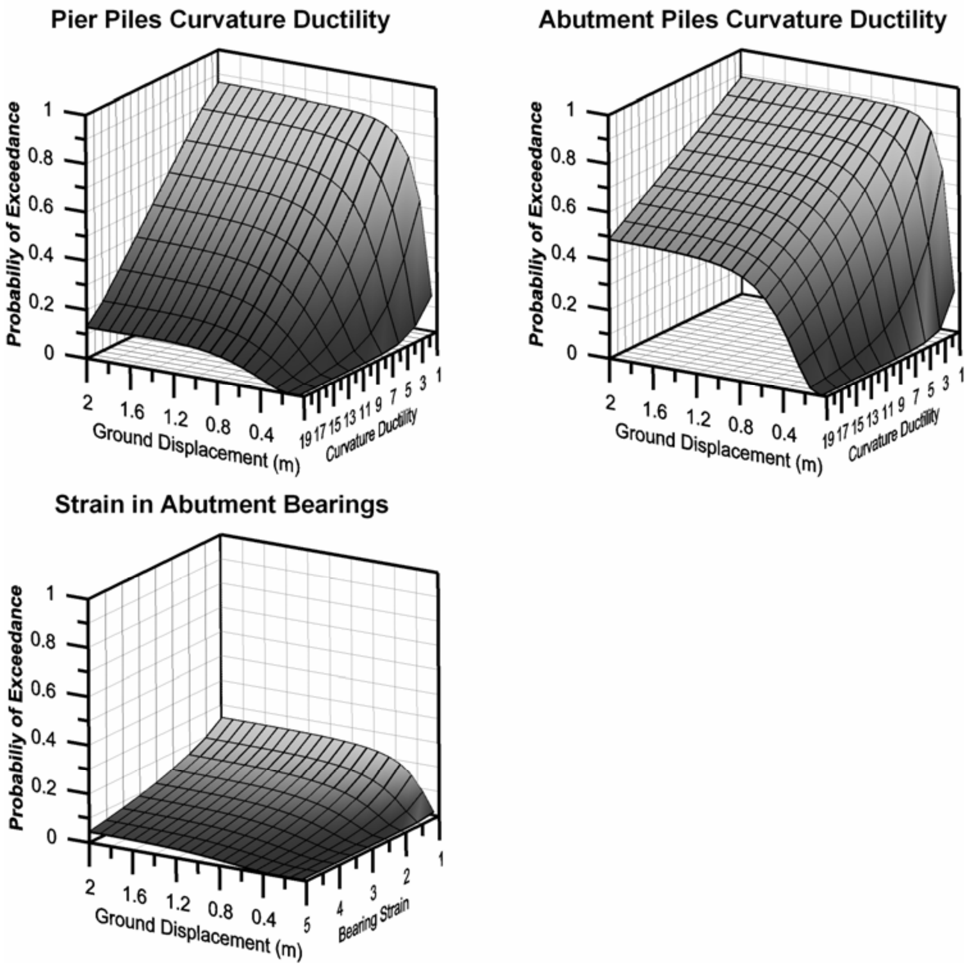

Figure 4.28: -Continued

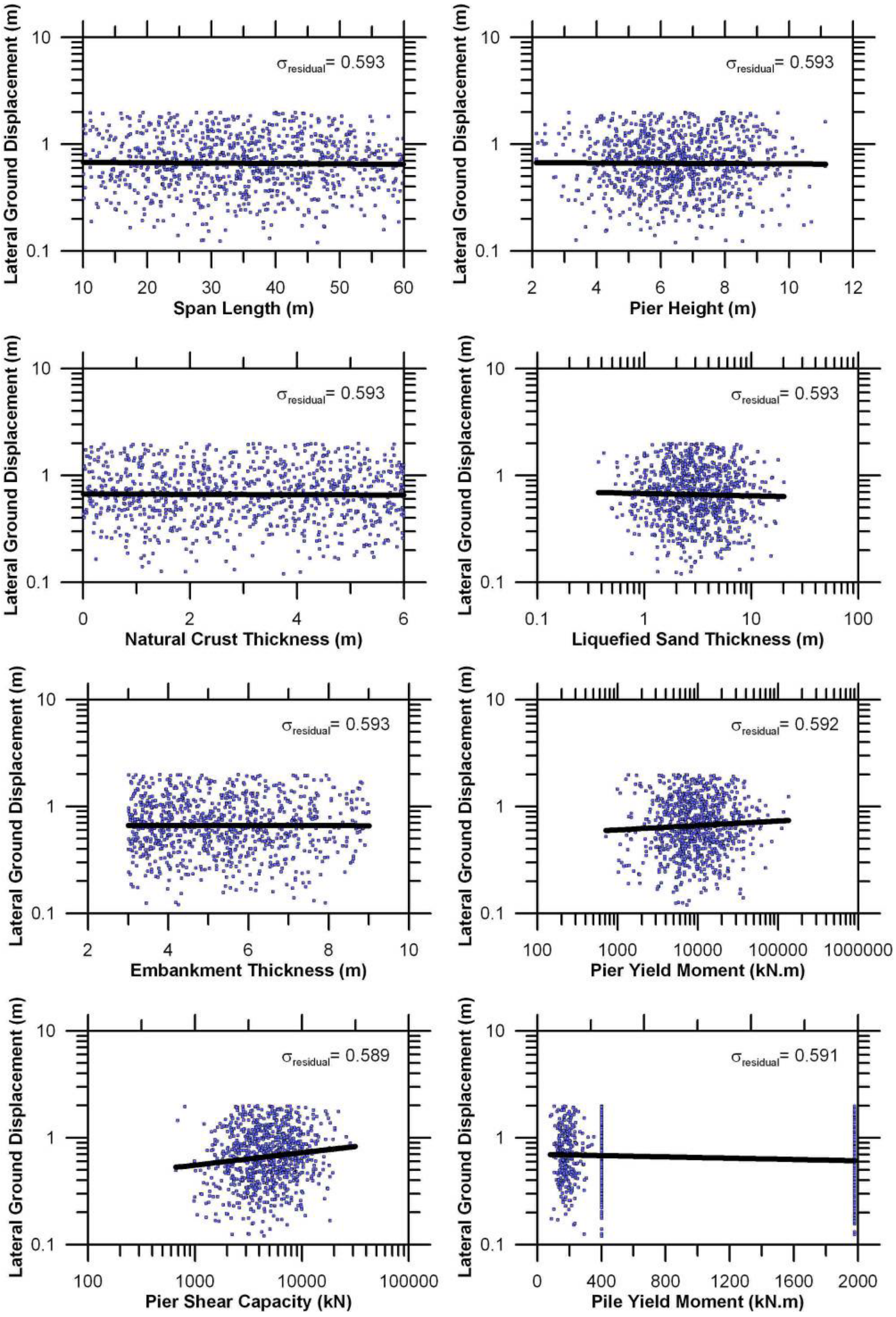

Figure 4.29: Disaggregation of input parameters at curvature ductility of 7 in post-1971 simply-supported bridges

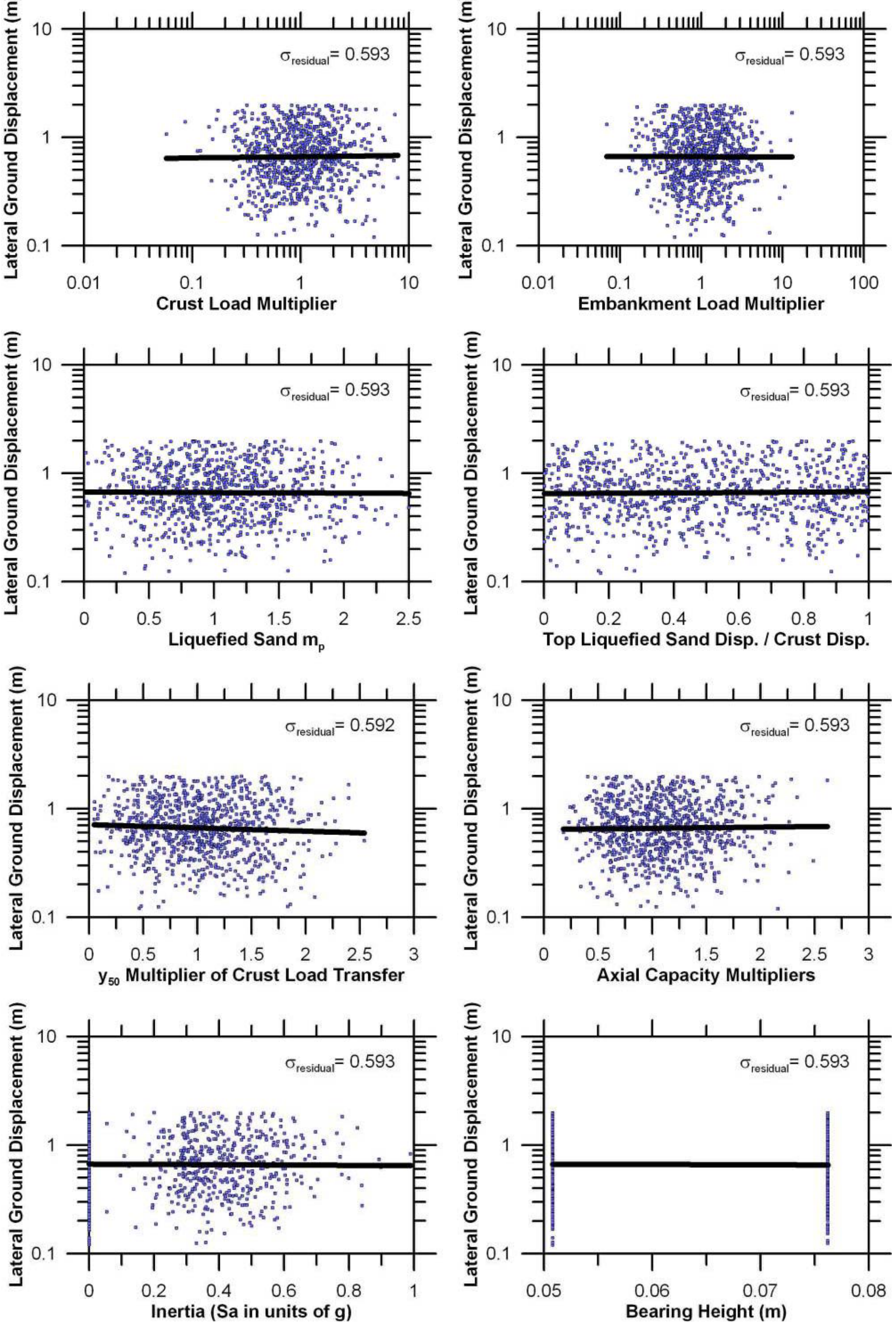

Figure 4.29: -Continued

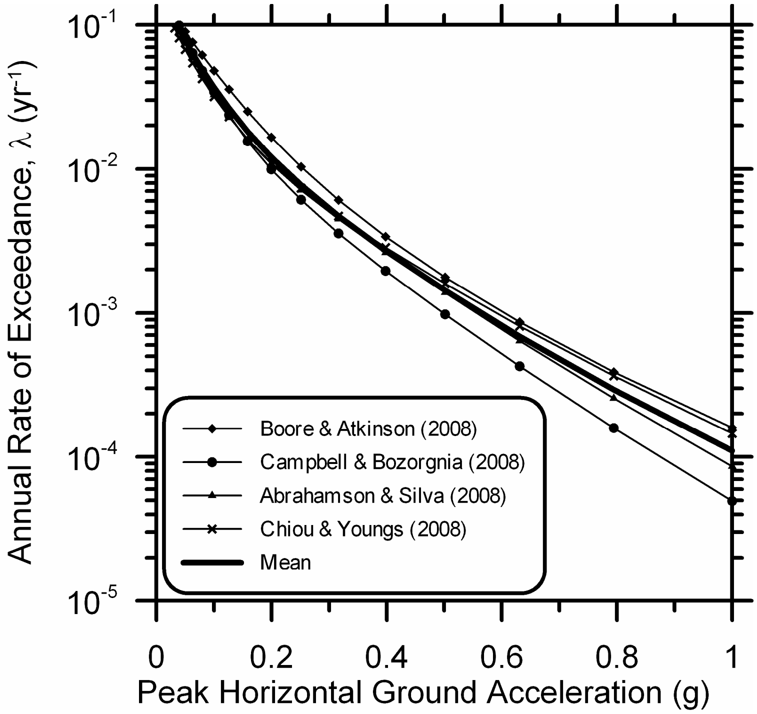

Figure 4.30: Hazard curves from probabilistic seismic hazard analysis of Santa Monica site.

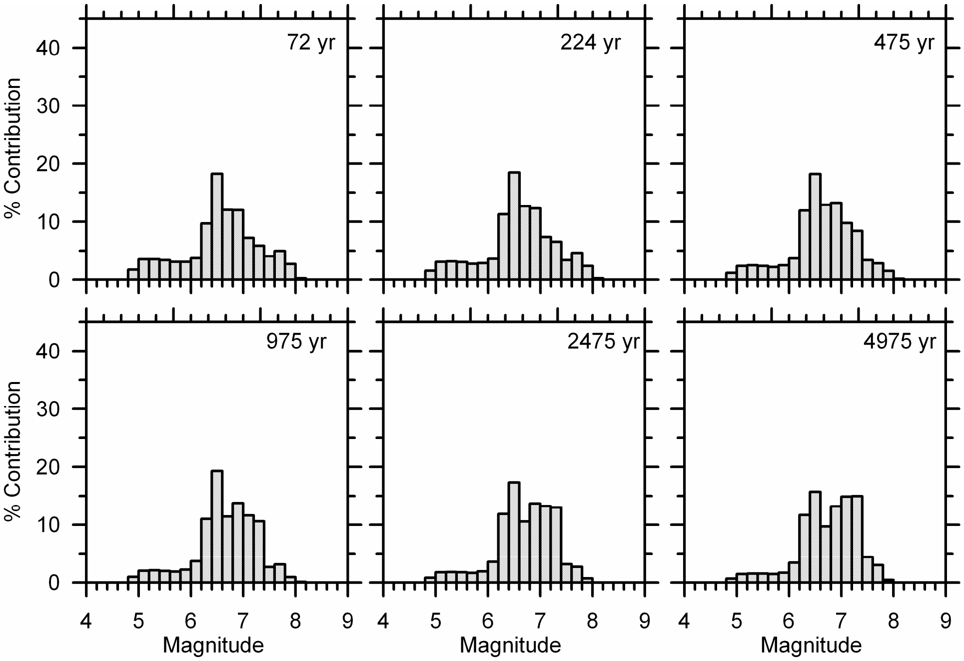

Figure 4.31: Distributions of magnitude contributions to seismic hazard

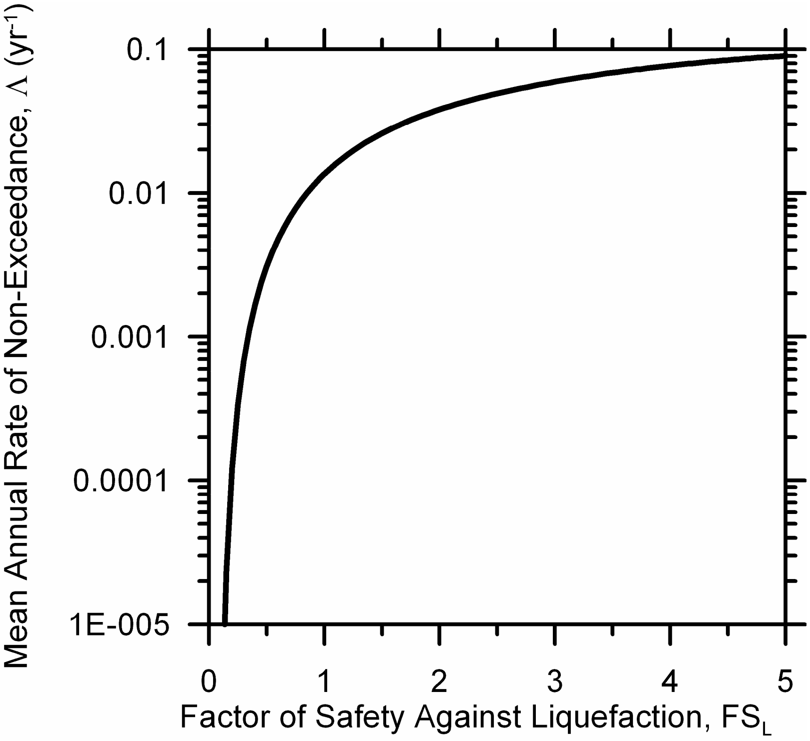

Figure 4.32: Liquefaction triggering hazard curve

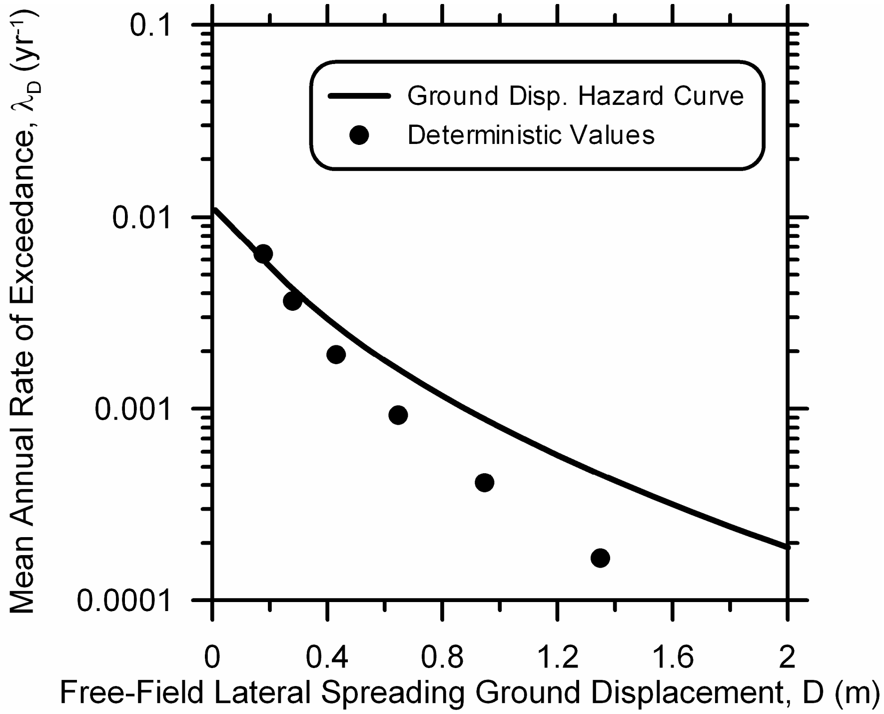

Figure 4.33: Free-field lateral spreading ground displacement hazard

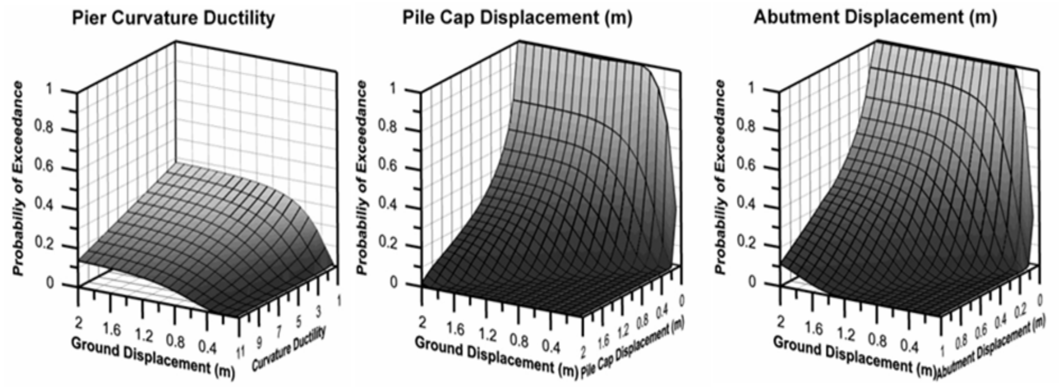

Figure 4.34: Demand fragility surfaces for post-1971 bridges with simply-supported spans, seat-type abutments, and 24” CIDH piles

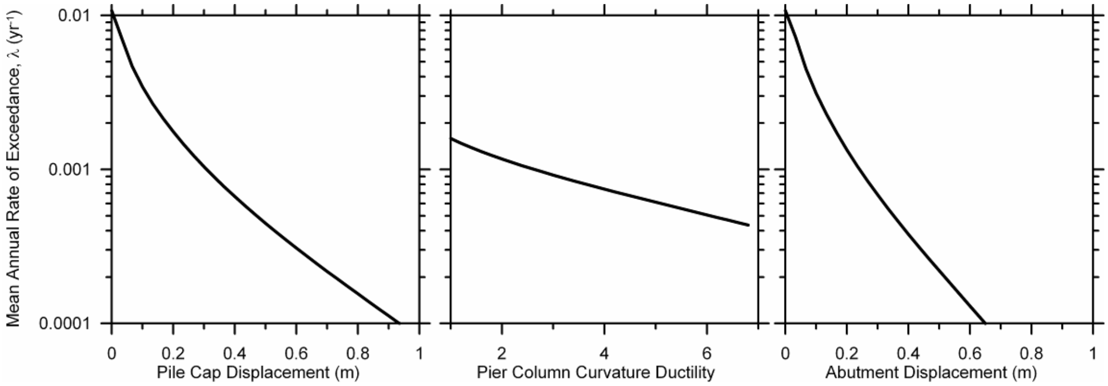

Figure 4.35: Mean annual rate of exceedance of pile cap displacement, pier column curvature ductility, and abutment displacement.

5 Summary, Conclusions and Future Work

5.1 *Summary and Scope of the Research*

The purpose of this research has been to evaluate the fragility of bridges in liquefied laterally spreading ground and generate demand fragility surfaces for different engineering demand parameters at a range of values for each of the engineering demand parameters typically of interest to the engineers and/or decision makers. The analyses have been performed numerically using the Finite Element Framework OpenSees developed by Pacific Earthquake Engineering Research Center. The method used to perform the finite element analyses is referred to "Global Equivalent Static Analysis Method" as outlined in detail in Chapter 2 of this dissertation. In this method the entire structural components of the bridge, at both the superstructure and the foundation level are modeled, and the lateral spreading displacement demands of the soil are modeled using nonlinear soil-structure (p-y, t-z, and q-z) springs. The method accounts for the effects of liquefaction by providing appropriate guidelines regarding load transfer mechanisms characteristic of liquefied laterally spreading grounds as well as the modifications of inertia demands for sites undergoing liquefaction, according to the findings of recent research. This method could be applied also in Local Equivalent Static Analyses were only a single component of the bridge is modeled, although local analyses generally perform poorly in predicting the proper “response” of the bridge, and should be used only for validation of the designs, in cases where the local analyses predict acceptable performance for design purposes.

In order to evaluate the fragility of the bridges, the bridges were classified into different classes based on vintage, structural configuration, number of columns per piers and pile type (for newer vintage bridges). To capture the variability in the bridge properties and site properties, the structural and geotechnical properties of the bridge were varied according to their corresponding distributions, estimated from available information (e.g. maximum span length from the National Bridge Inventory), and in some cases based on engineering judgment. For example, the moment, and shear capacity of the bridge piers were calculated using some normalized relationships that related the moment and shear capacity of the pier to the size of the pier as well as material properties and reinforcement ratios, while the sizing of the pier was based on the dead loads acting on the piers.

During the analyses, several engineering demand parameters such as pier curvature ductility, pile cap displacement and abutment displacements were controlled at certain values, by recording the maximum free-field ground displacements at those values. Fragility functions at each value of each of the engineering demand parameters were then generated by sorting the free-field ground displacement in increasing order, and calculating the cumulative probability by summing the probability mass of the analyses that mobilized the level of demand of interest. The demand probability function was simply the plot of the cumulative probability (probability of exceedance) versus the maximum free-field ground displacements.

The demand fragility surfaces for each EDP were generated by fitting a surface to the fragility functions at every individual values of the EDP. Six parameters were sufficient to fully describe the demand fragility surface for each of the parameters. This is a very convenient way of presenting the fit, since a table of coefficients is all that is needed to evaluate the probability of exceeding different demand levels for all of the EDPs any value of free-field ground displacements and at every value of engineering demand parameter for all the bridges within a class. This way the demand fragility surfaces could easily be utilized in a transportation network study or damage or loss analysis of the bridge.

In addition to the generation of the demand fragility surfaces for each EDP for the bridge, the correlations between the EDPs were also presented.

5.2 Research Findings and Conclusions

The findings of the research consist of the observed patterns of the response of the bridge in the deterministic global equivalent static analyses as well as the trends of the overall performance of the bridges within a class and in comparison to other classes of bridges, analyzed. Some of the most important conclusions are outlined here.

5.2.1 Findings of the Deterministic Global Static Analyses

One of the conclusions of the deterministic global equivalent static analyses is that the pattern of the lateral spreading is extremely important in the performance of the bridge. Unfortunately, the patterns of lateral spreading ground displacements observed in the cases histories have shown that ground displacement patterns in a site are often difficult to predict prior to an event of an earthquake. Therefore, it is imperative that several ground displacements patterns be considered when evaluating the performance of a bridge under such loads. As a result, in the evaluation of the fragility of the bridges within each class, the ground displacement pattern was treated as a varying input parameter.

Another observation from the deterministic analyses of the bridges was that while the demand is usually higher in the foundation of the spreading component the demand in the piers in the spreading components may be lower than the demands in the piers of the non-spreading component. For example, it was shown that in a case that the spreading was occurring in the left side of the bridge and at the left abutment and the left pier of a three-span bridge, the spreading at the abutment shifted the superstructure to the right, while the spreading at the left pier caused pile cap displacements in the left pier. Consequently, since the left pier was moved laterally both at the top and the bottom, very little demand was applied to the left pier and it stayed intact. On the other hand, in the non-spreading side of the bridge, the translation of the superstructure, without the spreading in the foundation, applied significant demands on the pier. This observation was also mentioned in Shin et al. (2008).

The shaking inertia demand on the bridge is an oscillatory demand that applies load on the bridge in different directions. However, in static analyses the inertia demand can only be applied in one direction during the analyses. Yet, it is not clear which direction of the inertia loads applies the maximum demand on the bridge. Therefore, it is recommended that for two-dimensional global analyses the inertia demand be applied in both longitudinal directions, since it was shown that sometimes applying the inertia load in the opposite direction of the spreading, imposes more demand in the piers. The same recommendation is applicable also to the local static analyses of a component of the bridge.

Furthermore, it was observed that the bridges with continuous superstructure and monolithic abutments typically mobilize less foundation displacements (pile cap displacement and abutment displacement) under the same load case relative to their simply-supported counterpart bridge with seat-type abutments, due to their higher stiffness at the pier level.

5.2.2 Findings of the Demand Fragility Surfaces

Comparison of the Demand Fragility Surfaces showed that for classes belonging to different era (i.e. pre-1971 versus post-1971), vintage plays a big role in the fragility of the bridges. This is primarily attributed to the fact that bridges built prior to 1971 typically had poor transverse reinforcement, which translated to lower moment and shear capacity in their piers. On the other hand, the piles used in older vintage bridges, were often not designed to perform well laterally. Thus, the pre-1971 bridges are often consistently weaker in both the super-structure (i.e. piers) and the foundation level. The demands on all components are generally higher for pre-1971 bridges.

Structure type is another important criterion that affects the performance of the bridge. The piers of the simply-supported bridges are free to rotate at the top which allows for more flexibility in the piers. As a result, the mobilized curvature ductility in the piers of the simply-supported bridges within any class is consistently lower than the bridges in the classes of continuous bridges with single-columns. On the other hand, the flexibility (i.e. lower stiffness) of the piers in the simply-supported bridges, allows for more displacements and rotations both at pile caps and at abutments.

Single-column continuous bridges tend to mobilize higher curvature ductility due to their double fixity, but generally foundation displacements and rotations are lower in them, due to having stiffer piers. Since multi-column continuous bridges have a pinned connection at the pile cap, they are less stiff than their single-column counterparts, however they allow for excessive pile cap displacements (because of the pin connection) which in turn result in mobilizing higher curvature ductility in their piers as well. Generally speaking multi-column continuous bridges are more fragile whether or not they have seat-type abutments or monolithic abutments.

Bridges with multi-columns tend to have higher moment and shear capacities relative to the bridges with single-column piers. As a result, the maximum mobilized curvature ductility in the piers of the simply-supported bridges and multiple columns is generally lower than the simply-supported bridges with single column piers since their connection types are the same for both single-columns and multi-columns. However, this means that demand is translated to other components more effectively, which results in more demand in every other component of the bridge (i.e. foundation components).

The effect of the pile type on the bridge performance is clearer when the piles are strong enough to withstand the lateral spreading demands. Consequently, some of the bridges with strong 24" CISS piles had very little pile cap and abutment displacements and rotations, if the piles stayed intact under lateral spreading.

Correlation tables were generated that related the correlation between different engineering demand parameters for simply-supported and continuous bridges. It was observed that the engineering demand parameters were more correlated with each other for continuous bridges. This is attributed to the relative stiffness of the continuous and simply-supported bridges. Stiffer continuous bridges are better able to transfer the demands. However the correlations are not as strong for continuous bridges with multi-column piers because of the pinned connection at the pile cap.

Disaggregation of the input parameters was also performed. The results of the disaggregation analyses showed that none of the input parameters is a dominant factor in the performance of the bridge.

The demand fragility surfaces, characterize the demand in different components of the bridge. If the demand was consistently higher or lower for all engineering demand parameters in a bridge class, the decision about the overall fragility of the bridge could have been made easily. However for bridges within an era, demand was often lower in a few engineering demand parameters and higher in other ones. As a result, the evaluating the overall performance of the bridge depends on the relative cost of the damage in different components of the bridge, in terms of life-safety, repair cost or downtime cost to the bridge.

5.3 Future Work

Since one of the goals of the research has been to develop a screening tool that would allow for evaluating the bridge performance using a few characteristics of the bridge, work is underway to utilize the characterization of the liquefaction and lateral spreading demands at the site of the bridge carried out in a separate study by Keith Knudsen and his colleagues at the California Geological Survey, in conjunction with the results of the demand fragility surfaces to develop a useful tool for screening and prioritize retrofit for the California bridges, using only a few peaces of information about the bridge.

Work is underway to evaluate the performance of the bridges using two-dimensional dynamic analyses with soil elements connected to the structure using soil-structure elements that account for generation of the pore pressures. The goal is to compare some of the findings of the global equivalent static analysis method with the dynamic method. Some of the epistemic uncertainty in the characterization of the parameters can be removed using dynamic methods, which improves the prediction of the performance of the bridge in liquefied laterally spreading ground. The dynamic analyses can also improve the issue of pinning at the abutments, since the limitations of the beam-on-nonlinear-Winkler foundation assumption, produces unrealistic demands on the piles in the abutments that are not likely to happen in reality.

REFERENCES

Abdoun, T., Dobry, R., O'Rourke, T. D., and Goh, S. H. (2003). "Pile response to lateral spreads: Centrifuge modeling." *J. Geotech. Geoenviron. Eng., ASCE.* 129(10), 869–878

American Petroleum Institute (API). (1993). *Recommended Practice for Planning, Design, and Constructing Fixed Offshore Platforms*. API RP 2A - WSD, 20th ed., American Petroleum Institute.

Ashford, S. A., and Rollins, K. M. (2002). *TILT: The Treasure Island Liquefaction Test: Final Report*, Report SSRP-2001/17, Department of Structural Engineering, University of California, San Diego.

Ashford, S.A., Juirnarongrit, T., (2006). "Push-over analyses of piles in laterally spreading soil." *Proceedings of Seismic Performance and Simulation of Pile Foundations in Liquefied and Laterally Spreading Ground Conf.* ASCE

Berrill, J.B., Christensen, S.A., Keenan, R.P., Okada, W., and Pettinga, J.R. (2001). "Case study of lateral spreading forces on a piled foundation." *Geotechnique*, 51(6). 501-517.

Boulanger, R.W., and Idriss, I.M., (2006). "Liquefaction Susceptibility Criteria for Silts and Clays." *J. of Geotech. Geoenviron. Eng.* 132(11). 1413-1426.

Boulanger, R. W., Kutter, B.L., Brandenberg, S.J., Singh, P., and Chang, D. (2003). “Pile foundations in liquefied and laterally spreading ground during earthquakes: centrifuge experiments and analyses.” Report No. UCD/CGM-03/01, University of California, Davis.

Boulanger, R. W., Wilson, D. W., Kutter, B. L., Brandenberg, S. J., and Chang, D. (2004). "Nonlinear FEM analyses of soil-pile interaction in liquefying sand." Proceedings, Geotechnical Engineering for Transportation Projects, Geotechnical Special Publication No. 126, M. K. Yegian and E. Kavazanjian, eds., ASCE, 470-478

Boulanger, R.W., Chang, D., Brandenberg, S.J., Armstrong, R.J., and Kutter, B.L. (2007). “Seismic design of pile foundations for liquefaction effects.” Earthquake Geotechnical Engineering, 4th International Conference on Earthquake Geotechnical Engineering – Invited Lectures, K.D. Pitilakis, ed., Springer, The Netherlands, 277-302.

Box, G. E. P. and Muller, M.E. *A Note on the Generation of Random Normal Deviates*, The Annals of Mathematical Statistics (1958), Vol. 29, No. 2 pp. 610-611

Brandenberg, S.J., Boulanger, R.W., Kutter, B.L., and Chang, D. (2007). "Liquefaction-induced softening of load transfer between pile groups and laterally spreading crusts." *J. of Geotech. Geoenviron. Eng.* 133(1). 91-103.

Brandenberg, S.J., Boulanger, R.W., Kutter, B.L., and Chang, D. (2007b). "Static pushover analyses of pile groups in liquefied and laterally spreading ground in centrifuge tests." *J. of Geotech. Geoenviron. Eng. 133(9). 1055-1066.*

Dobry, R., Taboada, V, and Liu., L. (1995). "Centrifuge modeling of liquefaction effects during earthquakes." *Proc. 1st Intl. Conf. On Earthquake Geotechnical Engineering*,

K. Ishihara, ed., Tokyo, Japan, Vol. 3, pp. 1291-1324.

Duncan, M. J., and Mokwa, R. L. (2001). "Passive earth pressures: Theories and tests." *J. of Geotechnical and Geoenviron. Eng.,* ASCE, Vol. 127(3), pp. 248-257.

Elgamal, A., Yan, L., Yang, Z., and Conte, J.P. (2008) “Three-dimensional seismic response of Humboldt Bay Bridge-Foundation-Ground system.” *J. Struct. Eng.*, 134(7), 1165-1176

Faris, A.T. (2004). “Probabilistic Models for Engineering Assessment of Liquefaction-Induced Lateral Spreading Displacements.” *Ph.D. dissertation*, University of California, Berkeley.

HAZUS (1999), Earthquake Loss Estimation, Technical Manual, National Institute of Building Sciences, Washington D.C.

Ishihara, K., (1985). “Stability of natural deposits durings earthquakes”. *Proc. 11th International Conference on Soil Mechanics and Foundation Engineering.*

Kayen, R., Pujol, S., Collins, B.D., Abrahamson, N., Ashford, S.A., Brandenberg, S.J., Dickenson, S., Johnson, L., Kabeyasawa, T., Kawamata, Y., Koumoto, H., Tanaka, Y., Marubashi, N., Tokimatsu, K., Tsai, B., Yanev, P., Yashinsky, M., and Yousok, K. (2007). "Preliminary Observations on the Niigata-Chuetsu Oki, Japan, Earthquake of July 16, 2007." *EERI-GEER Web Report 2007–1 v.6,* August.

Kiremidjian, A., Moore, J., Fan, Y.Y., Basoz, N., Yazali, O., and Williams, M. (2006) "Pacific Earthquake Engineering Research Center highway demonstration project." *Pacific Earthquake Engineering Research Center*, Report No. PEER 2006/02.

Kramer, S.L., Arduino, P., Shin, H. (2008) “Using OpenSees for Performance-Based Evaluation of Bridges on Liquefiable Soils.” *Pacific Earthquake Engineering Research Center*, Report No. PEER 2008/07 November 2008.

Lemnitzer, A., Ahlberg, E.R., Nigbor, R.L., Shamsabadi, A., Wallace, J.W., and Stewart, J.P. (2009). “Lateral performance of full-scale bridge abutment wall with granular backfill.” *J.Geotech. Geoenviron. Eng.* 135(4), 506-514.

LPILE Plus v5.0. A program for the analysis of piles and drilled shafts under lateral loads., Developed by ENSOFT, INC, *www.ensoftinc.com*

Malvick, E. J., Kutter, B. L., and Boulanger, R. W. (2008). "Postshaking shear strain localization in a centrifuge model of a saturated sand slope." Journal of Geotechnical and Geoenvironmental Engineering, ASCE, 134(2), 164-174.

Matlock, H. (1970). "Correlations of design of laterally loaded piles in soft clay." *Proc. Offshore Technology Conference*, Houston, TX, Vol 1, No.1204, pp. 577-594.

Mazindrani, Z.H., and Ganjali, M.H. (1997) “Lateral earth pressure problem of cohesive backfill with inclined surface.” *J. Geotech. Geoenviron. Eng.* ASCE, 123(2), 110-112.

McKenna, F., Scott, M.H., and Fenves, G.L. (2006). "Open system for earthquake engineering simulation user command-language manual." *Pacific earthquake engineering research center*, University of California, Berkeley. 465 p.

Mokwa, R. L., and Duncan, J. M. (2001). "Experimental evaluation of lateral-load resistance of pile caps." *J. Geotech. Geoenviron. Eng., ASCE.* 127(2) pp. 185-192.

Mononobe, N. and Matsuo, H. (1929). "On the determination of earth pressures during earthquakes." *Proceedings, World Engineering Congress, 9 p.*

Newmark, N. M. (1965). "Effects of earthquakes on dams and embankments." *Geotechnique*, London, 15(2), 139–160.

Okabe, S. (1926). "General theory of earth pressures." *Journal of the Japan Society of Civil Engineering*, Vol. 12(1).

Porter, K., Kennedy, R., and Bachman, R. (2007). "Creating fragility functions for performance-based earthquake engineering." *Earthquake Spectra*, 23(2), 471-489.

Rollins, K. M., and Sparks, A. (2002). "Lateral resistance of full-scale pile cap with gravel backfill." *J. Geotech. Geoenviron. Eng., ASCE.* 128(9), 711-723.

Rollins, K. M., Gerber, T.M., Lane, J.D., and Ashford, S.A. (2005). "Lateral Resistance of a Full-Scale Pile Group in Liquefied Sand." *J. of Geotechnical & Geoenvironmental Engrg.,* ASCE, Vol. 131, No.1, pp. 115-125.

SDC (2006), Caltrans Seismic Design Criteria 2006.

Shin, H., Arduino, P., Kramer, S. L., and Mackie, K. (2008). “Seismic response of a typical highway bridge in liquefiable soil.” *Proc. Geotechnical Earthquake Engineering and Soil Dynamics IV Conf.*, Sacramento, California, CD Rom.

Slide v 5.0 A program for slope stability analysis, Developed by Rocscience. www.rocscience.com

Tokimatsu, K., Suzuki, H., and Suzuki, Y. (2001). "Back-calculated p-y relation of liquefied soils from large shaking table tests." *Fourth International Conference on Recent Advances in Geotechnical Earthquake Engineering and Soil Dynamics*, S. Prakash, ed, University of Missouri – Rolla, paper 6.24.

Transportation Research Board (TRB). (2002). *Comprehensive specification for the seismic design of bridges.* National Cooperative Highway Research Program (NCHRP) Report 472, National Research Council, 47 pp

Wilson, D. W., Boulanger, R. W., and Kutter, B. L. (1998). "Signal processing for and analyses of dynamic soil-pile-interaction experiments." Proceedings, Centrifuge 98, Kimura, Kusakabe and Takemura, eds., Balkema, Rotterdam, 1: 135-140.

Wilson, D. W., Boulanger, R. W., and Kutter, B. L. (2000). "Seismic lateral resistance of liquefying sand." *J. of Geotechnical & Geoenvironmental Engrg.*, ASCE, Vol. 126, No.10, pp. 898-906.

Xtract, v.3.0.7. A program for the analysis of structural cross sections., Developed by TRC/Imbsen Software Systems. www.imbsen.com

Zhang, Y., Conte, J.P., Yang, Z., Elgamal, A., Bielak, J., and Acero, G. (2008). "Two-dimensional nonlinear earthquake response analysis of a bridge-foundation-ground system." *Earthquake Spectra*, 24(2), 343-386

Zhu, D. and Qian, Q. (2000). “Determination of passive earth pressure coefficients by themethod of triangular slices.” *Can. Geotech. J.*, 37(2), 485-491.